

Three-Nucleon  
Hadronic and Electromagnetic Reactions  
with  $\Delta$ -Isobar Excitation

Vom Fachbereich Physik  
der Universität Hannover

zur Erlangung des Grades  
Doktor der Naturwissenschaften  
– Dr. rer. nat. –

genehmigte Dissertation

von

Arnoldas Deltuva B.Sc. M.Sc.  
geboren am 16. Juli 1976 in Kazlų Rūdos sav., Litauen

(2003)

Referent: Prof. Dr. P. U. Sauer  
Korreferent: Prof. Dr. D. Zawischa  
Tag der Promotion: 13.11.2003

Gedruckt mit Unterstützung des Deutschen Akademischen Austauschdienstes

## Abstract

The description of few-nucleon systems in terms of a two-nucleon potential and a corresponding electroweak current of one- and two-nucleon nature has been quite successful in general. Disagreements remain in detail. They are indicators for necessary corrections of the employed dynamics. The standard hypothesis for resolving those disagreements is the addition of a three-nucleon potential to the Hamiltonian and of corresponding parts to the electroweak exchange current. This thesis follows that idea in a particular way: Beside nucleons the  $\Delta$ -isobar degree of freedom is considered explicitly in the description, i.e., in the Hilbert space and by use of a two-baryon coupled-channel potential and of a coupled-channel electroweak current. The  $\Delta$  isobar is the lowest resonance of the nucleon; it has spin and isospin  $\frac{3}{2}$ ; it shows up in a pronounced way in pion-nucleon scattering. In the three-nucleon system the  $\Delta$  isobar mediates an effective three-nucleon force beside two-nucleon effects and yields effective two- and three-nucleon contributions to the current. The thesis investigates to what extent mechanisms due to the virtual excitation of a  $\Delta$ -isobar are able to remove the discrepancies existing between the standard purely nucleonic description and experimental data. Three-nucleon hadronic reactions, i.e., elastic nucleon-deuteron scattering and nucleon-deuteron breakup, and three-nucleon electromagnetic reactions, i.e., nucleon-deuteron radiative capture and two- and three-body photo and electro disintegration of the three-nucleon bound state, are considered. The available reaction energy remains below pion-production threshold.

A new realistic coupled-channel potential CD Bonn +  $\Delta$  is constructed; it is an extension of the purely nucleonic charge-dependent CD Bonn potential; its  $\chi^2/\text{datum} = 1.02$  is as good as for the best existing purely nucleonic potentials. The employed electroweak current is adapted to the coupled-channel potential as much as possible. In contrast to traditional irreducible three-nucleon forces and to irreducible two- and three-nucleon contributions to the electroweak current, based solely on pion exchange, the effective nucleonic forces and the effective nucleonic electroweak currents arising from the coupled-channel potential take exchanges of pion, rho, omega and sigma mesons into account; the coupled-channel potential and the coupled-channel electroweak current make all those effective nucleonic contributions mutually consistent.

A novel momentum-space technique for solving the three-baryon bound-state and scattering equations exactly is developed. The technique is applicable to any two-baryon potential, however, not to Coulomb with its long range. It is based on the expansion of the two-baryon transition matrix and of the deuteron wave function in terms of Chebyshev polynomials. The Chebyshev expansion is found to be highly efficient, reliable when used for interpolation and systematic.

The new coupled-channel potential and the new technique for solving three-particle equations are the theoretical backbone of the thesis. Selected results of calculations are compared with the available experimental data of the three-nucleon bound state and of the considered three-nucleon reactions. The coupled-channel potential yields additional binding in the three-nucleon bound state, but it remains unable to account for its binding in full. In all reactions  $\Delta$ -isobar effects are very small at low energies, except for observables scaling with three-nucleon binding. Thus, long-standing discrepancies like the  $A_y$ -puzzle of elastic nucleon-deuteron scattering around 10 MeV nucleon lab energy and the space star anomaly in nucleon-deuteron breakup around 13 MeV nucleon lab energy cannot be resolved. The  $\Delta$ -isobar effects become more visible at higher energies; they are often beneficial for a satisfactory description of the experimental data, e.g., they significantly reduce the discrepancies for the differential cross section and for the nucleon analyzing power of elastic nucleon-deuteron scattering above 100 MeV nucleon lab energy, though their success is not a general one for all measured observables.

**Keywords:** Three-nucleon system, baryon-baryon interaction,  $\Delta$ -isobar excitation



## Kurzzusammenfassung

Die Beschreibung von Wenignukleonen Systemen, basierend auf einem Zweinukleonen Potential und einem entsprechenden elektroschwachen Strom von Ein- und Zweinukleonen Natur, ist im allgemeinen ziemlich erfolgreich. Es gibt aber auch einige Ausnahmen, die auf die Notwendigkeit für Korrekturen in der benutzten Dynamik hinweisen. Die übliche Korrektur ist die Ergänzung des Hamiltonoperators durch eine Dreinukleonen Kraft und die Hinzunahme eines entsprechenden Strombeitrags. Diese Arbeit folgt dieser Idee auf eine besondere Weise: Neben Nukleonen wird auch das  $\Delta$ -Isobar explizit berücksichtigt, d.h. im Hilbertraum, durch Benutzung eines Zweibaryonen-Potentials mit Kanalkopplung und eines elektroschwachen Stroms mit Kanalkopplung. Das  $\Delta$ -Isobar ist die niedrigste Resonanz des Nukleons; es hat Spin und Isospin  $\frac{3}{2}$ ; es wird besonders in der Pion-Nukleon Streuung sichtbar. Im Dreinukleonen System liefert das  $\Delta$ -Isobar eine effektive Dreinukleonen Kraft neben Zweinukleonen Effekten und effektive Zwei- und Dreinukleonen Beiträge zum Strom. Diese Arbeit untersucht, inwieweit die existierenden Diskrepanzen zwischen der rein nukleonischen Standardbeschreibung und experimentellen Daten durch die von dem  $\Delta$ -Isobar vermittelten effektiven Kräfte und Ströme behoben werden können. Hadronische Dreinukleonen Reaktionen, d.h., elastische Nukleon-Deuteron Streuung und Nukleon-Deuteron Aufbruch, sowie elektromagnetische Dreinukleonen Reaktionen, d.h., Nukleon-Deuteron Strahlungseinfang und Zwei- und Dreikörper Photo- und Elektrodisintegration des Dreinukleonen Bindungszustandes, werden betrachtet. Die Reaktionsenergien verbleiben unterhalb der Pionenproduktionsschwelle.

Ein neues realistisches Potential mit Kanalkopplung CD Bonn +  $\Delta$  ist in dieser Arbeit konstruiert; es ist eine Erweiterung des rein nukleonischen ladungsabhängigen CD Bonn Potentials; sein Fehlerquadrat  $\chi^2/\text{datum} = 1.02$  ist so gut wie bei den besten rein nukleonischen Potentialen. Während die traditionellen irreduziblen Dreinukleonen Kräfte und irreduziblen Zwei- und Dreinukleonen Ströme gewöhnlich auf den Austausch des Pions beschränkt sind, berücksichtigen die von dem neuen Potential durch  $\Delta$ -Isobar Anregung vermittelten effektiven nukleonischen Kräfte und die effektiven nukleonischen elektroschwachen Ströme den Austausch von Pion, Rho, Omega und Sigma Mesonen. Das Potential mit Kanalkopplung und der elektroschwache Strom mit Kanalkopplung machen alle effektiven nukleonischen Beiträge gegenseitig konsistent.

Ein neues Verfahren zur exakten Lösung der Dreibaryonen Gleichungen im Impulsraum ist in der vorliegenden Arbeit entwickelt. Das Verfahren ist anwendbar auf beliebige Zweibaryonen Potentiale, aber nicht auf das langreichweitige Coulomb Potential. Das Verfahren basiert auf der Darstellung der Zweibaryonen Übergangsmatrix und der Deuteron Wellenfunktion durch Chebyshev Polynome. Diese Darstellung erlaubt eine effiziente und verlässliche Interpolation, und sie ist systematisch.

Das neue Potential mit Kanalkopplung und das neue Verfahren zur Lösung der Dreiteilchen Gleichungen bilden das theoretische Rückgrat der Arbeit. Ausgewählte Ergebnisse der Rechnungen werden mit den experimentellen Daten für Dreinukleonen Observable verglichen. Das Potential mit Kanalkopplung liefert zusätzliche Bindung im Dreinukleonen Bindungszustand, kann aber trotzdem den experimentellen Wert der Bindungsenergie nicht exakt reproduzieren. In allen Reaktionen sind die  $\Delta$ -Isobar Effekte sehr klein bei niedrigen Energien, bis auf die Observablen, die mit der Bindungsenergie skalieren. Somit können die schon seit langem bestehenden Diskrepanzen, wie die sogenannte  $A_y$ -puzzle in der elastischen Nukleon-Deuteron Streuung bei 10 MeV Nukleon Laborenergie und die *Space Star* Anomalie im Nukleon-Deuteron Aufbruch bei 13 MeV Nukleon Laborenergie, nicht behoben werden. Die  $\Delta$ -Isobar Effekte werden größer bei höheren Energien; sie verbessern oft die Übereinstimmung zwischen den theoretischen Vorhersagen und den experimentellen Daten, z.B., sie verringern merklich die Diskrepanz im differentiellen Wirkungsquerschnitt und in der Nukleon Analysierstärke der elastischen Nukleon-Deuteron Streuung oberhalb 100 MeV Laborenergie des Nukleons. Es gibt jedoch auch einige Observable, für die das  $\Delta$ -Isobar keine Verbesserung der Beschreibung liefert.

**Schlagwörter:** Dreinukleonen System, Baryon-Baryon Wechselwirkung,  $\Delta$ -Isobar Anregung



# Contents

<b>1</b>	<b>Introduction</b>	<b>1</b>
<b>2</b>	<b>Three-Nucleon Dynamics with <math>\Delta</math>-Isobar Excitation</b>	<b>5</b>
2.1	Hilbert Space . . . . .	5
2.2	Hamiltonian . . . . .	7
2.3	Coupled-Channel Potential . . . . .	8
2.3.1	Fit of New Realistic Coupled-Channel Potential . . . . .	9
2.3.2	Effective Phenomena in Three-Nucleon System . . . . .	13
2.4	Electromagnetic Interaction . . . . .	14
2.4.1	Coupled-Channel One-Baryon and Two-Baryon Current . . . . .	15
2.4.2	Effective Nucleonic Currents . . . . .	17
<b>3</b>	<b>Three-Particle Equations: Nucleons and Single <math>\Delta</math>-Isobar Excitation</b>	<b>19</b>
3.1	Three-Nucleon Bound State . . . . .	19
3.2	Three-Nucleon Scattering . . . . .	20
3.3	Three-Nucleon Electromagnetic Reactions . . . . .	22
3.4	Charge-Dependent Two-Baryon Transition Matrix . . . . .	24
<b>4</b>	<b>Hadronic Properties of Three-Nucleon Bound State</b>	<b>25</b>
<b>5</b>	<b>Nucleon-Deuteron Scattering</b>	<b>27</b>
5.1	Spin-Averaged and Spin-Dependent Cross Sections . . . . .	27
5.1.1	Elastic Nucleon-Deuteron Scattering . . . . .	28
5.1.2	Nucleon-Deuteron Breakup . . . . .	29
5.2	Calculational Advances . . . . .	30
5.2.1	Chebyshev Expansion . . . . .	30
5.2.2	Solution of Three-Particle Equations . . . . .	32
5.2.3	Comparison of Different Potentials . . . . .	33
5.3	Results . . . . .	34
5.3.1	Elastic Nucleon-Deuteron Scattering . . . . .	36
5.3.2	Nucleon-Deuteron Breakup . . . . .	43
<b>6</b>	<b>Three-Nucleon Photo Reactions</b>	<b>49</b>
6.1	Spin-Averaged and Spin-Dependent Cross Sections . . . . .	49
6.1.1	Nucleon-Deuteron Radiative Capture . . . . .	50
6.1.2	Two-Body Photo Disintegration of Trinucleon Bound State . . . . .	51
6.1.3	Three-Body Photo Disintegration of Trinucleon Bound State . . . . .	51

6.1.4	Total Photo Disintegration Cross Section . . . . .	52
6.2	Results . . . . .	53
6.2.1	Standard Calculational Procedure . . . . .	53
6.2.2	Nucleon-Deuteron Radiative Capture . . . . .	54
6.2.3	Three-Body Photo Disintegration of Three-Nucleon Bound State . . . . .	57
6.3	Shortcomings of the Description . . . . .	59
6.3.1	Shortcomings of the Theoretical Form of the Cross Section . . . . .	59
6.3.2	Shortcomings of the Dynamics . . . . .	60
6.3.3	Shortcomings of the e.m. Current . . . . .	61
<b>7</b>	<b>Electron Scattering from Trinucleon Bound State</b>	<b>67</b>
7.1	Spin-Averaged and Spin-Dependent Cross Sections . . . . .	67
7.1.1	Two-Body Electro Disintegration of Trinucleon Bound State . . . . .	68
7.1.2	Three-Body Electro Disintegration of Trinucleon Bound State . . . . .	69
7.1.3	Inclusive Electron Scattering from Trinucleon Bound State . . . . .	70
7.2	Results . . . . .	71
7.3	Shortcomings of the Description . . . . .	74
<b>8</b>	<b>Perturbation Theory</b>	<b>75</b>
8.1	General Formalism of Perturbation Theory . . . . .	75
8.2	Validity of Perturbation Theory . . . . .	76
8.2.1	$\Delta$ -Isobar Degrees of Freedom . . . . .	76
8.2.2	Charge Dependence of Hadronic Interaction . . . . .	79
8.2.3	Higher Two-Baryon Partial Waves . . . . .	82
8.3	Use of Perturbation Theory . . . . .	84
<b>9</b>	<b>Conclusions</b>	<b>85</b>
<b>A</b>	<b>Parameters and Special Properties of the Coupled-Channel Potential</b>	<b>89</b>
<b>B</b>	<b>Coupled-Channel Current Operators</b>	<b>93</b>
B.1	One-Baryon Operators in Nonrelativistic Order . . . . .	93
B.2	Two-Baryon Operators in Nonrelativistic Order . . . . .	94
B.3	Operator Corrections of Lowest Relativistic Order . . . . .	96
<b>C</b>	<b>Numerical Solution of Three-Particle Equations</b>	<b>97</b>
C.1	Chebyshev Interpolation . . . . .	97
C.1.1	Two-Baryon Transition Matrix and Deuteron Wave Function . . . . .	99
C.1.2	Three-Particle Equations . . . . .	101
C.1.3	Calculation of Chebyshev Coefficients . . . . .	104
C.2	Treatment of Singularities . . . . .	105
C.2.1	Deuteron Bound-State Pole . . . . .	106
C.2.2	Kinematical Singularities . . . . .	106
C.2.3	Numerical Integration by Special Weights . . . . .	109
C.3	Spline Interpolation . . . . .	109
C.4	Padé Summation . . . . .	110



---

<b>D</b>	<b>Scattering Observables</b>	<b>113</b>
D.1	Spin-Dependent Observables . . . . .	113
D.1.1	Elastic Nucleon-Deuteron Scattering . . . . .	113
D.1.2	Nucleon-Deuteron Breakup . . . . .	115
D.1.3	Electromagnetic Reactions . . . . .	116
D.2	Problem in the Comparison of Theoretical Predictions and Experimental Data for Breakup . . . . .	116
<b>E</b>	<b>Calculation of Current Matrix Elements</b>	<b>119</b>
E.1	Multipole Decomposition of Current . . . . .	119
E.2	Instability Problem in Calculation of Current Matrix Elements . . . . .	120
	<b>Bibliography</b>	<b>123</b>



# 1

## Introduction

The three-nucleon system has played and still plays an important role in the development of understanding the forces between nucleons. Though from a present point of view quarks and gluons are the elementary strongly-interacting particles which build mesons, nucleons and other baryons and though the nuclear forces are believed to be effective interactions resulting from the fundamental quark-gluon interaction, the underlying theory, i.e., quantum chromodynamics, has not yet been successfully applied for a quantitative explanation of low-energy nuclear phenomena in general and of nuclear forces in particular. Instead, the construction of nuclear forces is based on effective non-fundamental interactions, i.e., on meson exchange between the nucleons, supplemented by phenomenological assumptions. The resulting potential models for the nucleon-nucleon ( $NN$ ) force contain a number of free parameters which are fitted to the two-nucleon data; the three-nucleon system, being simple enough to be solved exactly and at the same time being rich physicswise, provides an excellent field to test such semi-phenomenological interaction models in a nontrivial way.

A mathematically rigorous three-particle quantum scattering theory was developed in 1960 by L. D. Faddeev [1], who proposed a set of coupled integral equations with a compact kernel which have a unique solution in contrast to earlier formulations based on the Lippmann-Schwinger formalism; in addition, the Faddeev equations simplified also the solution of the three-particle bound-state problem. Since then, a lot of calculations for the three-nucleon system have been carried out. Whereas the first of them still involved various approximations, later on, with the advent of more advanced computers, it has become possible to gain numerically exact solutions of the Faddeev or their equivalent Alt-Grassberger-Sandhas (AGS) equations [2] both for the three-nucleon bound-state and recently also for the three-nucleon continuum problem.

At the same time, more and more realistic  $NN$ -potential models have been developed; the most refined of them, the so-called new-generation potentials [3–5], describe the two-nucleon data up to the pion-production threshold almost perfectly, i.e., their values of  $\chi^2/\text{datum}$  are close to one. Together with the advanced numerical methods for solving few-particle equations, those potentials form a solid basis to study few-nucleon systems. It was found that a nuclear Hamiltonian with those  $NN$  potentials describes few-nucleon systems rather well. However, there are disagreements in detail which are indicators for corrections of such a simple nuclear Hamiltonian. E.g., none of the  $NN$  potentials can reproduce the experimental value of the three-nucleon binding energy; furthermore, all light nuclei beyond the deuteron are systematically underbound [6]. With respect to low-energy nucleon-deuteron ( $Nd$ ) scattering, the theoretical description in terms of realistic two-nucleon potentials has been generally quite successful with few exceptions, i.e., some very-low-energy observables are correlated with the underbinding of the three-nucleon bound-state and there are also long-standing discrepancies in the nucleon and deuteron vector analyzing powers around 10 MeV nucleon lab energy [7, 8]. In recent years experimental efforts have been made in getting high-precision data of nucleon-deuteron

scattering at intermediate energies [9–13]. There, also clear discrepancies between the theoretical predictions and experimental data for a number of observables were found; the most famous one is the underestimation of the differential cross section of elastic nucleon-deuteron scattering in the diffraction minimum region, the so-called *Sagara discrepancy*. An additional test of the nuclear Hamiltonian and of the corresponding nuclear current can be done by investigating electroweak processes in the three-nucleon system. Though the experimental data for electroweak reactions are much scarcer, some of them also indicate possible discrepancies between theory and experiment.

One hypothesis for resolving those problems for hadronic processes is the addition of a three-nucleon force (3NF) to the nuclear Hamiltonian. The dominant part of most three-nucleon forces is based on two-pion exchange with intermediate  $\Delta$ -isobar excitation, the so-called Fujita-Miyazawa force [14]. However, strictly speaking, most irreducible three-nucleon forces are an artefact of the theory; they are created by freezing out degrees of freedom contained in a richer Hamiltonian of the same problem under consideration. This fact suggests how one may learn some more physics from few-nucleon systems: When beside the nucleon a new degree of freedom is introduced, i.e., it is allowed to become active, it should be taken into account consistently in the two- and three-nucleon problem; in this way, an irreducible three-nucleon force mediated by that new degree of freedom gets resolved into a reducible effective one. That idea carries over to the exchange current in a corresponding way.

The work of this thesis follows that coupled-channel idea in a particular way: Beside the nucleon, it considers also the  $\Delta$  isobar explicitly in the Hilbert space, in a two-baryon coupled-channel potential and in a coupled-channel current. The  $\Delta$  isobar makes the dominant contribution to the pion-nucleon resonance at 1232 MeV in the  $P_{33}$  partial wave. In a quark-model description, it has an internal structure comparable to that of the nucleon: The  $\Delta$  isobar has the same spatial quark distribution with the same quark flavors as the nucleon, though its flavor-spin distribution is different, i.e., it has spin and isospin  $\frac{3}{2}$ . Thus, the  $\Delta$  isobar is a baryon which in the nuclear medium should be treated on the same footing as the nucleon. Even at low energies it can virtually be excited by interactions. In the three-nucleon system the  $\Delta$  isobar mediates an effective three-nucleon force and contributes to the effective two- and three-nucleon electroweak exchange current; they have different properties compared to the corresponding irreducible ones. At intermediate energies the  $\Delta$  isobar yields, in principle, a mechanism for pion production and absorption. A non-covariant Hamiltonian with a two-baryon coupled-channel potential allowing the  $\Delta$  isobar a further coupling to pion-nucleon states can therefore provide a common unifying basis [15] for nuclear phenomena at low and intermediate energies. However, the description in this thesis is confined to processes below the pion-production threshold; the coupling of the  $\Delta$  isobar to pion-nucleon states is therefore omitted, and the  $\Delta$  isobar is considered a stable baryon of mass 1232 MeV.

Thus, the objective of this thesis is to investigate to what extent mechanisms due to  $\Delta$ -isobar excitation, i.e., the effective three-nucleon force and the effective two- and three-nucleon exchange current, are able to remove the existing discrepancies between theoretical description and experimental data for elastic nucleon-deuteron scattering and for nucleon-deuteron breakup, i.e., for

$$N + d \rightarrow N + d, \quad (1.1a)$$

$$N + d \rightarrow N + N + N, \quad (1.1b)$$

for nucleon-deuteron radiative capture and for photo disintegration of the three-nucleon bound state,

i.e., for

$$N + d \rightarrow {}^3\text{He}({}^3\text{H}) + \gamma, \quad (1.2a)$$

$$\gamma + {}^3\text{He}({}^3\text{H}) \rightarrow N + d, \quad (1.2b)$$

$$\gamma + {}^3\text{He}({}^3\text{H}) \rightarrow N + N + N, \quad (1.2c)$$

and for inelastic electron scattering from the three-nucleon bound state, i.e., for

$$e + {}^3\text{He}({}^3\text{H}) \rightarrow e' + N + d, \quad (1.3a)$$

$$e + {}^3\text{He}({}^3\text{H}) \rightarrow e' + N + N + N. \quad (1.3b)$$

The Coulomb interaction between two protons is not taken into account; integral equations in momentum space are not suited for the long-range Coulomb interaction. The predictions of this thesis were therefore without flaw for neutron-deuteron (*nd*) scattering and for electromagnetic (e.m.) reactions on  ${}^3\text{H}$ . However, the comparison with data has mostly to be carried out with the much more abundant and much more accurate data of proton-deuteron (*pd*) scattering and of e.m. reactions on  ${}^3\text{He}$ ; thus, the charge-dependent description of the *npp* system uses the proper proton-proton (*pp*) and neutron-proton (*np*) potentials, though without Coulomb.

The  $\Delta$ -isobar effects in the three-nucleon system have been already investigated in the past. The properties of the three-nucleon bound state were described in Ref. [16], elastic nucleon-deuteron scattering and breakup in Refs. [17–19] and some inelastic e.m. reactions of the three-nucleon system in Refs. [20, 21]. However, compared with those earlier calculations the present description is with respect to the dynamic input and with respect to the scope of applications a substantial improvement:

- A new technique [22] for solving three-particle equations is developed; it is based on the *Chebyshev expansion* of the two-baryon transition matrix; it is found highly reliable and efficient. The new technique replaces the old one of Refs. [17–21] requiring a *separable expansion* of the two-baryon transition matrix; though also quite reliable, at least at low energies, the need for a separable expansion made the old technique rather inflexible in applications. In contrast, the new one allows to use directly any two-nucleon potential and any coupled-channel extension of it as dynamic input for the description of the three-nucleon bound state and of the three-nucleon continuum. Thus, whereas the results of Refs. [16–21] were limited to the rather old Paris potential [23], the present calculations will use modern new-generation *NN* potentials [3–5].
- The old construction of the two-baryon coupled-channel potential with  $\Delta$ -isobar excitation, using the simple subtraction technique of Ref. [16], has a serious defect: It ensures phase equivalence with the nucleonic reference potential at zero two-nucleon kinetic energy only; phase inequivalence arises in general and increases with increasing two-nucleon scattering energy, making the potential not a realistic one. That fact has been known for long [24], but was considered tolerable as long as only the properties of the three-nucleon bound state and of low-energy three-nucleon reactions were in focus. However, that phase inequivalence becomes unacceptable, once three-nucleon processes at moderate energies up to the pion-production threshold are discussed. This thesis repairs the coupled-channel part of the dynamic input for the description of the three-nucleon hadronic and e.m. reactions; it develops a new, well-fitted coupled-channel potential [25], corresponding to a given nucleonic reference potential fully in its realistic nature.
- The description of the considered reactions is extended to energies up to the pion-production threshold, whereas the results of Refs. [16–21] were limited mostly to rather low energies.

Furthermore, the description of three-body photo and electro disintegration of the three-nucleon bound state with  $\Delta$ -isobar excitation and full final-state interaction is given for the first time.

Chapter 2 describes the three-baryon Hilbert space and the dynamics employed, i.e., the newly developed two-baryon coupled-channel potential and the one- and two-baryon coupled-channel e.m. current. Chapter 3 recalls the basic three-particle equations with channel coupling on which the theory of this thesis rests; it indicates the calculational apparatus, relegating technical details to the appendices. Chapter 4 presents the results for the three-nucleon bound state, Chapter 5 for elastic and inelastic nucleon-deuteron scattering, Chapter 6 for three-nucleon photo reactions, and Chapter 7 for three-nucleon electro disintegration. Chapter 8 discusses perturbation theory for nucleon-deuteron scattering as a tool which may help to facilitate the physics understanding of three-nucleon processes. Conclusions are given in Chapter 9.

## 2

# Three-Nucleon Dynamics with $\Delta$ -Isobar Excitation

For notational convenience I use a system of units in which  $\hbar = c = 1$ ; if needed, the expressions containing  $\hbar$  and  $c$  can easily be recovered by dimensional analysis.

### 2.1 Hilbert Space

In the description of three-nucleon reactions I take the  $\Delta$  isobar explicitly into account. Thus, the three-baryon Hilbert space should be extended to contain beside the purely nucleonic sector  $H_N$  with three nucleons also a sectors in which nucleons are excited to  $\Delta$  isobars. Furthermore, the  $\Delta$  isobar makes the dominant contribution to the pion-nucleon resonance at 1232 MeV in the  $P_{33}$  partial wave and it yields, in principle, a mechanism for pion production and absorption. A non-covariant Hamiltonian with a two-baryon coupled-channel potential allowing the  $\Delta$ -isobar further coupling to pion-nucleon states can therefore provide a common unifying basis [15] for nuclear phenomena at low and intermediate energies. In this case the Hilbert space should include even a sectors with pions. However, since the inelasticities of two-nucleon scattering remain very small in isospin singlet two-nucleon partial waves up to about 500 MeV center of mass (c.m.) energy and since the inelasticities in the isospin triplet partial waves are in the same energy regime mostly due to single-pion production, though energies may be well above two-pion threshold, the inelastic two-baryon channels are assumed to have single  $\Delta$ -isobar excitation at most [26]. Furthermore, the description is confined at present to processes *below* the pion-production threshold. I therefore omit in this thesis, as in Refs. [16–21], the coupling of the  $\Delta$  isobar to pion-nucleon states and consider the  $\Delta$  isobar a stable baryon of mass 1232 MeV with spin and isospin  $\frac{3}{2}$ . Thus, the considered Hilbert space has two sectors, i.e., the purely nucleonic one  $H_N$  and the sector  $H_\Delta$  in which one nucleon is turned into a  $\Delta$  isobar as displayed in Fig. 2.1.

The physical three-nucleon states have to be totally antisymmetric under the permutations of the particles. In contrast, the Hilbert sector  $H_\Delta$  contains states without any symmetry requirement for the  $\Delta$  isobar, since it is a baryon distinct from the nucleon. However, states with a  $\Delta$  isobar do not have life on their own; they couple to purely nucleonic, hence totally antisymmetric configurations. Since the excitation of a nucleon to a  $\Delta$  isobar is symmetric in the nucleons, only the totally antisymmetric states with a  $\Delta$  isobar couple and therefore need to be considered for the calculations of this thesis.

In the framework of the nonrelativistic quantum mechanics the c.m. and the internal motion can

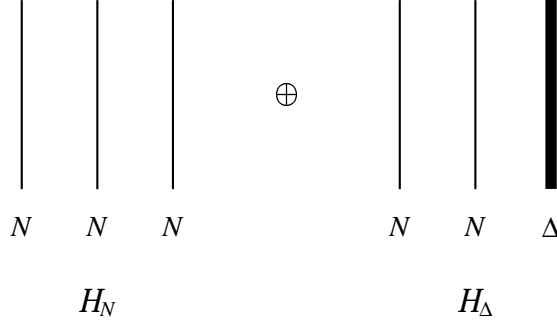


Figure 2.1: Hilbert space considered. It consists of a purely nucleonic sector  $H_N$  and a sector  $H_\Delta$  in which one nucleon is turned into a  $\Delta$  isobar, indicated by a thick vertical line.

be trivially separated by introducing Jacobi momenta

$$\mathbf{p}_\alpha = \frac{m_\gamma \mathbf{k}_\beta - m_\beta \mathbf{k}_\gamma}{m_\beta + m_\gamma}, \quad (2.1a)$$

$$\mathbf{q}_\alpha = \frac{m_\alpha (\mathbf{k}_\beta + \mathbf{k}_\gamma) - (m_\beta + m_\gamma) \mathbf{k}_\alpha}{m_\alpha + m_\beta + m_\gamma}, \quad (2.1b)$$

$$\mathbf{K} = \mathbf{k}_\alpha + \mathbf{k}_\beta + \mathbf{k}_\gamma, \quad (2.1c)$$

with  $(\alpha\beta\gamma)$  being cyclic permutations of (123);  $\mathbf{k}_\alpha$  are the individual momenta,  $m_\alpha$  the particle masses, with  $m_\alpha$  standing either for the averaged nucleon mass  $m_N = 938.9$  MeV or for the mass  $m_\Delta = 1232$  MeV of the  $\Delta$  isobar. The definition of Jacobi momenta (2.1) singles out baryon  $\alpha$  which is the spectator to the  $(\beta\gamma)$  particle pair. For the internal motion the partial-wave basis is employed, i.e.,

$$|pqv(Ij)\rangle_\alpha = \sum_{M_I m_j} \sum_{M_T m_t} |p(LS)IM_I T M_T B\rangle_\alpha |q(ls)jm_j t m_t b\rangle_\alpha \times \langle IM_I j m_j | J M_J \rangle \langle T M_T t m_t | T M_T \rangle. \quad (2.2)$$

The quantum numbers of the basis states are indicated in Fig. 2.2. The basis states (2.2) obviously do not satisfy the full symmetry requirements of the physical states. They are antisymmetrized only in the pair  $(\beta\gamma)$ , i.e.,

$$|p(LS)IM_I T M_T B\rangle_\alpha = \frac{1}{\sqrt{2(1+B^2)}} (1 - P_{\beta\gamma}) |p[L(s_\beta s_\gamma)S]IM_I(t_\beta t_\gamma)T M_T\rangle_\alpha |b\rangle_\beta |b\rangle_\gamma, \quad (2.3)$$

$P_{\beta\gamma}$  being the permutation operator of the particles  $\beta$  and  $\gamma$ . The subscript  $\alpha$  at quantum numbers is omitted, unless ambiguities could arise. The  $(Ij)$  coupling scheme is used. The orbital angular momenta of the pair  $L$  and of the spectator  $l$  are first coupled with their respective spins  $S$  and  $s$  to total pair and spectator angular momenta  $I$  and  $j$  which are then combined to total angular momentum  $J$  with projection  $M_J$ ; the parity quantum number can be derived according to  $\Pi = (-)^L (-)^l$ . The isospin coupling of the pair isospin  $T$  and of the spectator isospin  $t$  is done correspondingly for total isospin  $T$  with projection  $M_T$ . The additional quantum numbers  $(Bb)$  give the baryon characteristics of the pair and of the spectator baryons,  $B = 1(0)$  standing for a two-nucleon (nucleon- $\Delta$ ) pair,  $b = \frac{1}{2}(-\frac{1}{2})$  for a spectator nucleon ( $\Delta$ ); baryon characteristics could be read off from the individual spin and isospin quantum numbers  $s$  and  $t$ ; the additional quantum numbers  $(Bb)$  are introduced



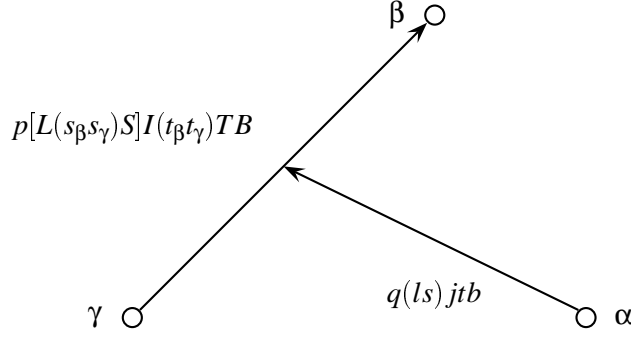


Figure 2.2: Three-baryon Jacobi momenta and discrete quantum numbers. The spectator baryon is labeled  $\alpha$ , the pair is made up of baryons  $\beta$  and  $\gamma$ . The Jacobi momenta are denoted by  $p$  and  $q$ . The abbreviation  $v(Ij)$  for the employed partial-wave basis states  $|pqv(Ij)\rangle_\alpha$  stands for the set  $\{\{[L(s_\beta s_\gamma)S]I(l s)j\}JM_J[(t_\beta t_\gamma)Tt]TM_TBb\}$  of discrete quantum numbers.

for convenience. In Eq. (2.2) the sum is over the projection quantum numbers  $M_I$ ,  $m_j$ ,  $M_T$  and  $m_t$  of the pair and spectator total angular momentum and of the pair and spectator isospin. The discrete quantum numbers, distinct from the continuous Jacobi momenta  $p$  and  $q$ , are abbreviated by  $v(Ij) = \{\{[L(s_\beta s_\gamma)S]I(l s)j\}JM_J[(t_\beta t_\gamma)Tt]TM_TBb\}$ . The practical calculations may suggest other coupling schemes in intermediate steps, e.g., for the description of the trinucleon bound-state wave function the  $(LS)$ -coupling scheme will be used in which the orbital angular momenta of the pair  $L$  and of the spectator  $l$  and their respective spins  $S$  and  $s$  are coupled to the total orbital angular momentum  $L$  and to the total spin  $S$ , respectively, and are then combined to total angular momentum  $J$ , i.e.,  $v(LS) = \{\{(Ll)L[(s_\beta s_\gamma)S]S\}JM_J[(t_\beta t_\gamma)Tt]TM_TBb\}$ . Another possibility is the channel-spin coupling scheme in which the spectator orbital angular momentum  $l$  is coupled with the channel spin  $K$ , consisting of the total pair angular momentum  $I$  and the spectator spin  $s$ , to total angular momentum  $J$ , i.e.,  $v(lK) = \{(l\{[L(s_\beta s_\gamma)S]Is\}K)JM_J[(t_\beta t_\gamma)Tt]TM_TBb\}$ . All those coupling schemes are related to each other by unitary transformations.

## 2.2 Hamiltonian

The basis states (2.2) are the eigenstates of the free Hamiltonian  $H_0$  which contains the rest mass differences  $\delta m_\alpha = m_\alpha - m_N$  and kinetic energy operators of single baryons, i.e.,

$$H_0 = \sum_{\alpha=1}^3 h_0(\alpha). \quad (2.4a)$$

It can be split up into the sum of kinetic energy operators of the three-baryon c.m. motion  $H_0^{\text{c.m.}}$  and of the internal motion, i.e.,

$$H_0 = H_0^{\text{c.m.}} + h_0^{\text{rel}}(\beta\gamma) + h_0^{\text{c.m.}}(\beta\gamma) + h_0^{\text{rel}}(\alpha), \quad (2.4b)$$

with the internal motion contributions  $h_0^{\text{rel}}(\beta\gamma)$ ,  $h_0^{\text{c.m.}}(\beta\gamma)$  and  $h_0^{\text{rel}}(\alpha)$  referring to the relative motion of the pair  $(\beta\gamma)$ , to the motion of the c.m. of the pair  $(\beta\gamma)$  and to the motion of the spectator  $\alpha$  in the three-baryon c.m. system, respectively. The rest mass differences are attached to  $h_0^{\text{rel}}(\beta\gamma)$  and  $h_0^{\text{rel}}(\alpha)$ . The  $H_0$  eigenvalue corresponding to the eigenstate  $|pqv(Ij)\rangle_\alpha|\mathbf{K}\rangle$  is  $\delta M + p^2/2\mu_\alpha + q^2/2M_\alpha + \mathbf{K}^2/2M$  with the reduced mass of the pair  $\mu_\alpha = m_\beta m_\gamma/(m_\beta + m_\gamma)$  and of the spectator

$M_\alpha = m_\alpha(m_\beta + m_\gamma)/(m_\alpha + m_\beta + m_\gamma)$  and with the full three-particle mass  $M = m_\alpha + m_\beta + m_\gamma$ ,  $\delta M = M - 3m_N$  being the full rest mass difference.

Assuming only pairwise interactions between the baryons the interaction part  $H_I$  of the full Hamiltonian  $H = H_0 + H_I$  takes the form

$$H_I = \sum_{\alpha=1}^3 v_\alpha \quad (2.5)$$

with the potential  $v_\alpha$  acting between the pair  $(\beta\gamma)$ . In contrast to the free Hamiltonian  $H_0$ ,  $H_I$  couples the two Hilbert sectors  $H_N$  and  $H_\Delta$ . Since the interaction Hamiltonian  $H_I$  acts on relative coordinates only, the eigenstates of the full Hamiltonian  $H$  are products of states referring to the internal and c.m. motion, i.e., the fully correlated three-nucleon bound state  $|\Psi_B \mathbf{K}\rangle$  and scattering states  $|\Psi_\alpha^{(\pm)}(\mathbf{q}) \mathbf{v}_\alpha \mathbf{K}\rangle$  and  $|\Psi_0^{(\pm)}(\mathbf{p}\mathbf{q}) \mathbf{v}_0 \mathbf{K}\rangle$  have the form

$$|\Psi_B \mathbf{K}\rangle = |B\rangle |\mathbf{K}\rangle, \quad (2.6a)$$

$$|\Psi_\alpha^{(\pm)}(\mathbf{q}) \mathbf{v}_\alpha \mathbf{K}\rangle = |\Psi_\alpha^{(\pm)}(\mathbf{q}) \mathbf{v}_\alpha\rangle |\mathbf{K}\rangle, \quad (2.6b)$$

$$|\Psi_0^{(\pm)}(\mathbf{p}\mathbf{q}) \mathbf{v}_0 \mathbf{K}\rangle = |\Psi_0^{(\pm)}(\mathbf{p}\mathbf{q}) \mathbf{v}_0\rangle |\mathbf{K}\rangle. \quad (2.6c)$$

The internal parts of the states (2.6) and their quantum numbers  $\mathbf{v}_\alpha$  and  $\mathbf{v}_0$  will be discussed in Chapter 3.

### 2.3 Coupled-Channel Potential

The two-baryon coupled-channel potential is graphically defined in Fig. 2.3. In isospin-singlet partial waves it is purely nucleonic. In addition, in isospin-triplet partial waves it has a transition potential from nucleonic to nucleon- $\Delta$  states and a diagonal potential between the latter ones. The coupled-channel potential provides additional attraction between two nucleons by the virtual excitation of a nucleon to a  $\Delta$  isobar. Characteristic effective two-nucleon processes are shown in Fig. 2.4. An instantaneous two-nucleon potential incorporates them, in an implicit average way, in its intermediate-range attraction, often modeled as sigma ( $\sigma$ ) exchange by one-boson exchange (OBE) potentials. Thus, the previous strategy [16, 27] for achieving approximate phase equivalence with an underlying nucleonic reference potential, the so-called subtraction technique, amounted to taking these processes out from the intermediate-range attraction in an *energy-independent* way: The processes which the

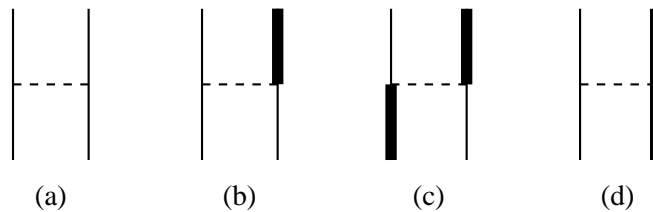


Figure 2.3: Two-baryon coupled-channel potential. A thin vertical line denotes a nucleon, a thick vertical line a  $\Delta$  isobar and a dashed horizontal line the instantaneous potential. The Hermitian-conjugate of the transition process (b) is not shown.

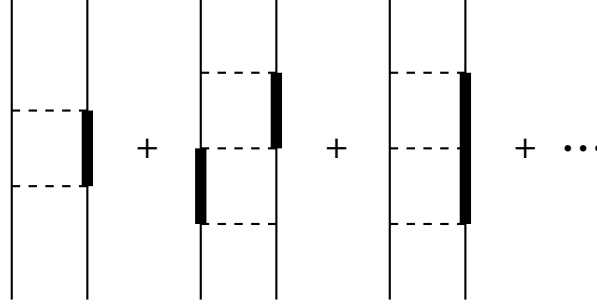


Figure 2.4: Contributions to the effective two-nucleon interaction. The processes up to third order in the potential are shown.

explicit channel coupling provides in an *energy-dependent* way, are subtracted at a physically important reference energy, for which zero kinetic energy was chosen; at that energy, phase equivalence is assured by construction. However, there is phase inequivalence at higher energies [24], it increases with increasing energy, and that phase inequivalence renders a potential, constructed in this way, not a realistic one. Changing the reference energy to higher values does not help much. Furthermore, I notice a dependence of calculated three-nucleon scattering observables on the choice of that reference energy. I therefore felt forced to create a new, this time well-fitted, coupled-channel potential, corresponding to a given nucleonic reference potential. This section describes the chosen procedure and the resulting interaction.

### 2.3.1 Fit of New Realistic Coupled-Channel Potential

I choose as underlying purely nucleonic reference potential the charge-dependent CD-Bonn potential [3]; it is an OBE model which includes single pion ( $\pi$ ), rho ( $\rho$ ) and omega ( $\omega$ ) exchanges; it assumes vanishing coupling of the eta ( $\eta$ ) meson to the nucleon. In addition, the OBE model typically introduces a scalar isoscalar  $\sigma$  meson which has to simulate multimeson exchanges, in particular  $\pi\pi$  and  $\pi\rho$  exchanges with an intermediate  $\Delta$  isobar; those multimeson exchanges are, however, not of purely scalar isoscalar nature. Furthermore, the contributions of  $\pi\pi$  and  $\pi\rho$  exchanges cover rather broad range that cannot be reproduced well by a single boson mass. The CD-Bonn potential therefore introduces two effective scalar isoscalar  $\sigma$  mesons, denoted by  $\sigma_1$  and  $\sigma_2$ , whose parameters are partial-wave dependent. The potential form, meson parameters and regularizing hadronic form factors of CD Bonn are given in Ref. [3]. I choose the isospin triplet components of its coupled-channel extension in close correspondence to CD Bonn. The nucleonic part is taken over in form.

The transition potential of Fig. 2.3(b) from two-nucleon to nucleon- $\Delta$  states is based on  $\pi$  and  $\rho$  exchange and is taken to have the contributions

$$\langle \mathbf{p}' | v(NN \rightarrow N\Delta, \pi) | \mathbf{p} \rangle = - \frac{f_{\pi NN} f_{\pi N\Delta}}{(2\pi)^3 m_\pi^2} \boldsymbol{\tau}_1 \cdot \mathbf{T}_2 \frac{m_N}{(E'E)^{1/2}} \frac{\boldsymbol{\sigma}_1 \cdot \mathbf{p}_E \mathbf{S}_2 \cdot \mathbf{p}_E}{\mathbf{p}_m^2 + m_\pi^2} F_{\pi N}(\mathbf{p}_m^2) F_{\pi \Delta}(\mathbf{p}_m^2), \quad (2.7a)$$

$$\langle \mathbf{p}' | v(NN \rightarrow N\Delta, \rho) | \mathbf{p} \rangle = - \frac{f_{\rho NN} f_{\rho N\Delta}}{(2\pi)^3 m_\rho^2} \boldsymbol{\tau}_1 \cdot \mathbf{T}_2 \frac{m_N}{(E'E)^{1/2}} \frac{(\boldsymbol{\sigma}_1 \times \mathbf{p}_E) \cdot (\mathbf{S}_2 \times \mathbf{p}_E)}{\mathbf{p}_m^2 + m_\rho^2} F_{\rho N}(\mathbf{p}_m^2) F_{\rho \Delta}(\mathbf{p}_m^2) \quad (2.7b)$$

with the initial and final two-baryon relative momenta  $\mathbf{p}$  and  $\mathbf{p}'$ ,

$$E = (m_N^2 + \mathbf{p}^2)^{1/2}, \quad (2.8a)$$

$$E' = (m_N^2 + \mathbf{p}'^2)^{1/2}, \quad (2.8b)$$

$$\mathbf{p}_m = \mathbf{p}' - \mathbf{p}, \quad (2.8c)$$

$$\mathbf{p}_E = [(E' + m_N)(E + m_N)]^{1/2} \left( \frac{\mathbf{p}'}{E' + m_N} - \frac{\mathbf{p}}{E + m_N} \right) \quad (2.8d)$$

and the hadronic form factors

$$F_{\xi B}(\mathbf{p}_m^2) = \frac{\Lambda_{\xi B}^2 - m_\xi^2}{\Lambda_{\xi B}^2 + \mathbf{p}_m^2}, \quad (2.8e)$$

$\sigma$  ( $\tau$ ) and  $\mathbf{S}$  ( $\mathbf{T}$ ) being the nucleonic spin (isospin) operator and transition spin (isospin) operator from nucleonic to  $\Delta$ -isobar states with the reduced matrix elements  $(\frac{1}{2}||\sigma||\frac{1}{2}) = (\frac{1}{2}||\tau||\frac{1}{2}) = \sqrt{6}$  and  $(\frac{3}{2}||\mathbf{S}||\frac{1}{2}) = (\frac{3}{2}||\mathbf{T}||\frac{1}{2}) = 2$ . The nonlocality of the potential forms (2.7) arises from the fact that  $\mathbf{p}_E \neq \mathbf{p}_m$  and from the factor  $m_N/(E'E)^{1/2}$ . In Eqs. (2.7) the second nucleon is turned into a  $\Delta$  isobar; of course, the symmetrized transition contribution is added. The form factor (2.8e) acts at purely nucleonic vertices and at vertices with at least one  $\Delta$  isobar; the subscript  $B$  being  $N$  or  $\Delta$  distinguishes the two cases.

The exchange nucleon- $\Delta$  potential of Fig. 2.3(c) is based on  $\pi$  and  $\rho$  exchange and is taken to have the contributions

$$\langle \mathbf{p}' | v(\Delta N \rightarrow N\Delta, \pi) | \mathbf{p} \rangle = - \frac{f_{\pi N\Delta}^2}{(2\pi)^3 m_\pi^2} \mathbf{T}_1^\dagger \cdot \mathbf{T}_2 \frac{m_N}{(E'E)^{1/2}} \frac{\mathbf{S}_1^\dagger \cdot \mathbf{p}_E \mathbf{S}_2 \cdot \mathbf{p}_E}{\mathbf{p}_m^2 + m_\pi^2} F_{\pi\Delta}^2(\mathbf{p}_m^2), \quad (2.9a)$$

$$\langle \mathbf{p}' | v(\Delta N \rightarrow N\Delta, \rho) | \mathbf{p} \rangle = - \frac{f_{\rho N\Delta}^2}{(2\pi)^3 m_\rho^2} \mathbf{T}_1^\dagger \cdot \mathbf{T}_2 \frac{m_N}{(E'E)^{1/2}} \frac{(\mathbf{S}_1^\dagger \times \mathbf{p}_E) \cdot (\mathbf{S}_2 \times \mathbf{p}_E)}{\mathbf{p}_m^2 + m_\rho^2} F_{\rho\Delta}^2(\mathbf{p}_m^2). \quad (2.9b)$$

The direct nucleon- $\Delta$  potential of Fig. 2.3(d) is based on  $\pi$ ,  $\rho$ ,  $\omega$  and *one*  $\sigma$  exchange and is taken to have the contributions

$$\langle \mathbf{p}' | v(N\Delta \rightarrow N\Delta, \pi) | \mathbf{p} \rangle = - \frac{f_{\pi NN} f_{\pi\Delta\Delta}}{(2\pi)^3 m_\pi^2} \tau_1 \cdot \tau_{\Delta 2} \frac{m_N}{(E'E)^{1/2}} \frac{\sigma_1 \cdot \mathbf{p}_E \sigma_{\Delta 2} \cdot \mathbf{p}_E}{\mathbf{p}_m^2 + m_\pi^2} F_{\pi N}(\mathbf{p}_m^2) F_{\pi\Delta}(\mathbf{p}_m^2), \quad (2.10a)$$

$$\begin{aligned} \langle \mathbf{p}' | v(N\Delta \rightarrow N\Delta, \rho) | \mathbf{p} \rangle = & - \frac{f_{\rho NN} f_{\rho\Delta\Delta}}{(2\pi)^3 m_\rho^2} \tau_1 \cdot \tau_{\Delta 2} \frac{m_N}{(E'E)^{1/2}} \frac{(\sigma_1 \times \mathbf{p}_E) \cdot (\sigma_{\Delta 2} \times \mathbf{p}_E)}{\mathbf{p}_m^2 + m_\rho^2} F_{\rho N}(\mathbf{p}_m^2) F_{\rho\Delta}(\mathbf{p}_m^2) \\ & + \frac{g_{\rho NN} g_{\rho\Delta\Delta}}{(2\pi)^3} \tau_1 \cdot \tau_{\Delta 2} \frac{F_{\rho N}(\mathbf{p}_m^2) F_{\rho\Delta}(\mathbf{p}_m^2)}{\mathbf{p}_m^2 + m_\rho^2}, \end{aligned} \quad (2.10b)$$

$$\langle \mathbf{p}' | v(N\Delta \rightarrow N\Delta, \sigma) | \mathbf{p} \rangle = - \frac{g_{\sigma NN} g_{\sigma\Delta\Delta}}{(2\pi)^3} \frac{F_{\sigma N}(\mathbf{p}_m^2) F_{\sigma\Delta}(\mathbf{p}_m^2)}{\mathbf{p}_m^2 + m_\sigma^2}, \quad (2.10c)$$

$$\begin{aligned} \langle \mathbf{p}' | v(N\Delta \rightarrow N\Delta, \omega) | \mathbf{p} \rangle = & - \frac{g_{\omega NN} g_{\omega\Delta\Delta}}{(2\pi)^3 (2m_N)^2} \frac{m_N}{(E'E)^{1/2}} \frac{(\sigma_1 \times \mathbf{p}_E) \cdot (\sigma_{\Delta 2} \times \mathbf{p}_E)}{\mathbf{p}_m^2 + m_\omega^2} F_{\omega N}(\mathbf{p}_m^2) F_{\omega\Delta}(\mathbf{p}_m^2) \\ & + \frac{g_{\omega NN} g_{\omega\Delta\Delta}}{(2\pi)^3} \frac{F_{\omega N}(\mathbf{p}_m^2) F_{\omega\Delta}(\mathbf{p}_m^2)}{\mathbf{p}_m^2 + m_\omega^2}, \end{aligned} \quad (2.10d)$$

$\sigma_\Delta$  ( $\tau_\Delta$ ) being the  $\Delta$ -isobar spin (isospin) operator with the reduced matrix element  $(\frac{3}{2}||\sigma_\Delta||\frac{3}{2}) = (\frac{3}{2}||\tau_\Delta||\frac{3}{2}) = 2\sqrt{15}$ . The spin-independent terms are local, they do not involve  $\mathbf{p}_E$  and the corresponding factor  $m_N/(E'E)^{1/2}$ .

As in Refs. [16–21] the potential forms (2.7), (2.9) and (2.10) are not derived cleanly from field theory, but postulated [28] by substituting spin and isospin operators in nucleonic OBE potentials with the corresponding transition and diagonal  $\Delta$ -isobar operators. However, the potential forms relating to the  $\Delta$  isobar differ from those [16–21, 28] used previously in several respects:

- (1) They are made to have the same relativistic factors as CD Bonn, which is based upon the relativistic Feynman amplitudes for meson exchange; i.e.,  $\mathbf{p}_E$  replaces  $\mathbf{p}_m$  in the spin-dependent vertex terms and the factors  $m_N/(E'E)^{1/2}$  are added appropriately; for simplicity no distinction between nucleon and  $\Delta$ -isobar masses is made in those factors. Their nonlocal relativistic forms are especially important for the tensor force; their local approximations change them drastically off shell: Locality makes the tensor-force part substantially stronger off shell [29].
- (2) The regularizing hadronic form factors are dipole ones for each meson exchange as in CD Bonn.
- (3) The diagonal hadronic nucleon- $\Delta$  potential (2.9) – (2.10) is taken to be nonzero, in contrast to the assumptions in Refs. [16–21].

The fit of the isospin triplet part of the two-baryon coupled-channel potential proceeds as follows and thereby yields the following characteristics for the resulting potential:

1. The CD-Bonn potential form is adopted as nucleonic part. The parameters of the  $\sigma_1$  and  $\sigma_2$  exchanges are retuned. However, in the  $^3P_0$  and  $^3P_1$  partial waves the readjustment of the  $\sigma_1$  and  $\sigma_2$  parameters alone is not enough; there, also the  $\omega$  parameters have to be retuned slightly. Thus, the readjustment of the  $\sigma_1$ ,  $\sigma_2$  and  $\omega$  exchanges is partial-wave dependent. The resulting parameters are given in Table A.1 of Appendix A. I remind, the  $\sigma_1$ ,  $\sigma_2$  and  $\omega$  parameters of the purely nucleonic CD Bonn are also partial-wave dependent.
2. In the potential parts referring to the  $\Delta$  isobar the parameters, except for the  $\sigma$  coupling strength, are chosen according to empirical values or quark counting rules; they are summarized in Table A.2 of Appendix A. Since these parameters are not subjected to the fit, the fit is not allowed to return to the purely nucleonic reference potential, i.e., to choose these parameters to vanish. The coupling strength of  $\sigma$ , in fact, the combination  $g_{\sigma NN}g_{\sigma \Delta\Delta}/4\pi$ , is the real fit parameter; it is allowed to be partial-wave dependent as in CD Bonn; the resulting parameters of  $\sigma$  exchange are given in Table A.3 of Appendix A. The coupled-channel potential is charge dependent. However, the potential contributions related to the  $\Delta$  isobar are chosen as charge independent; the charge dependence of the complete coupled-channel potential results from its purely nucleonic part.
3. The CD-Bonn potential can be considered to provide a very reliable energy-dependent phase-shift analysis of nucleon-nucleon scattering data below 350 MeV, known up to the year 2000. It can be considered an update of the corresponding Nijmegen phase-shift analysis [30] which is based on data up to 1993. The coupled-channel potential is therefore tuned to the phase shifts of CD Bonn; however, the resulting  $\chi^2$  values are calculated with respect to the proper data as in Ref. [3]. Furthermore, the actual fit sequence for the different charge states is the same as in Ref. [3].
4. The point Coulomb interaction is added in the partial waves with two charged baryons, i.e., in the coupled proton-proton ( $pp$ ) and  $p\Delta^+$  partial waves and in the  $p\Delta^-$  partial waves coupled to the neutron-neutron ( $nn$ ) partial waves. The long range Coulomb potential is cut off at a radius  $R$ , outside the range of the hadronic potentials. In the  $pp$  partial waves the proper Coulomb

boundary conditions are exactly restored from the cut-off ones; with respect to the cut off in  $N\Delta$  partial waves, the independence of results from that cut off for values of  $R \geq 10$  fm is numerically established.

5. The fit aims first at the  $pp$  potential with channel coupling, since the  $pp$  data are the most accurate ones. The  $pp$  potential is fitted to the CD Bonn  $pp$  phase shifts, using the Nijmegen  $pp$  error matrix [31] for determining an intermediate  $\chi^2$ . The subsequent direct comparison with all experimental  $pp$  data below 350 MeV, available in the year 2000, yields  $\chi^2/\text{datum} = 1.01$ , very close to that of the original CD Bonn. Thus, there is no need for any further tuning of parameters in the comparison with the proper  $pp$  data.
6. The coupled-channel potential is charge dependent as CD Bonn. Its parameters in isospin triplet partial waves with isospin projection  $M_T = 1$ , fitted in step 5., are transcribed to the neutron-proton ( $np$ ), i.e.,  $M_T = 0$ , and to the  $nn$ , i.e.,  $M_T = -1$ , parts in the same way as for CD Bonn, i.e., omitting Coulomb, except in the  $p\Delta^-$  channel coupled to  $nn$ , correspondingly replacing the masses of the nucleons and adjusting the coupling constants of the  $\sigma_1$  and  $\sigma_2$  mesons such that the phase shift differences, predicted by the charge-independence and the charge-symmetry breaking of CD Bonn, are reproduced. The subsequent direct comparison with experimental  $np$  data below 350 MeV, available in the year 2000, yields  $\chi^2/\text{datum} = 1.02$ , again very close to that of the original CD Bonn. Thus, there is no need for any further tuning of parameters in the comparison with the proper  $np$  data. Furthermore, the resulting  $^1S_0$   $nn$  scattering length, i.e.,  $-18.95$  fm, agrees well with the experimental one of Ref. [32], i.e., with  $-18.9 \pm 0.4$  fm, within the experimental error bars.

The meson parameters resulting from the fit are collected in the tables of Appendix A. The overall fit yields a  $\chi^2/\text{datum} = 1.02$ . Thus, the new coupled-channel potential is as realistic as any of the modern nucleonic potentials; it is phase equivalent with CD Bonn as nucleonic reference potential in the limits of the fit. Nevertheless, a word of caution is appropriate: The fit is based on nucleon-nucleon scattering data below pion-production threshold, whereas the nucleon- $\Delta$  channel is the remainder of the description of inelasticity yielding single-pion production. Thus, those physics data, for which the nucleon- $\Delta$  channel is most important, are not used yet for determining its properties. The developed coupled-channel potential is applicable only for phenomena below pion-production threshold in the same way as the nucleonic reference potential CD Bonn; both are unrealistic beyond pion-production threshold. Of course, this fact is unfortunate, but its repair is far beyond the scope of this thesis; only for reasons of curiosity, Appendix A also discusses characteristic predictions of the coupled-channel potential for the energy domain, where single-pion inelasticity is important.

In the Chapters 4 to 7 I present results for the three-nucleon bound state, for nucleon-deuteron scattering and for three-nucleon e.m. reactions derived from the new realistic coupled-channel potential with  $\Delta$ -isobar excitation, denoted in the following as CD Bonn +  $\Delta$ . I shall give three additional results for comparison. I shall give results for the nucleonic reference potential CD Bonn in order to isolate  $\Delta$ -isobar effects. I shall also give results for coupled-channel potentials constructed according to the old subtraction technique [16, 28] without fit; both are phase-equivalent at zero kinetic energy only. One version, denoted in the following as CD Bonn +  $\Delta$  (sub1), is based on the contributions (2.7) - (2.10) with the parameters of Appendix A; its  $\chi^2/\text{datum} = 6.34$  is poor compared to the new coupled-channel potential. The other version is the one employed in Ref. [22]; it will be denoted as CD Bonn +  $\Delta$  (sub2); it is based on a local transition potential without diagonal nucleon- $\Delta$  contributions; its  $\chi^2/\text{datum} = 13.8$  is even poorer. The partial and the complete  $\chi^2$  values of all coupled-channel

	$\chi^2/\text{datum } (pp)$	$\chi^2/\text{datum } (np)$	$\chi^2/\text{datum } (pp + np)$
CD Bonn	1.01	1.02	1.02
CD Bonn + $\Delta$	1.01	1.02	1.02
CD Bonn + $\Delta$ (sub1)	10.5	2.36	6.34
CD Bonn + $\Delta$ (sub2)	23.8	4.11	13.8

Table 2.1:  $\chi^2$  values for the potentials used in this thesis. The coupled-channel potential CD Bonn +  $\Delta$  is the fitted one. The other coupled-channel potentials are constructed without fit.

potentials, used in this thesis, and of the nucleonic reference potential CD Bonn are collected in Table 2.1.

### 2.3.2 Effective Phenomena in Three-Nucleon System

A virtual  $\Delta$ -isobar excitation in the three-nucleon system yields an effective three-nucleon force which simulates traditional irreducible three-nucleon forces in a reducible energy-dependent way. In lowest order, i.e., in second order of the two-baryon interaction, the  $\Delta$ -isobar contribution to the effective three-nucleon force displayed in Fig. 2.5 is of the Fujita-Miyazawa force [14] type; in contrast to that irreducible three-nucleon force based solely on the two-pion exchange, the effective three-nucleon force due to  $\Delta$ -isobar excitation takes also  $\pi\rho$  and  $\rho\rho$  exchanges into account. In higher order the coupled-channel potential simulates, among other processes, the three-pion ring parts of the Illinois force [6] as shown in Fig. 2.6. Again, the effective three-nucleon force due to  $\Delta$ -isobar excitation takes

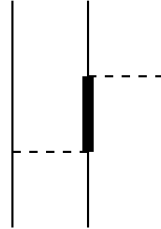


Figure 2.5: Contribution to the effective three-nucleon force arising from the coupled-channel potential in second order of the two-baryon interaction. It is of Fujita-Miyazawa force type.

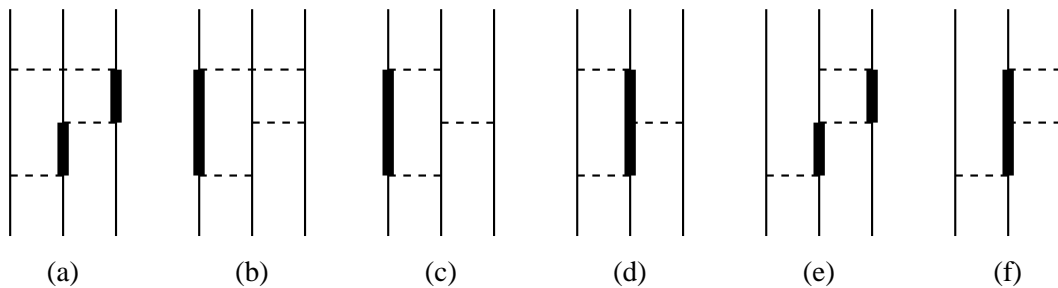


Figure 2.6: Contributions to the effective three-nucleon force arising from the coupled-channel potential in third order of the two-baryon interaction. The parts (a) and (b) are of the pion-ring type in the Illinois three-nucleon force.

into account the exchanges of all mesons included in the coupled-channel potential, i.e.,  $\pi$ ,  $\rho$ ,  $\omega$  and  $\sigma$ . The coupled-channel potential makes all contributions to the three-nucleon force mutually consistent, what is not the case in Ref. [6]. However, there are some other processes included in irreducible three-nucleon forces, e.g., the Tucson-Melbourne (TM) force [33], which are not accounted for by the coupled-channel potential, e.g., pion-nucleon  $S$ -wave scattering.

## 2.4 Electromagnetic Interaction

The basic building block for the description of e.m. nuclear reactions is the e.m. Hamiltonian

$$H_I^{\text{e.m.}} = e_p \int d^3x J^\mu(x) A_\mu(x) \Big|_{x_0=0} \quad (2.11)$$

which couples baryonic states to the photon ( $\gamma$ ).  $e_p$  is the positive elementary charge, i.e.,  $e_p^2 \approx 1/137.036$ . The operators in Eq. (2.11) depend on space-time  $x$ , but are to be used as Schrödinger operators at time  $x_0 = 0$ ; the e.m. field operator  $A_\mu(x)$  is parametrized in the form

$$A_\mu(x) = \frac{(4\pi)^{1/2}}{(2\pi)^{3/2}} \int \frac{d^3k_\gamma}{(2k_\gamma^0)^{1/2}} \sum_\lambda [a_\lambda(\mathbf{k}_\gamma) \epsilon_\mu(k_\gamma \lambda) e^{-ik_\gamma x} + a_\lambda^\dagger(\mathbf{k}_\gamma) \epsilon_\mu^*(k_\gamma \lambda) e^{ik_\gamma x}] \Big|_{k_\gamma^0=|\mathbf{k}_\gamma|}. \quad (2.12)$$

The polarizations  $\lambda = \pm 1$  correspond to those of a real transverse photon;  $\epsilon(k_\gamma \lambda)$  are the polarization vectors, constrained by  $k_\gamma^\mu \epsilon_\mu(k_\gamma \lambda) = 0$ . A single-photon state of definite momentum  $\mathbf{k}_\gamma$  and polarization  $\lambda$ ,  $\delta$ -function normalized, is  $|\mathbf{k}_\gamma \lambda\rangle = a_\lambda^\dagger(\mathbf{k}_\gamma)|0\rangle$ . The polarizations  $\lambda \neq \pm 1$  correspond to polarizations of virtual photon needed for the description of electron scattering, i.e., to a photon with longitudinal polarization and to a scalar photon. In that description the e.m. interaction is used in one-photon exchange, i.e., the Hamiltonian  $H_I^{\text{e.m.}}$  of Eq. (2.11) is to be supplemented by a coupling of the e.m. field to electron current  $l^\mu(x)$  and it is then applied in second order resulting in the standard current-current coupling between charged particles. Thus, for electron scattering from hadrons the effective e.m. interaction

$$H_{I\text{eff}}^{\text{e.m.}} = -e_p^2 \int d^3x J^\mu(x) \left[ \int d^4y \frac{d^4Q}{(2\pi)^4} \frac{4\pi e^{-iQ \cdot (x-y)}}{Q^2 + i0} l_\mu(y) \right] \Big|_{x_0=0} \quad (2.13)$$

has to be used.

The e.m. current operator  $J^\mu(x)$  acts in the baryonic Hilbert space with two sectors  $H_N$  and  $H_\Delta$  displayed in Fig. 2.1. I use the current operator in its Fourier-transformed form, i.e.,

$$J^\mu(\mathbf{Q}) = \int d^3x e^{i\mathbf{Q} \cdot \mathbf{x}} J^\mu(x) \Big|_{x_0=0}, \quad (2.14)$$

and employ — specializing to a three-baryon system — a momentum-space representation, based on the three-particle Jacobi momenta (2.1), i.e.,

$$\langle \mathbf{p}' \mathbf{q}' \mathbf{K}' | J^\mu(\mathbf{Q}) | \mathbf{p} \mathbf{q} \mathbf{K} \rangle = \delta(\mathbf{K}' - \mathbf{Q} - \mathbf{K}) \langle \mathbf{p}' \mathbf{q}' | j^\mu(\mathbf{Q}, \mathbf{K}_+) | \mathbf{p} \mathbf{q} \rangle. \quad (2.15)$$

In Eq. (2.15)  $\mathbf{Q}$  is the three-momentum transfer by the photon; it will take on particular values depending on the considered reaction, e.g., in the photo reactions it is given by the momentum  $\mathbf{k}_\gamma$  of the real photon. A total momentum conserving  $\delta$ -function is split off; the remaining current operator  $j^\mu(\mathbf{Q}, \mathbf{K}_+)$  only acts on the internal momenta of the three-baryon system with a parametric dependence on the combination  $\mathbf{K}_+ = \mathbf{K}' + \mathbf{K}$  of total momenta.



### 2.4.1 Coupled-Channel One-Baryon and Two-Baryon Current

The current operator has one-baryon and two-baryon pieces, i.e.,  $J^\mu(\mathbf{Q}) = J^{[1]\mu}(\mathbf{Q}) + J^{[2]\mu}(\mathbf{Q})$ , the latter term being called meson-exchange current (MEC). It arises — as does the baryon-baryon interaction itself — as a consequence of the elimination of mesonic degrees of freedom in the considered Hamiltonian. In the underlying field theory mesons as well as baryons couple to the photons, i.e., carry the e.m. current. However, in the restricted purely baryonic Hilbert space of Fig. 2.1 only the nucleon and the  $\Delta$  isobar couple explicitly to the photon by the one-body current. The frozen mesonic degrees of freedom manifest themselves in many-baryon operators for charge and spatial current. The necessity to introduce the MEC follows also from the continuity equation, which in the Fourier-transformed form of the e.m. current reads

$$\mathbf{Q} \cdot \mathbf{J}(\mathbf{Q}) = [H_0 + H_I, \rho(\mathbf{Q})]. \quad (2.16)$$

Accepting Siegert's hypothesis [34], i.e., assuming the charge operator  $\rho(\mathbf{Q}) \equiv J^0(\mathbf{Q})$  in nonrelativistic approximation to be composed of one-baryon operators  $\rho^{[1]}(\mathbf{Q})$  only, the continuity equation for the e.m. current splits up into two parts, i.e.,

$$\mathbf{Q} \cdot \mathbf{J}^{[1]}(\mathbf{Q}) = [H_0, \rho^{[1]}(\mathbf{Q})], \quad (2.17a)$$

$$\mathbf{Q} \cdot \mathbf{J}^{[2]}(\mathbf{Q}) = [H_I, \rho^{[1]}(\mathbf{Q})]. \quad (2.17b)$$

Since the isospin-dependent or nonlocal potential  $H_I$  does not commute with the charge density  $\rho^{[1]}(\mathbf{Q})$ , a nonvanishing two-baryon spatial current  $\mathbf{J}^{[2]}(\mathbf{Q})$  is required in order to fulfill current conservation. Beside the standard nucleonic current part there are additional parts involving the  $\Delta$  isobar which then make effective two- and three-nucleon contributions to the exchange current, the contributions being consistent with each other. I take one-baryon and two-baryon contributions into account, shown in Figs. 2.7 - 2.9 and described in detail in the respective figure captions. The explicit analytic forms of the considered contributions are collected in Appendix B. The horizontal lines in the diagrams indicate that the meson exchanges are instantaneous. The dominant meson-exchange contributions arise from  $\pi$  and  $\rho$  exchanges; note, that those are the only contributions of two-baryon nature taken into account in the calculations of Refs. [35–37]. In my calculations also the meson-nondiagonal  $\rho\pi\gamma$  and  $\omega\pi\gamma$  contributions are taken into account for the currents of Figs. 2.7 and 2.8. The current of Fig. 2.8 couples purely nucleonic states with states containing one  $\Delta$  isobar. In contrast to Ref. [20], the contributions between  $\Delta$ -isobar states of one- and two-baryon nature are kept as shown in Fig. 2.9, though the corresponding two-baryon contributions will turn out to be quantitatively entirely irrelevant; I therefore take only the diagonal  $\pi$  contribution into account. The e.m. current is derived by the extended  $S$ -matrix method of Refs. [38–41], which is based on the comparison of  $S$ -matrix elements resulting from relativistic quantum field theory and from the corresponding quantum-mechanical description. However, the e.m. current, as given in Appendix B, satisfies current conservation only approximately with the corresponding  $\pi$  and  $\rho$  exchanges in the employed two-baryon interaction  $H_I$  of CD Bonn and CD Bonn +  $\Delta$ . The employed spatial current is systematically expanded up to first order in  $k/m_N$ ,  $k$  being a characteristic baryon momentum. The charge density is used in zeroth order in  $k/m_N$  in the standard calculations.

In the photo reactions, i.e., in the reactions with real transverse photons, the photon couples only to the transverse part of the spatial current. However, assuming current conservation, the dominant contribution of the spatial current is replaced by the charge density which is less affected by two-body effects according to Siegert's hypothesis. This assumption results in the so-called Siegert form of the current. In contrast, in the electron scattering from the trinucleon bound state the exchanged photon

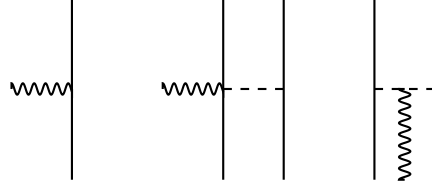


Figure 2.7: One- and two-baryon processes contained in the used e.m. current. In this figure only the purely nucleonic processes are depicted. In nonrelativistic order the one-nucleon process contributes to the charge density and to the spatial current, the two-nucleon processes only to the spatial current. The meson-diagonal isovector  $\pi$  and  $\rho$  exchanges are taken into account in the two-nucleon processes as well as the meson-nondiagonal  $\rho\pi\gamma$  and  $\omega\pi\gamma$  contributions.

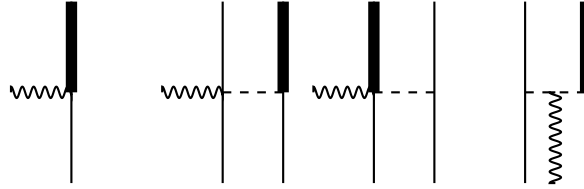


Figure 2.8: One- and two-baryon processes contained in the used e.m. current. In this figure processes are depicted in which one nucleon is turned into a  $\Delta$  isobar. The Hermitian-adjoint processes are taken into account, but are not diagrammatically shown. In nonrelativistic order the one-baryon and two-baryon processes contribute only to the spatial current. In the one-baryon current only the magnetic dipole transition is kept. The meson-diagonal isovector  $\pi$  and  $\rho$  exchanges are taken into account in the two-baryon processes as well as the meson-nondiagonal  $\rho\pi\gamma$  and  $\omega\pi\gamma$  contributions.

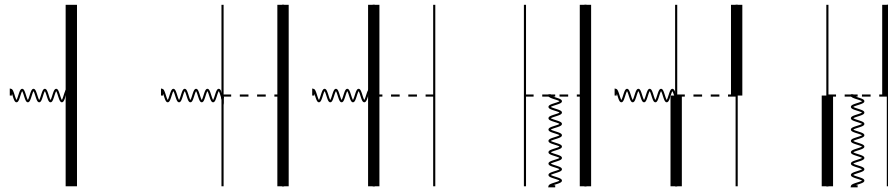


Figure 2.9: One- and two-baryon processes contained in the used e.m. current. In this figure processes are depicted which connect states with a  $\Delta$  isobar. In nonrelativistic order the one-baryon process contributes to charge density and spatial current, the two-baryon processes only to the spatial current. Only the meson-diagonal isovector  $\pi$  exchange is taken into account in the two-baryon processes.

is virtual and couples to all components of the e.m. current which in addition has to carry e.m. form factors. In this case, current conservation may be used in order to replace the longitudinal part of the spatial current by the charge density.

### 2.4.2 Effective Nucleonic Currents

In the same way as the coupled-channel potential yields the effective two-nucleon and three-nucleon forces of Figs. 2.4 – 2.6, the coupled-channel current yields effective currents which are of two-nucleon and of three-nucleon nature; the lowest order contributions are shown in Figs. 2.10 and 2.11, respectively. Since the effective nucleonic forces and currents are built from the same two-baryon coupled-channel potential and from the corresponding one-baryon and two-baryon coupled-channel current, they are consistent with each other. The meson exchanges included in the coupled-channel potential and in the coupled-channel current are contained also in the effective nucleonic forces and in the effective nucleonic currents.

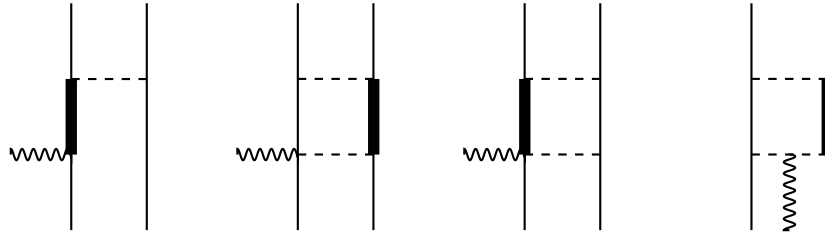


Figure 2.10: Contributions to the effective two-nucleon current arising from the coupled-channel potential and the coupled-channel current at lowest order.

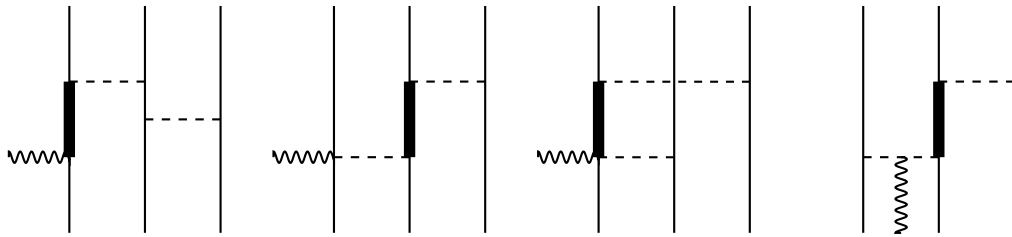


Figure 2.11: Contributions to the effective three-nucleon current arising from the coupled-channel potential and the coupled-channel current at lowest orders.



## 3

# Three-Particle Equations: Nucleons and Single $\Delta$ -Isobar Excitation

Since the c.m. and internal motion can be separated as described in Chapter 2.2, I consider in the following only the internal motion, i.e., I consider the free Hamiltonian (2.4b) without the contribution  $H_0^{\text{c.m.}}$  from the three-particle c.m. motion.

### 3.1 Three-Nucleon Bound State

The three-nucleon internal bound state  $|B\rangle$ , already introduced in Eq. (2.6a), with the binding energy  $E_B$  satisfies the Schrödinger equation

$$(H_0 + H_I)|B\rangle = E_B|B\rangle; \quad (3.1a)$$

its integral form is

$$|B\rangle = G_0(E_B) \sum_{\alpha=1}^3 v_{\alpha}|B\rangle \quad (3.1b)$$

with the free resolvent  $G_0(Z) = (Z - H_0)^{-1}$ ,  $Z$  being a general complex number which for physical amplitudes becomes the energy of the three-nucleon system. The kernel of Eq. (3.1b) is non-connected. In principle, it is possible to solve Eq. (3.1b) numerically, since the solution of the bound-state problem is well-behaved and square-integrable. However, it is much more advantageous to follow the Faddeev procedure which leads to an integral equation with a kernel connected after iteration and compact for short-ranged forces. I therefore decompose the bound-state wave function  $|B\rangle$  into its Faddeev components  $|\psi_{\alpha}\rangle = G_0(E_B)v_{\alpha}|B\rangle$ , i.e.,

$$|B\rangle = \sum_{\alpha=1}^3 |\psi_{\alpha}\rangle. \quad (3.2)$$

The Faddeev components obey the following equations, i.e.,

$$|\psi_{\alpha}\rangle = G_0(E_B)v_{\alpha} \sum_{\beta=1}^3 |\psi_{\beta}\rangle, \quad (3.3a)$$

$$|\psi_{\alpha}\rangle = [1 - G_0(E_B)v_{\alpha}]^{-1} G_0(E_B)v_{\alpha} \sum_{\beta \neq \alpha} |\psi_{\beta}\rangle, \quad (3.3b)$$

$$|\psi_{\alpha}\rangle = G_0(E_B)T_{\alpha}(E_B) \sum_{\beta \neq \alpha} |\psi_{\beta}\rangle. \quad (3.3c)$$

In the last equation the two-baryon interaction between the pair ( $\beta\gamma$ ) is summed up into the two-baryon transition matrix

$$T_\alpha(Z) = v_\alpha + v_\alpha G_0(Z) T_\alpha(Z) \quad (3.4)$$

in the three-particle Hilbert space. Since the bound state  $|B\rangle$  has to be totally antisymmetric under the exchange of the three baryons, the relation between Faddeev components is

$$|\psi_\beta\rangle = P_{\alpha\beta} P_{\beta\gamma} |\psi_\alpha\rangle, \quad (3.5)$$

$P_{\alpha\beta}$  being the permutation operator of the particles  $\alpha$  and  $\beta$ . It is therefore sufficient to determine only one of the Faddeev components according to

$$|\psi_\alpha\rangle = G_0(E_B) T_\alpha(E_B) P |\psi_\alpha\rangle, \quad (3.6)$$

where the permutation operator  $P$  is defined to be  $P = P_{\alpha\beta} P_{\beta\gamma} + P_{\alpha\gamma} P_{\beta\gamma}$ ; in fact,  $P$  is the sum of the cyclic and anticyclic permutations of three particles. The bound-state wave function is given by

$$|B\rangle = (1 + P) |\psi_\alpha\rangle. \quad (3.7)$$

It has to be normalized explicitly such that  $\langle B|B\rangle = 1$ .

### 3.2 Three-Nucleon Scattering

Nucleon-deuteron scattering is considered. In the initial nucleon-deuteron channel state

$$|\phi_\alpha(\mathbf{q})\mathbf{v}_\alpha\rangle = |dI_0M_IT_0M_{T_0}\rangle_\alpha |\mathbf{q}s_0m_s t_0m_t b_0\rangle_\alpha \quad (3.8)$$

the pair ( $\beta\gamma$ ) of nucleons is bound as deuteron in the state  $|dI_0M_IT_0M_{T_0}\rangle_\alpha$  with the quantum numbers  $I_0 = 1$  and  $T_0 = M_{T_0} = 0$ ; the third nucleon is in a plane-wave state with definite spin and isospin specification, the quantum numbers  $s_0, t_0$  and  $b_0$  being  $\frac{1}{2}$ ;  $\mathbf{v}_\alpha$  abbreviates all discrete quantum numbers. The state  $|\phi_\alpha(\mathbf{q})\mathbf{v}_\alpha\rangle$  is an eigenstate of the channel Hamiltonian  $H_\alpha = H_0 + v_\alpha$  with the eigenvalue

$$E_\alpha = e_d + \frac{\mathbf{q}^2}{2M_\alpha}, \quad (3.9)$$

$e_d$  being the deuteron binding energy; since all three particles are nucleons,  $M_\alpha = 2m_N/3$ . Due to their identity any pair of nucleons could be bound; I choose ( $\beta\gamma$ ) as representative pair. The scattering can be elastic, the deuteron bound state may get rearranged to another pair, unobservable for identical particles, or it may break up into a state of three free nucleons, i.e.,

$$|\phi_0(\mathbf{p}\mathbf{q})\mathbf{v}_0\rangle = \frac{1}{\sqrt{2}} (1 - P_{\beta\gamma}) |\mathbf{p}\rangle_\alpha |s_\beta m_{s_\beta} t_\beta m_{t_\beta} b_\beta\rangle |s_\gamma m_{s_\gamma} t_\gamma m_{t_\gamma} b_\gamma\rangle |\mathbf{q}s m_s t m_t b\rangle_\alpha. \quad (3.10)$$

The three particles in the final state are nucleons, i.e., all  $s = t = b = \frac{1}{2}$ . All discrete quantum numbers are summarized by  $\mathbf{v}_0$ . The  $H_0$  eigenvalue corresponding to the breakup state  $|\phi_0(\mathbf{p}\mathbf{q})\mathbf{v}_0\rangle$  is

$$E_0 = \frac{\mathbf{p}^2}{2\mu_\alpha} + \frac{\mathbf{q}^2}{2M_\alpha} \quad (3.11)$$

with  $\mu_\alpha = m_N/2$  and  $M_\alpha = 2m_N/3$ . Any set of Jacobi momenta could be used; I choose as representative states those which have the baryons ( $\beta\gamma$ ) as pair and the baryon  $\alpha$  as spectator. Both types of channel states,  $|\phi_\alpha(\mathbf{q})\nu_\alpha\rangle$  and  $|\phi_0(\mathbf{pq})\nu_0\rangle$ , are antisymmetrized with respect to the pair ( $\beta\gamma$ ).

The stationary scattering states [42, 43] corresponding to the channel states (3.8) and (3.10) are eigenstates of the full Hamiltonian  $H = H_0 + H_I$ ; they are obtained from the channel states using the full resolvent  $G(Z) = (Z - H_0 - H_I)^{-1}$ , i.e.,

$$|\psi_\alpha^{(\pm)}(\mathbf{q})\nu_\alpha\rangle = \pm i0G(E_\alpha \pm i0)|\phi_\alpha(\mathbf{q})\nu_\alpha\rangle, \quad (3.12a)$$

$$|\psi_0^{(\pm)}(\mathbf{pq})\nu_0\rangle = \pm i0G(E_0 \pm i0)|\phi_0(\mathbf{pq})\nu_0\rangle; \quad (3.12b)$$

they are not totally antisymmetric as required for physical states. Using the decomposition of the full resolvent  $G(Z)$  into channel resolvents  $G_\beta(Z) = (Z - H_0 - v_\beta)^{-1}$ , i.e.,

$$G(Z) = G_\beta(Z) + G_\beta(Z)(H_I - v_\beta)G(Z), \quad (3.13)$$

Eqs. (3.12) can be written as triads of Lippmann-Schwinger equations

$$|\psi_\alpha^{(\pm)}(\mathbf{q})\nu_\alpha\rangle = \delta_{\beta\alpha}|\phi_\alpha(\mathbf{q})\nu_\alpha\rangle + G_\beta(E_\alpha \pm i0)(H_I - v_\beta)|\psi_\alpha^{(\pm)}(\mathbf{q})\nu_\alpha\rangle, \quad (3.14a)$$

$$|\psi_0^{(\pm)}(\mathbf{pq})\nu_0\rangle = [1 + G_0(E_0 \pm i0)T_\beta(E_0 \pm i0)]|\phi_0(\mathbf{pq})\nu_0\rangle + G_\beta(E_0 \pm i0)(H_I - v_\beta)|\psi_0^{(\pm)}(\mathbf{pq})\nu_0\rangle \quad (3.14b)$$

with  $\alpha$  being fixed and  $\beta = 1, 2, 3$ ; they are necessary and sufficient to define the states  $|\psi_\alpha^{(\pm)}(\mathbf{q})\nu_\alpha\rangle$  and  $|\psi_0^{(\pm)}(\mathbf{pq})\nu_0\rangle$  uniquely. However, in scattering problems it is more convenient to work with the multichannel transition matrix  $U_{\beta\alpha}(Z)$  whose on-shell elements parametrize the  $S$  matrix. The calculations of this thesis are based on the AGS version [2] of three-particle scattering theory. It defines the multichannel transition matrix  $U_{\beta\alpha}(Z)$  between two-body channels by the decomposition of the full resolvent  $G(Z)$  into channel resolvents  $G_\alpha(Z)$  according to

$$G(Z) = \delta_{\beta\alpha}G_\alpha(Z) + G_\beta(Z)U_{\beta\alpha}(Z)G_\alpha(Z). \quad (3.15)$$

The multichannel transition matrix  $U_{\beta\alpha}(Z)$  describes elastic or rearrangement scattering; it is derived from the integral equation

$$U_{\beta\alpha}(Z) = (1 - \delta_{\beta\alpha})G_0^{-1}(Z) + \sum_\gamma (1 - \delta_{\beta\gamma})T_\gamma(Z)G_0(Z)U_{\gamma\alpha}(Z). \quad (3.16a)$$

The transition matrix  $U_{0\alpha}(Z)$  to final states with three free particles is obtained from the one between two-body channels by quadrature, i.e.,

$$U_{0\alpha}(Z) = G_0^{-1}(Z) + \sum_\gamma T_\gamma(Z)G_0(Z)U_{\gamma\alpha}(Z). \quad (3.16b)$$

Equation (3.16b) follows from the decomposition of the full resolvent  $G(Z)$  in the form (3.15) for  $\beta = 0$  and  $\alpha = 1, 2, 3$ .

The physical nucleon-deuteron and three-free-nucleon scattering states of Eqs. (2.6) are obtained from the states (3.12) by explicit antisymmetrization with respect to all baryons and by normalization, i.e.,

$$|\Psi_\alpha^{(\pm)}(\mathbf{q})\nu_\alpha\rangle = \frac{1}{\sqrt{3}}(1 + P)|\psi_\alpha^{(\pm)}(\mathbf{q})\nu_\alpha\rangle, \quad (3.17a)$$

$$|\Psi_0^{(\pm)}(\mathbf{pq})\nu_0\rangle = \frac{1}{\sqrt{3}}(1 + P)|\psi_0^{(\pm)}(\mathbf{pq})\nu_0\rangle. \quad (3.17b)$$

The corresponding symmetrized multichannel transition matrices for elastic nucleon-deuteron scattering and nucleon-deuteron breakup are given by

$$U(Z)|\phi_\alpha(\mathbf{q})\mathbf{v}_\alpha\rangle = \sum_\gamma U_{\alpha\gamma}(Z)|\phi_\gamma(\mathbf{q})\mathbf{v}_\gamma\rangle, \quad (3.18a)$$

$$U_0(Z)|\phi_\alpha(\mathbf{q})\mathbf{v}_\alpha\rangle = \sum_\gamma U_{0\gamma}(Z)|\phi_\gamma(\mathbf{q})\mathbf{v}_\gamma\rangle. \quad (3.18b)$$

The symmetrized multichannel transition matrix  $U(Z)$  satisfies the integral equation

$$U(Z) = PG_0^{-1}(Z) + PT_\alpha(Z)G_0(Z)U(Z) \quad (3.19a)$$

with a kernel connected after iteration and compact for short-ranged forces. The transition matrix  $U_0(Z)$ , as its non-symmetrized version, is obtained from the one between two-body channels  $U(Z)$  by quadrature

$$U_0(Z) = (1 + P)G_0^{-1}(Z) + (1 + P)T_\alpha(Z)G_0(Z)U(Z); \quad (3.19b)$$

the term  $(1 + P)G_0^{-1}(Z)$  does not contribute to the on-energy-shell matrix elements of  $U_0(Z)$  needed for the calculation of observables. Though one ends up with one integral equation (3.19a), the geometrical complexity of the three-nucleon problem is of course still present in the permutation operator  $P$ , defined in Sec. 3.1. The solution of the integral equation (3.19a) is described in Appendix C.

The  $S$  matrix for elastic nucleon-deuteron scattering and nucleon-deuteron breakup is given by the symmetrized on-shell transition matrices  $U(Z)$  and  $U_0(Z)$ , i.e.,

$$\begin{aligned} \langle\phi_\alpha(\mathbf{q}_f)\mathbf{v}_{\alpha_f}|S|\phi_\alpha(\mathbf{q}_i)\mathbf{v}_{\alpha_i}\rangle &= \delta(\mathbf{q}_f - \mathbf{q}_i)\delta_{\mathbf{v}_{\alpha_f}\mathbf{v}_{\alpha_i}} \\ &\quad - 2\pi i\delta(E_{\alpha_f} - E_{\alpha_i})\langle\phi_\alpha(\mathbf{q}_f)\mathbf{v}_{\alpha_f}|U(E_{\alpha_i} + i0)|\phi_\alpha(\mathbf{q}_i)\mathbf{v}_{\alpha_i}\rangle, \end{aligned} \quad (3.20a)$$

$$\langle\phi_0(\mathbf{p}_f\mathbf{q}_f)\mathbf{v}_{0_f}|S|\phi_\alpha(\mathbf{q}_i)\mathbf{v}_{\alpha_i}\rangle = -2\pi i\delta(E_{0_f} - E_{\alpha_i})\langle\phi_0(\mathbf{p}_f\mathbf{q}_f)\mathbf{v}_{0_f}|U_0(E_{\alpha_i} + i0)|\phi_\alpha(\mathbf{q}_i)\mathbf{v}_{\alpha_i}\rangle. \quad (3.20b)$$

When determining the  $S$  matrix, the initial and final states are fully antisymmetrized and normalized through  $(1 + P)/\sqrt{3}$  as in Eqs. (3.17); however, those symmetrization operators are incorporated into the definition of the symmetrized transition matrices  $U(Z)$  and  $U_0(Z)$  according to Eqs. (3.18); they are defined to act between the channel states which are antisymmetrized only with respect to the pair  $(\beta\gamma)$ . The basis states (2.2) have the same symmetry properties as the channel states.

### 3.3 Three-Nucleon Electromagnetic Reactions

The dynamical quantities needed for the description of the three-nucleon e.m. processes are the matrix elements of the e.m. nuclear current operator (2.15) between the three-nucleon bound and scattering states, i.e.,  $\langle\Psi_\alpha^{(-)}(\mathbf{q})\mathbf{v}_\alpha|j^\mu(\mathbf{Q}, \mathbf{K}_+)|B\rangle$  and  $\langle\Psi_0^{(-)}(\mathbf{p}\mathbf{q})\mathbf{v}_0|j^\mu(\mathbf{Q}, \mathbf{K}_+)|B\rangle$ . The bound state is calculated explicitly from the Faddeev amplitudes in Eq. (3.7). The nucleon-deuteron and the three-free-nucleon scattering states (3.17) can be given formally in terms of the multichannel transition matrix  $U(Z)$ , i.e.,

$$|\Psi_\alpha^{(\pm)}(\mathbf{q})\mathbf{v}_\alpha\rangle = \frac{1}{\sqrt{3}}(1 + P)[1 + G_0(E_\alpha \pm i0)T_\alpha(E_\alpha \pm i0)G_0(E_\alpha \pm i0)U(E_\alpha \pm i0)]|\phi_\alpha(\mathbf{q})\mathbf{v}_\alpha\rangle, \quad (3.21a)$$

$$\begin{aligned} |\Psi_0^{(\pm)}(\mathbf{p}\mathbf{q})\mathbf{v}_0\rangle &= \frac{1}{\sqrt{3}}(1 + P)[1 + G_0(E_0 \pm i0)T_\alpha(E_0 \pm i0)G_0(E_0 \pm i0)U(E_0 \pm i0)] \\ &\quad \times [1 + G_0(E_0 \pm i0)T_\alpha(E_0 \pm i0)]|\phi_0(\mathbf{p}\mathbf{q})\mathbf{v}_0\rangle. \end{aligned} \quad (3.21b)$$



The calculation of the nucleon-deuteron scattering state according to Eq. (3.21a) is possible and was carried out tentatively in Ref. [20]. In contrast, Eq. (3.21b) needs highly singular off-shell elements of  $U(Z)$  and therefore is unsuitable for the calculation of the scattering state with three free nucleons. It is much more advantageous to calculate the scattering states (3.17) only implicitly when forming the matrix elements of the e.m. current operator. For that purpose the multichannel transition matrix (3.19a) is used in the form of its Neumann series

$$U(Z) = \sum_{n=0}^{\infty} [PT_{\alpha}(Z)G_0(Z)]^n PG_0^{-1}(Z), \quad (3.22)$$

yielding the corresponding Neumann series for the matrix elements of the e.m. current operator, i.e.,

$$\begin{aligned} \langle \Psi_{\alpha}^{(-)}(\mathbf{q})v_{\alpha}|j^{\mu}(\mathbf{Q}, \mathbf{K}_{+})|B\rangle \\ = \langle \phi_{\alpha}(\mathbf{q})v_{\alpha}|\frac{1}{\sqrt{3}} \sum_{n=0}^{\infty} [PT_{\alpha}(E_{\alpha} + i0)G_0(E_{\alpha} + i0)]^n (1+P)j^{\mu}(\mathbf{Q}, \mathbf{K}_{+})|B\rangle, \end{aligned} \quad (3.23a)$$

$$\begin{aligned} \langle \Psi_0^{(-)}(\mathbf{pq})v_0|j^{\mu}(\mathbf{Q}, \mathbf{K}_{+})|B\rangle \\ = \langle \phi_0(\mathbf{pq})v_0|[1 + T_{\alpha}(E_0 + i0)G_0(E_0 + i0)] \\ \times \frac{1}{\sqrt{3}} \sum_{n=0}^{\infty} [PT_{\alpha}(E_0 + i0)G_0(E_0 + i0)]^n (1+P)j^{\mu}(\mathbf{Q}, \mathbf{K}_{+})|B\rangle. \end{aligned} \quad (3.23b)$$

The matrix elements (3.23) are calculated in two steps. First, I introduce the state  $|J^{\mu}(Z)\rangle$  whose Neumann series is in close correspondence with Eqs. (3.23), i.e.,

$$|J^{\mu}(Z)\rangle = \sum_{n=0}^{\infty} [PT_{\alpha}(Z)G_0(Z)]^n (1+P)j^{\mu}(\mathbf{Q}, \mathbf{K}_{+})|B\rangle; \quad (3.24a)$$

that Neumann series results from the following integral equation for  $|J^{\mu}(Z)\rangle$ , i.e.,

$$|J^{\mu}(Z)\rangle = (1+P)j^{\mu}(\mathbf{Q}, \mathbf{K}_{+})|B\rangle + PT_{\alpha}(Z)G_0(Z)|J^{\mu}(Z)\rangle; \quad (3.24b)$$

the dependence of  $|J^{\mu}(Z)\rangle$  on  $\mathbf{Q}$  and  $\mathbf{K}_{+}$  is suppressed in the notation for compactness. The integral equation (3.24b) for  $|J^{\mu}(Z)\rangle$  is analogous to (3.19a) for the symmetrized multichannel transition matrix  $U(Z)$ : Both equations have the same kernel, only their driving terms are different. Thus, they are solved using the same numerical techniques as described in Appendix C. Once  $|J^{\mu}(Z)\rangle$  is calculated, the current matrix elements required for the description of two- and three-body photo and electro disintegration of the trinucleon bound state are obtained according to

$$\langle \Psi_{\alpha}^{(-)}(\mathbf{q})v_{\alpha}|j^{\mu}(\mathbf{Q}, \mathbf{K}_{+})|B\rangle = \frac{1}{\sqrt{3}}\langle \phi_{\alpha}(\mathbf{q})v_{\alpha}|J^{\mu}(E_{\alpha} + i0)\rangle, \quad (3.25a)$$

$$\begin{aligned} \langle \Psi_0^{(-)}(\mathbf{pq})v_0|j^{\mu}(\mathbf{Q}, \mathbf{K}_{+})|B\rangle = \frac{1}{\sqrt{3}}\langle \phi_0(\mathbf{pq})v_0|(1+P)[j^{\mu}(\mathbf{Q}, \mathbf{K}_{+})|B\rangle \\ + T_{\alpha}(E_0 + i0)G_0(E_0 + i0)|J^{\mu}(E_0 + i0)\rangle]. \end{aligned} \quad (3.25b)$$

### 3.4 Charge-Dependent Two-Baryon Transition Matrix

Assuming charge independence, the trinucleon bound state and nucleon-deuteron scattering states are pure states with total isospin  $T = \frac{1}{2}$ ; the three-free-nucleon scattering states have total isospin  $T = \frac{1}{2}$  and  $T = \frac{3}{2}$ , but those parts are not dynamically coupled. If charge dependence is allowed for as in the calculations of this thesis, the two-baryon transition matrix  $T_\alpha(Z)$  becomes dependent on the projection  $M_T$  of the pair isospin  $T$ . Thus, its matrix elements in the three-particle basis  $|pqv(Ij)\rangle_\alpha$  couple states of total isospin  $T = \frac{1}{2}$  and  $T = \frac{3}{2}$ , i.e., with respect to the total isospin  $T$  the two-baryon transition matrix  $T_\alpha(Z)$  in the isospin-triplet partial waves has the general structure

$$T_\alpha(Z) = \sum_{T' M_T} |T' M_T\rangle_\alpha T_{2T' 2T, 2M_T}(Z) \langle T M_T| \quad (3.26a)$$

with the components

$$T_{11,1}(Z) = \frac{2}{3}T_{pp}(Z) + \frac{1}{3}T_{np}(Z), \quad (3.26b)$$

$$T_{31,1}(Z) = \frac{\sqrt{2}}{3}[T_{pp}(Z) - T_{np}(Z)], \quad (3.26c)$$

$$T_{13,1}(Z) = \frac{\sqrt{2}}{3}[T_{pp}(Z) - T_{np}(Z)], \quad (3.26d)$$

$$T_{33,1}(Z) = \frac{1}{3}T_{pp}(Z) + \frac{2}{3}T_{np}(Z) \quad (3.26e)$$

for the  $M_T = \frac{1}{2}$ , i.e., for the  $npp$  system, and

$$T_{11,-1}(Z) = \frac{2}{3}T_{nn}(Z) + \frac{1}{3}T_{np}(Z), \quad (3.26f)$$

$$T_{31,-1}(Z) = \frac{\sqrt{2}}{3}[T_{np}(Z) - T_{nn}(Z)], \quad (3.26g)$$

$$T_{13,-1}(Z) = \frac{\sqrt{2}}{3}[T_{np}(Z) - T_{nn}(Z)], \quad (3.26h)$$

$$T_{33,-1}(Z) = \frac{1}{3}T_{nn}(Z) + \frac{2}{3}T_{np}(Z) \quad (3.26i)$$

for the  $M_T = -\frac{1}{2}$ , i.e., for the  $mpn$  system. The calculation based on the full forms of Eqs. (3.26) is called *exact* treatment of the charge dependence; it is especially important in the  $^1S_0$  partial wave. For higher isospin-triplet partial waves an *approximative* treatment of charge dependence without coupling between the total isospin  $T = \frac{1}{2}$  and  $T = \frac{3}{2}$  states, i.e., with  $T_{31,2M_T}(Z) = T_{13,2M_T}(Z) = 0$ , is usually sufficient. In hadronic reactions that *approximative* treatment neglects also  $T = \frac{3}{2}$  components, i.e.,  $T_{33,2M_T}(Z) = 0$ . In contrast, the calculations of e.m. reactions require the total isospin  $T = \frac{3}{2}$  components of scattering states in *all* considered isospin-triplet two-baryon partial waves, since the e.m. current couples the  $T = \frac{1}{2}$  and  $T = \frac{3}{2}$  components strongly.

## 4

# Hadronic Properties of Three-Nucleon Bound State

The calculation is done separately for  ${}^3\text{He}$  and  ${}^3\text{H}$  since the dynamic input is charge dependent. Furthermore, I include the point Coulomb interaction by cutting off its technically dangerous long tail and adding that cutoff Coulomb to the hadronic potential; the independence of the results from the cutoff radius  $R$  for sufficiently large values is established; I find  $R = 12$  fm large enough. The point Coulomb interaction has to be included between the two protons in  ${}^3\text{He}$ , but also in channels with a  $\Delta$  isobar, i.e., in the  $np\Delta^+$  channel of  ${}^3\text{He}$  and in the  $pp\Delta^-$  channel of  ${}^3\text{H}$ . Partial waves up to total two-baryon angular momentum  $I = 6$  in purely nucleonic channels and up to  $I = 4$  in nucleon- $\Delta$  channels are taken into account. The charge dependence of the nucleon-nucleon and the Coulomb potentials is treated exactly in partial waves up to  $I = 2$ , yielding total isospin  $T = \frac{3}{2}$  channels; in other two-baryon isospin-triplet partial waves the charge dependence is treated approximately as explained in Sec. 3.4, i.e., without coupling to  $T = \frac{3}{2}$  states; in those higher partial waves the coupling to  $T = \frac{3}{2}$  states was checked to be quantitatively irrelevant. The results appear fully converged with all those truncations on partial waves.

Results on binding energy contributions are collected in Table 4.1. One notices, as observed and discussed already long ago [16], two sizable  $\Delta$ -isobar effects on binding which partially cancel each other, i.e., the repulsive two-nucleon dispersion  $\Delta E_2$  and the attractive three-nucleon force effect  $\Delta E_3$  proper; since the diagonal nucleon- $\Delta$  potential is strong, it contributes substantially to the three-nucleon binding; only about 75% of  $\Delta E_3$  is due to the contribution of the Fujita-Miyazawa type, arising solely from the transition potential according to Fig. 2.5. Though the purely nucleonic reference potential CD Bonn misses the three-nucleon binding by rather little and the  $\Delta$ -isobar effects arising from the new coupled-channel potential are beneficial, still, they are unable to account for the missing binding in full. The experimental  ${}^3\text{He} - {}^3\text{H}$  binding-energy difference is 0.764 MeV; most of it is due to the Coulomb interaction in  ${}^3\text{He}$ . When calculating  ${}^3\text{H}$  with a charge symmetric hadronic interaction, i.e., with the same hadronic part for  $pp$  and  $nn$ , Coulomb alone yields a binding energy difference of 0.685 MeV. The charge asymmetry of the coupled-channel potential makes an additional contribution of 0.059 MeV and the kinematic effects due to the  $p$ - $n$  mass difference add additional 0.012 MeV, yielding a total binding-energy difference of 0.756 MeV. That theoretical value agrees quite well with the experimental one of 0.764 MeV.

The two constructions of coupled-channel potentials without fit, CD Bonn +  $\Delta$  (sub1) and CD Bonn +  $\Delta$  (sub2), are unable to account for the three-nucleon binding energy with  $\Delta$ -isobar effects, obtained for the well-fitted coupled-channel potential CD Bonn +  $\Delta$ , accurately enough; both fail especially with respect to the two-nucleon dispersive repulsion  $\Delta E_2$ , CD Bonn +  $\Delta$  (sub2) also with respect to wave function probability  $P_\Delta$  and to the momentum distribution of the  $\Delta$  isobar as displayed in Fig. 4.1 for  ${}^3\text{H}$ , together with the nucleonic momentum distribution.

	$E_B$	$\Delta E_2$	$\Delta E_3$	$P_S$	$P_{S'}$	$P_P$	$P_D$	$P_{3/2}$	$P_\Delta$
CD Bonn	-8.004			91.621	1.307	0.047	7.020	0.0048	
CD Bonn + $\Delta$	-8.297	0.513	-0.806	89.922	1.301	0.064	7.216	0.0045	1.493
CD Bonn + $\Delta$ (sub1)	-8.515	0.353	-0.864	89.911	1.173	0.067	7.293	0.0047	1.552
CD Bonn + $\Delta$ (sub2)	-8.271	0.648	-0.915	88.799	1.207	0.073	7.237	0.0045	2.680
Experiment	-8.482								
CD Bonn	-7.258			91.403	1.538	0.046	7.002	0.0111	
CD Bonn + $\Delta$	-7.541	0.483	-0.766	89.776	1.515	0.063	7.197	0.0104	1.439
CD Bonn + $\Delta$ (sub1)	-7.752	0.328	-0.822	89.781	1.370	0.066	7.274	0.0105	1.499
CD Bonn + $\Delta$ (sub2)	-7.521	0.601	-0.864	88.711	1.412	0.072	7.216	0.0102	2.579
Experiment	-7.718								

Table 4.1: Hadronic properties of  $^3\text{H}$  (top) and  $^3\text{He}$  (bottom). The  $\Delta$ -isobar effect on the binding energy  $E_B$  is split into the two-nucleon dispersion  $\Delta E_2$  and the effective three-nucleon force effect  $\Delta E_3$ . The probability  $P_L$ ,  $L$  being  $S$ ,  $S'$ ,  $P$  or  $D$ , refers to purely nucleonic  $T = \frac{1}{2}$  wave function components with definite total three-nucleon orbital angular momentum  $L$  and definite permutation symmetry according to Refs. [44, 45],  $P_{3/2}$  to the  $T = \frac{3}{2}$  wave function component arising from charge dependence, and  $P_\Delta$  to the wave function components with  $\Delta$ -isobar configurations. All energies are given in MeV, all probabilities are given in percent; always three digits are quoted, only for the very small quantity  $P_{3/2}$  four digits are quoted; they appear converged.

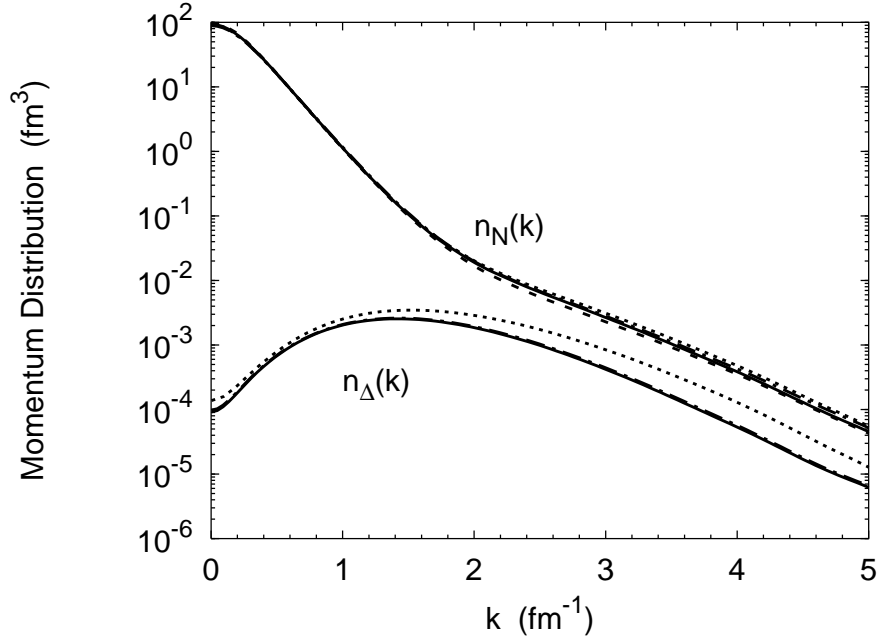


Figure 4.1:  $^3\text{H}$  nucleon and  $\Delta$ -isobar momentum distributions  $n_N(k)$  and  $n_\Delta(k)$  as functions of the magnitude of the single-particle momentum  $k$ . The distributions are normalized such that  $\int_0^\infty dk k^2 [n_N(k) + n_\Delta(k)] = 3$ . Compared are predictions of the different coupled-channel potentials, i.e., CD Bonn +  $\Delta$  (solid curves), CD Bonn +  $\Delta$  (sub1) (dashed-dotted curves), CD Bonn +  $\Delta$  (sub2) (dotted curves). The solid and dashed-dotted curves are almost indistinguishable in the plot. Results for  $n_N(k)$  based on the nucleonic CD Bonn potential without  $\Delta$ -isobar excitation are given by the dashed curve.

# 5

## Nucleon-Deuteron Scattering

The description of the hadronic dynamics in this thesis is nonrelativistic. Nevertheless, I like to make the step to observables by starting out from the relativistic form of the cross section, since other particles, i.e., electrons and photons, involved in the e.m. reactions to be described in the next chapters, are relativistic; the nonrelativistic reduction of the relativistic form of the cross section for hadrons can be easily done. Furthermore, the relativistic form of the cross section may enable me to estimate the theoretical error bars due to the use of the nonrelativistic description.

### 5.1 Spin-Averaged and Spin-Dependent Cross Sections

I consider the general scattering process

$$i_1 + i_2 \rightarrow f_1 + \dots + f_n. \quad (5.1)$$

The differential cross section has the general form

$$d\sigma_{i \rightarrow f} = |\langle f | M | i \rangle|^2 \frac{d\text{Lips}(k_{i_1} + k_{i_2}, \{k_{f_j} | j = 1, \dots, n\})}{4[(k_{i_1} \cdot k_{i_2})^2 - m_{i_1}^2 m_{i_2}^2]^{\frac{1}{2}}}, \quad (5.2a)$$

where the Lorentz-invariant singularity-free matrix element  $\langle f | M | i \rangle$  parametrizes the relativistic  $S$  matrix, i.e.,

$$\langle f | S | i \rangle = \langle f | i \rangle - i(2\pi)^4 \delta^{(4)}\left(\sum_{j=1}^n k_{f_j} - k_{i_1} - k_{i_2}\right) \langle f | M | i \rangle (2\pi)^{-\frac{3}{2}(n+2)} [2k_{i_1}^0 2k_{i_2}^0 \prod_{j=1}^n (2k_{f_j}^0)]^{-\frac{1}{2}}, \quad (5.2b)$$

$d\text{Lips}(k_{i_1} + k_{i_2}, \{k_{f_j} | j = 1, \dots, n\})$  is the Lorentz-invariant phase-space element, i.e.,

$$d\text{Lips}(k_{i_1} + k_{i_2}, \{k_{f_j} | j = 1, \dots, n\}) = (2\pi)^4 \delta^{(4)}\left(\sum_{j=1}^n k_{f_j} - k_{i_1} - k_{i_2}\right) \prod_{j=1}^n \frac{d^3 k_{f_j}}{(2\pi)^3 2k_{f_j}^0}, \quad (5.2c)$$

and the factor  $4[(k_{i_1} \cdot k_{i_2})^2 - m_{i_1}^2 m_{i_2}^2]^{\frac{1}{2}}$  contains the incoming flux, the target density and projectile and target normalization factors; the  $k_{h_j}$  with  $h = i (f)$  are the relativistic four momenta of the involved particles in the initial (final) states, i.e.,  $k_{h_j}^0 = (m_{h_j}^2 + \mathbf{k}_{h_j}^2)^{\frac{1}{2}}$ .

Since the relativistic description of hadronic dynamics is not available, the Lorentz-invariant matrix element  $\langle f | M | i \rangle$  is calculated from nonrelativistic quantum mechanics. The quantum-mechanical  $S$  matrix can be written in the form

$$\langle f | S | i \rangle = \langle f | i \rangle - 2\pi i \delta^{(3)}(\mathbf{P}_f - \mathbf{P}_i) \delta(E_f - E_i) \langle s_f | M(E_i \mathbf{k}_f) | s_i \rangle \quad (5.3)$$

with  $\mathbf{P}_i$  ( $\mathbf{P}_f$ ) and  $E_i$  ( $E_f$ ) being the total initial (final) momentum and the total initial (final) energy.  $\langle s_f | M(E_i \mathbf{k}_f) | s_i \rangle$  is the quantum-mechanical transition amplitude; its dependence on the spin projections of the particles in the initial and final states, collectively described by  $s_i$  and  $s_f$ , on the available initial energy  $E_i$  and on the final particle momenta, collectively described by  $\mathbf{k}_f$ , is indicated explicitly. Equating the relativistic and nonrelativistic  $S$  matrices (5.2b) and (5.3) as in Refs. [20, 21], the resulting matrix element

$$\langle f | M | i \rangle = (2\pi)^{\frac{3}{2}n} \langle s_f | M(E_i \mathbf{k}_f) | s_i \rangle [2k_{i_1}^0 2k_{i_2}^0 \prod_{j=1}^n (2k_{f_j}^0)]^{\frac{1}{2}} \quad (5.4)$$

loses the property of being a Lorentz scalar. In contrast, the kinematical factors in Eq. (5.2a) can be easily calculated relativistically; such a split calculational strategy, based on nonrelativistic dynamics and on relativistic kinematics, was used in Refs. [20, 21] for e.m. reactions.

However, I use a different strategy for the standard calculations of this thesis: Since the quantum-mechanical  $S$  matrix (5.3) represents the lowest order nonrelativistic reduction of the relativistic  $S$  matrix (5.2b), I consistently perform a corresponding nonrelativistic reduction for *all* quantities in Eqs. (5.2) and (5.4), i.e.,

- the hadron energy factors  $2k_{h_j}^0$  are replaced by their rest masses  $2m_{h_j}$ , and
- nonrelativistic hadron energies  $k_{h_j}^0 = m_{h_j} + \mathbf{k}_{h_j}^2 / 2m_{h_j}$  are used for the energy conserving  $\delta$  function and for the factor  $4[(k_{i_1} \cdot k_{i_2})^2 - m_{i_1}^2 m_{i_2}^2]^{\frac{1}{2}}$ .

The obtained expressions for cross sections are identical to the ones, derived from quantum mechanics directly, e.g., for reactions with hadrons only

$$d\sigma_{i \rightarrow f} = \frac{(2\pi)^4 |\langle s_f | M(E_i \mathbf{k}_f) | s_i \rangle|^2}{|\mathbf{k}_{i_1}/m_{i_1} - \mathbf{k}_{i_2}/m_{i_2}|} \delta^{(3)}(\mathbf{P}_f - \mathbf{P}_i) \delta(E_f - E_i) \prod_{j=1}^n d^3k_{f_j}. \quad (5.5)$$

The form of the cross section (5.5) is consistent with the fit of the underlying baryonic potentials, whereas the one based on Eqs. (5.2) and (5.4) is not. Furthermore, when total cross sections in hadronic and e.m. reactions or inelastic response functions in electron scattering are calculated by implicit integration over final states as described in Sec. 6.1.4 for the total photo cross section and in Sec. 7.1.3 for inelastic response functions in electron scattering, the energy conserving  $\delta$  function is rewritten as imaginary part of the full resolvent and has to be made consistent with the employed nonrelativistic dynamics. Thus, the split calculational strategy of Refs. [20, 21] cannot be carried through for total cross sections of all reactions and later on for inelastic structure functions in e.m. reactions.

### 5.1.1 Elastic Nucleon-Deuteron Scattering

Elastic nucleon-deuteron scattering is considered in the c.m. system. The nucleon-beam direction is taken to define the  $z$ -axis, i.e.,  $\hat{\mathbf{z}} = -\hat{\mathbf{q}}_i$ ,  $\mathbf{q}_i$  being the Jacobi momentum defined in Eq. (2.1). The available scattering energy  $E_i = e_d + 3\mathbf{q}_i^2 / 4m_N$  determines the magnitude of the final nucleon-deuteron momentum  $q_f$  by energy conservation, i.e.,  $q_f = q_i$ . The only independent continuous variable is the direction  $-\hat{\mathbf{q}}_f$  of the scattered nucleon (or the direction  $\hat{\mathbf{q}}_f$  of the scattered deuteron). The quantum-mechanical amplitude for the elastic nucleon-deuteron scattering can easily be read off from Eq. (3.20a), i.e.,

$$\langle s_f | M(E_i \mathbf{q}_f) | s_i \rangle = \langle \phi_\alpha(\mathbf{q}_f) \mathbf{v}_{\alpha_f} | U(E_i + i0) | \phi_\alpha(\mathbf{q}_i) \mathbf{v}_{\alpha_i} \rangle; \quad (5.6)$$

the matrix element is calculated – by definition – in the c.m. system, since it refers to the internal motion only and it is independent of the total momenta  $\mathbf{P}_i$  and  $\mathbf{P}_f$ . In Eq. (5.6) the initial and final spin projections of nucleon and deuteron are  $s_i = \{m_{s_i} M_{I_i}\}$  and  $s_f = \{m_{s_f} M_{I_f}\}$ . The spin-dependent differential c.m. cross section (5.5) for the elastic nucleon-deuteron scattering takes the compact form

$$\frac{d^2\sigma_{i \rightarrow f}}{d^2\hat{\mathbf{q}}_f} = |\langle s_f | M(E_i \mathbf{q}_f) | s_i \rangle|^2 \text{fps} \quad (5.7a)$$

with the phase-space factor

$$\text{fps} = (2\pi)^4 (2m_N/3)^2. \quad (5.7b)$$

The spin-averaged differential c.m. cross section is

$$\overline{\frac{d^2\sigma}{d^2\hat{\mathbf{q}}_f}} = \frac{1}{6} \sum_{s_f s_i} \frac{d^2\sigma_{i \rightarrow f}}{d^2\hat{\mathbf{q}}_f}, \quad (5.8a)$$

$$\overline{\frac{d^2\sigma}{d^2\hat{\mathbf{q}}_f}} = \frac{1}{6} \text{Tr}[M(E_i \mathbf{q}_f) M^\dagger(E_i \mathbf{q}_f)] \text{fps}, \quad (5.8b)$$

where  $M(E_i \mathbf{q}_f)$  is treated as an operator in spin space. In the figures the spin-averaged differential cross section is denoted by  $d\sigma/d\Omega$ , the traditional notation.

The calculation of the spin-dependent cross sections and of various spin observables is described in Appendix D.

### 5.1.2 Nucleon-Deuteron Breakup

Nucleon-deuteron breakup is considered in the lab system. The target deuteron is at rest, i.e., its momentum  $\mathbf{k}_d = 0$ , the impinging nucleon has momentum  $\mathbf{k}_{\alpha_i}$ , which defines the  $z$ -axis, i.e.,  $\hat{\mathbf{z}} = \hat{\mathbf{k}}_{\alpha_i}$ . The changes which arise when the deuteron impinges on a nucleon target are obvious. The nucleon momentum  $\mathbf{k}_{\alpha_i}$  determines also the initial nucleon-deuteron momentum  $\mathbf{q}_i = -\frac{2}{3}\mathbf{k}_{\alpha_i}$  and the available initial energy in the c.m. system  $E_i = e_d + 3\mathbf{q}_i^2/4m_N$ . The quantum-mechanical amplitude for the nucleon-deuteron breakup according to Eq. (3.20b) is

$$\langle s_f | M(E_i \mathbf{p}_f \mathbf{q}_f) | s_i \rangle = \langle \Phi_0(\mathbf{p}_f \mathbf{q}_f) \mathbf{v}_{0f} | U_0(E_i + i0) | \Phi_\alpha(\mathbf{q}_i) \mathbf{v}_{\alpha_i} \rangle, \quad (5.9)$$

the matrix element again being calculated – by definition – in the c.m. system, since it refers to the internal motion only and it is independent of the total momenta  $\mathbf{P}_i$  and  $\mathbf{P}_f$ . In Eq. (5.9) the initial and final spin projections are  $s_i = \{m_{s_i} M_{I_i}\}$  and  $s_f = \{m_{s_1} m_{s_2} m_{s_3}\}$ . The neutron and proton nature of the nucleons (123) in the final state is notationally not indicated, but always determined by experiment. The final-state Jacobi momenta  $\mathbf{p}_f$  and  $\mathbf{q}_f$  are determined from the final single-nucleon momenta  $\mathbf{k}_1, \mathbf{k}_2, \mathbf{k}_3$  according to Eqs. (2.1). Due to momentum conservation  $\mathbf{k}_3 = \mathbf{k}_{\alpha_i} - \mathbf{k}_1 - \mathbf{k}_2$ , thus,  $\mathbf{p}_f = \frac{1}{2}(\mathbf{k}_1 - \mathbf{k}_2)$  and  $\mathbf{q}_f = (\mathbf{k}_1 + \mathbf{k}_2) - \frac{2}{3}\mathbf{k}_{\alpha_i}$ . Furthermore, energy conservation puts an additional constraint  $E_i = \mathbf{p}_f^2/m_N + 3\mathbf{q}_f^2/4m_N$ , keeping only five independent continuous variables. For example, if the momentum  $\mathbf{k}_1$  and the direction  $\hat{\mathbf{k}}_2$  were measured, all three nucleon momenta are determined in the final state, although not always uniquely. In practice, the two nucleon scattering angles with respect to the beam direction  $(\theta_1, \varphi_1)$  and  $(\theta_2, \varphi_2)$ , usually notationally shortened to  $(\theta_1, \theta_2, \varphi_2 - \varphi_1)$ , and their kinetic energies without rest masses  $E_1$  and  $E_2$  are measured. Those energies are related by

momentum and energy conservation and therefore lie on a fixed kinematical curve. The observables are therefore given as function of the arclength  $S$  along that curve, i.e.,

$$S = \int_0^S dS \quad (5.10)$$

with  $dS = \sqrt{dE_1^2 + dE_2^2}$  and  $E_2$  being considered a function of  $E_1$  or vice versa depending on numerical convenience; the arclength is always taken counterclockwise along the kinematical curve. The normalization of the arclength value zero is chosen differently in different kinematical situations.

The spin-dependent fivefold differential lab cross section takes the compact form

$$\frac{d^5\sigma_{i \rightarrow f}}{dS d^2\hat{\mathbf{k}}_1 d^2\hat{\mathbf{k}}_2} = |\langle s_f | M(E_i \mathbf{p}_f \mathbf{q}_f) | s_i \rangle|^2 \text{fps} \quad (5.11a)$$

with the phase-space factor

$$\text{fps} = (2\pi)^4 \frac{m_N}{|\mathbf{k}_{\alpha_i}|} m_N^2 \mathbf{k}_1^2 \mathbf{k}_2^2 \left\{ \mathbf{k}_1^2 [2|\mathbf{k}_2| - \hat{\mathbf{k}}_2 \cdot (\mathbf{k}_{\alpha_i} - \mathbf{k}_1)]^2 + \mathbf{k}_2^2 [2|\mathbf{k}_1| - \hat{\mathbf{k}}_1 \cdot (\mathbf{k}_{\alpha_i} - \mathbf{k}_2)]^2 \right\}^{-1/2}. \quad (5.11b)$$

The spin-averaged fivefold differential lab cross section is

$$\frac{\overline{d^5\sigma}}{dS d^2\hat{\mathbf{k}}_1 d^2\hat{\mathbf{k}}_2} = \frac{1}{6} \text{Tr}[M(E_i \mathbf{p}_f \mathbf{q}_f) M^\dagger(E_i \mathbf{p}_f \mathbf{q}_f)] \text{fps}. \quad (5.12)$$

In the figures the spin-averaged fivefold differential cross section is denoted by  $d^5\sigma/dS d\Omega_1 d\Omega_2$ , the traditional notation.

The calculation of the spin-dependent cross sections and of various spin observables is described in Appendix D. A problem in the comparison of theoretical predictions and experimental data arising in the case when the latter are analyzed using relativistic kinematics is discussed in Sec. D.2 of the same appendix.

## 5.2 Calculational Advances

This section describes technical and physics improvements this thesis was able to achieve. First, it discusses the Chebyshev technique for expanding the dynamic input in form of the two-baryon transition matrix and the deuteron wave function and compares it with alternative techniques. Second, it discusses the solution of three-particle equations without using separable potentials. Third, it discusses the importance of a realistic dynamic input, i.e., of well-fitted purely nucleonic and coupled-channel potentials, for reliable physics predictions.

### 5.2.1 Chebyshev Expansion

The two-baryon transition matrix and the deuteron wave function are expanded in terms of Chebyshev polynomials as motivated and described in Appendix C.1. The Chebyshev expansion for the two-baryon transition matrix is given in Eqs. (C.4) and for the deuteron wave function in Eqs. (C.9). It works equally well for both quantities. Figure 5.1 displays examples of the Chebyshev coefficients  $T_{\eta'\eta}^{\prime i}(\chi q, Z)$  of the two-baryon transition matrix and of the Chebyshev coefficients  $d_L^i$  of  $v_\alpha |dq\chi_d\rangle_\alpha$ ; their fast decrease with increasing order of the polynomial is impressive; the convergence appears subgeometric as described in Appendix C.1.3; the expansion converges therefore rapidly as shown in



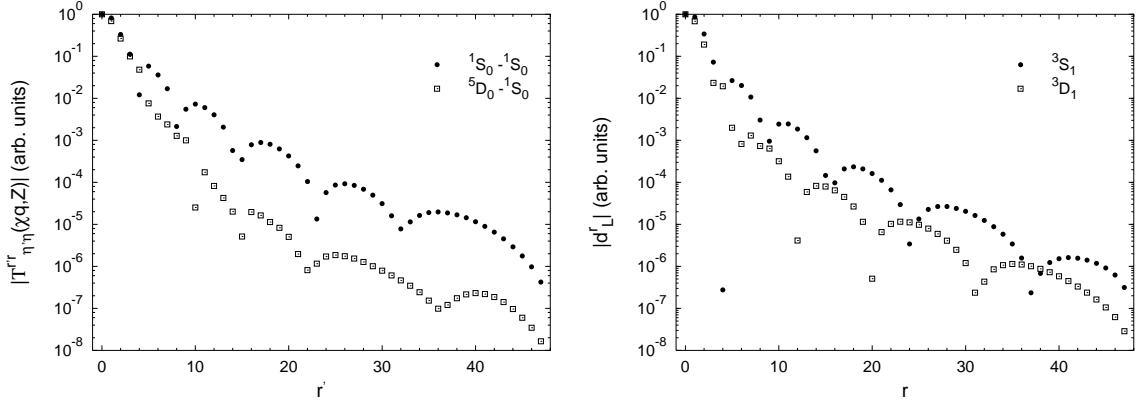


Figure 5.1: Chebyshev coefficients  $T_{\eta\eta}^{r'r}(\chi q, Z)$  of the  $^1S_0(NN) - ^5D_0(N\Delta)$  two-baryon transition matrix for  $r = 1$ ,  $q = 0$  and  $Z = 100$  MeV and Chebyshev coefficients  $d_L^r$  of the deuteron wave function as functions of the order  $r'$  or  $r$  of the Chebyshev polynomials.

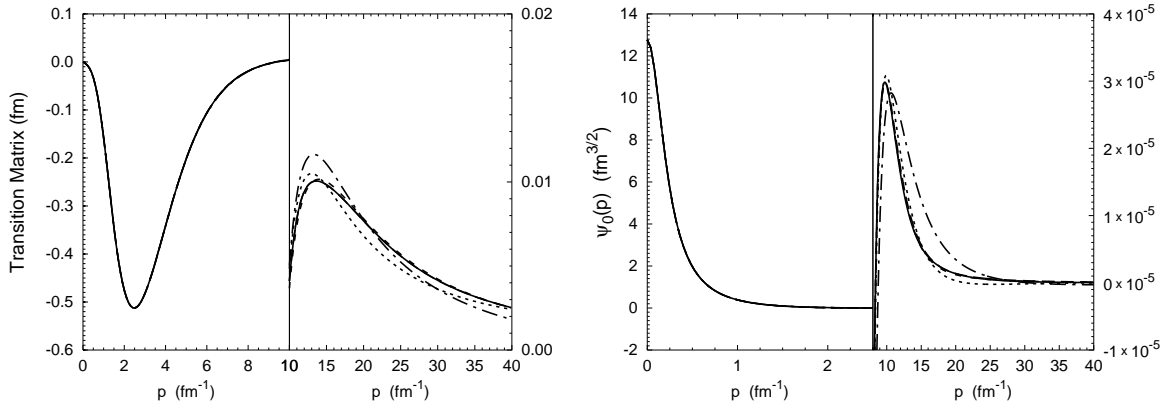


Figure 5.2: Convergence of the Chebyshev expansion. On the left side the real part of the  $^1S_0(NN) - ^5D_0(N\Delta)$  two-baryon transition matrix is shown as function of the final momentum  $p$ . The transition  $^1S_0 \rightarrow ^5D_0$  at  $q = 0$  with the available energy  $Z = 100$  MeV for the initial pair momentum  $p_i = 1 \text{ fm}^{-1}$  is plotted. On the right side the  $L = 0$  component of the deuteron wave function  $\psi_L(p) \equiv \langle p(LS)I_0M_IT_0M_{T_0}B | dI_0M_IT_0M_{T_0} \rangle$  is shown. The dot-dashed, dotted, dashed and solid curves correspond to Chebyshev interpolation using 12, 16, 24 and 48 polynomials, respectively. All curves are indistinguishable in the resolution adopted for momenta up to  $10 \text{ fm}^{-1}$ . Differences can only be seen for momenta beyond  $10 \text{ fm}^{-1}$  with an especially fine resolution. The standard of reference is spline interpolation with 48 spline functions. Most curves, based on much fewer Chebyshev polynomials, turn out to be indistinguishable from those reference curves.

Fig. 5.2. Thus, the truncation of the Chebyshev expansion at the rather small orders 16 or 24 is well justified, except for very large momenta, unimportant for three-nucleon scattering at the rather modest available energies considered in this thesis. The Chebyshev expansion is systematic and efficient; in contrast, when using spline interpolation for the same quantities all spline functions are of same importance; there is no way for a corresponding systematic truncation of the spline expansion.

### 5.2.2 Solution of Three-Particle Equations

I use the Chebyshev expansion of the two-baryon transition matrix and of the deuteron wave function as interpolation scheme for solving the three-particle equations without further approximations with respect to the dynamic input. I performed the following tests, in order to assure its technical reliability. The numerical apparatus is described in Appendix C.1.

1. References [17–19, 46] employed the coupled-channel potential A2 [16] and the Paris potential [23] as its nucleonic reference potential in separable forms as dynamic input for calculations. I take those separable forms now as numerical test cases, but do not exploit their separable structure. Instead, I apply a Chebyshev expansion for their separable forms and interpolate them accordingly when solving integral equation (3.19a) with the technique of Appendix C.1. The agreement with results derived from the explicit use of the separable expansion is so excellent that differences cannot be documented in any plot. This fact is one indication that the new technique of Appendix C.1.1 is reliable.
2. Figure 5.3 studies the convergence of sample physics observables with the number of Chebyshev polynomials employed. The convergence is impressively rapid. Understandably it is faster for lower energies. Nevertheless, as an alternative, also spline interpolation is used, as usually adopted in few-body numerics when solving the integral equation (3.19a). In both interpolation schemes the basic integral (C.13) has the same general structure as discussed in Appendix C.3. The results provided by both interpolation schemes are indistinguishable; however, spline interpolation reaches the same quality of results only with a considerably larger number of functions than the corresponding Chebyshev expansion. The results of Fig. 5.3 confirm my previous conclusion: *The Chebyshev expansion is systematic and efficient and thereby superior to spline interpolation.* All results given in the following are obtained with 24 Chebyshev polynomials.

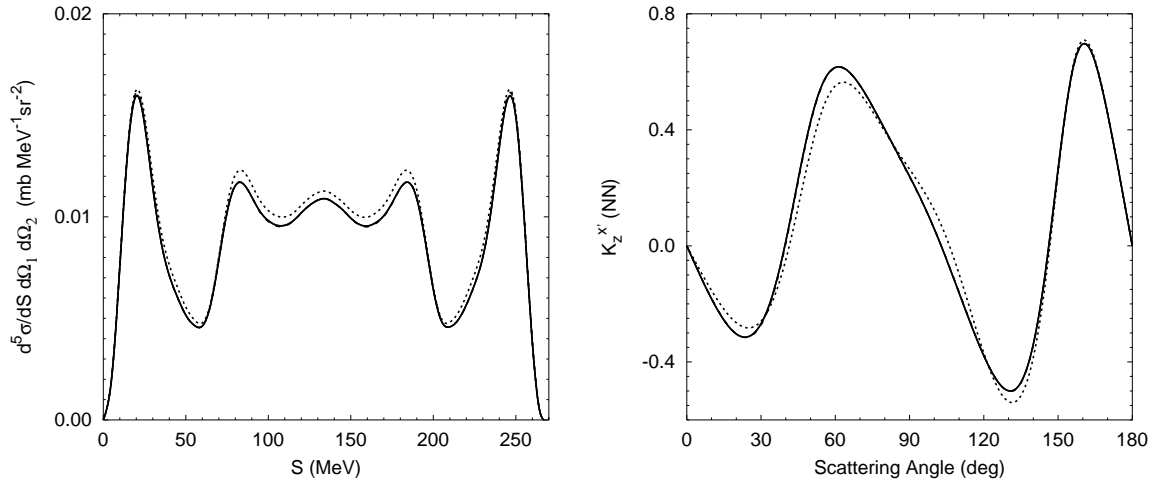


Figure 5.3: Fivefold differential cross section of  $Nd$  breakup at 190 MeV nucleon lab energy in the collinear configuration  $(59.8^\circ, 59.8^\circ, 180.0^\circ)$  and nucleon to nucleon polarization transfer coefficient  $K_z^x$  (NN) of elastic  $Nd$  scattering at 190 MeV nucleon lab energy. The convergence of the Chebyshev expansion is studied. The dotted and dashed curves are results obtained with 8 and 12 Chebyshev polynomials, respectively, the solid curve corresponds to the indistinguishable results obtained with 16, 24 and 48 Chebyshev polynomials and with 48 spline functions; always more than 24 spline functions are needed to reproduce the solid curve very well.

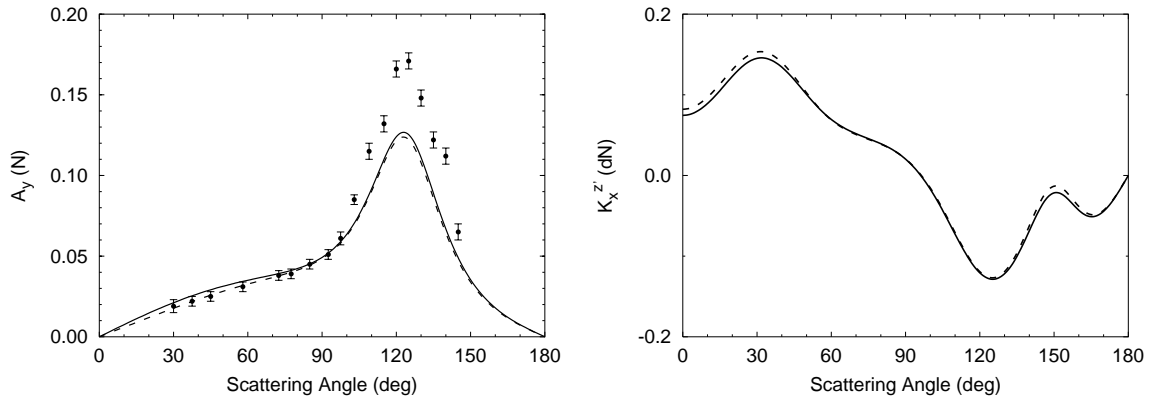


Figure 5.4: Nucleon analyzing power  $A_y(N)$  of elastic  $Nd$  scattering at 10 MeV nucleon lab energy and deuteron to nucleon polarization transfer coefficient  $K_x^z(dN)$  of elastic  $Nd$  scattering at 135 MeV nucleon lab energy as function of the c.m. scattering angle. The separable expansion of the two-baryon potential A2 with  $\Delta$ -isobar excitation is tested. The dashed curves are results of the separably expanded potential form, the solid curves of the unexpanded form. The experimental data are from Ref. [47].

3. The quality of the separable expansion employed in Refs. [17–19, 46] is well established for the purely nucleonic Paris potential; for the two-baryon coupled-channel potential the separable expansion could be tested in the two-nucleon system and for the three-nucleon bound state and was found to be quite accurate [46]. I am now able to complete the latter tests also for three-nucleon scattering. Sample results based on the coupled-channel potential A2 of Refs. [17–19, 46] and obtained with the technique of Appendix C.1 are compared in Fig. 5.4 with corresponding results for the separably expanded form of A2 derived either by the technique of Appendix C.1 or by the technique of Ref. [19]. Differences of results obtained for the separably expanded and the unexpanded forms of A2 are discernible, but the separable expansion is again proven to be quite reliable, enforcing the conclusions of Ref. [46].

### 5.2.3 Comparison of Different Potentials

Compared to the results of Refs. [17–19, 46] based on the Paris potential [23] and its coupled-channel extension, most observables of elastic nucleon-deuteron scattering and of breakup get changed in predictions based on modern potentials and their extensions. Two typical examples are shown in Fig. 5.5, where predictions of CD Bonn [3], AV18 [5] and the Nijmegen potentials [4] are compared to that of the Paris potential. The results of the modern potentials are very close to each other, but differ markedly in detail from those of the Paris potential. The modern potentials incorporate the charge dependence of the two-nucleon interaction and are fitted to the new and precise data, unavailable when the Paris potential was created. Since the difference in fits is responsible for the difference in predictions, Fig. 5.5 only shows results with purely nucleonic potentials. The difference in the sample prediction for nucleon-deuteron breakup at 13 MeV nucleon lab energy reflects the charge dependence of the modern potentials which is not taken into account in the Paris potential. The difference in the sample prediction for elastic nucleon-deuteron scattering at 135 MeV nucleon lab energy reflects the improved fit of the modern potentials to more recent data for spin observables of

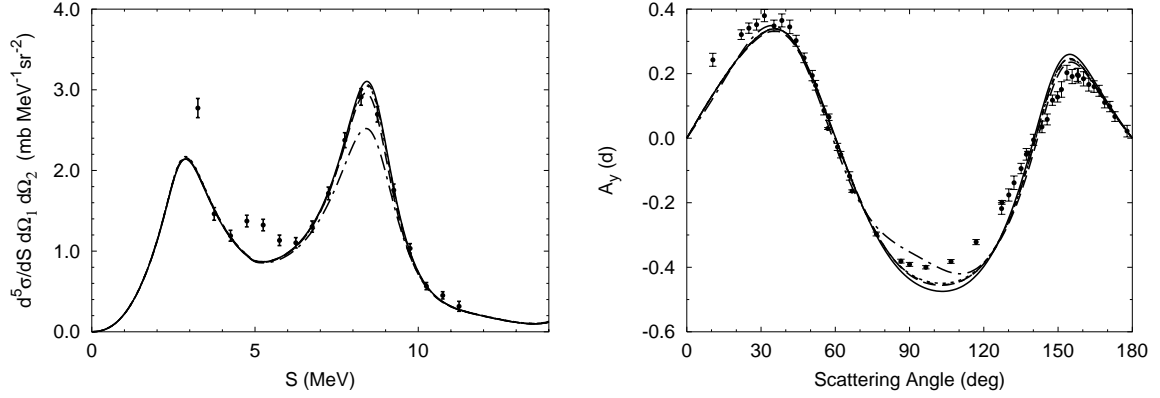


Figure 5.5: Comparison of observables derived from various purely nucleonic potentials, i.e., CD-Bonn (solid), AV18 (long-dashed), Nijmegen I (short-dashed), Nijmegen II (dotted) and Paris (dashed-dotted). Differential cross section of  $Nd$  breakup at 13 MeV nucleon lab energy as function of the arclength  $S$  along the kinematical curve in collinear configuration ( $39.0^\circ, 75.5^\circ, 180.0^\circ$ ) and deuteron analyzing power  $A_y(d)$  of elastic  $Nd$  scattering at 135 MeV nucleon lab energy as function of the c.m. scattering angle are shown. The results of the modern potentials cluster around each other and are hardly distinguishable from each other in the plots. The experimental data are from Refs. [11, 48].

two-nucleon scattering. Thus, the use of well-fitted potentials is important. This conclusion is also confirmed by the comparison of the predictions based on the well-fitted coupled-channel potential CD Bonn +  $\Delta$  and on the two constructions without fit, i.e., CD Bonn +  $\Delta$  (sub1) and CD Bonn +  $\Delta$  (sub2). At low energies, i.e., up to about 30 MeV nucleon lab energy,  $\Delta$ -isobar effects remain small; they are at least qualitatively the same for all coupled-channel potentials discussed in the past and in this thesis. However, at higher energies  $\Delta$ -isobar effects become more visible and there the realistic nature of the employed coupled-channel potential becomes important. Figure 5.6 gives examples. There, the coupled-channel potentials constructed according to the old subtraction scheme can overestimate the  $\Delta$ -isobar effects sizably.

### 5.3 Results

This section presents results for spin-averaged and spin-dependent observables of elastic nucleon-deuteron scattering and breakup using the developed coupled-channel potential. The definitions of spin-dependent observables are given in Appendix D. The calculations omit the Coulomb potential between charged baryons. However, the theoretical description is charge dependent. For  $pd$  processes the  $pp$  and  $np$  parts of the interaction are used, for  $nd$  processes the  $nn$  and  $np$  parts; except for very low energies, where the omission of Coulomb is fatal anyhow, and except for some breakup observables, both calculations yield results, indistinguishable in plots. The charge dependence of the nucleon-nucleon interaction is treated exactly in the  $^1S_0$  partial wave, yielding total isospin  $T = \frac{3}{2}$  channels; in the other two-baryon isospin-triplet partial waves up to  $I = 4$  the charge dependence is treated approximately as described in Sec. 3.4, i.e., without coupling to  $T = \frac{3}{2}$  states; in those higher partial waves the coupling to  $T = \frac{3}{2}$  states was checked to be quantitatively irrelevant. Partial waves up to total two-baryon angular momentum  $I = 5$  in purely nucleonic channels, up to  $I = 4$  in nucleon- $\Delta$

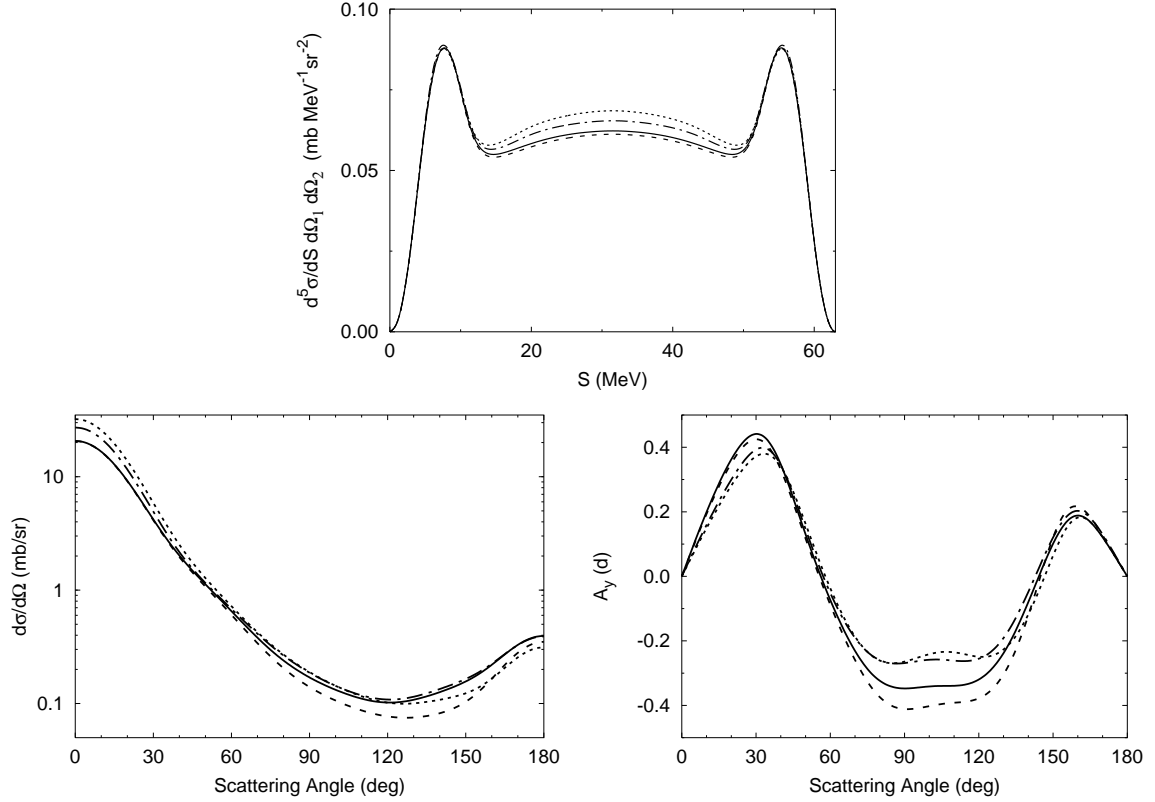


Figure 5.6: Differential cross section of  $Nd$  breakup at 65 MeV nucleon lab energy as function of the arclength  $S$  along the kinematical curve in the space star configuration ( $54.0^\circ, 54.0^\circ, 120.0^\circ$ ) and differential cross section and deuteron analyzing power  $A_y(d)$  of elastic  $Nd$  scattering at 190 MeV nucleon lab energy as function of the c.m. scattering angle. Compared are predictions of different coupled-channel potentials, i.e., CD Bonn +  $\Delta$  (solid curves), CD Bonn +  $\Delta$  (sub1) (dashed-dotted curves), and CD Bonn +  $\Delta$  (sub2) (dotted curves). Results for the nucleonic CD Bonn potential without  $\Delta$ -isobar excitation (dashed curves) are given as reference for an indication of the complete  $\Delta$ -isobar effects.

channels and up to total three-baryon angular momentum  $J = \frac{31}{2}$  are taken into account. The results appear fully converged with respect to higher two-baryon angular momenta  $I$ , with respect to higher three-baryon angular momenta  $J$ , and with respect to  $\Delta$ -isobar coupling on the scale of accuracy which present-day experimental data require with only one exception: Some breakup observables at 135 and 200 MeV nucleon lab energy still show, in some kinematical regimes, a residual dependence on the cut off in  $I$  and  $J$ ; the results presented in figures for breakup observables at those higher energies are therefore based on the extended cut offs  $I = 6$  and  $J = \frac{51}{2}$ . Though the technical apparatus enables me to calculate all observables in the considered energy regime, I concentrate on few most interesting cases only; furthermore, I focus on the  $\Delta$ -isobar effects in observables.

### 5.3.1 Elastic Nucleon-Deuteron Scattering

The theoretical description of elastic nucleon-deuteron scattering up to about 100 MeV nucleon lab energy in terms of realistic two-nucleon potentials has been generally quite successful [7] with few exceptions.

At very low energies some scattering observables and bound-state properties are correlated; thus, an appropriate three-nucleon force has to be added to account for trinucleon binding and for those scattering observables in full. Since the  $\Delta$ -isobar effects on the three-nucleon bound state are already described in Chapter 4, I do not discuss anymore those *scaling* effects, which the  $\Delta$  isobar yields due to the resulting additional binding.

The description of proton-deuteron scattering at very low energies for most angles and at higher energies predominantly in forward direction requires the inclusion of the Coulomb interaction between the protons; this has not yet been done in the momentum-space calculations based on realistic potentials [7, 17–19], and it is not done in this thesis.

There are long-standing discrepancies in the nucleon and deuteron vector analyzing powers  $A_y(N)$  and  $A_y(d)$  around 10 MeV nucleon lab energy, the so-called  *$A_y$ -puzzle*. All calculations based on realistic two-nucleon potentials and complemented by a three-nucleon force, either by an irreducible one or by an effective one as due to  $\Delta$ -isobar excitation, are unable to account for the experimental height of the peak. Reference [49] discusses a three-nucleon force as possible remedy which has a phenomenological spin-orbit component with rather long range. I therefore test an effective three-nucleon force which obtains a microscopically motivated spin-orbit component arising from the spin-orbit part of the  $\rho$ -meson exchange mediating single  $\Delta$ -isobar excitation; that spin-orbit component is of rather short range, its strength and range being predetermined by the  $\rho$  parameters used in the other parts of transition potential from two-nucleon to nucleon- $\Delta$  states. The predictions for the neutron analyzing power  $A_y(n)$  of elastic neutron-deuteron scattering at 10 MeV nucleon lab energy are given in Fig. 5.7. The obtained results are disappointing: The inclusion of the spin-orbit mechanism of  $\rho$  exchange does not significantly decrease the long-standing discrepancy. Although the three-nucleon force effect is quite significant, it is canceled by the dispersive effect, leaving the full  $\Delta$ -isobar effect small. A similar small effect is found for the deuteron vector analyzing power  $A_y(d)$ . The spin-orbit contribution to  $\Delta$ -isobar effects is negligible for other observables.

In general, the  $\Delta$ -isobar effects in elastic nucleon-deuteron scattering at nucleon lab energies up to about 100 MeV remain small and rather unimportant, and the overall agreement with the experimental data is pretty good — with the few exceptions mentioned above.

I therefore concentrate on observables above 100 MeV nucleon lab energy; this is an energy regime in which a number observables shows discrepancies between the experimental data and the theoretical predictions based on two-nucleon potentials only and in which noticeable  $\Delta$ -isobar effects are expected, in contrast to lower energies. Figures 5.8 and 5.9 study the evolution of the  $\Delta$ -isobar effects on the spin-averaged differential cross section and on the nucleon analyzing power at 108, 120, 135, 150, 170 and 190 MeV nucleon lab energy. There is a clear disagreement in the diffraction minima of the spin-averaged differential cross section between experiment and theory based on the purely nucleonic CD-Bonn potential, the *Sagara discrepancy*; the inclusion of the  $\Delta$  isobar reduces that discrepancy significantly, though it is unable to remove it in full. The discrepancy between the different sets [10, 11] of experimental data is not understood yet. A corresponding beneficial  $\Delta$ -isobar effects are also seen for the nucleon analyzing power.

Figure 5.10 shows deuteron vector and tensor analyzing powers at 100 and 135 MeV nucleon lab energy, corresponding to 200 and 270 MeV deuteron lab energy in the real experiments with a deuteron beam [11]. The  $\Delta$ -isobar effects are not always beneficial, e.g., for the deuteron tensor

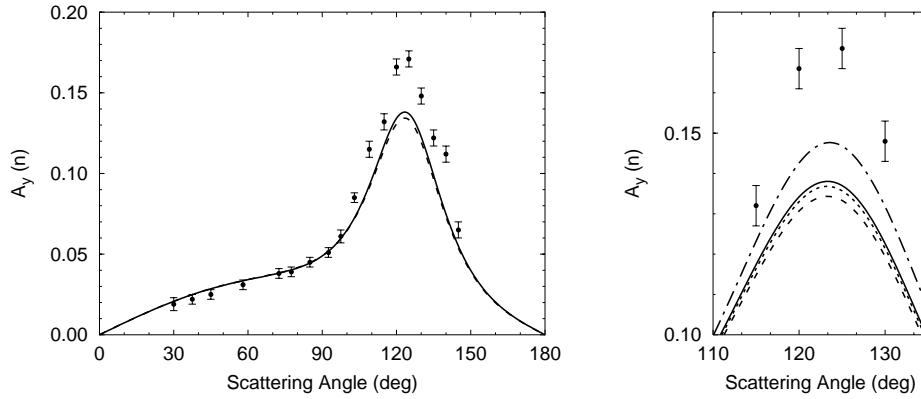


Figure 5.7: Neutron analyzing power  $A_y(n)$  of elastic  $nd$  scattering at 10 MeV neutron lab energy as function of the c.m. scattering angle. Results of the coupled-channel potential with  $\Delta$ -isobar excitation CD Bonn +  $\Delta$  (sub2) including the spin-orbit interaction (solid curve) are compared with reference results of the purely nucleonic CD-Bonn potential (dashed curve). On the right side the peak is shown in finer resolution; there also the results for  $\Delta$ -isobar excitation without spin-orbit interaction (dotted) are shown. The partial three-nucleon force effect arising from the  $\Delta$ -isobar excitation is also given for comparison (dashed-dotted). The experimental data are from Ref. [47].

analyzing power  $A_{yy}$  at intermediate scattering angles.

Recently, a complete set of proton spin observables in  $\vec{p}d$  elastic scattering at 250 MeV nucleon lab energy has been measured [13]. Though the energy is already slightly above the pion-production threshold, I apply the theory without pion production nevertheless, since the inelasticity remains small. In Fig. 5.11 I show theoretical predictions for the differential cross section and for the nucleon to nucleon polarization transfer coefficients. As in Fig. 5.8, the inclusion of the  $\Delta$  isobar significantly reduces the Sagara discrepancy in the differential cross section. The polarization transfer coefficient  $K_y^{y'}(NN)$  also shows rather large  $\Delta$ -isobar effects, whereas other coefficients are affected only by little. Nevertheless, even at this comparatively high energy the inclusion of the  $\Delta$  isobar improves the general agreement between theory and experiment rather significantly.

Figure 5.12 compares theoretical predictions with the preliminary experimental data [12] for deuteron to nucleon polarization transfer coefficients. The  $\Delta$ -isobar effects are rather insignificant.

With respect to spin correlation coefficients, experimental data exist only for  $C_{yy}$  at 197 MeV nucleon lab energy [51]; simultaneously also the deuteron vector analyzing power  $A_y(d)$  has been measured. Figure 5.13 compares that data with theoretical predictions. The  $\Delta$ -isobar effects are especially important for  $A_y(d)$ .

Instead of letting the  $\Delta$  isobar yield an effective three-nucleon force beside other  $\Delta$ -isobar effects as I do, Refs. [9, 11, 13, 52] add an irreducible three-nucleon force to the purely nucleonic two-nucleon interaction. The two-pion exchange Tucson-Melbourne potential TM' with revised parameters [53] repairing a substantial violation of chiral symmetry, and the Urbana IX force [54] are the favorable choices; their parameters are fitted to the trinucleon binding energy. When comparing the results of this thesis with the predictions of Refs. [9, 11, 13, 52] for the observables of Figs. 5.8 - 5.13, I observe an encouraging qualitative agreement for most of them. The agreement is almost quantitative for the differential cross sections of Fig. 5.8. The most remarkable qualitative disagreement is found for the deuteron analyzing power  $A_{xx}$  of Fig. 5.10; there the full  $\Delta$ -isobar effect and the effect of TM' or Urbana IX go into opposite directions; I observe that the  $\Delta$ -isobar effect is beneficial.

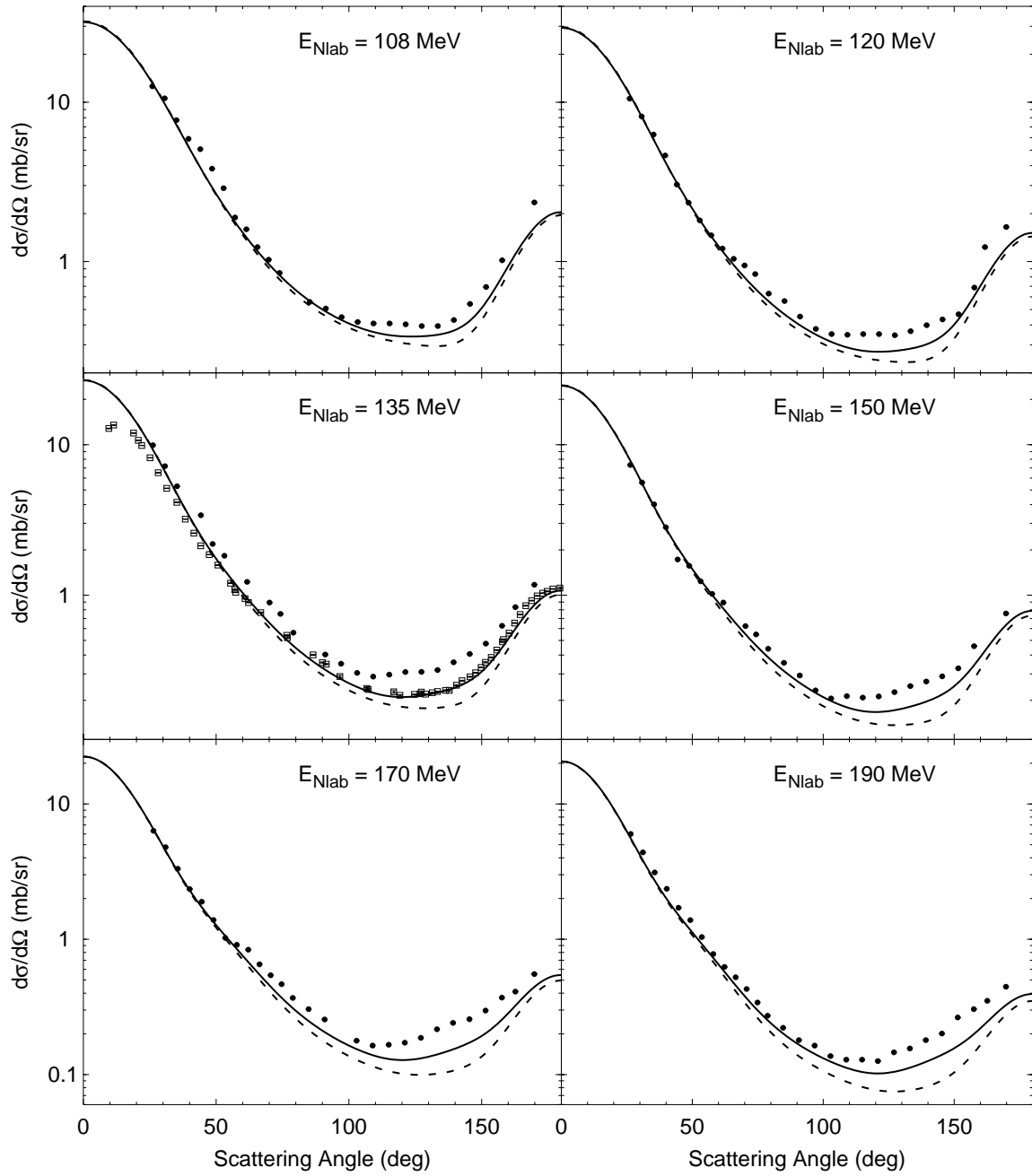


Figure 5.8: Differential cross section of elastic  $Nd$  scattering at 108, 120, 135, 150, 170 and 190 MeV nucleon lab energy as function of the c.m. scattering angle. Results of the coupled-channel potential with  $\Delta$ -isobar excitation (solid curves) are compared with reference results of the purely nucleonic CD-Bonn potential (dashed curves). The experimental data are from Ref. [10] (●) and from Ref. [11] (□) and refer to  $pd$  scattering.



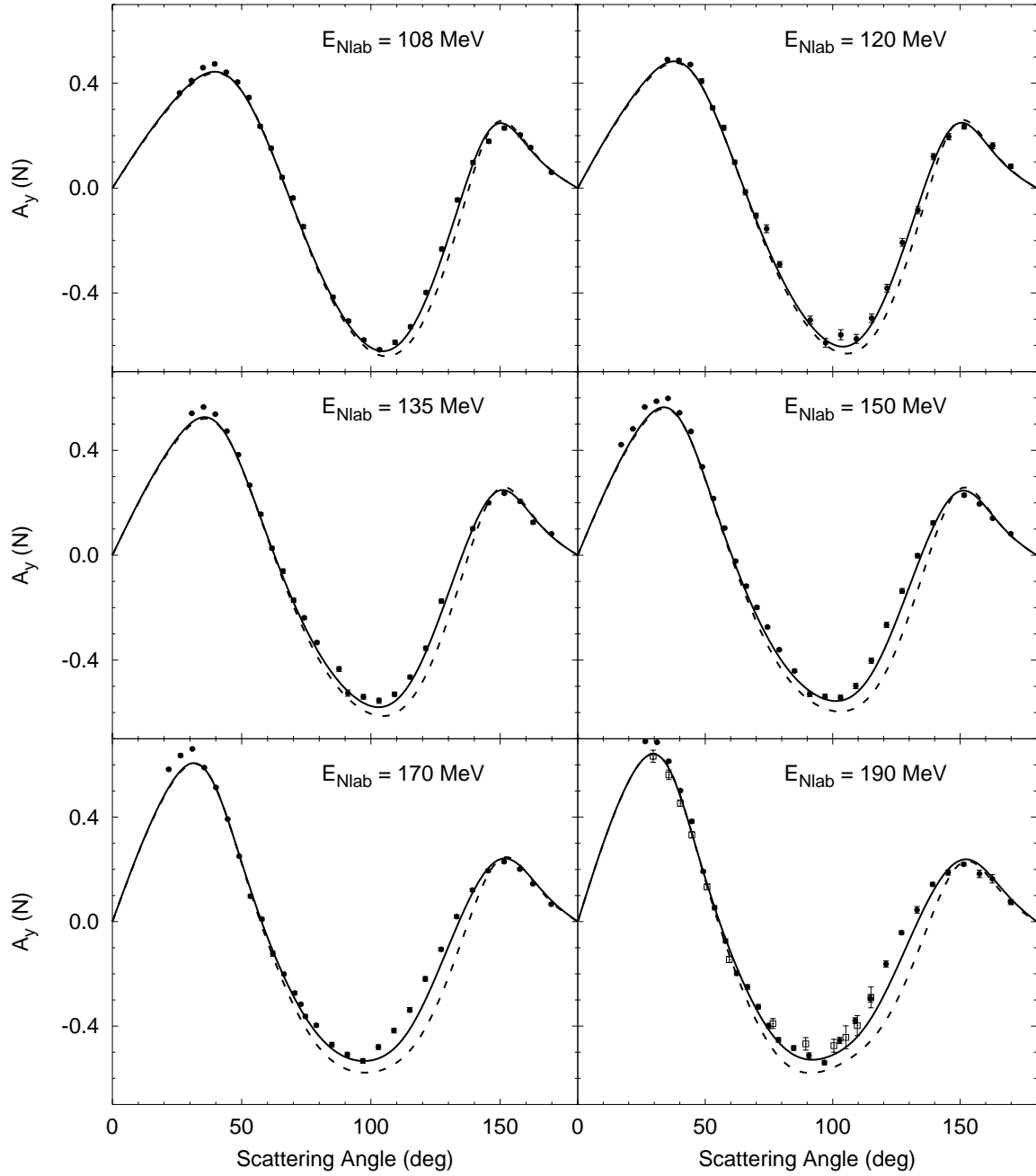


Figure 5.9: Nucleon analyzing power  $A_y(N)$  of elastic  $Nd$  scattering at 108, 120, 135, 150, 170 and 190 MeV nucleon lab energy as function of the c.m. scattering angle. Results of the coupled-channel potential with  $\Delta$ -isobar excitation (solid curves) are compared with reference results of the purely nucleonic CD-Bonn potential (dashed curves). The experimental data are from Ref. [9] ( $\bullet$ ) and from Ref. [50] ( $\square$ ) and refer to  $pd$  scattering.

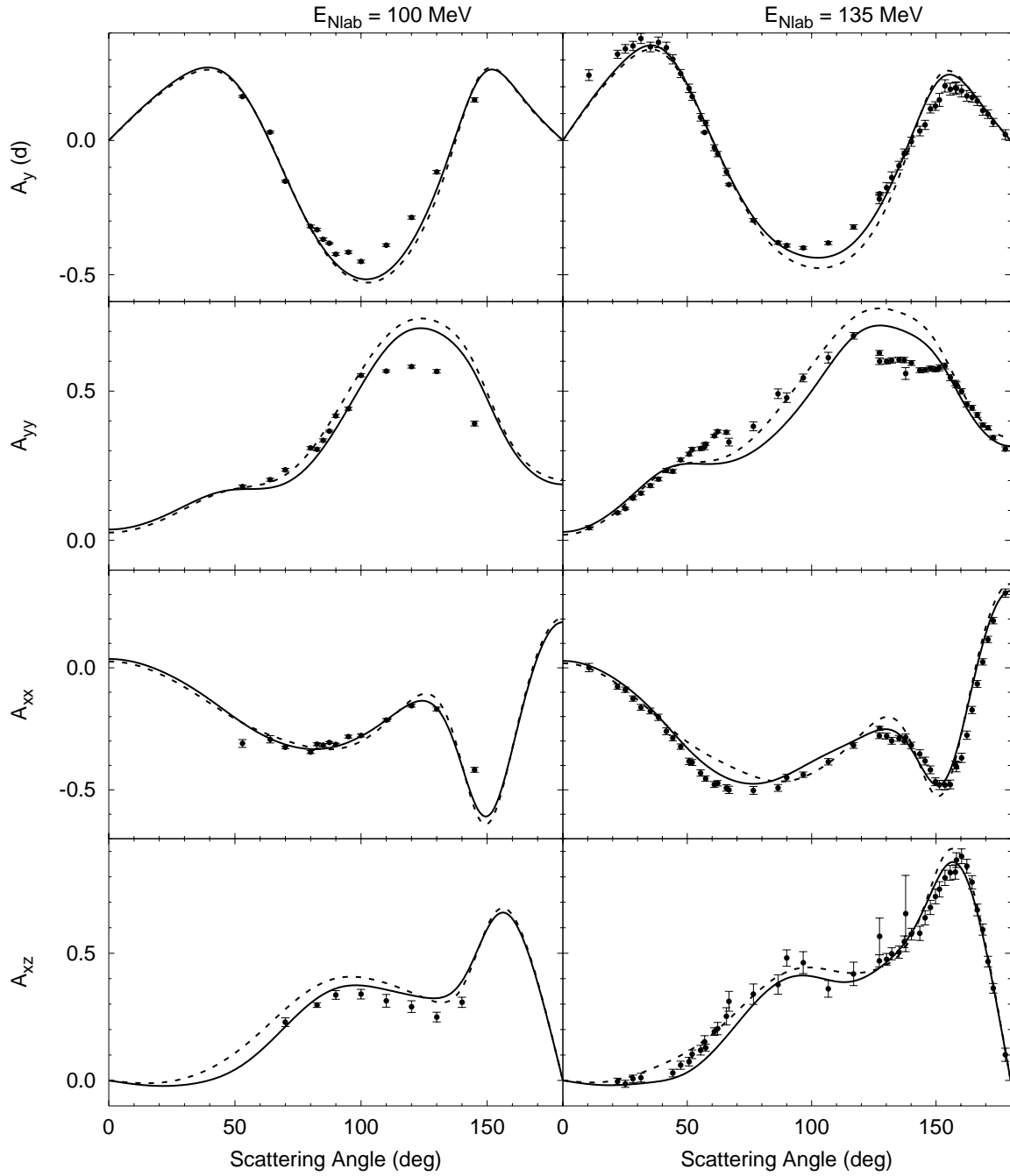


Figure 5.10: Deuteron analyzing powers  $A_y(d)$ ,  $A_{yy}$ ,  $A_{xx}$  and  $A_{xz}$  of elastic  $Nd$  scattering at 100 MeV (left side) and 135 MeV (right side) nucleon lab energy as functions of the c.m. scattering angle. Results of the coupled-channel potential with  $\Delta$ -isobar excitation (solid curves) are compared with reference results of the purely nucleonic CD-Bonn potential (dashed curves). The experimental data are from Ref. [11] and refer to  $pd$  scattering.

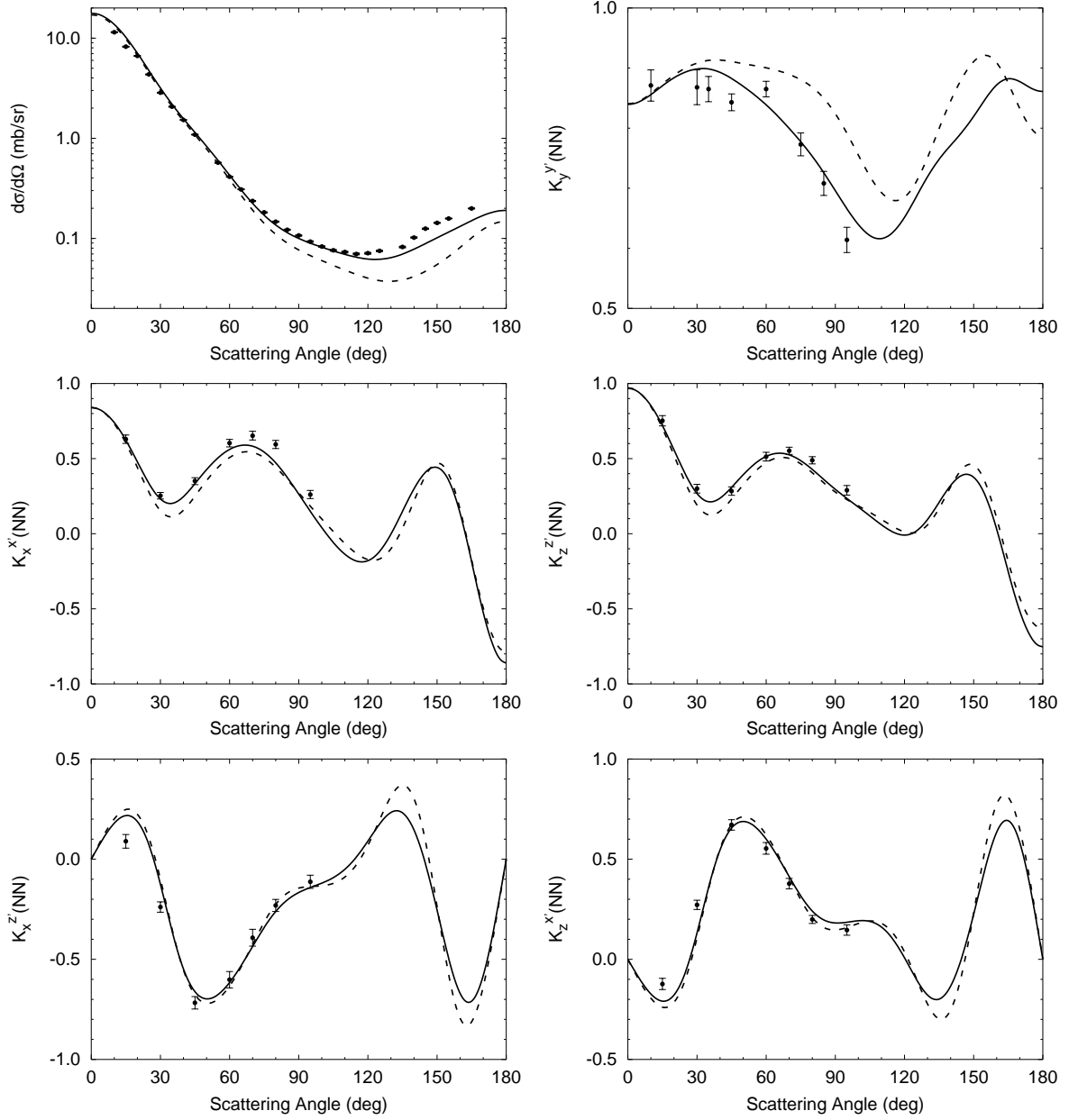


Figure 5.11: Differential cross section and all nucleon to nucleon polarization transfer coefficients of elastic  $Nd$  scattering at 250 MeV nucleon lab energy as functions of the c.m. scattering angle. Results of the coupled-channel potential with  $\Delta$ -isobar excitation (solid curves) are compared with reference results of the purely nucleonic CD-Bonn potential (dashed curves). The experimental data are from Ref. [13] and refer to  $pd$  scattering.

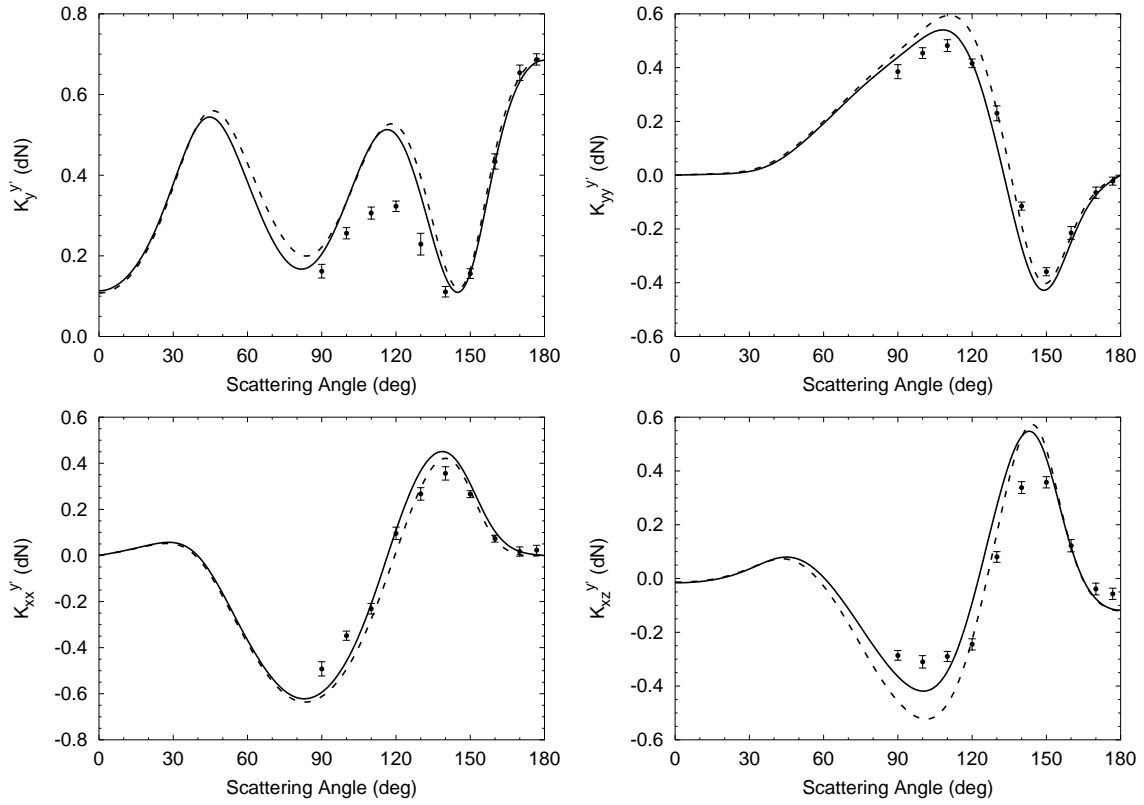


Figure 5.12: Deuteron to nucleon polarization transfer coefficients  $K_y^y(dN)$ ,  $K_{yy}^y(dN)$ ,  $K_{xx}^y(dN)$  and  $K_{xz}^y(dN)$  of elastic  $Nd$  scattering at 135 MeV nucleon lab energy as functions of the c.m. scattering angle. Results of the coupled-channel potential with  $\Delta$ -isobar excitation (solid curves) are compared with reference results of the purely nucleonic CD-Bonn potential (dashed curves). The preliminary experimental data are from Ref. [12] and refer to  $pd$  scattering.

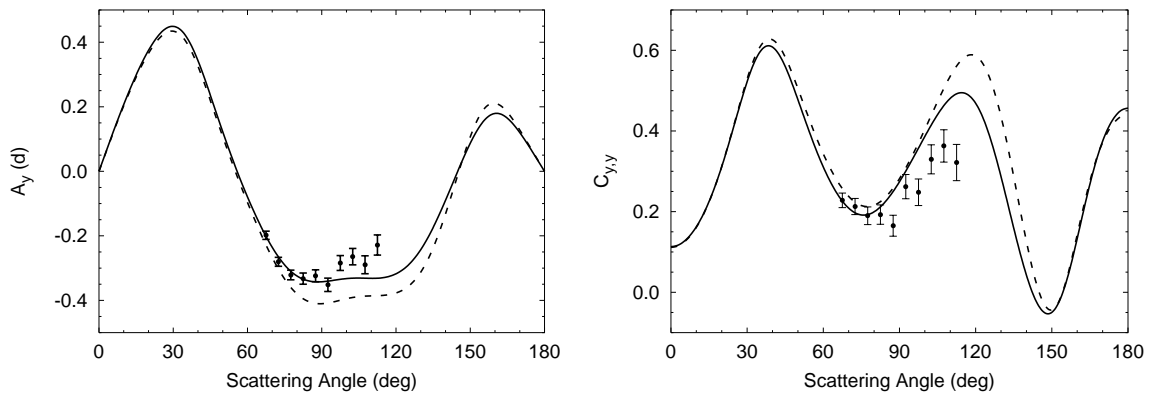


Figure 5.13: Deuteron analyzing power  $A_y(d)$  and nucleon-deuteron spin correlation coefficient  $C_{y,y}$  of elastic  $Nd$  scattering at 197 MeV nucleon lab energy as function of the c.m. scattering angle. Results of the coupled-channel potential with  $\Delta$ -isobar excitation (solid curves) are compared with reference results of the purely nucleonic CD-Bonn potential (dashed curves). The experimental data are from Ref. [51] and refer to  $pd$  scattering.

### 5.3.2 Nucleon-Deuteron Breakup

Experimental data for breakup in nucleon-deuteron scattering are scarcer than for elastic scattering. All theoretical predictions and all experimental data refer to the situations in which the two detected nucleons 1 and 2 have the same isospin projection, i.e., both detected nucleons 1 and 2 are protons in the proton-deuteron breakup and neutrons in the neutron-deuteron breakup.

Results for spin-averaged and spin-dependent observables at 13 MeV nucleon lab energy are given in Fig. 5.14. The disagreement between the theoretical predictions and the experimental data is most striking for the differential cross section in the space star configuration of Fig. 5.14; the experimental data for proton-deuteron and neutron-deuteron breakup are surprisingly far apart; neither data set is accounted for by theory as has already been observed in previous calculations [7, 19]. The calculations of Ref. [19] failed also in accounting for the differential cross section in the vicinity of final state interaction (FSI) points; the correct treatment of charge dependence in the calculations of this thesis resolves that problem. Examples are the collinear configurations of Figs. 5.5 and 5.14, where the peaks around  $S = 8$  MeV and  $S = 10$  MeV are not far from the FSI points, and the FSI configuration of Fig. 8.2 where the effect of the charge dependence is discussed in more detail in the context of perturbation theory. In the studied low-energy observables the effects of the  $\Delta$  isobar are irrelevant.

Results for deuteron analyzing powers of deuteron-proton scattering at 52 MeV deuteron lab energy are given in Fig. 5.15. The experimental data are still preliminary; they are given as function of  $S/S_{\max}$ ,  $S_{\max}$  being the full arclength of the kinematical curve; I follow that procedure also for the theoretical predictions. The  $\Delta$ -isobar effects on the considered observables remain very small.

Results for spin-averaged and spin-dependent observables at 65 MeV nucleon lab energy are given in Figs. 5.16 and 5.17. All experimental data refer to proton-deuteron scattering. The agreement between theoretical predictions and experimental data is satisfactory.  $\Delta$ -isobar effects are small; they appear to be most pronounced in space star and collinearity configurations, as already pointed out in Ref. [19]. In contrast to Ref. [19], there are almost no  $\Delta$ -isobar effects in coplanar star and quasi-free scattering (QFS) configurations; this is typical also for higher energies; I do not document the results on that finding.

Though sizable effects, arising from the three-nucleon force and therefore giving information on it, are hoped to be seen in nucleon-deuteron breakup [61], I am not able to confirm that expectation using the coupled-channel potential as a theoretical tool. I do not repeat the impressive search for three-nucleon force effects carried out in Ref. [61], where dramatic effects were seen in particular kinematics regions. However, they were based on a Tucson-Melbourne potential violating chiral symmetry; results obtained for CD Bonn together with the modified TM' three-nucleon force and for AV18 together with the Urbana IX three-nucleon force show much milder effects. The  $\Delta$ -isobar effects of this thesis are pretty consistent with the latter ones. Examples of observables, likely to show three-nucleon force effects according to Ref. [61] and showing rather modest  $\Delta$ -isobar effects, are given in Fig. 5.18.

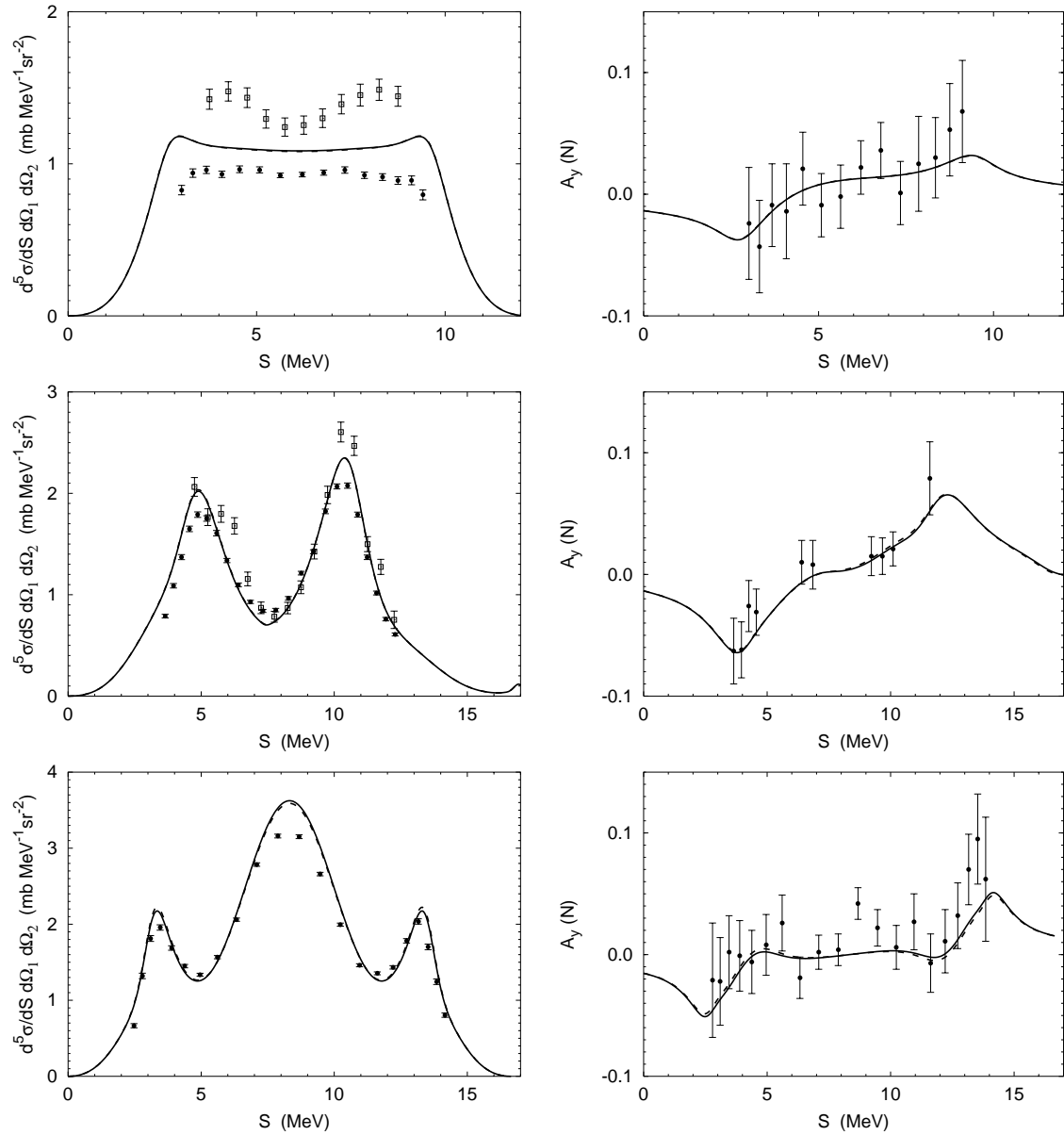


Figure 5.14: Differential cross section and nucleon analyzing power  $A_y(N)$  of  $Nd$  breakup at 13 MeV nucleon lab energy as function of the arclength  $S$  along the kinematical curve for various configurations: space star configuration ( $50.5^\circ, 50.5^\circ, 120.0^\circ$ ) on the top, collinearity configuration ( $50.5^\circ, 62.5^\circ, 180.0^\circ$ ) in the middle, and QFS configuration ( $39.0^\circ, 39.0^\circ, 180.0^\circ$ ) on the bottom. Results of the coupled-channel potential with  $\Delta$ -isobar excitation (solid curves) are compared with reference results of the purely nucleonic CD Bonn potential (dashed curves). The experimental data are from Ref. [48] ( $\square$ ) referring to  $nd$  scattering and from Ref. [55] referring to  $pd$  scattering ( $\bullet$ ).

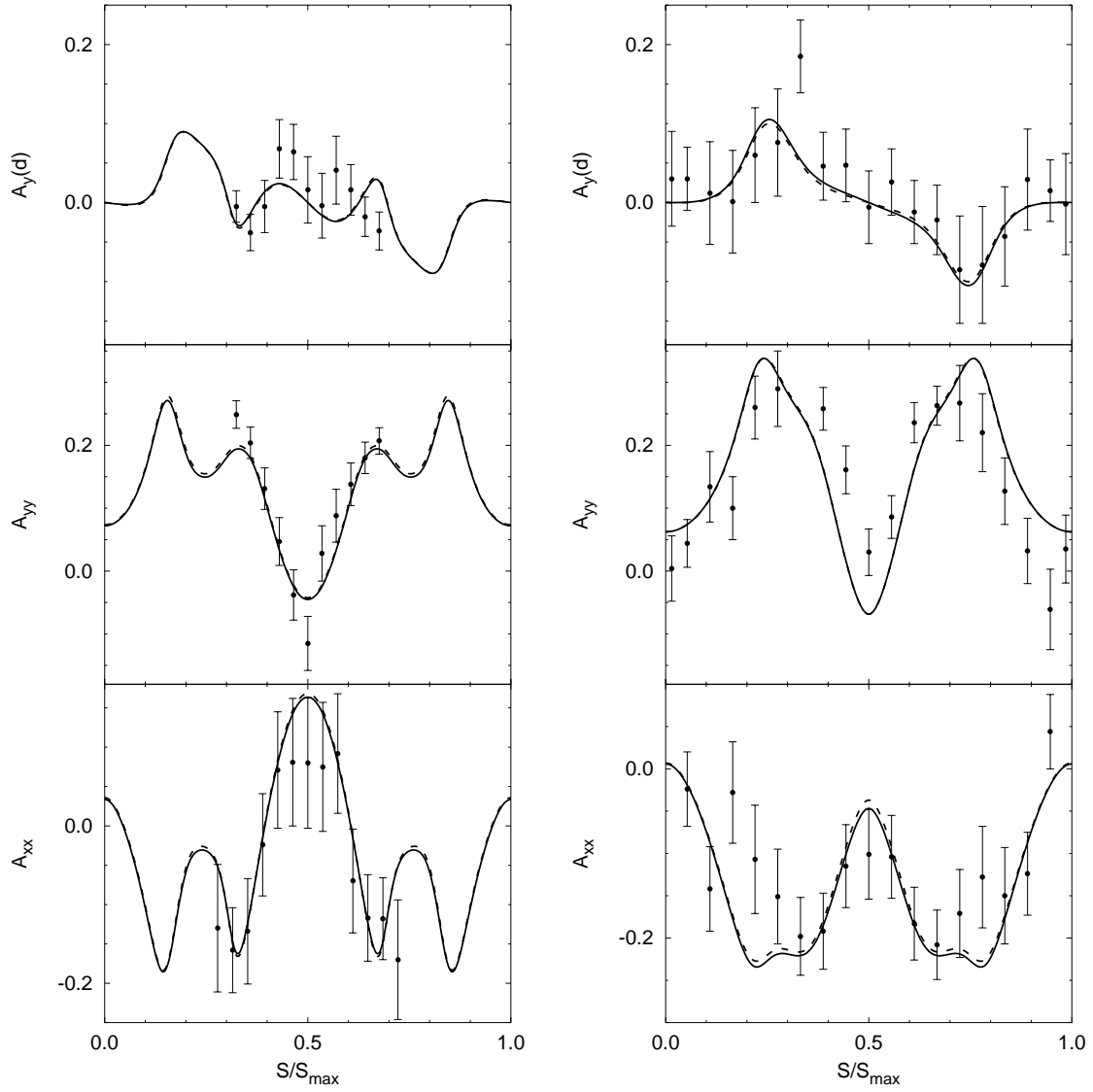


Figure 5.15: Deuteron analyzing powers  $A_y(d)$ ,  $A_{yy}$  and  $A_{xx}$  of  $Nd$  breakup at 52 MeV deuteron lab energy as function of the fractional arclength  $S/S_{\max}$  along the kinematical curve for the configuration  $(32.5^\circ, 32.5^\circ, 180.0^\circ)$  on the left and for the configuration  $(38.7^\circ, 38.7^\circ, 180.0^\circ)$  on the right. Results of the coupled-channel potential with  $\Delta$ -isobar excitation (solid curves) are compared with reference results of the purely nucleonic CD Bonn potential (dashed curves). The preliminary experimental data are from Ref. [56] and refer to  $pd$  scattering.

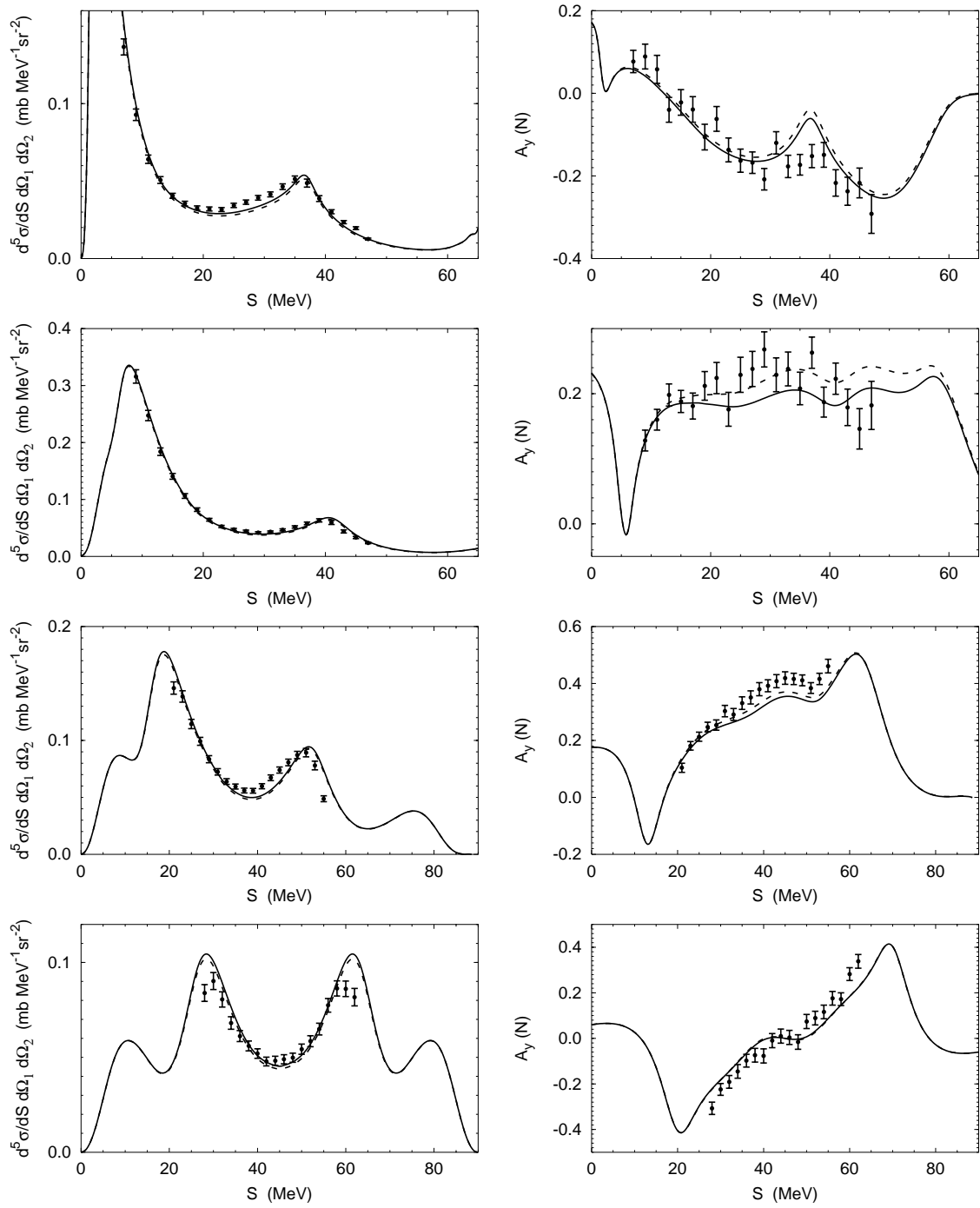


Figure 5.16: Differential cross section and nucleon analyzing power  $A_y(N)$  of  $Nd$  breakup at 65 MeV nucleon lab energy as function of the arclength  $S$  along the kinematical curve for collinear configurations (from top to bottom)  $(20.0^\circ, 116.2^\circ, 180.0^\circ)$ ,  $(30.0^\circ, 98.0^\circ, 180.0^\circ)$ ,  $(45.0^\circ, 75.6^\circ, 180.0^\circ)$ , and  $(59.5^\circ, 59.5^\circ, 180.0^\circ)$ . Results of the coupled-channel potential with  $\Delta$ -isobar excitation (solid curves) are compared with reference results of the purely nucleonic CD-Bonn potential (dashed curves). The experimental data are from Ref. [57] and refer to  $pd$  scattering.



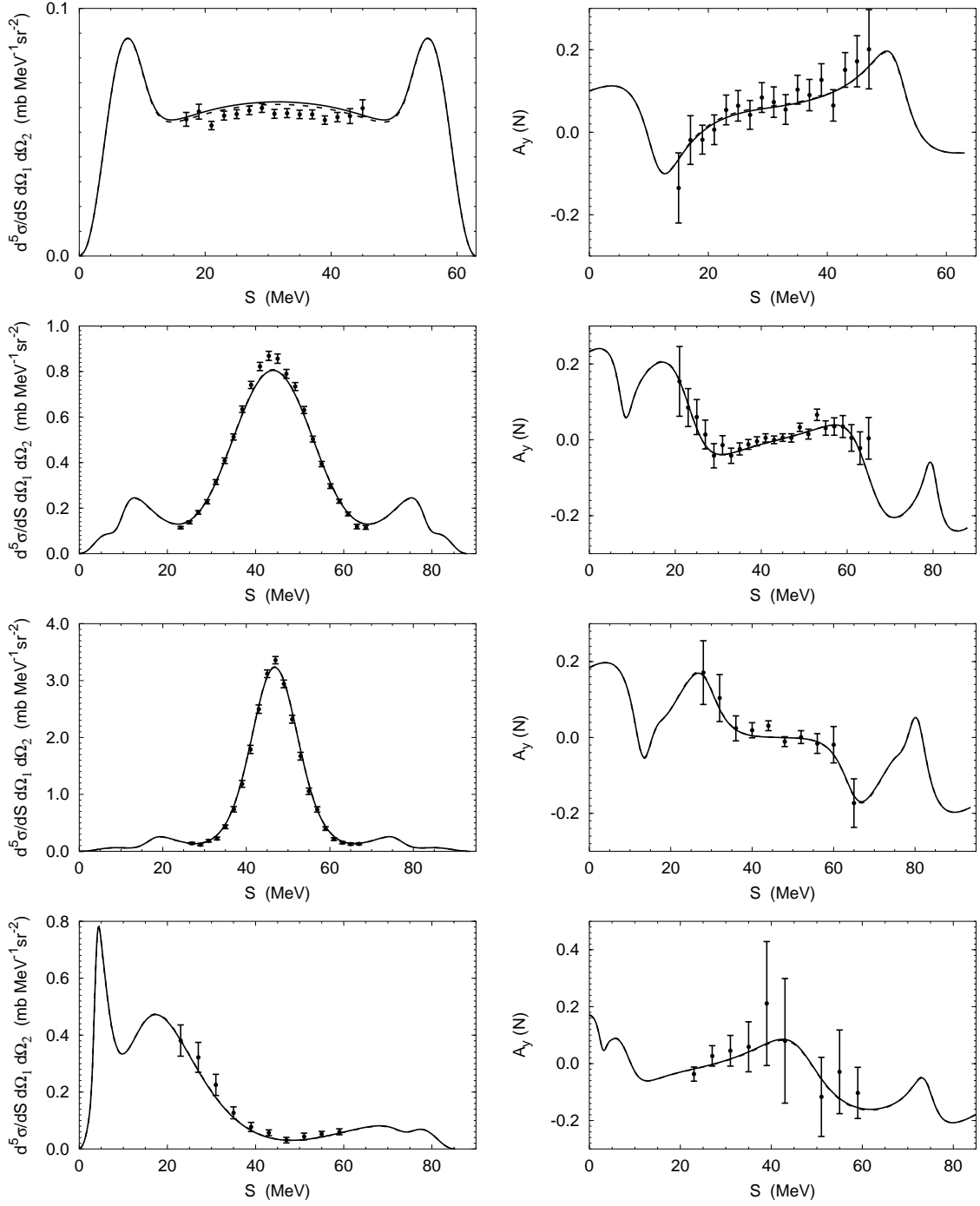


Figure 5.17: Differential cross section and nucleon analyzing power  $A_y(N)$  of  $Nd$  breakup at 65 MeV nucleon lab energy as function of the arclength  $S$  along the kinematical curve for various configurations (from top to bottom): Space star configuration ( $54.0^\circ, 54.0^\circ, 120.0^\circ$ ), coplanar star configuration ( $35.2^\circ, 35.2^\circ, 180.0^\circ$ ), QFS configuration ( $44.0^\circ, 44.0^\circ, 180.0^\circ$ ), and nonspecific configuration ( $20.0^\circ, 45.0^\circ, 180.0^\circ$ ). Results of the coupled-channel potential with  $\Delta$ -isobar excitation (solid curves) are compared with reference results of the purely nucleonic CD-Bonn potential (dashed curves). The experimental data are from Refs. [58–60] and refer to  $pd$  scattering.

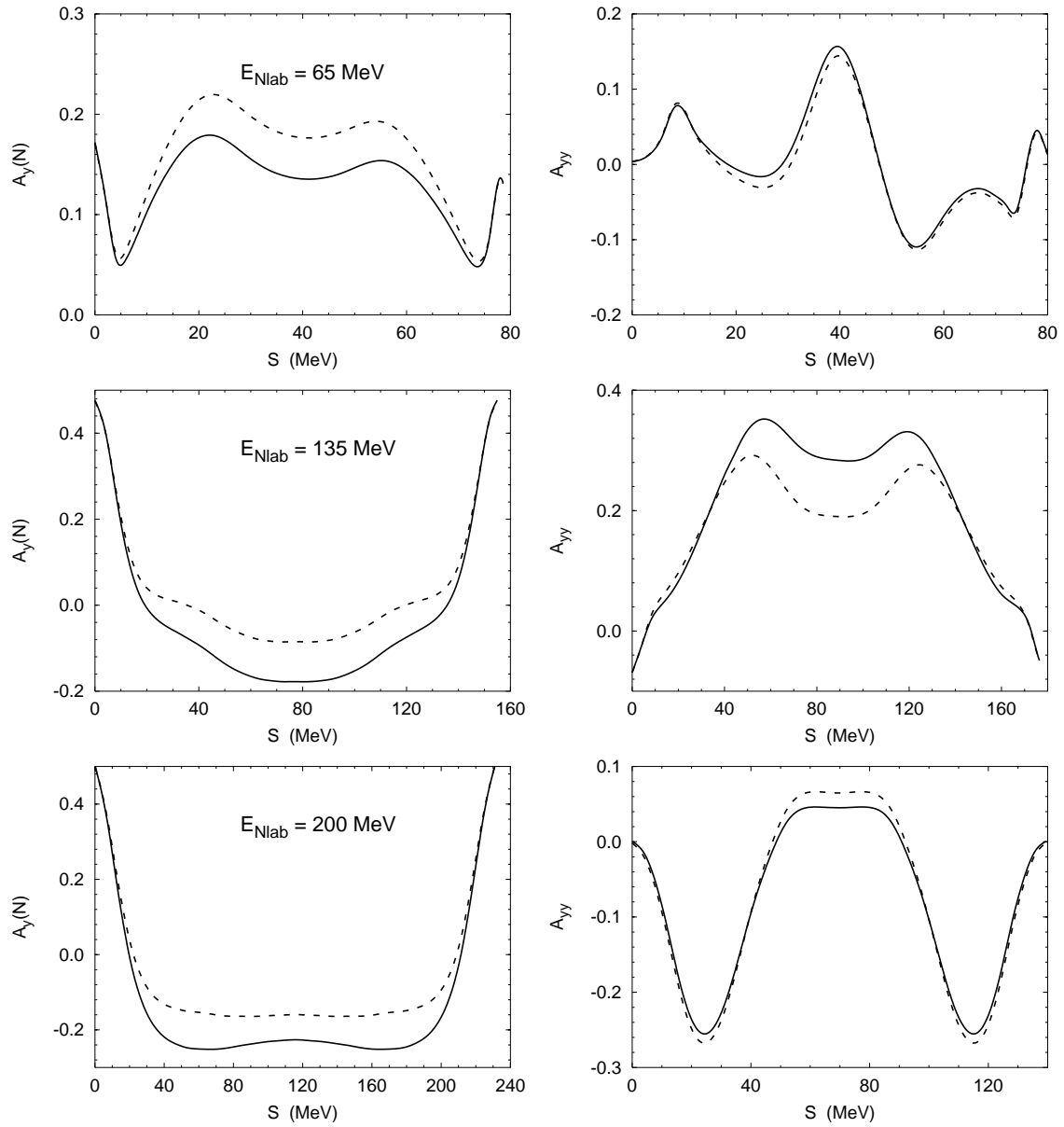


Figure 5.18: Left side: Nucleon analyzing power  $A_y(N)$  of  $Nd$  breakup as function of the arclength  $S$  along the kinematical curve for three different nucleon lab energies: 65 MeV, configuration  $(20^\circ, 20^\circ, 40^\circ)$  on the top, 135 MeV, configuration  $(25^\circ, 25^\circ, 0^\circ)$  in the middle, and 200 MeV, configuration  $(25^\circ, 25^\circ, 0^\circ)$  on the bottom. Right side: Deuteron analyzing power  $A_{yy}$  of  $Nd$  breakup as function of the arclength  $S$  along the kinematical curve for three different nucleon lab energies: 65 MeV, configuration  $(40^\circ, 30^\circ, 140^\circ)$  on the top, 135 MeV, configuration  $(15^\circ, 15^\circ, 20^\circ)$  in the middle, and 200 MeV, configuration  $(45^\circ, 45^\circ, 0^\circ)$  on the bottom. Results of the coupled-channel potential with  $\Delta$ -isobar excitation (solid curve) are compared with reference results of the purely nucleonic CD-Bonn potential (dashed curve).

# 6

## Three-Nucleon Photo Reactions

The considered photo reactions are schematically shown in Fig. 6.1.

### 6.1 Spin-Averaged and Spin-Dependent Cross Sections

The starting point for calculating the cross sections of three-nucleon photo reactions is the general form (5.2). The required matrix element  $\langle f|M|i\rangle$  is calculated from the quantum-mechanical model. In the perturbative spirit for the evolution of photo processes, the e.m. interaction  $H_I^{\text{e.m.}}$  (2.11) acts only once, whereas the hadronic interaction  $H_I$  has to be taken into account exactly up to all orders. Thus, the matrix elements of the e.m. interaction require fully correlated hadronic states (2.6). The quantum-mechanical  $S$  matrix for photo reactions is parametrized in the form

$$\langle f|S|i\rangle = -2\pi i \delta^{(3)}(\mathbf{P}_f - \mathbf{P}_i) \delta(E_f - E_i) \frac{(4\pi)^{1/2}}{(2\pi)^{3/2} (2k_\gamma^0)^{1/2}} \langle s_f|M_\gamma(E_i\mathbf{k}_f)|s_i\rangle. \quad (6.1)$$

It is slightly different from the general form (5.3): The kinematical factors of the photon are taken out from  $\langle s_f|M_\gamma(E_i\mathbf{k}_f)|s_i\rangle$  explicitly.  $\langle s_f|M_\gamma(E_i\mathbf{k}_f)|s_i\rangle$  is then determined by the matrix element of the e.m. nuclear current operator (2.15) between the three-nucleon bound and scattering states without any additional factors and is given explicitly in the following subsections for all considered photo reactions. I calculate that matrix element in the c.m. system using the following computational strategy. The strategy is nonunique, since, according to Table 4.1, the model calculations, due to dynamic limitations, miss the trinucleon binding energy; the necessary correction for that miss has arbitrary features.

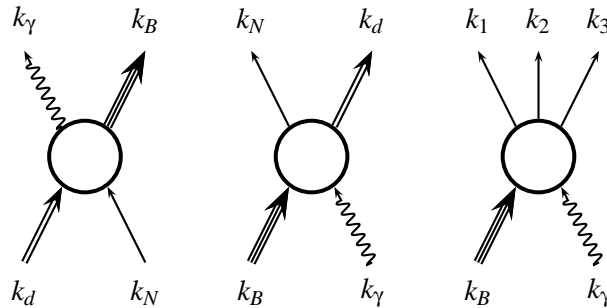


Figure 6.1: Schematic illustration of all considered three-nucleon photo reactions. The lines for the two-baryon and three-baryon particles are drawn in a special form to indicate their compositeness.

1. The experimental lab energy  $e_d + \mathbf{k}_{N\text{lab}}^2/2m_N$  for radiative capture with nucleon beam and  $|\mathbf{k}_{\gamma\text{lab}}| + E_B$  for photo disintegration determines the available internal energy, i.e., for radiative capture  $E_i = e_d + 3\mathbf{q}_i^2/4m_N$  as for nucleon-deuteron scattering, and for photo disintegration  $E_i = |\mathbf{k}_{\gamma\text{lab}}| + E_B - \mathbf{k}_{\gamma\text{lab}}^2/6m_N$ ; this step is done using the experimental trinucleon binding energy  $E_B$ . I.e., the available internal energy is the true experimental one, and the experimental two-body and three-body breakup thresholds are exactly reproduced.
2. The matrix element  $\langle s_f | M_\gamma(E_i \mathbf{k}_f) | s_i \rangle$  is calculated in the c.m. system as *on-energy-shell element* under nonrelativistic model assumptions. Under those assumptions the internal energy  $E_i = |\mathbf{k}_\gamma| + E_B + \mathbf{k}_\gamma^2/6m_N$  determines the c.m. photon momentum  $\mathbf{k}_\gamma$  to be used for the current matrix element in the c.m. system, i.e., the momentum transfer  $\mathbf{Q} = \mathbf{k}_\gamma$  and  $\mathbf{K}_+ = -\mathbf{k}_\gamma$ , since the trinucleon bound state is moving with momentum  $\mathbf{K}_B = -\mathbf{k}_\gamma$ . This step uses the computed trinucleon model binding energy  $E_B$ . Since the model binding energy  $E_B$  is not the experimental one, neither for  ${}^3\text{He}$  nor for  ${}^3\text{H}$ , and since the c.m. contribution to the total three-nucleon energy is assumed to be nonrelativistic with mass  $3m_N$ , that photon momentum  $\mathbf{k}_\gamma$  does not have the experimental value.

Performing consistently a nonrelativistic reduction in Eqs. (5.2) for hadrons as described in Sec. 5.1, I obtain the differential cross sections analytically given in the following subsections for all considered photo reactions. In contrast to the matrix element  $\langle s_f | M(E_i \mathbf{k}_f) | s_i \rangle$ , the phase-space factors are calculated using the experimental photon momentum.

### 6.1.1 Nucleon-Deuteron Radiative Capture

The initial state with spin characterization  $s_i$  is the same as in nucleon-deuteron scattering of Sec. 5.1.1 and does not need to be discussed anymore. The final state is characterized by the photon polarization  $\lambda$ , by the spin projection  $M_B$  of the three-nucleon bound state, i.e.,  $s_f = \{\lambda M_B\}$ , and by the direction of the photon momentum, since its magnitude is determined by momentum and energy conservation as described above. The resulting spin-dependent differential cross section in the c.m. system is

$$\frac{d^2\sigma_{i \rightarrow f}}{d^2\hat{\mathbf{k}}_\gamma} = |\langle s_f | M_\gamma(E_i \mathbf{k}_\gamma) | s_i \rangle|^2 \text{fps} \quad (6.2a)$$

with the amplitude

$$\langle s_f | M_\gamma(E_i \mathbf{k}_\gamma) | s_i \rangle = e_p \langle B | j^\mu(-\mathbf{k}_\gamma, -\mathbf{k}_\gamma) | \Psi_\alpha^{(+)}(\mathbf{q}_i) \nu_{\alpha_i} \rangle \varepsilon_\mu^*(k_\gamma \lambda) \quad (6.2b)$$

and the phase-space factor

$$\text{fps} = (2\pi)^2 \frac{2m_N}{3} \frac{|\mathbf{k}_\gamma|}{|\mathbf{q}_i|}. \quad (6.2c)$$

The spin-averaged differential cross section, in the figures traditionally denoted by  $d\sigma/d\Omega$ , is

$$\overline{\frac{d^2\sigma}{d^2\hat{\mathbf{k}}_\gamma}} = \frac{1}{6} \text{Tr}[M_\gamma(E_i \mathbf{k}_\gamma) M_\gamma^\dagger(E_i \mathbf{k}_\gamma)] \text{fps}. \quad (6.3)$$

Since the radiative capture is time reversed reaction of two-body photo disintegration, the matrix element (6.2b) is obtained from the one for two-body photo disintegration, defined later in Eq. (6.4b), by time reversal as described in Ref. [20]. With respect to spin observables, I consider polarization in the initial nucleon-deuteron system only; those spin observables are defined in Sec. D.1.3.

### 6.1.2 Two-Body Photo Disintegration of Trinucleon Bound State

The photon momentum  $\mathbf{k}_\gamma$  defines the  $z$ -axis, i.e.,  $\hat{\mathbf{z}} = \hat{\mathbf{k}}_\gamma$  and determines the internal three-nucleon energy as described above. The considered reaction is inverse to the nucleon-deuteron radiative capture; thus, the initial and final states of Sec. 6.1.1 are just interchanged, i.e., the spin quantum numbers are  $s_i = \{\lambda M_B\}$  and  $s_f = \{m_{s_f} M_{I_f}\}$ . The magnitude of the final nucleon-deuteron momentum  $\mathbf{q}_f$  is determined by momentum and energy conservation, i.e.,  $E_i = e_d + 3\mathbf{q}_f^2/4m_N$ . The resulting spin-dependent differential cross section in the c.m. system is

$$\frac{d^2\sigma_{i \rightarrow f}}{d^2\hat{\mathbf{q}}_f} = |\langle s_f | M_\gamma(E_i \mathbf{q}_f) | s_i \rangle|^2 \text{fps} \quad (6.4a)$$

with the amplitude

$$\langle s_f | M_\gamma(E_i \mathbf{q}_f) | s_i \rangle = e_p \langle \Psi_\alpha^{(-)}(\mathbf{q}_f) \mathbf{v}_{\alpha f} | j^\mu(\mathbf{k}_\gamma, -\mathbf{k}_\gamma) | B \rangle \varepsilon_\mu(k_\gamma \lambda) \quad (6.4b)$$

and the phase-space factor

$$\text{fps} = (2\pi)^2 \frac{2m_N}{3} \frac{|\mathbf{q}_f|}{|\mathbf{k}_\gamma|}. \quad (6.4c)$$

The spin-averaged differential cross section is

$$\overline{\frac{d^2\sigma}{d^2\hat{\mathbf{q}}_f}} = \frac{1}{4} \text{Tr}[M_\gamma(E_i \mathbf{q}_f) M_\gamma^\dagger(E_i \mathbf{q}_f)] \text{fps}. \quad (6.5)$$

### 6.1.3 Three-Body Photo Disintegration of Trinucleon Bound State

Since two-body photo disintegration is the time reversed reaction of radiative capture, it is also discussed in the c.m. system. In contrast, three-body photo disintegration is considered in the lab system, i.e., in the rest system of the initial trinucleon bound state.

The photon momentum  $\mathbf{k}_{\gamma\text{lab}}$  defines the  $z$ -axis, i.e.,  $\hat{\mathbf{z}} = \hat{\mathbf{k}}_{\gamma\text{lab}}$  and determines the internal three-nucleon energy as described above. The initial and final states are already discussed in the context of two-body photo disintegration and hadronic nucleon-deuteron breakup, i.e., the spin quantum numbers are  $s_i = \{\lambda M_B\}$  and  $s_f = \{m_{s_1} m_{s_2} m_{s_3}\}$ . The neutron and proton nature of the nucleons (123) in the final state is notationally not indicated, but always determined by experiment. The final-state Jacobi momenta  $\mathbf{p}_f$  and  $\mathbf{q}_f$  are determined from the final single-particle momenta  $\mathbf{k}_1, \mathbf{k}_2, \mathbf{k}_3$  according to Eqs. (2.1). Due to momentum conservation  $\mathbf{k}_3 = \mathbf{k}_{\gamma\text{lab}} - \mathbf{k}_1 - \mathbf{k}_2$ , thus,  $\mathbf{p}_f = \frac{1}{2}(\mathbf{k}_1 - \mathbf{k}_2)$  and  $\mathbf{q}_f = (\mathbf{k}_1 + \mathbf{k}_2) - \frac{2}{3}\mathbf{k}_{\gamma\text{lab}}$ . Furthermore, energy conservation puts an additional constraint  $E_i = \mathbf{p}_f^2/m_N + 3\mathbf{q}_f^2/4m_N$ , keeping only five independent continuous variables as in hadronic nucleon-deuteron breakup. Again, the scattering angles of two nucleons with respect to the beam direction, i.e.,  $(\theta_1, \varphi_1)$  and  $(\theta_2, \varphi_2)$ , notationally shortened to  $(\theta_1, \theta_2, \varphi_2 - \varphi_1)$ , and the arclength  $S$  along that kinematical curve (5.10) are chosen as independent variables. The resulting spin-dependent five-fold differential lab cross section takes the compact form

$$\frac{d^5\sigma_{i \rightarrow f}}{dS d^2\hat{\mathbf{k}}_1 d^2\hat{\mathbf{k}}_2} = |\langle s_f | M_\gamma(E_i \mathbf{p}_f \mathbf{q}_f) | s_i \rangle|^2 \text{fps} \quad (6.6a)$$

with the amplitude

$$\langle s_f | M_\gamma(E_i \mathbf{p}_f \mathbf{q}_f) | s_i \rangle = e_p \langle \Psi_0^{(-)}(\mathbf{p}_f \mathbf{q}_f) \mathbf{v}_{0f} | j^\mu(\mathbf{k}_\gamma, -\mathbf{k}_\gamma) | B \rangle \varepsilon_\mu(k_\gamma \lambda) \quad (6.6b)$$

and the phase-space factor

$$\text{fps} = \frac{(2\pi)^2}{k_{\gamma\text{lab}}^0} m_N^2 \mathbf{k}_1^2 \mathbf{k}_2^2 \left\{ \mathbf{k}_1^2 [2|\mathbf{k}_2| - \hat{\mathbf{k}}_2 \cdot (\mathbf{k}_{\gamma\text{lab}} - \mathbf{k}_1)]^2 + \mathbf{k}_2^2 [2|\mathbf{k}_1| - \hat{\mathbf{k}}_1 \cdot (\mathbf{k}_{\gamma\text{lab}} - \mathbf{k}_2)]^2 \right\}^{-1/2}. \quad (6.6c)$$

The spin-averaged fivefold differential cross section is

$$\frac{\overline{d^5\sigma}}{dS d^2\hat{\mathbf{k}}_1 d^2\hat{\mathbf{k}}_2} = \frac{1}{4} \text{Tr}[M_\gamma(E_i \mathbf{p}_f \mathbf{q}_f) M_\gamma^\dagger(E_i \mathbf{p}_f \mathbf{q}_f)] \text{fps}; \quad (6.7)$$

in the figures it is denoted by  $d^5\sigma/dS d\Omega_1 d\Omega_2$ , the traditional notation.

The current matrix elements determining the amplitudes (6.4b) and (6.6b) for the two- and three-body photo disintegration of the trinucleon bound state are calculated as described in Sec. 3.3.

### 6.1.4 Total Photo Disintegration Cross Section

The total photo disintegration cross section can be calculated performing the integration over all final states implicitly, i.e.,

$$\sigma = \frac{(2\pi)^2 e_p^2}{k_\gamma^0} \frac{1}{4} \sum_{M_B \lambda} \varepsilon_\nu^*(k_\gamma \lambda) \langle B | [j^\nu(\mathbf{k}_\gamma, \mathbf{K}_+)]^\dagger \delta(E_i - H_0 - H_I) j^\mu(\mathbf{k}_\gamma, \mathbf{K}_+) | B \rangle \varepsilon_\mu(k_\gamma \lambda), \quad (6.8a)$$

$$\sigma = - \frac{(2\pi)^2 e_p^2}{4\pi k_\gamma^0} \sum_{M_B \lambda} \text{Im} \left\{ \varepsilon_\nu^*(k_\gamma \lambda) \langle B | [j^\nu(\mathbf{k}_\gamma, \mathbf{K}_+)]^\dagger G(E_i + i0) j^\mu(\mathbf{k}_\gamma, \mathbf{K}_+) | B \rangle \varepsilon_\mu(k_\gamma \lambda) \right\}. \quad (6.8b)$$

The auxiliary state  $G(E_i + i0) j^\mu(\mathbf{k}_\gamma, \mathbf{K}_+) | B \rangle$  of Eq. (6.8b) is related to  $|J^\mu(E_i + i0)\rangle$  of Eqs. (3.24) according to

$$G(E_i + i0) j^\mu(\mathbf{k}_\gamma, \mathbf{K}_+) | B \rangle = \frac{1}{3} (1 + P) G_0(E_i + i0) [j^\mu(\mathbf{k}_\gamma, \mathbf{K}_+) | B \rangle + T_\alpha(E_i + i0) G_0(E_i + i0) | J^\mu(E_i + i0) \rangle]. \quad (6.8c)$$

The total cross section is then obtained in the form

$$\begin{aligned} \sigma = & - \frac{(2\pi)^2 e_p^2}{12\pi k_\gamma^0} \sum_{M_B \lambda} \text{Im} \left\{ \varepsilon_\nu^*(k_\gamma \lambda) \langle B | [j^\nu(\mathbf{k}_\gamma, \mathbf{K}_+)]^\dagger (1 + P) G_0(E_i + i0) \right. \\ & \times \left. [j^\mu(\mathbf{k}_\gamma, \mathbf{K}_+) | B \rangle + T_\alpha(E_i + i0) G_0(E_i + i0) | J^\mu(E_i + i0) \rangle] \varepsilon_\mu(k_\gamma \lambda) \right\}. \end{aligned} \quad (6.8d)$$

I note that Eqs. (6.8) perform the integration over all final states implicitly using the nonrelativistic Hamiltonian. This is in contrast to the strategy of Ref. [20] which keeps the final state phase space relativistic and therefore in principle does not allow to calculate the total cross section as described above.

## 6.2 Results

This section presents results for spin-averaged and spin-dependent observables of nucleon-deuteron radiative capture and of three-nucleon photo disintegration; results of two-nucleon photo disintegration are transformed to corresponding ones of radiative capture. The results are derived from calculations based on the purely nucleonic CD-Bonn potential [3] and its coupled-channel extension constructed in Sec. 2.3. I describe first the *standard calculational procedure*.

### 6.2.1 Standard Calculational Procedure

The hadronic interaction in purely nucleonic and in nucleon- $\Delta$  partial waves is taken into account up to the total two-baryon angular momentum  $I = 4$ . The calculations omit the Coulomb potential between charged baryons. Nevertheless, the theoretical description is charge dependent as described in Sec. 3.4. The charge dependence is treated in the  $^1S_0$  partial wave exactly, and in all other partial waves approximately. In contrast to hadronic reactions, that approximative treatment in e.m. reactions requires total isospin  $T = \frac{3}{2}$  components of the hadronic scattering states in *all* considered isospin-triplet two-baryon partial waves, since the e.m. current couples the  $T = \frac{1}{2}$  and  $T = \frac{3}{2}$  components strongly.

The three-particle equations for the trinucleon bound state  $|B\rangle$  and for the corresponding scattering states are solved as described in Chapter 3; in fact, the scattering states need to be calculated only implicitly according to Sec. 3.3. The resulting binding energies of  $^3\text{He}$  are -7.941 and -8.225 MeV for CD Bonn and CD Bonn +  $\Delta$ , respectively. If the Coulomb interaction were taken into account, as proper for  $^3\text{He}$ , the binding energies shift to -7.261 and -7.544 MeV, whereas the experimental value is -7.718 MeV. Nevertheless, I use the purely hadronic energy values and bound-state wave functions for consistency when calculating the current matrix elements, since I am unable to include the Coulomb interaction in the scattering states.

Whereas the hadronic interaction is considered up to  $I = 4$ , the e.m. current is allowed to act between partial waves up to  $I = 6$ , the higher partial waves being created by the geometry of antisymmetrization. The e.m. current is taken over from Refs. [38, 62] with some necessary modifications:

1. The e.m. current is richer than the one used in Refs. [20, 38, 62]; diagonal two-baryon current connecting states with  $\Delta$  isobar is taken into account.
2. More recent values for the e.m. couplings of the  $\Delta$  isobar are used according to Refs. [63, 64].
3. Meson coupling constants, meson masses and hadronic form factors used in meson-exchange currents are chosen consistently with the employed hadronic interactions CD Bonn and CD Bonn +  $\Delta$ ; they are listed in Appendix A.

The employed contributions to the e.m. current are collected in Appendix B. The current is expanded in electric and magnetic multipoles as described in Appendix E. The technique for calculating multipole matrix elements is described in Ref. [62]; a special stability problem [20] arising in the calculation requires some modifications of that technique as discussed in Appendix E. The magnetic multipoles are calculated from the one- and two-baryon parts of the spatial current. The electric multipoles use the Siegert form of the current *without* long-wavelength approximation; assuming current conservation, the dominant parts of the one-baryon convection current and of the diagonal  $\pi$ - and  $\rho$ -exchange current are taken into account implicitly in the Siegert part of the electric multipoles by the Coulomb multipoles of the charge density; the remaining non-Siegert part of the electric multipoles not accounted for by the charge density is calculated using explicit one- and two-baryon spatial currents. The charge density contributing to the Siegert term has diagonal single-nucleon and single- $\Delta$

contributions only; the nucleon- $\Delta$  transition contribution as well as two-baryon contributions are of relativistic order and are therefore omitted in the charge-density operator when calculating Coulomb multipoles.

The number of considered current multipoles is limited by the maximal total three-baryon angular momentum  $J_{\max} = \frac{15}{2}$ , taken into account for the hadronic scattering states. The results for the considered photo reactions up to pion-production threshold appear fully converged with respect to higher two-baryon angular momenta  $I$ , with respect to  $\Delta$ -isobar coupling and with respect to higher three-baryon angular momenta  $J$  on the scale of accuracy which present-day experimental data require.

That is the *standard calculational procedure*. Section 6.3 discusses the shortcomings of that standard description. In the rest of this section I focus on  $\Delta$ -isobar effects in sample observables.

### 6.2.2 Nucleon-Deuteron Radiative Capture

Low-energy photo reactions with two-body initial and final states have been investigated in Ref. [20]; the effects of the  $\Delta$  isobar were found to be small. My control calculations at low energies indicate that the results of Ref. [20] do not get essential physics changes though the hadronic interaction and the e.m. current are improved. The results therefore are not shown here; an example for low-energy observable is given in Sec. 6.3.2 which discusses shortcomings of the standard description. I concentrate on energies well above those of Ref. [20], but still below pion-production threshold. Figures 6.2 and 6.3 present results for spin-averaged and spin-dependent observables of nucleon-deuteron radiative capture at 100, 150 and 200 MeV nucleon lab energy. There are noticeable  $\Delta$ -isobar effects on some of the considered observables, e.g., on differential cross section and nucleon analyzing power. There is a disagreement between old [65] and new, still preliminary [66] differential cross section data, especially in the maximum region; the new preliminary data are in good agreement with my results including the  $\Delta$  isobar. The nucleon and deuteron vector analyzing powers  $A_y(N)$  and  $A_y(d)$  are quite well described with the inclusion of the  $\Delta$  isobar, whereas deuteron tensor analyzing powers, especially  $A_{xx}$ , indicate a possible sizable discrepancy between theoretical predictions and experimental data; on the scale of that discrepancy the  $\Delta$ -isobar effects for deuteron tensor analyzing powers are small.

The results of this thesis are qualitatively rather consistent with those of Refs. [35, 36], though the calculations of Refs. [35, 36] are based on a different strategy, on a different hadronic potential with explicit irreducible three-nucleon force and on a somehow different e.m. current operators.



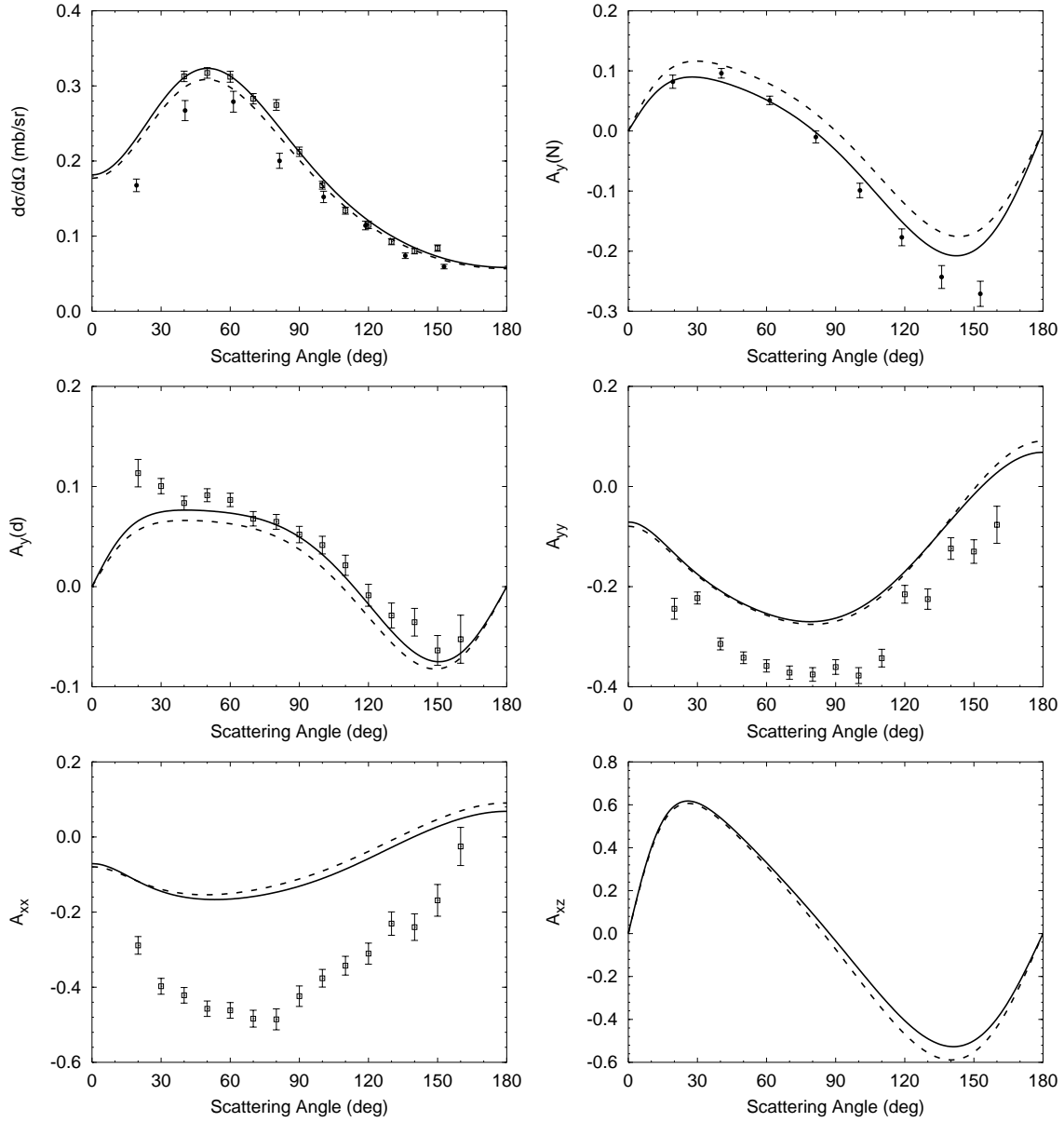


Figure 6.2: Differential cross section and analyzing powers of  $pd$  radiative capture at 100 MeV nucleon lab energy as functions of the c.m. nucleon-photon scattering angle. Results of the coupled-channel potential with  $\Delta$ -isobar excitation (solid curves) are compared with reference results of the purely nucleonic CD-Bonn potential (dashed curves). The experimental data are from Ref. [65] ( $\bullet$ ) and from Ref. [66] ( $\square$ ); the latter data are still preliminary.

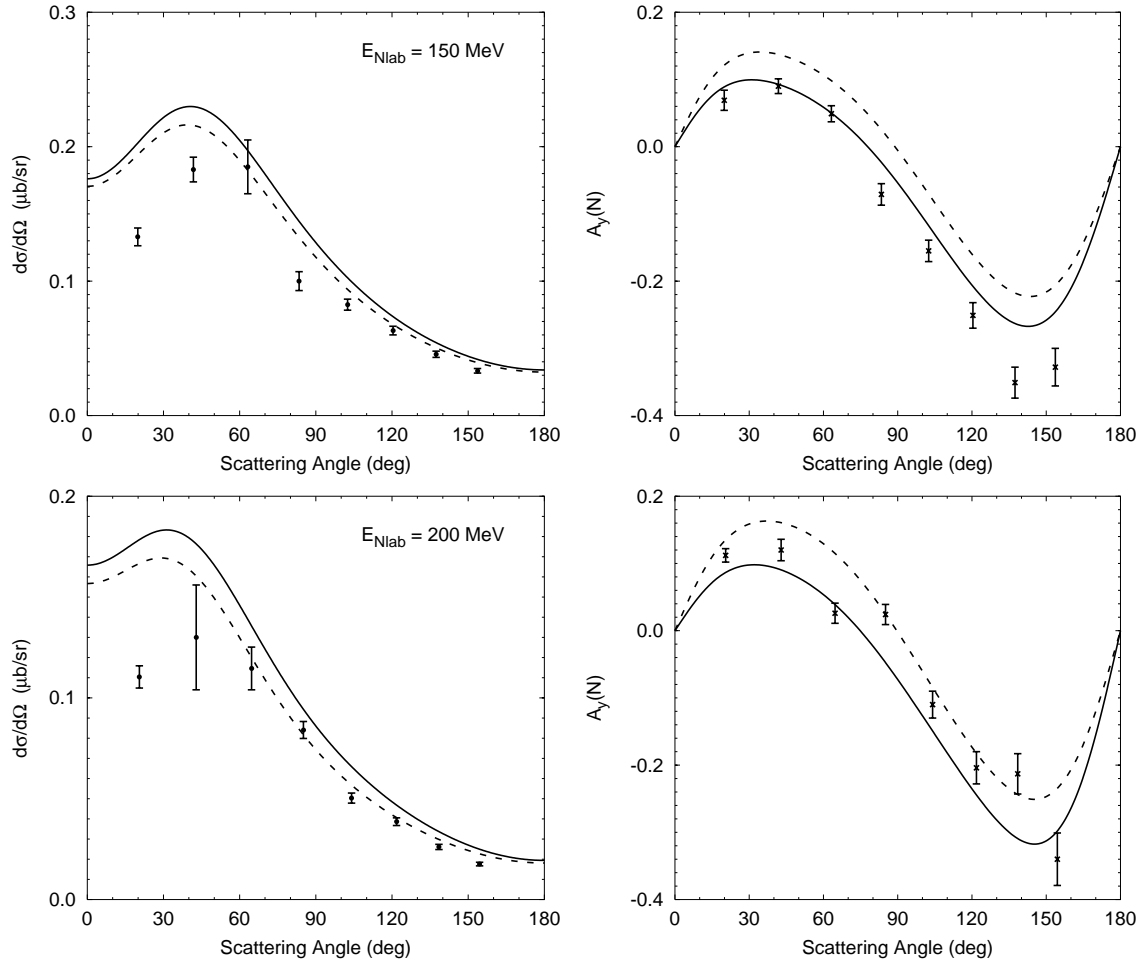


Figure 6.3: Differential cross section and nucleon analyzing power  $A_y(N)$  of  $pd$  radiative capture at 150 and 200 MeV nucleon lab energy as function of the c.m. nucleon-photon scattering angle. Results of the coupled-channel potential with  $\Delta$ -isobar excitation (solid curves) are compared with reference results of the purely nucleonic CD-Bonn potential (dashed curves). The experimental data are from Ref. [65].

### 6.2.3 Three-Body Photo Disintegration of Three-Nucleon Bound State

Experimental data for three-nucleon breakup are much scarcer than for two-body photo disintegration or radiative capture. To the best of my knowledge, there are no fully exclusive experimental data in the considered energy regime; I therefore show in Figs. 6.4 – 6.6 predictions for inclusive and semi-exclusive observables and compare them with existing experimental data. Figure 6.4 shows results for the total  ${}^3\text{H}$  three-nucleon photo disintegration cross section in the low energy region; there is no significant  $\Delta$ -isobar effect. In contrast, Ref. [37] sees a larger three-nucleon force effect for this observable; this discrepancy is partly due to a larger three-nucleon force effect on trinucleon binding and subsequent scaling and partly due to a different computational strategy when choosing kinematics for a theoretically underbound three-nucleon bound state as discussed in Sec. 6.3.2. Figures 6.5 – 6.6 show semi-exclusive fourfold differential cross section of  ${}^3\text{He}$  photo disintegration at higher energies; it is obtained from the fivefold differential cross section (6.7) by integrating over the kinematical curve  $S$ . Again, the  $\Delta$ -isobar effects for those particular observables appear rather small, smaller than the experimental error bars. There is also disagreement between theoretical predictions and experimental data in some kinematical regimes which in part may be caused by experimental conditions, e.g., by finite geometry, not taken into account in my calculations.

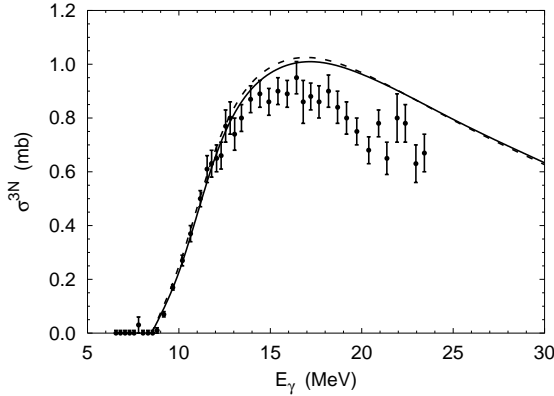


Figure 6.4: Total  ${}^3\text{H}$  three-nucleon photo disintegration cross section as function of the photon lab energy  $E_\gamma$ . Results of the coupled-channel potential with  $\Delta$ -isobar excitation (solid curve) are compared with reference results of the purely nucleonic CD-Bonn potential (dashed curve). The experimental data are from Ref. [67].

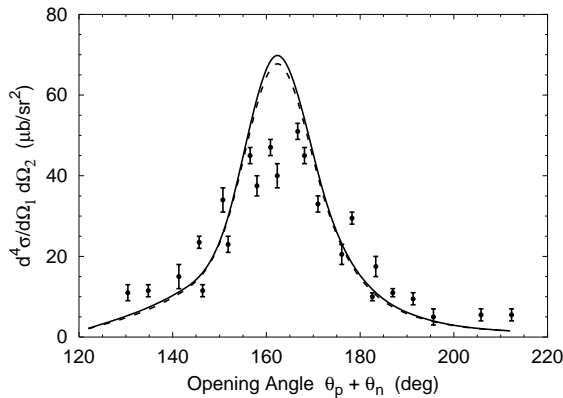


Figure 6.5: The fourfold differential cross section of the  ${}^3\text{He}(\gamma, pn)p$  reaction at 85 MeV photon lab energy as function of the  $pn$  opening angle at  $\theta_p = 81^\circ$ . Results of the coupled-channel potential with  $\Delta$ -isobar excitation (solid curve) are compared with reference results of the purely nucleonic CD-Bonn potential (dashed curve). The experimental data are from Ref. [68].

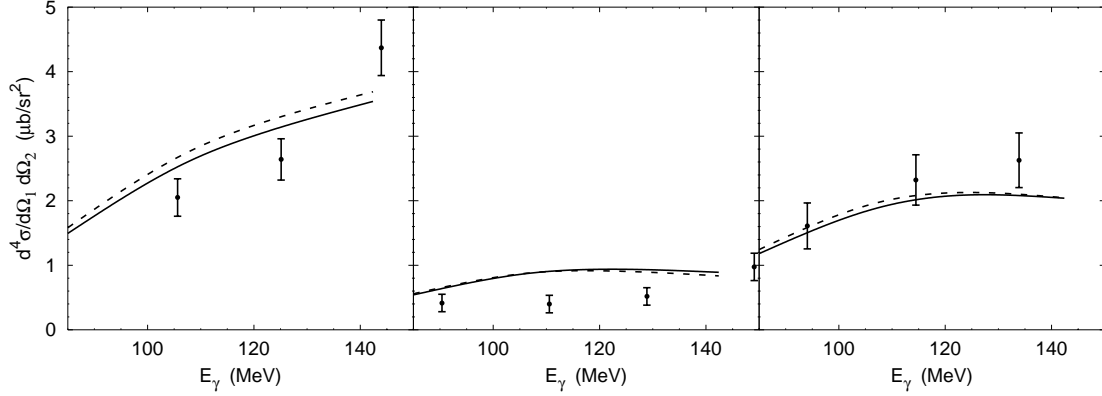


Figure 6.6: The fourfold differential cross section of the  ${}^3\text{He}(\gamma, pp)n$  reaction as function of the photon lab energy  $E_\gamma$  in various kinematical configurations:  $(81.0^\circ, 81.3^\circ, 180.0^\circ)$  (left),  $(92.2^\circ, 91.4^\circ, 180.0^\circ)$  (middle), and average of  $(81.5^\circ, 90.8^\circ, 180.0^\circ)$  and  $(91.7^\circ, 80.9^\circ, 180.0^\circ)$  (right). Results of the coupled-channel potential with  $\Delta$ -isobar excitation (solid curve) are compared with reference results of the purely nucleonic CD-Bonn potential (dashed curve). The experimental data are from Ref. [69].

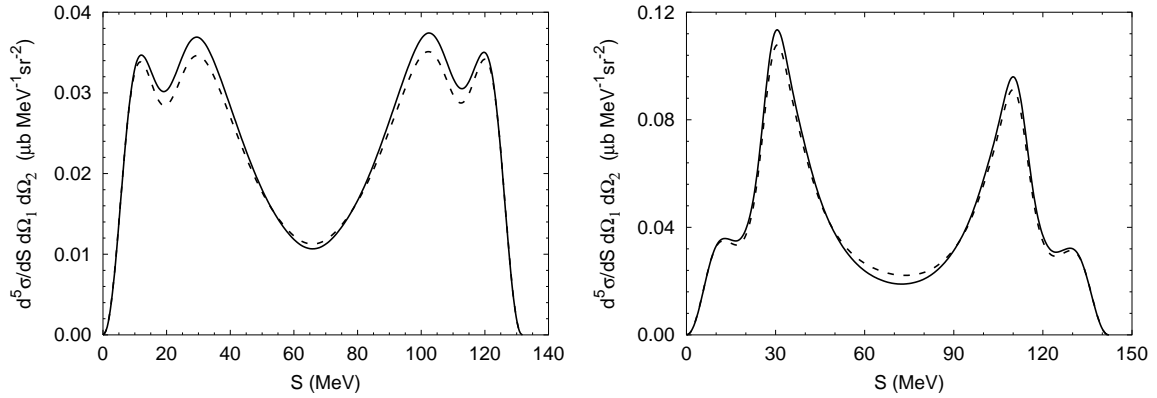


Figure 6.7: The fivefold differential cross section of three-nucleon photo disintegration at 120 MeV photon lab energy as function of the arclength  $S$  along the kinematical curve for configuration  $(92.2^\circ, 91.4^\circ, 180.0^\circ)$  on the left and  $(81.5^\circ, 90.8^\circ, 180.0^\circ)$  on the right. Results of the coupled-channel potential with  $\Delta$ -isobar excitation (solid curve) are compared with reference results of the purely nucleonic CD-Bonn potential (dashed curve).

Finally, in Fig. 6.7 I show fully exclusive sample fivefold differential cross section of three-nucleon photo disintegration at 120 MeV photon lab energy for two kinematical configurations which were shown semi-exclusively in Fig. 6.6; even at that higher energy the  $\Delta$ -isobar effects are rather mild.

### 6.3 Shortcomings of the Description

The present description of photo reactions is with respect to the dynamic input, i.e., with respect to the hadronic interaction and to the e.m. current, and with respect to the scope of applications a substantial improvement compared with Ref. [20]. But it is still not a unique and in itself consistent description. I am unable to repair the existing deficiencies. However, this section points those shortcomings out and tries at least to estimate their size. I identify three different problem areas.

#### 6.3.1 Shortcomings of the Theoretical Form of the Cross Section

The standard strategy uses the nonrelativistic form (6.2) – (6.7) for cross sections; this choice appears to be consistent with the underlying two-baryon dynamics, though inconsistent with the experimental relativistic kinematics. I therefore compare results obtained from Eqs. (6.2) – (6.7) with corresponding ones obtained from the relativistic form of the cross section (5.2) which uses relativistic kinetic energies for the Lorentz-invariant phase space element and the kinematic locus (5.10) combined with the matrix element obtained according to the strategy of Eq. (5.4) without further nonrelativistic reduction, i.e.,

$$\langle f|M|i\rangle = (2\pi)^{\frac{3}{2}(n-1)} \langle s_f|M_\gamma(E_i\mathbf{k}_f)|s_i\rangle \left(\frac{4\pi}{2k_\gamma^0}\right)^{\frac{1}{2}} [2k_{i_1}^0 2k_{i_2}^0 \prod_{j=1}^n (2k_{f_j}^0)]^{\frac{1}{2}}. \quad (6.9)$$

The comparison is possible for observables in fully exclusive reactions. The difference between those aspects of relativistic and nonrelativistic kinematics is minor for all considered observables of radiative capture, i.e., less than 1%, but more significant, i.e., up to order of 10%, for three-nucleon photo disintegration as shown in Fig. 6.8. Of course, the indicated effect does not represent the true difference between nonrelativistic quantum-mechanical and fully relativistic quantum-field-theoretical results, but it may indicate the order of magnitude of the shortcomings of nonrelativistic calculations. In the light of the accuracy of present-day data of photo reactions, this shortcoming of the theoretical description is rather inconsequential.

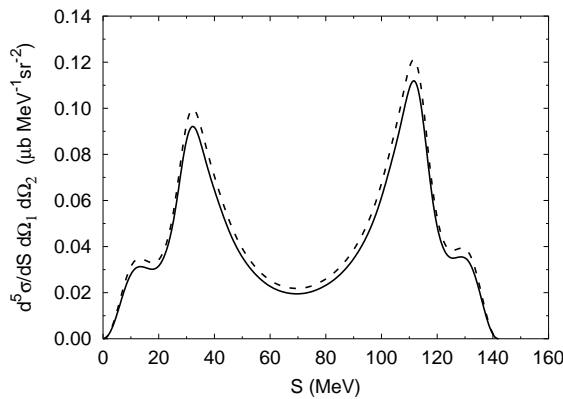


Figure 6.8: Differential cross section of three-nucleon photo disintegration at 120 MeV photon lab energy as function of the arclength  $S$  along the kinematical curve for configuration  $(91.7^\circ, 80.9^\circ, 180.0^\circ)$ . Results of the coupled channel potential with  $\Delta$ -isobar excitation based on the nonrelativistic form of the cross section (solid curve) are compared with results based on the relativistic form of the cross section (dashed curve).

### 6.3.2 Shortcomings of the Dynamics

#### Nonunique Choice of Kinematics

The computational strategy in choosing the kinematics for the matrix element  $\langle s_f | M_\gamma(E_i \mathbf{k}_f) | s_i \rangle$  is described in Sec. 6.1. In this *first* option, suggested there,  $\langle s_f | M_\gamma(E_i \mathbf{k}_f) | s_i \rangle$  is calculated in the c.m. system. I opt to let the experimental beam energy determine the energy of hadronic nucleon-deuteron state in radiative capture and the energy of the hadronic two-body and three-body final states in photo disintegration exactly. Since the trinucleon model binding energy is not the experimental one and the kinematics is nonrelativistic for hadrons when calculating  $\langle s_f | M_\gamma(E_i \mathbf{k}_f) | s_i \rangle$ , the energy of the photon does not have the experimental value when assuming energy conservation. At very low energies, i.e., at the two-body photo-disintegration threshold, the deviation of the photon energy can get as large as 10%, whereas at higher energies considered in this thesis it remains around 1 - 2%. In contrast, in a *second* option one could let the experimental beam energy determine the c.m. photon energy exactly; then the energies of the hadronic nucleon-deuteron and three-nucleon states are not experimental ones. A *third* option may use experimental energies for both initial and final states, but then the matrix element determining physical amplitudes is slightly off-shell; this is the computational strategy of Refs. [36, 37]. The difference in results between those three choices is minor at higher energies, i.e., above 100 MeV nucleon lab energy, for all considered observables in all considered kinematical regimes. However, there are differences up to 10% for observables at low energies. There, the observed  $\Delta$ -isobar effects depend strongly on the choice of computational strategy. An example is shown in Fig. 6.9.

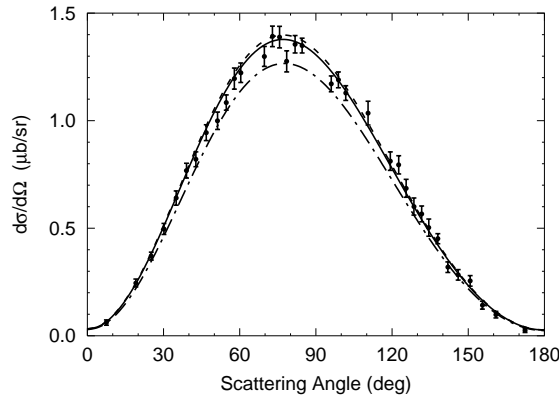


Figure 6.9: Differential cross section of  $pd$  radiative capture at 19.8 MeV deuteron lab energy as function of the c.m. nucleon-photon scattering angle. Results of the coupled-channel potential with  $\Delta$ -isobar excitation derived from the standard approach (solid curve) are compared with results of option three which uses experimental energies for both initial and final states, but the matrix element (6.2b) is off-shell (dashed-dotted curve). The results of option two are rather close to the solid curve. In order to appreciate the effect of the nonunique choice of kinematics in relation to the size of the  $\Delta$ -isobar effect, results of a standard calculation with the purely nucleonic reference potential are also given as dashed curve. The experimental data are from Ref. [70].

### Omission of Coulomb Interaction between Protons

I am unable to include the Coulomb interaction in the calculation of the three-nucleon scattering states. In contrast, the selected inclusion of the Coulomb interaction in the trinucleon bound state is easily possible, as discussed in Chapter 4, but this inclusion creates an additional inconsistency: Initial and final hadronic states become eigenstates of different Hamiltonians, and, strictly speaking, the Siegert form of the current operator is not applicable. Nevertheless, I do such an inconsistent calculation which Refs. [36, 37] chooses to do as their standard calculation, in order to estimate the effect of the omitted Coulomb interaction at least partially. The inclusion of the Coulomb interaction in the trinucleon bound state systematically reduces the spin-averaged cross sections; in contrast, spin observables appear to be almost unaffected. A characteristic result is shown in Fig. 6.10. Even at higher energies the observed Coulomb effect may be of the same order of magnitude as the full  $\Delta$ -isobar effect; however, it is not clear in how far the indicated effect represents a true Coulomb effect or in how far it just reflects the dynamic incompatibility between bound and scattering states.

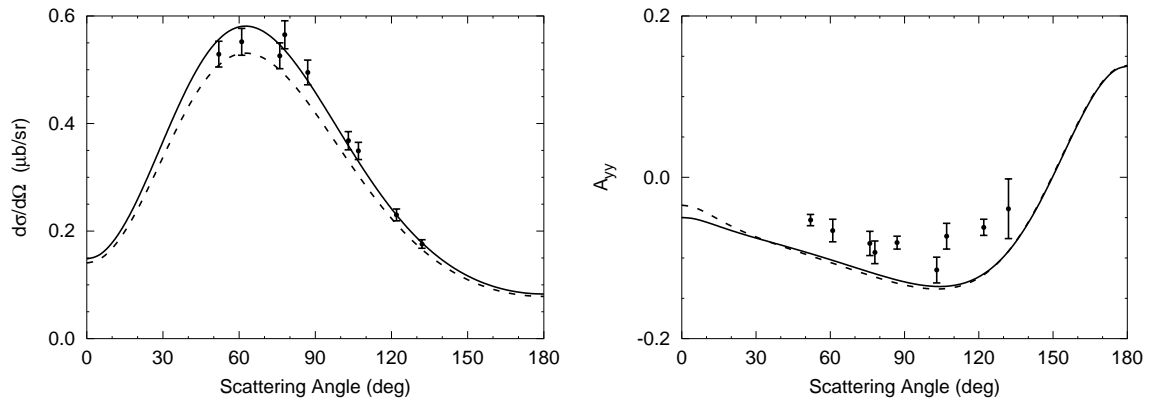


Figure 6.10: Differential cross section and deuteron analyzing power  $A_{yy}$  of  $pd$  radiative capture at 95 MeV deuteron lab energy as function of the c.m. nucleon-photon scattering angle. Results of the coupled-channel potential with  $\Delta$ -isobar excitation derived from the standard approach (solid curve) are compared with results including the Coulomb interaction in the three-nucleon bound state (dashed curve). The experimental data are from Ref. [71].

### 6.3.3 Shortcomings of the e.m. Current

#### Lack of Current Conservation

The potentials CD Bonn and CD Bonn +  $\Delta$  used in this thesis have nonlocal structures, whereas the e.m. current, given explicitly in Appendix B, is employed in a local nonrelativistic form. Thus, the continuity equation is not fulfilled for the current. As measure for this deficiency predictions are compared based on two different approaches for the electric multipoles, i.e.,

- (1) the standard calculation with the Siegert operator accounting for the two-baryon current implicitly by assumed current conservation, and
- (2) the explicit use of the meson-exchange current also for all of the electric multipoles.

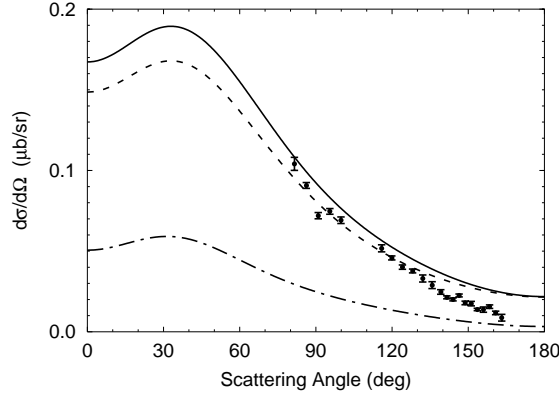


Figure 6.11: Differential cross section of  $pd$  radiative capture at 190 MeV nucleon lab energy as function of the c.m. nucleon-photon scattering angle. Results of the coupled-channel potential with  $\Delta$ -isobar excitation derived from the Siegert approach for electric multipoles (solid curve) are compared with results based on the explicit use of meson-exchange current (dashed curve). In order to appreciate the size of the two-baryon current contribution, the results of non-Siegert calculation with one-baryon current only are also given as dashed-dotted curve. The experimental data are from Ref. [72].

The discrepancy between those two calculations measures the importance of the existing lack of current conservation; indeed, the violation can be significant as Fig. 6.11 proves. I believe that calculations with the Siegert form of the current operator repair the violation of current conservation in part; I therefore employ the Siegert form of the current operator in the standard calculational strategy. However, at this stage it is useful to discuss the lack of current conservation in more detail:

1. The  $\sigma$ ,  $\rho$  and  $\omega$  exchanges yield a spin-orbit interaction. That spin-orbit interaction makes, even in local approximation and even for isoscalar-meson exchanges, a contribution to the continuity equation (2.17b). Thus, there is a corresponding contribution to the exchange current; it is used in local form [73]. There are also additional contributions to the  $\rho$ -exchange current [39] not listed in Appendix B and therefore not taken into account in standard calculations. All those contributions are implicitly contained in the Siegert-part of the electric multipoles. In the tentative calculations described in this paragraph they are used explicitly for the non-Siegert part of the electric multipoles and for the magnetic multipoles. There, those additional contributions yield only small corrections, of the order of 2% at most, for observables considered in this thesis. I therefore conclude that spin-orbit contributions and additional  $\rho$ -exchange currents can quite safely be neglected in the Siegert form of the current operator when calculating the photo reactions of this thesis. However, they are more important for calculations based fully and explicitly on the exchange current and they therefore make a non-negligible contribution to the difference seen in Fig. 6.11.
2. The employed potentials have explicit nonlocal structures. That explicit nonlocality makes a contribution to the two-baryon exchange current.

I compared the results of the following models for the purely nucleonic potential. The models are based on  $\pi$ ,  $\rho$  and  $\omega$  exchanges and on a scalar isoscalar and a *scalar isovector*  $\sigma$  exchange; one model uses the nonlocal structures of CD-Bonn type and the other their local approxima-



tions. Both models are tuned to deuteron binding and to  $^1S_0$  and  $^3S_1 - ^3D_1$  phase shifts only. Though non realistic models, both usually predict observables in qualitative agreement with the realistic descriptions. When employing the local potential model I obtain very good agreement between the results based on the Siegert form of the current operator and the results based on explicit exchange-current contributions to all multipoles. However, when employing the non-local potential model, the results can differ substantially; the difference can be as large as seen in Fig. 6.11 for the coupled-channel potential CD Bonn +  $\Delta$ . I conclude: The explicit nonlocality of the employed potentials is a significant source for current nonconservation. Future calculations should attempt to design nonlocal exchange-current contributions consistent with the nonlocality of the underlying baryon-baryon potentials.

3. The employed potentials have an implicit nonlocality and isospin dependence due to the general partial-wave dependence of the meson exchanges. That partial-wave dependence is slight for the  $\pi$ ,  $\rho$  and  $\omega$  exchanges, but substantial for the  $\sigma$  exchange. That implicit nonlocality and isospin dependence make a contributions to the two-baryon exchange current.

The nucleonic CD Bonn as well as CD Bonn +  $\Delta$  show a small partial-wave dependence in  $\pi$  and in  $\rho$  exchange. Fitting CD Bonn with partial-wave-independent  $\pi$  and  $\rho$  exchanges decreases the quality of the fit to data only by very little;  $\chi^2/\text{datum}$  increases from 1.02 to 1.03. When comparing observables of the hadronic processes and of the photo reactions of this thesis for both potentials, no distinguishable difference is found in plots. I conclude: The implicit nonlocality arising from the partial-wave dependence in  $\pi$  and  $\rho$  exchange of CD Bonn and CD Bonn +  $\Delta$  is of no consequence for the prediction of observables.

The local model used for the discussion of problem 2. is modified to simulate the partial-wave dependence of  $\omega$  exchange in the nucleonic CD Bonn, it is retuned as under 2. The  $\omega$  exchange is taken to be without hadronic cut off in the  $^1P_1$  partial wave as in CD Bonn; this partial-wave dependence violates current conservation. However, the observed difference between calculations based on the Siegert form of the current operator and calculations based on explicit exchange-current contributions to all multipoles is much smaller than that shown in Fig. 6.11. I conclude: The implicit nonlocality arising from the partial-wave dependence in the  $\omega$ -exchange of CD Bonn and CD Bonn +  $\Delta$  is of no real consequence for the prediction of observables.

With respect to the partial-wave dependence of  $\sigma$  exchange the local model used for the discussion of problem 2. is studied. I concentrate on the difference of  $\sigma$  exchange between isospin singlet and triplet partial waves, i.e., on the effective isovector nature of the  $\sigma$  meson introduced in the model and in CD Bonn and CD Bonn +  $\Delta$ . Furthermore, even if the  $\sigma$  exchange were truly an isoscalar one in the purely nucleonic potential, the explicit treatment of the  $\Delta$  isobar in the coupled-channel extension introduces an isovector correction: The employed coupled-channel potential CD Bonn +  $\Delta$ , acting in isospin-triplet partial waves, has a weakened  $\sigma$  exchange compared to the purely nucleonic CD Bonn; part of the intermediate-range attraction simulated by  $\sigma$  exchange is taken over by  $\Delta$ -isobar excitation in the coupled-channel approach. Thus, the  $\Delta$ -isobar current has to be supplemented by changed  $\sigma$ -exchange current. Omitting the  $\sigma$ -meson contribution to the exchange current, quite significant differences, comparable to that of Fig. 6.11, arise for observables of the photo reactions in this thesis between calculations based on the Siegert form of the current and on the full explicit exchange-current contributions. In contrast, the explicit  $\sigma$ -meson exchange-current contributions to the non-Siegert part of the electric multipoles and to the magnetic multipoles remain small. I arrive to qualitatively the same results when including the  $\sigma$ -meson exchange-current for CD Bonn and CD Bonn +  $\Delta$

with the  $\sigma$ -meson parameters of  $S$  waves. I conclude: Though the partial-wave dependence of the  $\sigma$ -meson exchange is a significant source of current nonconservation, the standard calculation based on the Siegert form of the current for part of the electric multipoles and on explicit exchange-current contributions to all other multipoles appears to be quite a reliable calculational scheme.

4. The employed potentials are charge dependent. The charge dependence of the interaction is due to the charge dependence of the parameters of exchanged  $\pi$ ,  $\rho$  and  $\sigma$  mesons in the nucleonic part of the potentials and due to the charge dependence of the nucleonic masses. The isospin structure of the charge-dependent potential contributions is given in terms of the baryonic isospin projections; thus, that isospin dependence, giving rise to charge dependence, does not require an exchange current by itself; it only does so, if its potential forms are nonlocal. In the case of the employed potentials it is so indeed, but that explicit nonlocality was already discussed in problem 2. The diagonal  $\pi$ - and  $\rho$ -exchange contributions to the exchange current should be built from the charged-meson parameters. The nondiagonal  $\pi$  and  $\rho$  exchanges are carried by the mesons of all charges. However, the standard calculation uses averaged meson parameters and an averaged nucleon masses for all meson-exchange currents; it was checked that both calculational simplifications are without any consequence for the observables of this thesis.

From this lengthy, but I think necessary discussion of the problems 1. to 4. I conclude for the calculations of this thesis: When the Siegert form of the current is used for part of the electric multipoles and explicit exchange-current contributions to all other multipoles in the operator form of Appendix B, the implicit nonlocality of CD Bonn and CD Bonn +  $\Delta$  arising from the partial-wave dependence of the meson exchanges is without consequences for prediction. In contrast, the explicit nonlocality of CD Bonn and CD Bonn +  $\Delta$ , also responsible for current nonconservation, is of serious concern; its consequence on the non-Siegert parts of the current could not be estimated yet by any of the models. Still, I believe that the standard calculation, based on the Siegert form of the current, effectively corrects the current nonconservation and is therefore quite reliable for the observables of photo reactions considered in this thesis.

### Lack of Covariance

If a fully covariant description of dynamics were available, the matrix element  $\langle f|M|i \rangle$  of Eq. (6.9) were a Lorentz scalar and could therefore be calculated in any frame with identical results. However, the description of hadron dynamics is nonrelativistic, and the results therefore are frame-dependent. I investigate that frame dependence calculating the same matrix elements  $\langle s_f|M_\gamma(E_i\mathbf{k}_f)|s_i \rangle$  in lab and in c.m. frames, i.e., in the rest frames of the initial and final three-nucleon systems. The two frames differ by the sum  $\mathbf{K}_+$  of three-nucleon total momenta and by the photon momentum  $\mathbf{k}_\gamma$ . A typical result is shown in Fig. 6.12; I conclude that the frame dependence is minor and at present of no real theoretical concern.

### Higher Order Contributions to the Current Operator in $(k/m_N)$ Expansion

In the standard calculational scheme the Siegert form of the current operator is used together with explicit meson-exchange contributions not accounted for by the Siegert part. The charge-density operator in the Siegert part is of one-baryon nature and is taken to be nonrelativistic in the standard

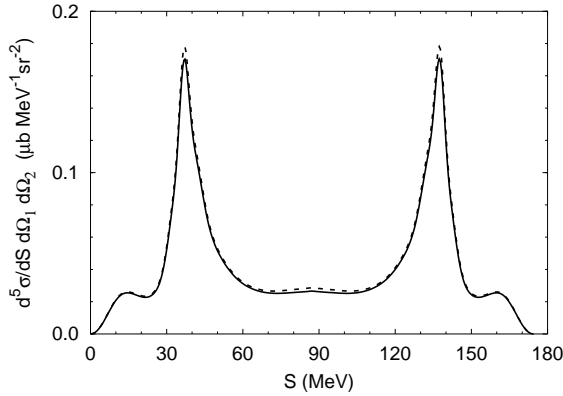


Figure 6.12: Differential cross section of three-nucleon photo disintegration at 142 MeV photon lab energy as function of the arclength  $S$  along the kinematical curve for configuration  $(82.3^\circ, 82.3^\circ, 180.0^\circ)$ . Results based on matrix elements  $\langle s_f | M_\gamma(E_i \mathbf{k}_f) | s_i \rangle$  calculated in c.m. (solid curve) and in lab system (dashed curve) are compared.

calculations. However, the one-baryon purely nucleonic charge-density operator has relativistic corrections of order  $(k/m_N)^2$ . Leading contributions to the nucleon- $\Delta$  transition charge density and to the two-nucleon charge density, used in Ref. [41] for the calculation of trinucleon elastic charge form factors, are both of the relativistic order  $(k/m_N)^2$ ; they are included in additional calculations testing relativistic operator corrections. The resulting corrections reduce the cross sections; they appear beneficial; a characteristic results are shown in Fig. 6.13. The effect shown there is dominated by the one-nucleon charge-density correction; the two-nucleon charge-density, quite important for the elastic trinucleon charge form factors [41], shows noticeable effects only in some spin observables, whereas the nucleon- $\Delta$  transition charge appears to be insignificant for all calculated observables of this thesis. Correspondingly large corrections of the same origin were also found in photo reactions on

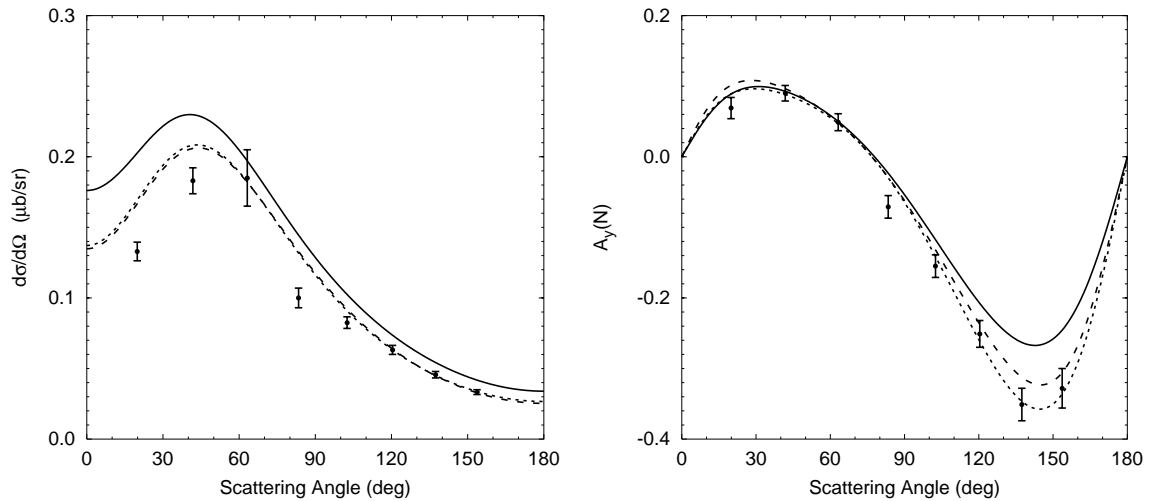


Figure 6.13: Differential cross section and nucleon analyzing power  $A_y(N)$  of  $pd$  radiative capture at 150 MeV nucleon lab energy as function of the c.m. nucleon-photon scattering angle. Results of the coupled-channel potential with  $\Delta$ -isobar excitation derived from the standard approach (solid curves) are compared with results including relativistic one-nucleon charge corrections (dashed curves) and with results including relativistic one- and two-baryon charge corrections (dotted curves). The experimental data are from Ref. [65].

the deuteron [74]. Thus, the results of this subsection are not surprising. The current corrections of this subsection should be included in future calculations of photo reactions.

## Electron Scattering from Trinucleon Bound State

The considered reactions of inelastic electron scattering are schematically shown in Fig. 7.1.

### 7.1 Spin-Averaged and Spin-Dependent Cross Sections

I start the cross section calculation from the general form (5.2); the matrix element  $\langle f|M|i\rangle$  is obtained with the help the quantum-mechanical model for hadronic interaction. The effective e.m. interaction (2.13) is taken into account perturbatively, whereas the hadronic interaction  $H_I$  has exactly to be taken into account up to all orders. Thus, the matrix elements of the e.m. interaction require fully correlated hadronic states (2.6). The quantum-mechanical  $S$  matrix for the considered processes, i.e., for the two- and three-body electro disintegration of the trinucleon bound state is parametrized in the general form

$$\langle f|S|i\rangle = -i\delta^{(3)}(\mathbf{P}_f - \mathbf{P}_i)\delta(E_f - E_i)\frac{1}{(2\pi)^2}(2k_{e_i}^0 2k_{e_f}^0)^{-\frac{1}{2}}\frac{4\pi e_p^2}{Q^2}\langle s_f|M_e(E_i\mathbf{k}_f)|s_i\rangle, \quad (7.1a)$$

$$\langle s_f|M_e(E_i\mathbf{k}_f)|s_i\rangle = \bar{u}(\mathbf{k}_{e_f}s_{e_f})\gamma_\mu u(\mathbf{k}_{e_i}s_{e_i})\langle\Psi_f^{(-)}|j^\mu(\mathbf{Q},\mathbf{K}_+)|B\rangle, \quad (7.1b)$$

$|\Psi_f^{(-)}\rangle$  standing for the fully correlated states  $|\Psi_\alpha^{(-)}(\mathbf{q}_f)\mathbf{v}_{\alpha_f}\rangle$  or  $|\Psi_0^{(-)}(\mathbf{p}_f\mathbf{q}_f)\mathbf{v}_{0_f}\rangle$  defined in Eqs. (3.17). The initial and final electron four-momenta  $k_{e_i}$  and  $k_{e_f}$  determine the four-momentum transfer to the

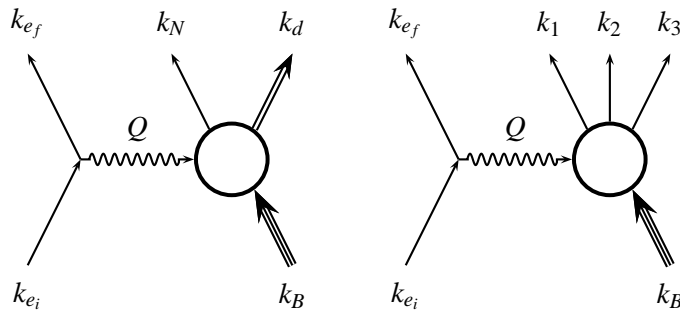


Figure 7.1: Schematic illustration of all considered reactions in inelastic electron scattering from the trinucleon bound state. The lines for the two-baryon and three-baryon particles are drawn in a special form to indicate their compositeness.

three-nucleon system  $Q = k_{e_i} - k_{e_f}$ . The spin quantum numbers of individual particles are collectively denoted by  $s_i = \{s_{e_i} M_B\}$  for the initial electron and the trinucleon bound state and by  $s_f$  for all spin projections of the final states.  $\gamma^\nu$  are the Dirac matrices and  $u(\mathbf{k}s)$  is the electron Dirac spinor with the normalization  $\bar{u}(\mathbf{k}s')u(\mathbf{k}s) = m_e \delta_{s's}$ , with  $m_e$  being the electron mass. The matrix element  $\langle s_f | M_e(E_i \mathbf{k}_f) | s_i \rangle$  is build up from the leptonic and hadronic e.m. currents and is given explicitly in the following subsections for the considered reactions.

The inelastic electron scattering from the trinucleon bound state is considered in the lab frame, i.e., in the rest frame of the initial three-nucleon system. The spatial components of the initial and final electron momenta and the three-momentum transfer  $\mathbf{Q} = \mathbf{k}_{e_i} - \mathbf{k}_{e_f}$  determine the coordinate axes, i.e.,  $\hat{\mathbf{z}} = \hat{\mathbf{Q}}$ ,  $\hat{\mathbf{y}} = \mathbf{k}_{e_i} \times \mathbf{k}_{e_f} / |\mathbf{k}_{e_i} \times \mathbf{k}_{e_f}|$ , and  $\hat{\mathbf{x}} = \hat{\mathbf{y}} \times \hat{\mathbf{z}}$ . The strategy for calculating the matrix element of e.m. current operator is slightly different compared to photo reactions.

1. The experimental four-momentum transfer  $Q$  determines the available internal energy of the final three-nucleon system with total lab momentum  $\mathbf{Q}$ , i.e.,  $E_i = Q_0 + E_B - \mathbf{Q}^2/6m_N$ ; this step is done using the experimental trinucleon binding energy  $E_B$ . I.e., the energy of the three-nucleon system is the true experimental one; the experimental two-body and three-body breakup thresholds are exactly reproduced.
2. The current matrix element is calculated in the lab system as *on-energy-shell element* under nonrelativistic model assumptions. Under those assumptions the internal energy  $E_i = Q_0 + E_B - \mathbf{Q}^2/6m_N$  and the experimental  $Q^2$  determine the momentum transfer  $\mathbf{Q}$  and the energy transfer  $Q_0$  to be used for the current matrix element in the lab system. This step uses the computed trinucleon model binding energy  $E_B$ . Since the model binding energy  $E_B$  is not the experimental one, neither for  ${}^3\text{He}$  nor for  ${}^3\text{H}$ , the components of the four-momentum transfer  $Q$  do not have the experimental values; however,  $Q^2$  has the experimental value by construction.

Performing consistently a nonrelativistic reduction in Eqs. (5.2) for hadrons as described in Sec. 5.1, I obtain the differential cross sections analytically given in the following subsections for all considered reactions. In contrast to the matrix element  $\langle s_f | M_e(E_i \mathbf{k}_f) | s_i \rangle$ , the phase-space factors are calculated using the experimental four-momentum transfer. The electron will always be highly relativistic, i.e.,  $k_{e_i}^0 \approx |\mathbf{k}_{e_i}| \gg m_e$  and  $k_{e_f}^0 \approx |\mathbf{k}_{e_f}| \gg m_e$ .

### 7.1.1 Two-Body Electro Disintegration of Trinucleon Bound State

The initial state is already discussed above. The final electron, nucleon and deuteron state is characterized by the respective spin quantum numbers  $s_f = \{s_{e_f} m_{s_f} M_{I_f}\}$  and by the respective particle momenta  $\mathbf{k}_{e_f}$ ,  $\mathbf{k}_N$  and  $\mathbf{k}_d$ ; due to momentum and energy conservation they are not all independent. Usually, the experiment determines the final energy of the electron  $k_{e_f}^0$  and its scattering angle  $\theta_e = \arccos(\hat{\mathbf{k}}_{e_f} \cdot \hat{\mathbf{k}}_{e_i})$ . Measuring the direction of one momentum of the final two hadrons fixes also  $\mathbf{k}_N$  and  $\mathbf{k}_d$ , although not always uniquely. I chose the  $\hat{\mathbf{k}}_N$  as independent variable. The matrix element  $\langle s_f | M_e(E_i \mathbf{k}_f) | s_i \rangle$  of Eq. (7.1) is

$$\langle s_f | M_e(E_i \mathbf{k}_f \mathbf{k}_N) | s_i \rangle = \bar{u}(\mathbf{k}_{e_f} s_{e_f}) \gamma_\mu u(\mathbf{k}_{e_i} s_{e_i}) \langle \Psi_\alpha^{(-)}(\mathbf{q}_f) \mathbf{v}_{\alpha_f} | j^\mu(\mathbf{Q}, \mathbf{K}_+) | B \rangle, \quad (7.2a)$$

$$\langle s_f | M_e(E_i \mathbf{k}_f \mathbf{k}_N) | s_i \rangle = \sum_\lambda (-1)^\lambda \bar{u}(\mathbf{k}_{e_f} s_{e_f}) \gamma^\nu u(\mathbf{k}_{e_i} s_{e_i}) \epsilon_\nu^*(Q\lambda) \langle \Psi_\alpha^{(-)}(\mathbf{q}_f) \mathbf{v}_{\alpha_f} | j^\mu(\mathbf{Q}, \mathbf{K}_+) | B \rangle \epsilon_\mu(Q\lambda) \quad (7.2b)$$

with the relative nucleon-deuteron momentum  $\mathbf{q}_f = (\mathbf{k}_d - 2\mathbf{k}_N)/3$ . In Eq. (7.2b) the contraction of the leptonic and hadronic currents is carried out by projecting them on the polarization vectors  $\epsilon(Q\lambda)$

with  $\lambda = 0, \pm 1$  and  $Q^\mu \epsilon_\mu(Q\lambda) = 0$ ; they are given explicitly in Appendix E. The hadronic e.m. current in Eq. (7.2b) formally has the same structure as used in the photo reactions and is calculated according to Appendix E. The resulting fivefold differential cross section is

$$\frac{d^5 \sigma_{i \rightarrow f}}{dk_{ef}^0 d^2 \hat{\mathbf{k}}_{ef} d^2 \hat{\mathbf{k}}_N} = \frac{\sigma_{\text{Mott}}}{4k_{ei}^0 k_{ef}^0 \cos^2(\theta_e/2)} |\langle s_f | M_e(E_i \mathbf{k}_{ef} \mathbf{k}_N) | s_i \rangle|^2 \text{fps} \quad (7.3a)$$

with the Mott cross section

$$\sigma_{\text{Mott}} = \left( \frac{e_p^2 \cos(\theta_e/2)}{2k_{ei}^0 \sin^2(\theta_e/2)} \right)^2 \quad (7.3b)$$

and the phase-space factor

$$\text{fps} = \frac{2m_N |\mathbf{k}_N|^3}{3\mathbf{k}_N^2 - \mathbf{Q} \cdot \mathbf{k}_N}. \quad (7.3c)$$

The spin averaged differential cross section is

$$\frac{\overline{d^5 \sigma}}{dk_{ef}^0 d^2 \hat{\mathbf{k}}_{ef} d^2 \hat{\mathbf{k}}_N} = \frac{1}{4} \sum_{s_f s_i} \frac{d^5 \sigma_{i \rightarrow f}}{dk_{ef}^0 d^2 \hat{\mathbf{k}}_{ef} d^2 \hat{\mathbf{k}}_N}. \quad (7.4)$$

In the figures it is denoted by  $d^5 \sigma / dE_e d\Omega_e d\Omega_N$ , the traditional notation. The spin-dependent observables are discussed in Sec. D.1.3.

### 7.1.2 Three-Body Electro Disintegration of Trinucleon Bound State

The final scattering state, composed of the electron and three free nucleons, is characterized by the respective particle momenta  $\mathbf{k}_{ef}$ ,  $\mathbf{k}_1$ ,  $\mathbf{k}_2$  and  $\mathbf{k}_3$  and by the respective spin quantum numbers  $s_f = \{s_{ef} m_{s_1} m_{s_2} m_{s_3}\}$ ; due to momentum and energy conservation the momenta are not all independent. The final energy of the electron  $k_{ef}^0$  and its scattering angle  $\theta_e = \arccos(\hat{\mathbf{k}}_{ef} \cdot \hat{\mathbf{k}}_{ei})$  are usually determined by the experiment. As in hadronic nucleon-deuteron breakup and in three-nucleon photo disintegration, the two nucleon scattering angles with respect to the beam direction  $(\theta_1, \varphi_1)$  and  $(\theta_2, \varphi_2)$  and the arclength  $S$  along the kinematical curve (5.10) are chosen as independent hadronic variables. However, since the coordinate axes are already determined by the electron kinematics, all four angles  $(\theta_1, \varphi_1, \theta_2, \varphi_2)$  are required in order to specify the kinematical configuration of hadrons. The neutron and proton nature of the nucleons (123) in the final state is notationally not indicated, but also determined by the experiment.

The matrix element  $\langle s_f | M_e(E_i \mathbf{k}_f) | s_i \rangle$  of Eqs. (7.1) is calculated in close analogy with the one (7.2) for two-body electro disintegration, i.e.,

$$\langle s_f | M_e(E_i \mathbf{k}_{ef} \mathbf{p}_f \mathbf{q}_f) | s_i \rangle = \bar{u}(\mathbf{k}_{ef} s_{ef}) \gamma_\mu u(\mathbf{k}_{ei} s_{ei}) \langle \Psi_0^{(-)}(\mathbf{p}_f \mathbf{q}_f) v_{0f} | j^\mu(\mathbf{Q}, \mathbf{K}_+) | B \rangle, \quad (7.5a)$$

$$\langle s_f | M_e(E_i \mathbf{k}_{ef} \mathbf{p}_f \mathbf{q}_f) | s_i \rangle = \sum_\lambda (-1)^\lambda \bar{u}(\mathbf{k}_{ef} s_{ef}) \gamma^\lambda u(\mathbf{k}_{ei} s_{ei}) \epsilon_\nu^*(Q\lambda) \langle \Psi_0^{(-)}(\mathbf{p}_f \mathbf{q}_f) v_{0f} | j^\mu(\mathbf{Q}, \mathbf{K}_+) | B \rangle \epsilon_\mu(Q\lambda). \quad (7.5b)$$

The final-state Jacobi momenta  $\mathbf{p}_f$  and  $\mathbf{q}_f$  are determined from the final single-particle momenta  $\mathbf{k}_1$ ,  $\mathbf{k}_2$ ,  $\mathbf{k}_3$  according to Eqs. (2.1). Due to momentum conservation  $\mathbf{k}_3 = \mathbf{Q} - \mathbf{k}_1 - \mathbf{k}_2$ , thus,  $\mathbf{p}_f =$

$\frac{1}{2}(\mathbf{k}_1 - \mathbf{k}_2)$  and  $\mathbf{q}_f = (\mathbf{k}_1 + \mathbf{k}_2) - \frac{2}{3}\mathbf{Q}$ . Furthermore, energy conservation puts an additional constraint  $E_i = \mathbf{p}_f^2/m_N + 3\mathbf{q}_f^2/4m_N$ . The resulting eightfold differential cross section is

$$\frac{d^8\sigma_{i \rightarrow f}}{dk_{ef}^0 d^2\hat{\mathbf{k}}_{ef} dS d^2\hat{\mathbf{k}}_1 d^2\hat{\mathbf{k}}_2} = \frac{\sigma_{\text{Mott}}}{4k_{ef}^0 k_{ef}^0 \cos^2(\theta_e/2)} |\langle s_f | M_e(E_i; \mathbf{k}_{ef}, \mathbf{p}_f, \mathbf{q}_f) | s_i \rangle|^2 \text{fps} \quad (7.6a)$$

with the Mott cross section (7.3b) and the phase-space factor

$$\text{fps} = m_N^2 \mathbf{k}_1^2 \mathbf{k}_2^2 \left\{ \mathbf{k}_1^2 [2|\mathbf{k}_2| - \hat{\mathbf{k}}_2 \cdot (\mathbf{Q} - \mathbf{k}_1)]^2 + \mathbf{k}_2^2 [2|\mathbf{k}_1| - \hat{\mathbf{k}}_1 \cdot (\mathbf{Q} - \mathbf{k}_2)]^2 \right\}^{-1/2}. \quad (7.6b)$$

The spin averaged differential cross section is

$$\frac{\overline{d^8\sigma}}{dk_{ef}^0 d^2\hat{\mathbf{k}}_{ef} dS d^2\hat{\mathbf{k}}_1 d^2\hat{\mathbf{k}}_2} = \frac{1}{4} \sum_{s_f s_i} \frac{d^8\sigma_{i \rightarrow f}}{dk_{ef}^0 d^2\hat{\mathbf{k}}_{ef} dS d^2\hat{\mathbf{k}}_1 d^2\hat{\mathbf{k}}_2}. \quad (7.7)$$

In the figures it is denoted by  $d^8\sigma/dE_e d\Omega_e dS d\Omega_1 d\Omega_2$ , the traditional notation.

### 7.1.3 Inclusive Electron Scattering from Trinucleon Bound State

When in the final state only the energy and scattering angle of the electron are measured, the inclusive spin averaged threefold differential cross section is obtained by integration of the differential cross sections (7.4) and (7.7) over all final hadronic states. Usually it is parametrized in terms of the longitudinal and transverse inclusive response functions [75], i.e.,

$$\frac{\overline{d^3\sigma}}{dk_{ef}^0 d^2\hat{\mathbf{k}}_{ef}} = \sigma_{\text{Mott}} \left[ \left( \frac{Q^2}{Q^2} \right)^2 R_L(Q) + \left( -\frac{Q^2}{2Q^2} + \tan^2 \frac{\theta_e}{2} \right) R_T(Q) \right]. \quad (7.8)$$

The integration over all final states can be performed either explicitly or implicitly. The former option for numerical convenience uses the Jacobi momenta as integration variables instead of single-particle momenta, and the latter option uses the strategy of Sec. 6.1.4 for calculating the total cross section of photo disintegration.

The longitudinal response function  $R_L(Q)$  is determined by the longitudinal component of the spatial current and by the charge density. However, using the explicit expression for the longitudinal polarization vector  $\epsilon_\mu(Q0)$  given in Eq. (E.4) and assuming current conservation, the longitudinal component of the spatial current is usually replaced by the charge density, i.e.,

$$\langle \Psi_\alpha^{(-)}(\mathbf{q}_f) v_{\alpha_f} | j^\mu(\mathbf{Q}, \mathbf{K}_+) | B \rangle \epsilon_\mu(Q0) = (-Q^2/Q^2)^{1/2} \langle \Psi_\alpha^{(-)}(\mathbf{q}_f) v_{\alpha_f} | j^0(\mathbf{Q}, \mathbf{K}_+) | B \rangle, \quad (7.9a)$$

$$\langle \Psi_0^{(-)}(\mathbf{p}_f, \mathbf{q}_f) v_{0_f} | j^\mu(\mathbf{Q}, \mathbf{K}_+) | B \rangle \epsilon_\mu(Q0) = (-Q^2/Q^2)^{1/2} \langle \Psi_0^{(-)}(\mathbf{p}_f, \mathbf{q}_f) v_{0_f} | j^0(\mathbf{Q}, \mathbf{K}_+) | B \rangle. \quad (7.9b)$$

The longitudinal response function is then calculated from the charge density only, i.e.,

$$R_L(Q) = \frac{1}{2} \sum_{M_B} \langle B | [j^0(\mathbf{Q}, \mathbf{K}_+)]^\dagger \delta(E_i - H_0 - H_I) j^0(\mathbf{Q}, \mathbf{K}_+) | B \rangle, \quad (7.10a)$$

$$R_L(Q) = -\frac{1}{2\pi} \sum_{M_B} \text{Im} \left\{ \langle B | [j^0(\mathbf{Q}, \mathbf{K}_+)]^\dagger G(E_i + i0) j^0(\mathbf{Q}, \mathbf{K}_+) | B \rangle \right\}, \quad (7.10b)$$

$$R_L(Q) = -\frac{1}{6\pi} \sum_{M_B} \text{Im} \left\{ \langle B | [j^0(\mathbf{Q}, \mathbf{K}_+)]^\dagger (1 + P) G_0(E_i + i0) \right. \\ \left. \times [j^0(\mathbf{Q}, \mathbf{K}_+) | B \rangle + T_\alpha(E_i + i0) G_0(E_i + i0) | j^0(E_i + i0) \rangle \right\}. \quad (7.10c)$$



The transverse response function  $R_T(Q)$  is determined by the transverse components of the spatial current; it is calculated according to

$$R_T(Q) = \frac{1}{2} \sum_{M_B} \sum_{\lambda=\pm 1} \varepsilon_v^*(Q\lambda) \langle B | [j^v(\mathbf{Q}, \mathbf{K}_+)]^\dagger \delta(E_i - H_0 - H_I) j^\mu(\mathbf{Q}, \mathbf{K}_+) | B \rangle \varepsilon_\mu(Q\lambda), \quad (7.11a)$$

$$R_T(Q) = -\frac{1}{2\pi} \sum_{M_B} \sum_{\lambda=\pm 1} \text{Im} \left\{ \varepsilon_v^*(Q\lambda) \langle B | [j^v(\mathbf{Q}, \mathbf{K}_+)]^\dagger G(E_i + i0) j^\mu(\mathbf{Q}, \mathbf{K}_+) | B \rangle \varepsilon_\mu(Q\lambda) \right\}, \quad (7.11b)$$

$$R_T(Q) = -\frac{1}{6\pi} \sum_{M_B} \sum_{\lambda=\pm 1} \text{Im} \left\{ \varepsilon_v^*(Q\lambda) \langle B | [j^v(\mathbf{Q}, \mathbf{K}_+)]^\dagger (1 + P) G_0(E_i + i0) \right. \\ \left. \times [j^\mu(\mathbf{Q}, \mathbf{K}_+) | B \rangle + T_\alpha(E_i + i0) G_0(E_i + i0) | J^\mu(E_i + i0) \rangle] \varepsilon_\mu(Q\lambda) \right\}. \quad (7.11c)$$

## 7.2 Results

This section presents results for observables of two- and three-body electro disintegration of the trinucleon bound state. The results are derived from calculations based on the purely nucleonic CD-Bonn potential [3] and its coupled-channel extension constructed in Sec. 2.3. The *standard calculational procedure* is taken over from Sec. 6.2.1 for the description of photo reaction with the following necessary changes:

1. The e.m. current has to carry form factors, since the exchanged photon is virtual. The e.m. form factors of the nucleon are parametrized according to Ref. [76]; the form factors for the  $\Delta$ -isobar current are given explicitly in Appendix B.
2. The electric multipoles are calculated from the one- and two-baryon parts of the spatial current, in contrast to the photo reactions where the Siegert form is employed. Current conservation is assumed and always used for replacing the longitudinal component of the spatial current by the charge, i.e., for replacing the longitudinal multipoles by the Coulomb multipoles.
3. The number of considered current multipoles is limited by the maximal total three-baryon angular momentum  $J_{\max} = \frac{25}{2}$ , taken into account for the hadronic scattering states;  $J_{\max} = \frac{15}{2}$  used for photo reactions is not sufficient for the full convergence of the results for exclusive observables in electron scattering;  $J_{\max} = \frac{25}{2}$  is checked to be sufficient. However, some observables, not presented in the figures, show rather poor convergence with respect to the total three-baryon angular momentum, indicating the need for calculating the first term of the series (3.24a) *without* partial-wave decomposition of the final hadronic state [77].

In contrast to the hadronic and photo reactions, the electron scattering from the trinucleon bound state is not studied in all its details; I still see a number of possible extensions. However, the few examples given in this section demonstrate the potential of the developed technical apparatus. Furthermore, the  $\Delta$ -isobar effects on the calculated sample observables are also discussed.

Figure 7.2 shows results for the spin-averaged fivefold differential cross section of the two-body electro disintegration of  $^3\text{He}$  with momentum and energy transfer  $|\mathbf{Q}| = 250.2$  MeV and  $Q_0 = 113$  MeV; the agreement with the experimental data is quite satisfactory; on the scale of the experimental error bars the  $\Delta$ -isobar effects are rather insignificant.

Figure 7.3 presents results for the spin-averaged eightfold differential cross section of the three-body electro disintegration of  $^3\text{He}$  with the electron kinematics of Fig. 7.2. In the shown kinematical configurations the  $\Delta$ -isobar effects become more significant.

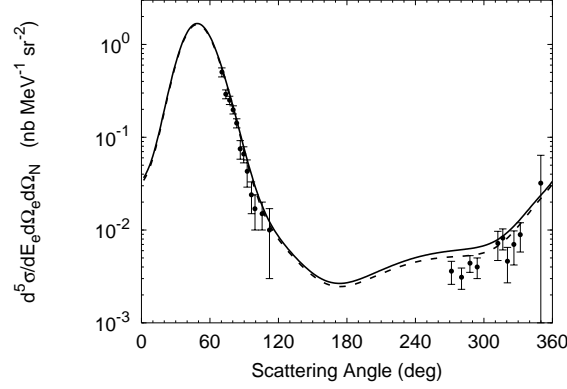


Figure 7.2: Fivefold differential cross section of two-body electro disintegration of  ${}^3\text{He}$  at 390 MeV electron lab energy as a function of the nucleon lab scattering angle with respect to the direction of the incoming electron. The electron scattering angle, the momentum and energy transfer are  $\theta_e = 39.7^\circ$ ,  $|\mathbf{Q}| = 250.2$  MeV and  $Q_0 = 113$  MeV, respectively. Results of the coupled-channel potential with  $\Delta$ -isobar excitation (solid curves) are compared with reference results of the purely nucleonic CD-Bonn potential (dashed curves). The experimental data are from Ref. [78].

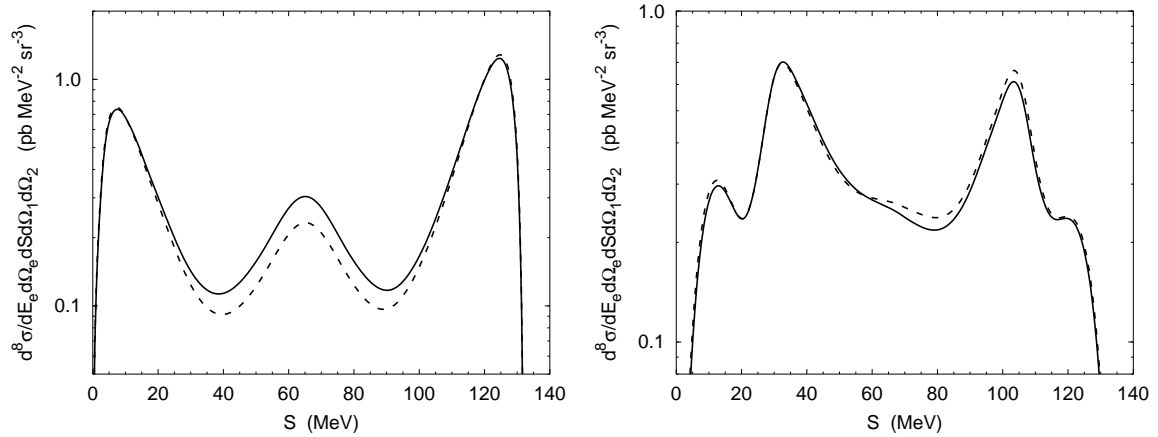


Figure 7.3: Eightfold differential cross section of three-body electro disintegration of  ${}^3\text{He}$ , i.e.,  ${}^3\text{He}(e, e' pp)n$ , at 390 MeV electron lab energy as a function of the arclength  $S$  along the kinematical curve. The electron scattering angle, the momentum and energy transfer are  $\theta_e = 39.7^\circ$ ,  $|\mathbf{Q}| = 250.2$  MeV and  $Q_0 = 113$  MeV, respectively. The observables refer to the configuration  $(30^\circ, 180^\circ, 45^\circ, 180^\circ)$  on the left side and to the configuration  $(30^\circ, 0^\circ, 120^\circ, 180^\circ)$  on the right side, the angles are given with respect to the direction of the incoming electron. Results of the coupled-channel potential with  $\Delta$ -isobar excitation (solid curves) are compared with reference results of the purely nucleonic CD-Bonn potential (dashed curves).

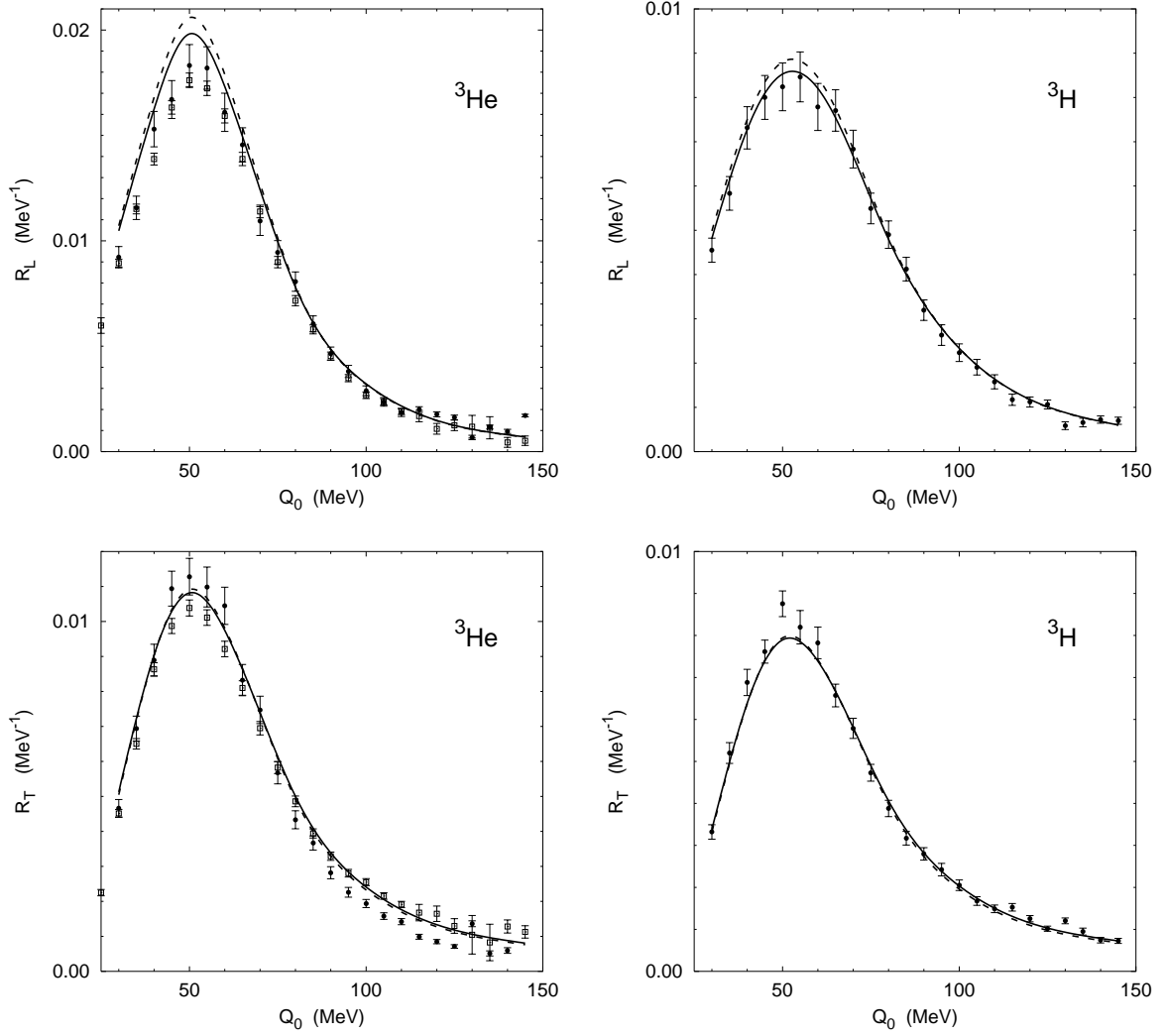


Figure 7.4:  ${}^3\text{He}$  and  ${}^3\text{H}$  inclusive longitudinal and transverse response functions  $R_L$  and  $R_T$  for the momentum transfer  $|\mathbf{Q}| = 300$  MeV as functions of the energy transfer  $Q_0$ . Results of the coupled-channel potential with  $\Delta$ -isobar excitation (solid curves) are compared with reference results of the purely nucleonic CD-Bonn potential (dashed curves). The experimental data are from Ref. [79] ( $\bullet$ ) and from Ref. [80] ( $\square$ ).

Finally, Fig. 7.4 presents sample results for inclusive longitudinal and transverse response functions of  ${}^3\text{He}$  and  ${}^3\text{H}$ . The overall agreement with the experimental data is rather good. The  $\Delta$ -isobar effects are visible around the maximum of the longitudinal response  $R_L(Q)$ ; in the transverse response  $R_T(Q)$  the  $\Delta$ -isobar effects are about 5% above  $Q_0 = 100$  MeV, but they are not discernible in Fig. 7.4.

### 7.3 Shortcomings of the Description

The theoretical shortcomings discussed in Sec. 6.3 for three-nucleon photo reactions are characteristic also for inelastic electron scattering from the trinucleon bound state. I do not repeat the study of Sec. 6.3 in full; I present only two examples.

The  $\Delta$ -isobar effects are small for the observables of Fig. 7.4. Figure 7.5 studies therefore the importance of MEC and of the existing lack of current conservation in the purely nucleonic calculations; it compares three theoretical predictions for the transverse response function  $R_T(Q)$ ; first predictions derived from the standard calculations, i.e., based on the explicit use of the one- and two-baryon current, second predictions derived from calculations using the Siegert form of the electric multipoles, and third predictions derived from calculations based on the one-nucleon current only. The effect of MEC is visible, though quantitatively it is far less important than for some photo reactions as shown in Fig. 6.11. The lack of current conservation is inconsequential for the considered observable.

Also Fig. 7.6 presents a purely nucleonic calculation. In analogy to the rather sizable relativistic effect of the one-nucleon charge in Fig. 6.13 for radiative capture, a corresponding effect is seen for the longitudinal response function  $R_L(Q)$ ; the two-nucleon charge contributes only a little also in this case.

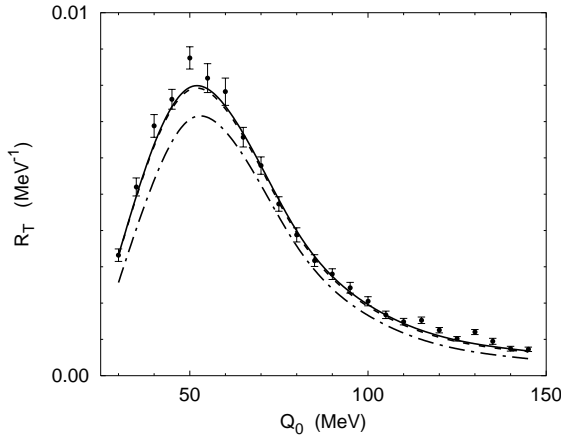


Figure 7.5:  ${}^3\text{H}$  inclusive transverse response function  $R_T$  for the momentum transfer  $|\mathbf{Q}| = 300$  MeV as function of the energy transfer  $Q_0$ . Results based on the explicit use of MEC (solid curve) are compared with results based on the Siegert form of the electric multipoles (dashed curve) and with results based on the one-baryon current only (dashed-dotted curve). Solid and dashed curves are almost indistinguishable. All results use purely nucleonic CD Bonn potential. The experimental data are from Ref. [79].

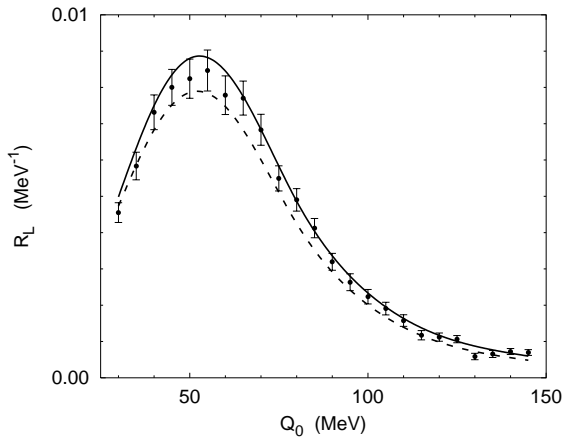


Figure 7.6:  ${}^3\text{H}$  inclusive longitudinal response function  $R_L$  for the momentum transfer  $|\mathbf{Q}| = 300$  MeV as function of the energy transfer  $Q_0$ . Results of the purely nucleonic CD Bonn potential derived from the standard approach (solid curves) are compared with results including relativistic one- and two-baryon charge corrections (dashed curve). The experimental data are from Ref. [79].

## 8

# Perturbation Theory

The calculational achievements reported in the previous chapters of this thesis are quite encouraging: The developed theoretical apparatus is based on realistic interactions; the computations are technically sound; the account of the existing experimental data is rather good. However, in one respect the given description of three-nucleon reactions is a bit disappointing: The description does not allow for an immediate physics understanding of the predictions, since the steps from the baryonic interaction, the calculational input, to the details of observables with and without polarization is clouded by highly complicated and intransparent numerics.

I admit, I am unable to change that situation of theoretical intransparency; this situation is not particular for my calculational scheme; it appears to be the fate of the physics of few-nucleon systems. However, this chapter is meant to supply a tool which may help to facilitate the physics understanding of three-nucleon reactions, at least in part and at least for particular situations. The tool is perturbation theory [81] of high calculational accuracy. Years ago, Ref. [82] developed a perturbative approach for studying properties of the three-nucleon bound state. The approach helped to understand effects arising from  $\Delta$ -isobar excitation better; it also clarified how the perturbative calculation of wave function components with a  $\Delta$  isobar and of exchange-current effects arising from the  $\Delta$  isobar should be carried out in a reliable fashion. This chapter extends and generalizes that approach to nucleon-deuteron scattering; it will be used for  $\Delta$ -isobar coupling, for charge dependence and for the interaction in the higher two-baryon partial waves. Though developed in this chapter only for nucleon-deuteron scattering, I believe the approach can also be used for the description of e.m. reactions.

### 8.1 General Formalism of Perturbation Theory

*Note:* I leave out the dependence of operators on the three-particle available energy  $Z$  and the pair subscript of the two-baryon transition matrix in the notation of this chapter, since they are not essential for the considerations and the equations become more compact by that omission.

In the following, a perturbative approach is developed which takes into account one part of the interaction exactly and the other part approximately. The two-baryon and three-baryon transition matrices are decomposed into two parts, i.e., in Eqs. (3.19)  $T$  is replaced by  $T + \Delta T$ ,  $U$  by  $U + \Delta U$  and  $U_0$  by  $U_0 + \Delta U_0$ . Here,  $U$  and  $U_0$  are defined to be exact solutions of the three-particle scattering equations (3.19) with the unperturbed part  $T$  of the two-baryon transition matrix. The remaining corrections  $\Delta U$  and  $\Delta U_0$  obey the following exact equations

$$\Delta U = PTG_0\Delta U + P\Delta TG_0(U + \Delta U), \quad (8.1a)$$

$$\Delta U_0 = (1 + P)[TG_0\Delta U + \Delta TG_0(U + \Delta U)]. \quad (8.1b)$$

The decompositions (8.1) can provide meaningful approximations, when the contribution of  $\Delta T$  to the full multi-channel transition matrices is small compared to that of  $T$ . In this case one can expect that

$\Delta U$  and  $\Delta U_0$  will be small and already their lowest-order approximations will account quite well for the required corrections to  $U$  and  $U_0$ , respectively. Equations (8.1) therefore are solved approximately by iteration, i.e.,

$$\Delta U^{(n)} = PTG_0\Delta U^{(n)} + P\Delta TG_0(U + \Delta U^{(n-1)}), \quad (8.2a)$$

$$\Delta U^{(n)} = UG_0\Delta TG_0(U + \Delta U^{(n-1)}), \quad (8.2b)$$

$$\Delta U_0^{(n)} = (1 + P)[TG_0\Delta U^{(n)} + \Delta TG_0(U + \Delta U^{(n-1)})] \quad (8.2c)$$

with  $\Delta U^{(0)} = \Delta U_0^{(0)} = 0$ . The exact solutions of Eqs. (8.1) are recovered in the limit  $\Delta U = \lim_{n \rightarrow \infty} \Delta U^{(n)}$  and  $\Delta U_0 = \lim_{n \rightarrow \infty} \Delta U_0^{(n)}$ . I admit I do not give the terms *small* and *large*, used in connection with the operators  $\Delta T$ ,  $\Delta U$  and  $\Delta U_0$ , a rigorous mathematical meaning.

Equation (8.2a) is an integral equation for  $\Delta U^{(n)}$ , analogous to that for  $U$ : Both equations have the same kernel, containing the unperturbed part  $T$  of the two-baryon transition matrix, only the driving terms being different. That integral equation should be solved, when the half-shell elements of  $\Delta U^{(n)}$  are used to compute the corresponding breakup transition matrix  $\Delta U_0^{(n)}$  according to Eq. (8.2c). If one is interested in the on-shell elements of  $\Delta U^{(n)}$  only, needed for elastic nucleon-deuteron scattering, the quadrature (8.2b) is more convenient. The numerical solution of Eqs. (8.2) uses the Chebyshev expansion of the perturbation  $\Delta T$  in the same way as the solution of the full scattering equation uses the Chebyshev expansion of the unperturbed transition matrix  $T$ . I admit, the Eqs. (8.2) are not simpler to solve than those for the corresponding exact dynamics; nevertheless, I hope the perturbative approach to enable me in future to isolate important physics mechanisms better.

The perturbative approach developed in this section will be applied in the following to particular physics cases. Always the lowest approximation order  $n$  will be used in which the studied physics effect shows up.

## 8.2 Validity of Perturbation Theory

In order to check the reliability of the developed perturbative approach I compare results for nucleon-deuteron scattering observables obtained with the technique of this chapter to the corresponding results of an exact calculation. I do so for both elastic and inelastic nucleon-deuteron scattering. The step from the calculated perturbed transition matrices  $U + \Delta U$  and  $U_0 + \Delta U_0$  to the respective observables is done without any further approximation as in the full calculations. Of course, the predominant perturbative corrections of observables are linear in  $\Delta U$  and  $\Delta U_0$ ; those linear relations are most useful for a qualitative understanding, as discussed in Sec. 8.2.2. In general, however, I choose to keep also the quadratic contributions of  $\Delta U$  and  $\Delta U_0$  to the observables; this choice turns out to improve the reliability of the perturbative approach. Though this choice appears to be somehow inconsistent with respect to the orders of perturbation, it seems to minimize a violation of the optical theorem: The optical theorem connects linear and quadratic terms of scattering amplitudes in a delicate form, and a violation of it is inherent in most perturbative approaches.

### 8.2.1 $\Delta$ -Isobar Degrees of Freedom

The effects of the  $\Delta$  isobar on observables of elastic and inelastic nucleon-deuteron scattering are studied in Chapter 5 exactly. This section investigates to what extent they can be accounted for using the perturbative approach of Sec. 8.1.

The employed two-baryon coupled-channel potential displayed in Fig. 2.3 yields a corresponding transition matrix whose components  $T_{\Delta N}$  and  $T_{N\Delta}$  couple the two Hilbert sectors in an obvious notation or act in the additional Hilbert sector  $H_\Delta$  through  $T_{\Delta\Delta}$ . But it also modifies the two-nucleon transition matrix within the purely nucleonic Hilbert sector by  $\Delta T_{NN}$  compared with  $T_{NN}$ , the two-nucleon transition matrix derived from the purely nucleonic reference potential. In the notation of Sec. 8.1 the full coupled-channel two-baryon transition matrix  $T + \Delta T$  is written as

$$T + \Delta T = T_{NN} + \Delta T_{NN} + T_{\Delta N} + T_{N\Delta} + T_{\Delta\Delta}. \quad (8.3)$$

I identify  $T_{NN}$  with the unperturbed transition matrix  $T$ , the corresponding multichannel three-nucleon transition matrices being

$$U_{NN} = P G_0^{-1} + P T_{NN} G_0 U_{NN}, \quad (8.4a)$$

$$U_{0NN} = (1 + P) G_0^{-1} + (1 + P) T_{NN} G_0 U_{NN}. \quad (8.4b)$$

The additional components of the two-baryon transition matrix  $\Delta T_{NN}$ ,  $T_{\Delta N}$ ,  $T_{N\Delta}$  and  $T_{\Delta\Delta}$  are generated by  $\Delta$ -isobar excitation and are therefore contained in  $\Delta T$ . I note that the components  $T_{\Delta N}$ ,  $T_{N\Delta}$  and  $T_{\Delta\Delta}$  are in general not small quantities in comparison with  $T_{NN}$ ; this fact is borne out in Fig. 5 of Ref. [46]; it is not surprising, since the corresponding components of the coupled-channel potential have comparable structure and are quantities of the same order of magnitude. However,  $T_{\Delta N}$  and  $T_{N\Delta}$  enter the expressions for physical amplitudes together with the free resolvent  $G_0$  in  $\Delta$ -isobar channels, which suppresses the contribution of the  $\Delta$  isobar at the considered scattering energies quite strongly, i.e., the dimensionless operators  $G_0 T_{\Delta N}$  and  $T_{N\Delta} G_0$  can be treated as small quantities in comparison with  $T_{NN} G_0$ ; on those small quantities the perturbative approach is based.  $T_{\Delta\Delta}$  shows up in the combination  $G_0 T_{\Delta\Delta} G_0$  and therefore formally contributes in higher order only. In contrast to  $T_{N\Delta}$ ,  $T_{\Delta N}$  and  $T_{\Delta\Delta}$ , the additional component  $\Delta T_{NN}$  of the coupled-channel transition matrix is small in comparison with  $T_{NN}$  according to Ref. [81].

In order to calculate the observables of elastic and inelastic nucleon-deuteron scattering in the lowest physically relevant order, only the components  $\Delta U_{NN}^{(2)}$ ,  $\Delta U_{0NN}^{(2)}$  and as an intermediate quantity  $\Delta U_{\Delta N}^{(1)}$  are needed, i.e.,

$$\Delta U_{\Delta N}^{(1)} = P T_{\Delta N} G_0 U_{NN}, \quad (8.5a)$$

$$\Delta U_{NN}^{(2)} = P T_{NN} G_0 \Delta U_{NN}^{(2)} + P \Delta T_{NN} G_0 U_{NN} + P T_{N\Delta} G_0 \Delta U_{\Delta N}^{(1)}, \quad (8.5b)$$

$$\Delta U_{NN}^{(2)} = U_{NN} G_0 (\Delta T_{NN} + T_{N\Delta} G_0 P T_{\Delta N}) G_0 U_{NN}, \quad (8.5c)$$

$$\Delta U_{0NN}^{(2)} = (1 + P) (T_{NN} G_0 \Delta U_{NN}^{(2)} + \Delta T_{NN} G_0 U_{NN} + T_{N\Delta} G_0 \Delta U_{\Delta N}^{(1)}), \quad (8.5d)$$

$$\Delta U_{0NN}^{(2)} = (1 + P) [T_{NN} G_0 \Delta U_{NN}^{(2)} + (\Delta T_{NN} + T_{N\Delta} G_0 P T_{\Delta N}) G_0 U_{NN}]. \quad (8.5e)$$

When deriving Eqs. (8.5) iteratively according to Eqs. (8.2), the term  $P \Delta T_{NN} G_0 \Delta U_{NN}^{(1)} = P \Delta T_{NN} G_0 U_{NN} G_0 \Delta T_{NN} G_0 U_{NN}$  is neglected as being of second order in the small quantity  $\Delta T_{NN}$ ; all remaining terms in Eqs. (8.5b) – (8.5e) are of first order in the corresponding small quantities; the used label  $n = 2$  is technical in the iterative spirit of Eqs. (8.2), it does not reflect the order of small quantities.

In Eqs. (8.5) one can clearly see two different  $\Delta$ -isobar effects, i.e., the two-nucleon dispersion and the effective three-nucleon force, described by the first and second terms proportional to  $\Delta T_{NN}$  and to  $T_{N\Delta} G_0 P T_{\Delta N}$  in Eq. (8.5c). The corresponding characteristic processes are shown in Figs. 2.4

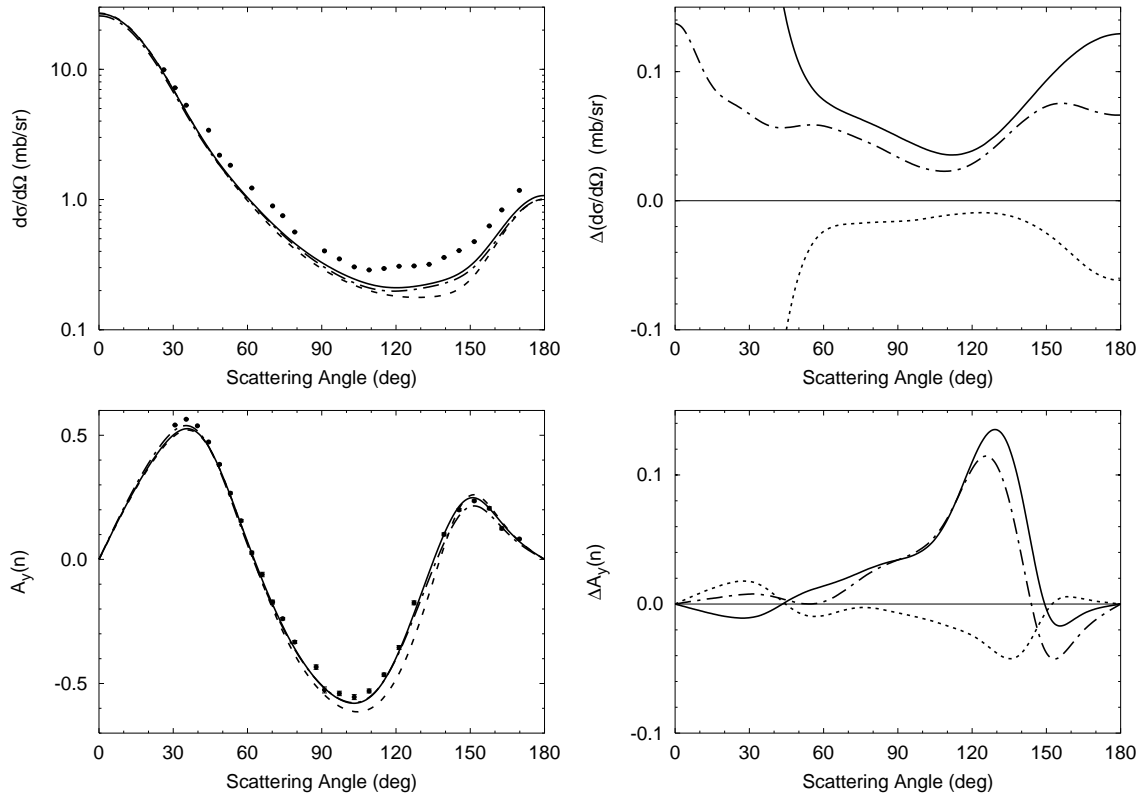


Figure 8.1: Differential cross section and nucleon analyzing power  $A_y(N)$  of elastic  $Nd$  scattering at 135 MeV nucleon lab energy as function of the c.m. scattering angle. On the left side the results of the perturbative treatment of the  $\Delta$  isobar (dash-dotted curves) are compared with results of the exact calculation with the  $\Delta$  isobar (solid curves). In order to appreciate the size of the  $\Delta$ -isobar effects to be perturbatively accounted for, the reference results of the purely nucleonic CD-Bonn potential are also given as dashed curves. On the right side the separated full two-nucleon (three-nucleon) force effects of the  $\Delta$  isobar are shown by the dotted (solid) curve around the horizontal zero line; they are obtained forming differences of the results of full calculations. They are compared to the corresponding perturbative results, calculated according to Eq. (8.5c). The perturbative two-nucleon effect almost coincides with the exact one and is not shown separately. The perturbative three-nucleon force effect is shown by dashed-dotted curves. The experimental data are from Refs. [9, 10] and refer to  $pd$  scattering.

and 2.5. Sample results are presented in Fig. 8.1; the perturbative approach reproduces the  $\Delta$ -isobar effects qualitatively rather well.

The right side of Fig. 8.1 studies the  $\Delta$ -isobar effects in more detail; it demonstrates the general competition between the  $\Delta$ -isobar effects of the two-nucleon and of the three-nucleon nature, clearly seen also in three-nucleon binding in Chapter 4. The  $\Delta$ -isobar effect of two-nucleon nature is perfectly given by perturbation theory. In contrast, the  $\Delta$ -isobar effect of three-nucleon nature is described qualitatively well, but not quantitatively accurate. This fact is right away understandable, since the coupled-channel potential CD Bonn +  $\Delta$  has a strong diagonal nucleon- $\Delta$  part which perturbation theory in the lowest order does not account for properly; for its effect, perturbation theory has to be carried to one order higher. I note that the perturbative calculations (8.5c) carried out in Ref. [81] with



less realistic coupled-channel potential CD Bonn +  $\Delta$ (sub2) which has vanishing diagonal nucleon- $\Delta$  part, yield a perfect account for the  $\Delta$ -isobar effects of the two-nucleon *and* of the three-nucleon nature.

### 8.2.2 Charge Dependence of Hadronic Interaction

The effect of charge dependence in the two-baryon interaction on observables of nucleon-deuteron scattering is calculated exactly in this thesis; it is quite small, except in special kinematic situations of breakup; this finding is consistent with other works, e.g., Ref. [7]. I therefore expect that it can be accounted for well using the perturbative approach as discussed in Sec. 8.1.

Older force models for the two-nucleon interaction assume charge independence, i.e., in the isospin-triplet partial waves  $pp$ ,  $np$  and  $nn$  potentials are taken to be the same. The three-nucleon bound state and the nucleon-deuteron scattering states, described without Coulomb interaction, only have wave function components with total isospin  $T = \frac{1}{2}$ . Charge dependence, allowed for in modern potentials as CD Bonn, changes the wave function components with total isospin  $T = \frac{1}{2}$  and develops additional components with total isospin  $T = \frac{3}{2}$ . This section tries to study those changes due to charge dependence perturbatively.

Neutron-deuteron scattering is considered. The two-baryon transition matrix  $T$  in three-particle Hilbert space has components (3.26) with respect to total isospin  $T$ , denoted by  $T_{2T'2T}$  in this section. The charge-independent starting point does not couple total isospin, i.e., the only nonvanishing components are  $T_{11}$  and  $T_{33}$ ; I assume the  $pp$  interaction to be representative for the complete isospin triplets, and therefore  $T_{11} = T_{33} = T_{pp}$ . I take the  $pp$  interaction as charge-independent reference, since most charge-independent potentials were based on a fit to  $pp$  data, the exception being the family of original Bonn potentials [83] which were tuned to  $np$  data. Of course, the actual intermediate effects of charge dependence are different when the  $np$  interaction is used as charge-independent reference.

The coupled-channel potential CD Bonn +  $\Delta$  is taken as example for a charge-dependent potential; its full charge-dependent transition matrix has the form

$$T + \Delta T = \sum_{TM_T} |TM_T\rangle T_{2T'2T} \langle TM_T| + \sum_{T'TM_T} |T'M_T\rangle \Delta T_{2T'2T} \langle TM_T|. \quad (8.6)$$

The unperturbed transition matrix  $T$  has only the diagonal components  $T_{11}$  and  $T_{33}$  with  $T_{33} = T_{11}$ , the corresponding multi-channel transition matrices being

$$U_{11} = PG_0^{-1} + PT_{11}G_0U_{11}, \quad (8.7a)$$

$$U_{011} = (1 + P)G_0^{-1} + (1 + P)T_{11}G_0U_{11}. \quad (8.7b)$$

The notation  $U_{2T'2T}$  and  $U_{02T'2T}$  makes the possible couplings of total isospin explicit. The initial nucleon-deuteron channel state has total isospin  $T = \frac{1}{2}$ ; the charge-independent interaction cannot couple to another total isospin component.

Charge dependence introduces isospin coupling into the two-baryon transition matrix as indicated by  $\Delta T_{2T'2T}$  in Eq. (8.6). The arising perturbing components have the following explicit forms

$$\Delta T_{11} = \frac{2}{3}T_{nn} + \frac{1}{3}T_{np} - T_{pp}, \quad (8.8a)$$

$$\Delta T_{31} = \frac{\sqrt{2}}{3}(T_{np} - T_{nn}), \quad (8.8b)$$

$$\Delta T_{13} = \Delta T_{31}, \quad (8.8c)$$

$$\Delta T_{33} = \frac{1}{3}T_{nn} + \frac{2}{3}T_{np} - T_{pp} \quad (8.8d)$$

for neutron-deuteron scattering. The perturbing components  $\Delta T_{2T'2T}$  can be considered to be small quantities compared with the unperturbed  $T$ . In order to calculate the observables of elastic and inelastic neutron-deuteron scattering in the lowest physically relevant order, only the components  $\Delta U_{11}^{(1)}$  for elastic scattering,  $\Delta U_{02T'1}^{(1)}$  for breakup and  $\Delta U_{31}^{(1)}$  as an intermediate quantity are needed, i.e.,

$$\Delta U_{11}^{(1)} = PT_{11}G_0\Delta U_{11}^{(1)} + P\Delta T_{11}G_0U_{11}, \quad (8.9a)$$

$$\Delta U_{11}^{(1)} = U_{11}G_0\Delta T_{11}G_0U_{11}, \quad (8.9b)$$

$$\Delta U_{31}^{(1)} = PT_{33}G_0\Delta U_{31}^{(1)} + P\Delta T_{31}G_0U_{11}, \quad (8.9c)$$

$$\Delta U_{02T'1}^{(1)} = (1+P)(T_{2T'2T'}G_0\Delta U_{2T'1}^{(1)} + \Delta T_{2T'1}G_0U_{11}). \quad (8.9d)$$

It is best to use Eq. (8.9b) for the on-shell correction  $\Delta U_{11}^{(1)}$  of elastic neutron-deuteron scattering. The on-shell breakup correction has transitions to total isospin  $T' = \frac{3}{2}$ ; the quadrature (8.9d) for that correction requires half-shell elements of the two components  $\Delta U_{2T'1}^{(1)}$ ; they are best calculated from the integral equations (8.9a) and (8.9c). The effect of charge dependence is most pronounced at low energies; there the simultaneous  $\Delta$ -isobar effects are negligible and will not be discussed in this section anymore.

Observables of elastic scattering are not documented in plots. For them the effect of charge dependence is very small, also for the sensitive neutron analyzing power  $A_y(n)$  at 10 MeV neutron lab energy. The effect of charge dependence is perfectly accounted for by perturbation theory and decreases with increasing energy. Furthermore, according to Eq. (8.9b) only total isospin  $T = \frac{1}{2}$  states contribute to corrections of elastic scattering in lowest order of perturbation theory.

Observables of breakup at 13 MeV nucleon lab energy are shown in Fig. 8.2. Even on the fine scale of the moderate effect of charge dependence the perturbative treatment of charge dependence is highly reliable. The full treatment of charge dependence is crucial for the differential cross sections in the vicinity of FSI peaks, as already pointed out in Ref. [7]. As illustrated in detail in Fig. 8.3, left side, about  $\frac{2}{3}$  of the effect of charge dependence in the  $np$  FSI peak is due to the coupling to total isospin  $T = \frac{3}{2}$ , only  $\frac{1}{3}$  due to changes in  $\Delta T_{11}$ ; the effect arises almost exclusively from the charge dependence in the  $^1S_0$  two-baryon partial wave. The effect of charge dependence in the isospin triplet  $P$  waves is negligible for the differential cross section; it contributes only to the much smaller effects in characteristic spin observables.

The ratio  $\frac{2}{3} : \frac{1}{3}$  can be explained in the following way: The  $np$  FSI should be described rather well — and, in fact, it is — using the  $np$  potential for all two-nucleon interactions without any charge dependence. Thus, when starting out with a  $pp$  potential for all, the correction  $T_{np} - T_{pp}$  has to be applied. However, allowing for charge dependence but keeping charge symmetry, Eq. (8.8a) yields  $\Delta T_{11} = \frac{1}{3}(T_{np} - T_{pp})$ ; according to Eqs. (8.9a) and (8.9d) the correction  $\Delta U_{011}^{(1)}$  is proportional to  $\Delta T_{11}$ . Thus, assuming predominant linearity in  $\Delta U_{011}^{(1)}$  for the corrections to observables, the changes in the  $T = \frac{1}{2}$  component yield only  $\frac{1}{3}$  of the full charge dependent effect; the  $T = \frac{3}{2}$  component  $\Delta U_{031}^{(1)}$  has to yield the remaining part, i.e.,  $\frac{2}{3}$ . Of course, the above consideration is valid only in the vicinity of the  $np$  FSI peak.

Depending on the assumed charge-independent reference, a model-dependent choice, the individual charge-dependent effects are of course different. If, in contrast to the strategy of this section, the  $np$  interaction is taken as charge-independent representative for all isospin-triplet components, the complete effect of charge dependence on the differential breakup cross section in the  $np$  FSI kinematics of Fig. 8.2 is almost zero; the  $np$  FSI is well described by a charge-independent reference based on

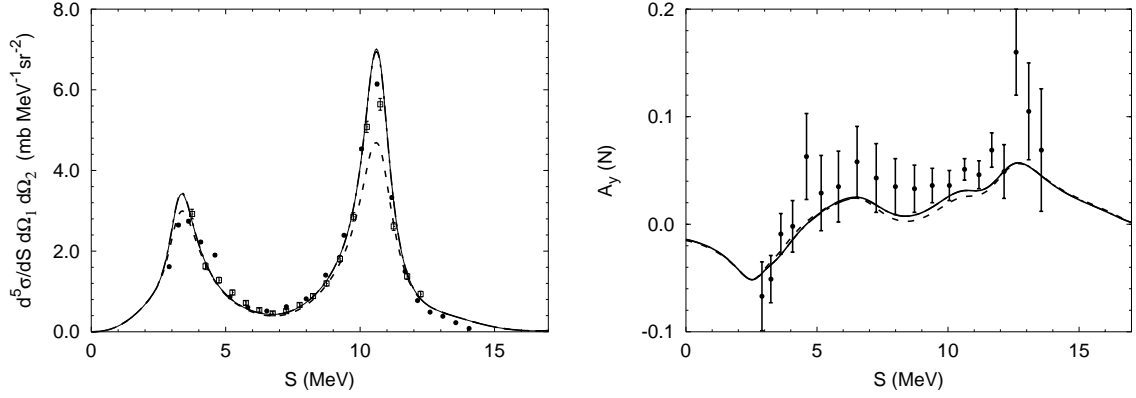


Figure 8.2: Differential cross section and nucleon analyzing power  $A_y(N)$  of  $Nd$  breakup at 13 MeV nucleon lab energy as function of the arclength  $S$  along the kinematical curve in the  $np$  FSI configuration  $(39.0^\circ, 62.5^\circ, 180.0^\circ)$ . Results of the perturbative treatment of the charge dependence (dashed-dotted curves) are compared with results of the exact treatment of charge dependence (solid curves); they are not distinguishable in both plots. In order to appreciate the size of the effect to be perturbatively accounted for, results of a calculation without charge dependence, i.e., with the  $pp$  interaction in all components of the isospin-triplet two-baryon partial waves, are also given as dashed curves. The experimental data are from Ref. [48] referring to  $nd$  scattering ( $\square$ ) and from Ref. [55] referring to  $pd$  scattering ( $\bullet$ ).

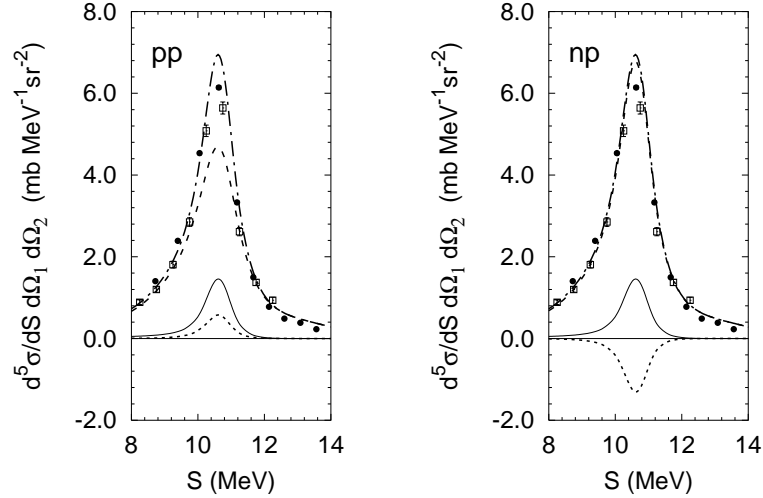


Figure 8.3: Model dependence of the charge-dependent effects on the assumed charge-independent reference. The effects on the differential cross section of  $Nd$  breakup at 13 MeV nucleon lab energy in the  $np$  FSI configuration  $(39.0^\circ, 62.5^\circ, 180.0^\circ)$ , which arise from the non-standard  $T = \frac{3}{2}$  component in the transition matrix (solid curves) and from changes in the standard  $T = \frac{1}{2}$  component (dotted curves), are shown. The left (right) figure corresponds to the  $pp$  ( $np$ ) interaction as charge-independent reference. Full results of the perturbative treatment of charge dependence (dashed-dotted curves) and results of a calculation without charge dependence (dashed curves) are also given; they almost coincide in the right figure. The experimental data are from Ref. [48] referring to  $nd$  scattering ( $\square$ ) and from Ref. [55] referring to  $pd$  scattering ( $\bullet$ ).

an  $np$  potential [7]. The effect due to the changes in the standard  $T = \frac{1}{2}$  component and the effect due to the nonstandard  $T = \frac{3}{2}$  component almost cancel each other, though being sizable individually; this fact is borne out in Fig. 8.3, right side. In fact, the theoretical explanation is the same as the reasoning in the previous paragraph for the previous charge-independent choice, however,  $\Delta T_{11} = -\frac{2}{3}(T_{np} - T_{pp})$  in contrast to Eq. (8.8a); this is why the effect due to  $\Delta U_{011}^{(1)}$  is of doubled magnitude and opposite in sign compared to that of the previous paragraph as shown in Fig. 8.3, left side. Correspondingly, in the  $nn$  FSI regions the complete effect of charge dependence is large, when the  $np$  interaction is the assumed reference; it was small before, when the  $pp$  interaction was the assumed reference [7]. Of course, irrespectively how the charge-independent reference is chosen, the full charge-dependent results are always the same; this fact can also be read off from Fig. 8.3.

### 8.2.3 Higher Two-Baryon Partial Waves

The contribution to the scattering amplitudes arising from the two-baryon interaction in higher partial waves gets increasingly small. I therefore expect that a perturbative treatment of sufficiently high partial waves is a reliable approximation.

The two-baryon interaction is split into two parts according to the total two-baryon angular momentum  $I$ : The interaction in the lower two-baryon partial waves consists of those with  $I \leq I_l$ , and the interaction in the higher two-baryon partial waves of those with  $I_l < I \leq I_h$ ,  $I_h$  being large enough to accommodate all significant dynamic aspects of the considered reaction. The additional condition  $I_l \geq 1$  guarantees that the interaction in the asymptotic nucleon-deuteron states belongs to the lower partial waves. The components of the two-baryon transition matrix in lower and higher partial waves are  $T_l$  and  $T_h$ , respectively. In the perturbative approach of Eqs. (8.2) I choose the unperturbed transition matrix  $T$  to be  $T_l$  and the perturbing part  $\Delta T$  to be  $T_h$ , i.e.,

$$T + \Delta T = T_l + T_h. \quad (8.10)$$

The solutions of the scattering equations (3.19) for the three-baryon transition matrices with the two-baryon interaction  $T_l$  in lower two-baryon partial waves only are

$$U_l = P G_0^{-1} + P T_l G_0 U_l, \quad (8.11a)$$

$$U_{0l} = (1 + P) G_0^{-1} + (1 + P) T_l G_0 U_l. \quad (8.11b)$$

The permutation operator  $P$  couples three-baryon states with lower and higher two-baryon quantum numbers  $I$ . Thus, the three-baryon transition matrices  $U_l$  and  $U_{0l}$  also have non-vanishing components with lower and higher two-baryon angular momenta  $I$ . The components of  $U_l$  in partial waves with lower  $I$  are obtained from the integral equation (8.11a), the components describing the transitions to partial waves with higher  $I$  are derived from the same equation (8.11a) by quadrature. The latter components are needed for the perturbative approach.

The perturbing part of the two-baryon transition matrix is  $T_h$ ;  $T_h$  is considered small compared to  $T_l$ . Thus, the approximations for  $\Delta U$  and  $\Delta U_0$  up to first order in  $T_h$  are

$$\Delta U^{(1)} = P T_l G_0 \Delta U^{(1)} + P T_h G_0 U_l, \quad (8.12a)$$

$$\Delta U^{(1)} = U_l G_0 T_h G_0 U_l, \quad (8.12b)$$

$$\Delta U_0^{(1)} = (1 + P)(T_l G_0 \Delta U^{(1)} + T_h G_0 U_l). \quad (8.12c)$$

With respect to observables of elastic and inelastic nucleon-deuteron scattering, it is obviously sufficient to calculate the components of  $\Delta U^{(1)}$  only between three-particle partial waves with low two-baryon angular momentum  $I$ .

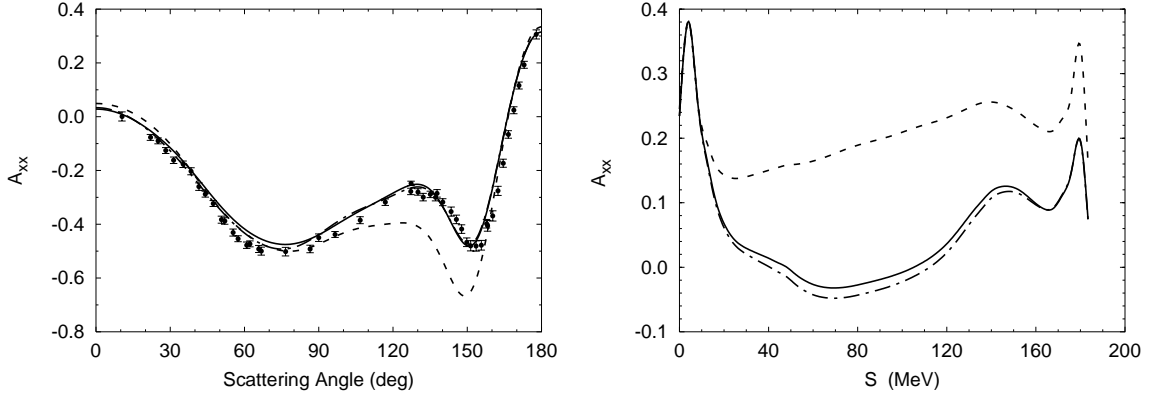


Figure 8.4: Deuteron analyzing power  $A_{xx}$  of  $Nd$  scattering at 135 MeV nucleon lab energy for elastic scattering on the left and for breakup in configuration  $(10^\circ, 10^\circ, 50^\circ)$  on the right; it is given as function of the c.m. scattering angle and of the arclength  $S$  along the kinematical curve, respectively. Results of the perturbative treatment of the two-baryon partial waves with  $3 \leq I \leq 5$  (dashed-dotted curves) are compared with results of the exact calculation including two-baryon partial waves up to  $I = 5$  (solid curves); differences are only discernible for breakup observable. In order to appreciate the size of the effect to be perturbatively accounted for, results of an exact reference calculation up to  $I = 2$  are also given as dashed curves. The experimental data are from Ref. [11] and refer to  $pd$  scattering.

I emphasize that in this section the transition matrices  $T_l$  and  $T_h$  may refer to a purely nucleonic potential or to a coupled-channel potential. Compared with Sec. 8.2.1 the perturbative treatment of the  $\Delta$  isobar is in the latter case slightly different: In Sec. 8.2.1 terms of the type  $T_{N\Delta}G_0PT_{\Delta N}$  may contain transition matrices of the higher included partial waves twice, in this section the perturbatively treated transition matrices  $T_{\Delta N}$  or  $T_{N\Delta}$  of higher partial waves are included in first order only; furthermore, also  $T_{\Delta\Delta}$  in higher partial waves contributes.

The contributions  $\Delta U$  and  $\Delta U_0$  to three-baryon transition matrices arising from the two-baryon interaction in higher partial waves increase with increasing energy. I therefore present a comparison for observables at higher energies only, i.e., at 135 MeV nucleon lab energy. The comparison is based on a nonvanishing two-baryon interaction in partial waves up to  $I = 5$ , the isospin triplet partial waves up to  $I = 4$  being coupled to the  $\Delta$  isobar. Beside the full calculation, a perturbative one is carried out, the unperturbed interaction being the coupled-channel interaction in two-baryon partial waves up to  $I_l = 2$ , the coupled-channel interaction in partial waves with  $I_l < I \leq I_h = 5$  being considered the perturbation. Selected results are compared in Fig. 8.4. The shown agreement between full and perturbative calculations is characteristic for all calculated observables; thus, the perturbative treatment of the interaction in higher two-baryon partial waves is highly reliable.

### 8.3 Use of Perturbation Theory

Though perturbation theory in lowest order cannot simulate all features of the  $\Delta$ -isobar effects of a full calculation correctly, nevertheless it appears quite useful for a qualitative understanding of reaction mechanisms mediated by the  $\Delta$  isobar. It is highly accurate for other dynamic features, i.e., charge dependence and higher partial waves. It can clearly be extended to higher orders, if need arises, and also to e.m. processes.

As an example for application of perturbation theory, the convergence of theoretical predictions with respect to the higher two-baryon partial waves is studied in Fig. 8.5 for going beyond the standard approach. Perturbatively, also partial waves up to  $I = 8$  are included. That study is done for the highest energy reaction considered in this thesis, i.e., for the elastic nucleon-deuteron scattering at 250 MeV nucleon lab energy. On the scale of accuracy required by present-day data the effect of partial waves with  $I > 5$  is small enough to be safely neglected. I found only few exceptions, e.g., the differential cross section at very small angles and the nucleon to nucleon polarization transfer coefficient  $K_y^{yy}(NN)$ . A sample result for the rapid convergence with respect to higher partial waves is given in Fig. 8.5; it is characteristic for most studied observables; the one exceptional case is also given in Fig. 8.5.

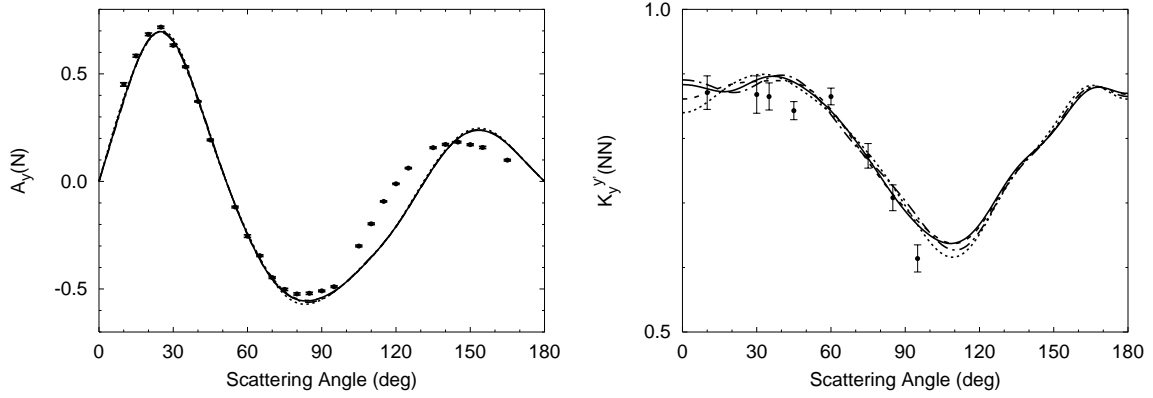


Figure 8.5: Nucleon analyzing power  $A_y(N)$  and nucleon to nucleon polarization transfer coefficient  $K_y^{yy}(NN)$  of elastic  $Nd$  scattering at 250 MeV nucleon lab energy as function of the c.m. scattering angle. Results including the interaction in partial waves up to two-baryon total angular momentum  $I = 8$  (solid curves),  $I = 7$  (dashed curves),  $I = 6$  (dashed-dotted curves), and  $I = 5$  (dotted curves) are shown; differences are only discernible for the observable  $K_y^{yy}(NN)$ . The experimental data are from Ref. [13] and refer to  $pd$  scattering.

## 9

# Conclusions

This thesis describes three-nucleon hadronic and e.m. reactions. The description allows for  $\Delta$ -isobar excitation and therefore contains an effective three-nucleon force and an effective two- and three-nucleon exchange current. Compared to previous works [16–21], the description of this thesis has a number of significant improvements.

There are *technical* improvements. They are very important for the applicability of coupled-channel dynamics, though their description in this thesis is mostly hidden in Appendix C: The ease of reading the physics evolution of this thesis should not be endangered. The technical improvements are:

- *Exact solution of three-particle equations:*

The most important technical improvement is a novel momentum-space technique for solving the three-baryon bound-state and scattering equations as described in Appendix C.1. The technique is applicable to any two-baryon potential. It is based on the expansion of the two-baryon transition matrix and of the deuteron wave function in terms of Chebyshev polynomials. The Chebyshev expansion is found to be highly efficient and reliable when used for interpolation and is found to be systematic in contrast to the separable expansion technique of Refs. [17–21].

- *Treatment of singularities:*

Other technical developments, important for the efficiency and reliability of the practical calculations as described in Appendix C.2, refer to the real-axis integration method when dealing with the singularities arising in the kernel of the three-particle scattering equations.

- *Perturbation theory:*

As a complement to the full calculations a perturbative approach for nucleon-deuteron scattering is developed in Chapter 8; it can easily be extended to the e.m. reactions. The perturbative approach may help to isolate the effects of individual reaction mechanisms present in the various observables and to facilitate the physics understanding of the three-nucleon reactions. Furthermore, in particular situations it may even be a reliable and efficient substitute for full calculations.

Due to the results of this thesis, there is an improved *physics* understanding of the few-nucleon systems. I have the following aspects of my thesis in mind:

- *Improved dynamic description:*

Whereas the results of Refs. [17–21], due to the need for a separable expansion, are derived from rather outdated potential models, the Chebyshev-expansion technique allows to use directly any two-nucleon potential and any coupled-channel extension of it as dynamic input for

the description of the three-nucleon system; the use of a well-fitted realistic potentials is important for quantitative predictions. The charge-dependent CD-Bonn potential [3] is chosen as a purely nucleonic reference in the present calculations. Furthermore, a new coupled-channel potential with single  $\Delta$ -isobar excitation [25] is developed in the present work. The new coupled-channel potential CD Bonn +  $\Delta$  is based on the exchange of  $\pi$ ,  $\rho$ ,  $\omega$  and  $\sigma$  mesons as CD Bonn. It is fitted to the two-nucleon scattering data up to 350 MeV nucleon lab energy. Since scattering energies just touch the pion-production threshold, the  $\Delta$  isobar is considered a stable baryon. The  $\chi^2$ /datum resulting from the fit of the new coupled-channel potential is with 1.02 as good as for the best new-generation purely nucleonic potentials; within the limits of the given  $\chi^2$  the potentials CD Bonn and CD Bonn +  $\Delta$  are phase equivalent. The developed new coupled-channel potential is a substantial advance, compared with the traditional construction of coupled-channel potentials with rather limited phase equivalence.

- *Included dynamic processes:*

In the three-nucleon system the  $\Delta$  isobar mediates effective two-nucleon and three-nucleon forces. The effective three-nucleon force, beside other contributions, simulates the two-pion exchange Fujita-Miyazawa force [14] of Fig. 2.5 and the three-pion ring parts in the Illinois forces [6] of Fig. 2.6 in a reducible energy-dependent form. In contrast to those irreducible three-nucleon forces based solely on  $\pi$  exchange employed by other groups [6, 52, 61] for few-nucleon systems, the effective three-nucleon force arising from the coupled-channel potential takes  $\pi$ ,  $\rho$ ,  $\omega$  and  $\sigma$  exchanges into account. The coupled-channel potential makes all contributions to the three-nucleon force *mutually consistent*.

The one-baryon and two-baryon coupled-channel current employed for the description of the e.m. processes correspond to the hadronic interaction, though full current conservation could not be achieved yet. The  $\Delta$  isobar mediates contributions to the exchange current of effective two-nucleon and three-nucleon nature; they are *structurally consistent* with the corresponding hadronic contributions.

- *$\Delta$ -isobar effects in three-nucleon bound state – beneficial or not?*

The coupled-channel potential yields additional binding, but it remains unable to account for three-nucleon binding in full. The competition between the  $\Delta$ -isobar effects of two-nucleon and three-nucleon nature, observed already long ago [16], is confirmed.

- *$\Delta$ -isobar effects in three-nucleon scattering – beneficial or not?*

With respect to three-nucleon scattering,  $\Delta$ -isobar effects are very small at low energies. The  $A_y$ -puzzle of elastic nucleon-deuteron scattering around 10 MeV nucleon lab energy cannot be resolved by the inclusion of the  $\Delta$  isobar, even if the  $\Delta$ -mediated three-nucleon force has a microscopically motivated spin-orbit contribution; according to Ref. [49] a three-nucleon force with phenomenological spin-orbit component of rather long range can resolve the  $A_y$ -puzzle. However, the considered spin-orbit contribution due to  $\Delta$ -isobar excitation is of short range, since it arises from the exchange of the  $\rho$ -meson. Also the space star anomaly in the nucleon-deuteron breakup cross section around 13 MeV nucleon lab energy cannot be resolved.

The  $\Delta$ -isobar effects become more visible at higher energies; they are often beneficial for a satisfactory description of the experimental data, e.g., they significantly reduce the discrepancies for the differential cross section and nucleon analyzing power of elastic nucleon-deuteron scattering above 100 MeV nucleon lab energy, though their success is not a general one for all measured observables.



- *$\Delta$ -isobar effects in three-nucleon photo reactions – beneficial or not?*

The  $\Delta$ -isobar effects in three-nucleon photo reactions are also more pronounced at higher energies. It is found that other theoretical ingredients neglected in conventional calculations of nuclear phenomena, e.g., the relativistic corrections of the e.m. current operator, may be even more important than the  $\Delta$ -isobar contributions. In general, quite a satisfactory description of photo reactions emerges given the scarcity of data, often still carrying large error bars.

- *$\Delta$ -isobar effects in inelastic electron scattering from trinucleon bound state – beneficial or not?*

This thesis presents only few results for the inelastic electron scattering from the trinucleon bound state; the given examples demonstrate the potential of the developed technical apparatus also for electron scattering.  $\Delta$ -isobar effects appear not very important at the considered kinematics for the few measured observables. Elastic form factors are not revisited. Moderate  $\Delta$ -isobar effects are predicted for the exclusive differential cross section in particular kinematical regimes, which are not yet measured experimentally.

- *$\Delta$ -isobar effects versus effects of irreducible three-nucleon force:*

The theoretical predictions given in Refs. [9, 11, 13, 36, 37, 52, 61, 84] use several irreducible three-nucleon forces, whose effects for some observables strongly disagree with each other. They often used outdated forces; accepted standard are now the modified Tucson-Melbourne TM' and Urbana IX forces. The  $\Delta$ -isobar effects seen in this thesis quite often agree with the effects of the latter three-nucleon forces qualitatively.

Compared to the results of Refs. [16–21] based on a coupled-channel potential with deficiencies, the  $\Delta$ -isobar effects seen in the results of this thesis based on a well-fitted coupled-channel potential are qualitatively rather similar at low energies, but there are also cases with important quantitative and even qualitative updates at higher energies.

Thus, I believe that the theoretical description of three-nucleon hadronic and e.m. reactions as given in this thesis is numerically highly reliable and physically realistic. The explicit treatment of the  $\Delta$  isobar is important for three-nucleon bound state and for three-nucleon reactions at higher energies and should remain to be included in future calculations of few-nucleon systems. However, at the end of the thesis I also see clearly what my present calculations still miss and where further improvements and developments are highly desirable.

- *Model dependence study:*

Various new-generation purely nucleonic potentials [3–5], i.e., CD Bonn, AV 18, Nijmegen I and II, differ in their predictions for three-nucleon bound state properties and for some sensitive spin observables. Coupled-channel extensions should be constructed for all of them as realistically as done in this thesis for CD Bonn in order to study the model dependence of the  $\Delta$ -isobar effects.

- *Dynamic improvements:*

An irreducible three-nucleon force should be added in order to account for those processes not contained in the effective three-nucleon force due to  $\Delta$ -isobar excitation and in order to at least cure the three-nucleon underbinding. Furthermore, the used e.m. current should be improved in order to satisfy the requirement of current conservation.

- *Inclusion of pion production:*

Though the quality of the fit of the new coupled-channel potential is gratifying, the low-energy elastic nucleon-nucleon scattering data do not form a stringent physics basis to constrain special

properties of the nucleon- $\Delta$  channel. The coupled-channel potential and the nucleonic reference potential CD Bonn therefore are both only applicable to phenomena below pion-production threshold. In future, the explicit  $\Delta$ -isobar coupling to the pion-nucleon states should be included and the fit at intermediate energies should be improved by tuning simultaneously to  $\pi$ -production data. This is a necessary step, since experimentalists move with their study of hadronic and e.m. processes far above the pion-production threshold.

- *Inclusion of Coulomb interaction:*

Experimentalists prefer to work with charged particles; the experimental data for  $npp$  system, i.e., for  $pd$  scattering and for e.m. reactions on  $^3\text{He}$  are more abundant and much more accurate than the corresponding data for the  $nnp$  system. Comparison of the  $npp$  data to theoretical predictions without the Coulomb force leaves an uncomfortable uncertainty, though the Coulomb effects are believed to be very small at higher energies, except for some special kinematical regimes. Nevertheless, the inclusion of the Coulomb force in the description of the three-nucleon continuum with two charged particles would be very welcome.

- *Extension to weak processes:*

The weak processes in the three-nucleon system, e.g., the muon ( $\mu$ ) capture by  $^3\text{He}$ , should also be studied. The developments of this thesis form a solid basis for the description of weak processes, the only missing ingredient is the axial weak current.

- *Extension to relativistic quantum mechanics:*

At intermediate energies relativistic effects become nonnegligible. First, they are clearly seen in the kinematics of the considered reactions. Second, I found that the relativistic corrections of the e.m. current operator are important for a successful description of some three-nucleon e.m. processes. However, *all* relativistic effects have to be taken into account consistently; this calls for a formulation of the three-particle equations in the framework of relativistic quantum mechanics, quite formidable undertaking.

# A

## Parameters and Special Properties of the Coupled-Channel Potential

The force parameters of the fitted coupled-channel potential are collected in this appendix. They are quoted with different accuracies. This fact is standard: The fit determines some parameters more sensitively than others. For reasons of reproducibility, the parameters are given with all digits, used in the practical calculations.

Table A.1 collects the retuned parameters of the nucleonic part of the coupled-channel potential; the retuning is done for two exchanges  $\sigma_1$  and  $\sigma_2$  and, in the  $^3P_0$  and  $^3P_1$  partial waves, also for the  $\omega$  exchange. The  $\sigma$  exchange is phenomenological; CD Bonn uses it in a partial-wave dependent form; its partial-wave dependent retuning is justified. The retuning of the  $\omega$  exchange is only minor; nevertheless, the retuned  $\sigma_1$ ,  $\sigma_2$  and  $\omega$  exchanges have more partial-wave dependence than the underlying CD-Bonn potential. The force parameters determining the potential parts connected with the  $\Delta$  isobar are given in Tables A.2 and A.3. Table A.2 contains all parameters chosen *before* the coupled-channel potential is subjected to the fit. Table A.3 contains the only fit parameter, i.e.,  $g_{\sigma NN}g_{\sigma\Delta\Delta}/4\pi$ ; it refers exclusively to  $\sigma$  meson exchange in the potential parts connected with the  $\Delta$  isobar.

$NN$	$m_{\sigma_1}$	$m_{\sigma_2}$	$\frac{g_{\sigma_1}^2(pp)}{4\pi}$	$\frac{g_{\sigma_2}^2(pp)}{4\pi}$	$\frac{g_{\sigma_1}^2(np)}{4\pi}$	$\frac{g_{\sigma_2}^2(np)}{4\pi}$	$\frac{g_{\sigma_1}^2(nn)}{4\pi}$	$\frac{g_{\sigma_2}^2(nn)}{4\pi}$	$\Lambda_\sigma$	$\frac{g_\omega^2}{4\pi}$	$\Lambda_\omega$
$^1S_0$	458	1225	1.92084	48.903	1.60887	55.844	1.93591	48.847	2000	20	1500
$^3P_0$	589		6.2318		6.1004		6.2528		1500	20	1800
$^3P_1$	376	1225	0.48685	0.0	0.50895	12.337	0.49778	2.6990	1500	22	2000
$^1D_2$	371	793	0.62970	8.8426	0.63628	8.9343	0.64134	8.8944	2500	20	1500
$^3P_2$	452	1225	2.8093	79.198	2.8354	78.622	2.8218	79.035	1600	20	1500
$^3F_2$	452	793	1.0511	51.447	1.1464	50.720	1.0755	51.406	1600	20	1500
$^3F_3$	600	793	6.9214	21.972	7.2132	21.697	7.2333	20.957	2500	20	1500
$^1G_4$	415		1.4793		1.4993		1.5019		2500	20	1500
$^3F_4$	431		2.4451		2.4544		2.4518		2500	20	1500
$^3H_4$	461		3.5415		3.5977		3.5736		2500	20	1500

Table A.1: Retuned  $\sigma_1$ ,  $\sigma_2$  and  $\omega$  parameters in the nucleonic part of the coupled-channel potential. A blank indicates that the meson contribution is not considered. Meson masses  $m_{\sigma_i}$  and cut-off parameters  $\Lambda_\sigma = \Lambda_{\sigma_1} = \Lambda_{\sigma_2}$  and  $\Lambda_\omega$  are given in MeV; they and  $g_\omega$  are chosen in a charge-independent form; the coupling constants  $g_{\sigma_i}$  are charge-dependent. The mass of the  $\omega$  meson remains with 781.94 MeV the physical one.

$\xi$	$m_\xi$	$\frac{f_{\xi NN}^2}{4\pi}$	$\frac{g_{\xi NN}^2}{4\pi}$	$\Lambda_{\xi N}$	$\frac{f_{\xi N\Delta}^2}{4\pi}$	$\frac{f_{\xi\Delta\Delta}^2}{4\pi}$	$\Lambda_{\xi\Delta}$
$\pi$	138.03	0.07348	13.6	1720	0.35	0.002939	1900
$\rho$	769.9	7.112	0.84	1310	33.786	0.2845	1500
$\omega$	781.94		20.0	1500			1500

Table A.2: Meson parameters employed in the potential parts referring to the  $\Delta$  isobar. Meson masses  $m_\xi$  and cut off parameters  $\Lambda_{\xi B}$  are given in MeV. All parameters of this table are kept fixed during the fit. The meson masses  $m_\xi$  and the other meson parameters  $f_{\xi NN}$ ,  $g_{\xi NN}$  and  $\Lambda_{\xi N}$  are taken over from CD Bonn;  $g_{\xi NN}$  and  $\Lambda_{\xi N}$  are identical to  $g_\xi$  and  $\Lambda_\xi$  of Ref. [3], whereas  $f_{\pi NN} = (m_\pi/2m_N)g_\pi$  and  $f_{\rho NN} = (m_\rho/2m_N)g_\rho(1 + \kappa_\rho)$  with  $\kappa_\rho = f_\rho/g_\rho = 6.1$  being the ratio of tensor/vector coupling constants of the  $\rho$  meson in CD Bonn. The coupling strength  $f_{\pi N\Delta}$  is taken over from Ref. [16], the others are chosen according to the quark counting rules, i.e.,  $f_{\rho N\Delta} = f_{\rho NN}f_{\pi N\Delta}/f_{\pi NN}$ ,  $f_{\xi\Delta\Delta} = \frac{1}{5}f_{\xi NN}$ , and  $g_{\xi\Delta\Delta} = g_{\xi NN}$ . The cut off parameters  $\Lambda_{\xi\Delta}$  are assumed, they are also not subjected to the fit.

$N\Delta$	$m_\sigma$	$\frac{g_{\sigma NN}^2}{4\pi}$	$\Lambda_{\sigma N}$	$\frac{g_{\sigma\Delta\Delta}^2}{4\pi}$	$\Lambda_{\sigma\Delta}$	$\frac{g_{\sigma NN}g_{\sigma\Delta\Delta}}{4\pi}$
${}^5D_0, {}^5P_3 - {}^3F_3 - {}^5F_3, {}^5D_4 - {}^5G_4, {}^3F_4 - {}^5F_4$	500	5.0	1500	5.0	1500	5.0
${}^3P_0, {}^3P_1 - {}^5P_1 - {}^5F_1, {}^3P_2 - {}^5P_2$	500	0.0	1500	0.0	1500	0.0
${}^5S_2 - {}^5D_2 - {}^5G_2$	500	8.7	1500	8.7	1500	8.7

Table A.3: Retuned  $\sigma$  exchange in the direct nucleon- $\Delta$  part of the coupled-channel potential. Note that only the quantity  $g_{\sigma NN}g_{\sigma\Delta\Delta}/4\pi$  is fitted. The mass  $m_\sigma$  and the cut off parameters  $\Lambda_{\sigma N}$  and  $\Lambda_{\sigma\Delta}$  are chosen beforehand and are kept fixed during the fit, the other columns are only shown separately for reasons of correspondence to Table A.1.

The coupled-channel potential has an inelastic channel, the nucleon- $\Delta$  channel. Thus, the potential yields inelasticities; they are not realistic, since they are not pionic. Nevertheless, for reasons of curiosity, Fig. A.1 shows the resulting  ${}^1D_2$  and  ${}^3F_3$  phase shifts and inelasticities also in the energy domain beyond the pion-production threshold not used for the fit. As expected, the produced inelasticities do not account for the inelastic data. First, due to the neglect of the coupling to pion states the inelastic threshold is wrong. Second, the  ${}^1D_2$  nucleon-nucleon channel is coupled to the  ${}^5S_2$  nucleon- $\Delta$  channel; without that coupling the nucleon- $\Delta$  potential supports a bound state; this is the reason for the sharp phase shift increase which the coupling to pion states would efficiently smear out. In contrast to  ${}^1D_2$ , the predictions for the  ${}^3F_3$  phase shifts show some realistic features qualitatively. In the energy domain of inelasticity the nucleonic CD-Bonn potential is also unrealistic.

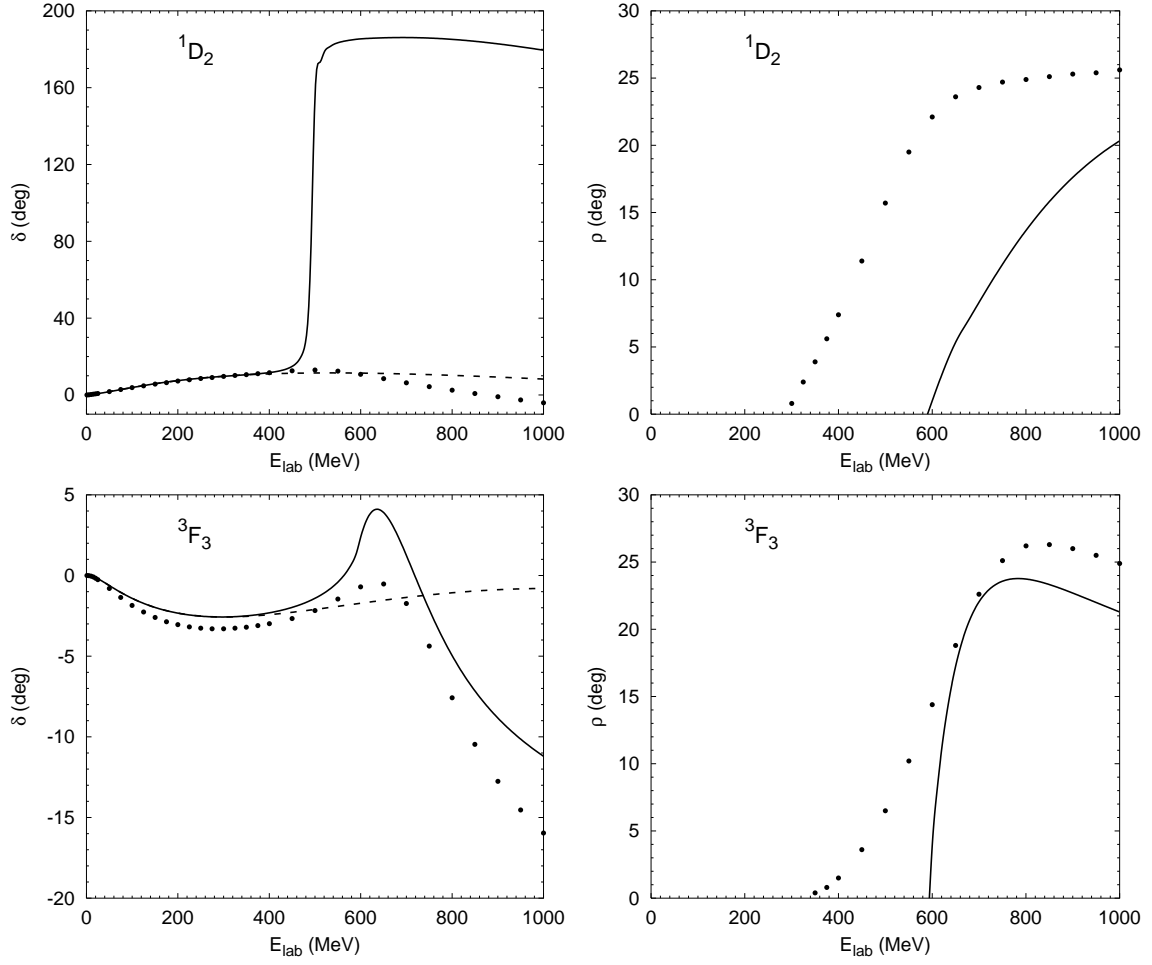


Figure A.1:  $^1D_2$  and  $^3F_3$   $np$  phase shifts  $\delta$  and inelasticities  $\rho$  as functions of nucleon lab energy. Results of the coupled-channel potential with  $\Delta$ -isobar excitation (solid curves) are compared with results of the CD-Bonn potential (dashed curves), for which the inelasticity  $\rho$  is exactly zero. The dots are the results of the partial-wave analysis of Ref. [85] without error bars. In the fit of this thesis only the phase shifts below 350 MeV nucleon lab energy are considered; the pion-production threshold is at 280 MeV.



## B

# Coupled-Channel Current Operators

Equation (2.15) defines the general momentum space form of the e.m. current  $J^\mu(\mathbf{Q}) = (\rho(\mathbf{Q}), \mathbf{J}(\mathbf{Q}))$  in the Jacobi coordinates of the three-particle basis. In contrast, this appendix gives its employed one-baryon and two-baryon parts, i.e.,  $J^\mu(\mathbf{Q}) = J^{[1]\mu}(\mathbf{Q}) + J^{[2]\mu}(\mathbf{Q})$ , in respective one-particle and two-particle bases. I keep the three-momentum transfer  $\mathbf{Q}$  and not the four-momentum transfer  $Q$  as independent variable since usually  $Q_0$  is determined by the three-momenta of the involved baryons. Despite that strategy,  $Q^2 = \mathbf{Q}^2 - Q_0^2 = -Q^2$  is used in all e.m. form factors; for photo reactions  $Q^2 = 0$ . The step from the single-particle representation of the current contributions to the three-particle Jacobi momenta is straightforward [62] and not repeated here. The objective of this appendix is the definition of the used input for the current. Since the e.m. coupling constant, i.e., the positive elementary charge  $e_p$ , is explicitly introduced in the e.m. Hamiltonians (2.11) and (2.13), the e.m. current  $J^\mu(\mathbf{Q})$  is given in units of  $e_p$ .

### B.1 One-Baryon Operators in Nonrelativistic Order

The momentum-space matrix elements of the one-baryon current operator have the general form

$$\langle \mathbf{k}' b' | J^{[1]\mu}(\mathbf{Q}) | \mathbf{k} b \rangle = \delta(\mathbf{k}' - \mathbf{Q} - \mathbf{k}) j_{b'b}^{[1]\mu}(\mathbf{Q}, \mathbf{k}', \mathbf{k}) \quad (\text{B.1})$$

with  $\mathbf{k}'$  ( $\mathbf{k}$ ) and  $\mathbf{Q}$  being the final (initial) single-baryon momentum and the three-momentum transfer by the photon, respectively, and  $b'$  ( $b$ ) being  $N$  or  $\Delta$  depending on the baryonic content of the final (initial) state. All components of  $j_{b'b}^{[1]\mu}(\mathbf{Q}, \mathbf{k}', \mathbf{k})$  are still operators in spin and isospin space; the spin (isospin) operators of the nucleon,  $\Delta$  isobar and the nucleon- $\Delta$  transition are denoted by  $\boldsymbol{\sigma}$  ( $\boldsymbol{\tau}$ ),  $\boldsymbol{\sigma}_\Delta$  ( $\boldsymbol{\tau}_\Delta$ ) and  $\mathbf{S}$  ( $\mathbf{T}$ ), respectively. The one-baryon charge density and spatial current operators, diagrammatically defined in Figs. 2.7 - 2.9 and used in the calculations of this thesis, are listed below:

$$\rho_{NN}^{[1]}(\mathbf{Q}, \mathbf{k}', \mathbf{k}) = e(Q^2), \quad (\text{B.2a})$$

$$\mathbf{j}_{NN}^{[1]}(\mathbf{Q}, \mathbf{k}', \mathbf{k}) = \frac{1}{2m_N} \{ e(Q^2)[\mathbf{k}' + \mathbf{k}] + [e(Q^2) + \kappa(Q^2)][i\boldsymbol{\sigma} \times \mathbf{Q}] \}, \quad (\text{B.2b})$$

$$\mathbf{j}_{\Delta N}^{[1]}(\mathbf{Q}, \mathbf{k}', \mathbf{k}) = \frac{1}{2m_\Delta} g_{\Delta N}^{\text{M1}}(Q^2)[i\mathbf{S} \times \mathbf{Q}]T_z, \quad (\text{B.2c})$$

$$\rho_{\Delta\Delta}^{[1]}(\mathbf{Q}, \mathbf{k}', \mathbf{k}) = g_\Delta^{\text{E0}}(Q^2), \quad (\text{B.2d})$$

$$\mathbf{j}_{\Delta\Delta}^{[1]}(\mathbf{Q}, \mathbf{k}', \mathbf{k}) = \frac{1}{2m_\Delta} \{ g_\Delta^{\text{E0}}(Q^2)[\mathbf{k}' + \mathbf{k}] + g_\Delta^{\text{M1}}(Q^2)[i\boldsymbol{\sigma}_\Delta \times \mathbf{Q}] \}. \quad (\text{B.2e})$$

The nucleonic e.m. form factors of Eqs. (B.2) are parametrized as linear combinations of the isospin-dependent Dirac and Pauli form factors  $f_1(Q^2)$  and  $f_2(Q^2)$ , which at zero four-momentum transfer  $Q^2$  are the charge and the anomalous magnetic moment of the nucleon, i.e.,

$$e(Q^2) = \frac{1}{2} [f_1^{\text{IS}}(Q^2) + f_1^{\text{IV}}(Q^2)\tau_z], \quad (\text{B.3a})$$

$$\kappa(Q^2) = \frac{1}{2} [f_2^{\text{IS}}(Q^2) + f_2^{\text{IV}}(Q^2)\tau_z], \quad (\text{B.3b})$$

the superscripts IS and IV denote their isoscalar and isovector parts, respectively. For electron scattering four-momentum transfer  $Q^2 > 0$  and the nucleonic e.m. form factors are parametrized according to Ref. [76]. The e.m. form factors related to the  $\Delta$  isobar are parameterized [16, 63, 64] by

$$g_{\Delta N}^{\text{M1}}(Q^2) = \frac{m_\Delta}{m_N} \frac{\mu_{\Delta N}}{(1 + Q^2/\Lambda_{\Delta N,1}^2)^2 (1 + Q^2/\Lambda_{\Delta N,2}^2)^{1/2}}, \quad (\text{B.4a})$$

$$g_\Delta^{\text{E0}}(Q^2) = \frac{1}{2} \{ f_1^{\text{IS}}(Q^2) + f_1^{\text{IV}}(Q^2) - Q^2/(4m_N^2) [f_2^{\text{IS}}(Q^2) + f_2^{\text{IV}}(Q^2)] \} \frac{1}{2} (1 + \tau_{\Delta z}), \quad (\text{B.4b})$$

$$g_\Delta^{\text{M1}}(Q^2) = \frac{m_\Delta}{6m_N} \frac{\mu_\Delta}{(1 + Q^2/\Lambda_\Delta^2)^2} \frac{1}{2} (1 + \tau_{\Delta z}). \quad (\text{B.4c})$$

The values of the parameters are  $\mu_{\Delta N} = 3\mu_N$ ,  $\mu_\Delta = 4.35\mu_N$ ,  $\mu_N$  being the nuclear magneton,  $\Lambda_{\Delta N,1} = \Lambda_\Delta = 0.84$  GeV and  $\Lambda_{\Delta N,2} = 1.2$  GeV.

## B.2 Two-Baryon Operators in Nonrelativistic Order

The matrix elements of the two-baryon current operator have the general form

$$\langle \mathbf{k}'_1 \mathbf{k}'_2 B' | J_\xi^{[2]\mu}(\mathbf{Q}) | \mathbf{k}_1 \mathbf{k}_2 B \rangle = \delta(\mathbf{k}'_1 + \mathbf{k}'_2 - \mathbf{Q} - \mathbf{k}_1 - \mathbf{k}_2) j_{\xi B' B}^{[2]\mu}(\mathbf{Q}, \mathbf{k}'_1 - \mathbf{k}_1, \mathbf{k}'_2 - \mathbf{k}_2) \quad (\text{B.5})$$

with  $\mathbf{k}'_i$  ( $\mathbf{k}_i$ ) being the final (initial) single-baryon momenta;  $\xi$  denotes the exchanged meson (or the two mesons in case of nondiagonal currents); the baryonic contents  $B'$  and  $B$  being  $N$  ( $\Delta$ ) correspond to the two-nucleon (nucleon- $\Delta$ -isobar) states. All components  $j_{\xi B' B}^{[2]\mu}(\mathbf{Q}, \mathbf{k}'_1 - \mathbf{k}_1, \mathbf{k}'_2 - \mathbf{k}_2)$  are still operators in spin and isospin space. The two-baryon spatial current operators, diagrammatically defined in Figs. 2.7 - 2.9, based on  $\pi$ ,  $\rho$  and  $\omega$  exchange and used in the standard calculations of this thesis, are listed below:

$$\begin{aligned} \mathbf{j}_{\pi NN}^{[2]}(\mathbf{Q}, \mathbf{p}_1, \mathbf{p}_2) = & -f_1^{\text{IV}}(Q^2) \{ [i\boldsymbol{\tau}_1 \times \boldsymbol{\tau}_2]_z F_{\pi NN}^{\text{con}}(\mathbf{p}_2^2) (\mathbf{p}_2 \cdot \boldsymbol{\sigma}_2) \boldsymbol{\sigma}_1 + (1 \leftrightarrow 2) \} \\ & + f_1^{\text{IV}}(Q^2) [i\boldsymbol{\tau}_1 \times \boldsymbol{\tau}_2]_z F_{\pi NN}^{\text{mes}}(\mathbf{p}_1^2, \mathbf{p}_2^2) (\mathbf{p}_1 \cdot \boldsymbol{\sigma}_1) (\mathbf{p}_2 \cdot \boldsymbol{\sigma}_2) (\mathbf{p}_1 - \mathbf{p}_2), \end{aligned} \quad (\text{B.6a})$$

$$\begin{aligned} \mathbf{j}_{\rho NN}^{[2]}(\mathbf{Q}, \mathbf{p}_1, \mathbf{p}_2) = & -f_1^{\text{IV}}(Q^2) \{ [i\boldsymbol{\tau}_1 \times \boldsymbol{\tau}_2]_z F_{\rho NN}^{\text{con}}(\mathbf{p}_2^2) [(\boldsymbol{\sigma}_2 \times \mathbf{p}_2) \times \boldsymbol{\sigma}_1] + (1 \leftrightarrow 2) \} \\ & + f_1^{\text{IV}}(Q^2) [i\boldsymbol{\tau}_1 \times \boldsymbol{\tau}_2]_z F_{\rho NN}^{\text{mes}}(\mathbf{p}_1^2, \mathbf{p}_2^2) [(\mathbf{p}_1 \times \boldsymbol{\sigma}_1) \cdot (\mathbf{p}_2 \times \boldsymbol{\sigma}_2)] (\mathbf{p}_1 - \mathbf{p}_2) \\ & + f_1^{\text{IV}}(Q^2) [i\boldsymbol{\tau}_1 \times \boldsymbol{\tau}_2]_z F_{\rho NN}^{\text{mes1}}(\mathbf{p}_1^2, \mathbf{p}_2^2) (\mathbf{p}_1 - \mathbf{p}_2) \\ & - f_1^{\text{IV}}(Q^2) [i\boldsymbol{\tau}_1 \times \boldsymbol{\tau}_2]_z F_{\rho NN}^{\text{mes}}(\mathbf{p}_1^2, \mathbf{p}_2^2) \mathbf{Q} \times [(\mathbf{p}_1 \times \boldsymbol{\sigma}_1) \times (\mathbf{p}_2 \times \boldsymbol{\sigma}_2)], \end{aligned} \quad (\text{B.6b})$$

$$\mathbf{j}_{\omega NN}^{[2]}(\mathbf{Q}, \mathbf{p}_1, \mathbf{p}_2) = -f_1^{\text{IS}}(Q^2) \{ (\boldsymbol{\tau}_1 \cdot \boldsymbol{\tau}_2) F_{\omega NN}^{\text{dis}}(\mathbf{p}_1^2, \mathbf{p}_2^2) (\mathbf{p}_2 \cdot \boldsymbol{\sigma}_2) [i\mathbf{p}_1 \times \mathbf{p}_2] + (1 \leftrightarrow 2) \}, \quad (\text{B.6c})$$

$$\mathbf{j}_{\omega NN}^{[2]}(\mathbf{Q}, \mathbf{p}_1, \mathbf{p}_2) = -f_1^{\text{IV}}(Q^2) \{ \tau_{2z} F_{\omega NN}^{\text{dis}}(\mathbf{p}_1^2, \mathbf{p}_2^2) (\mathbf{p}_2 \cdot \boldsymbol{\sigma}_2) [i\mathbf{p}_1 \times \mathbf{p}_2] + (1 \leftrightarrow 2) \}, \quad (\text{B.6d})$$



$$\begin{aligned} \mathbf{j}_{\pi\Delta N}^{[2]}(\mathbf{Q}, \mathbf{p}_1, \mathbf{p}_2) = & -f_1^{\text{IV}}(Q^2) \{ [i\boldsymbol{\tau}_1 \times \mathbf{T}_2]_z F_{\pi\Delta N}^{\text{con}}(\mathbf{p}_2^2) (\mathbf{p}_2 \cdot \mathbf{S}_2) \boldsymbol{\sigma}_1 + (1 \leftrightarrow 2) \} \\ & - f_1^{\text{IV}}(Q^2) \{ [i\mathbf{T}_1 \times \boldsymbol{\tau}_2]_z F_{\pi\Delta N}^{\text{con}}(\mathbf{p}_2^2) (\mathbf{p}_2 \cdot \boldsymbol{\sigma}_2) \mathbf{S}_1 + (1 \leftrightarrow 2) \} \\ & + f_1^{\text{IV}}(Q^2) \{ [i\boldsymbol{\tau}_1 \times \mathbf{T}_2]_z F_{\pi\Delta N}^{\text{mes}}(\mathbf{p}_1^2, \mathbf{p}_2^2) (\mathbf{p}_1 \cdot \boldsymbol{\sigma}_1) (\mathbf{p}_2 \cdot \mathbf{S}_2) (\mathbf{p}_1 - \mathbf{p}_2) + (1 \leftrightarrow 2) \}, \end{aligned} \quad (\text{B.7a})$$

$$\begin{aligned} \mathbf{j}_{\rho\Delta N}^{[2]}(\mathbf{Q}, \mathbf{p}_1, \mathbf{p}_2) = & -f_1^{\text{IV}}(Q^2) \{ [i\boldsymbol{\tau}_1 \times \mathbf{T}_2]_z F_{\rho\Delta N}^{\text{con}}(\mathbf{p}_2^2) [(\mathbf{S}_2 \times \mathbf{p}_2) \times \boldsymbol{\sigma}_1] + (1 \leftrightarrow 2) \} \\ & - f_1^{\text{IV}}(Q^2) \{ [i\mathbf{T}_1 \times \boldsymbol{\tau}_2]_z F_{\rho\Delta N}^{\text{con}}(\mathbf{p}_2^2) [(\boldsymbol{\sigma}_2 \times \mathbf{p}_2) \times \mathbf{S}_1] + (1 \leftrightarrow 2) \} \\ & + f_1^{\text{IV}}(Q^2) \{ [i\boldsymbol{\tau}_1 \times \mathbf{T}_2]_z F_{\rho\Delta N}^{\text{mes}}(\mathbf{p}_1^2, \mathbf{p}_2^2) [(\mathbf{p}_1 \times \boldsymbol{\sigma}_1) \cdot (\mathbf{p}_2 \times \mathbf{S}_2)] (\mathbf{p}_1 - \mathbf{p}_2) + (1 \leftrightarrow 2) \} \\ & - f_1^{\text{IV}}(Q^2) \{ [i\boldsymbol{\tau}_1 \times \mathbf{T}_2]_z F_{\rho\Delta N}^{\text{mes}}(\mathbf{p}_1^2, \mathbf{p}_2^2) \mathbf{Q} \times [(\mathbf{p}_1 \times \boldsymbol{\sigma}_1) \times (\mathbf{p}_2 \times \mathbf{S}_2)] + (1 \leftrightarrow 2) \}, \end{aligned} \quad (\text{B.7b})$$

$$\mathbf{j}_{\rho\pi\Delta N}^{[2]}(\mathbf{Q}, \mathbf{p}_1, \mathbf{p}_2) = -f_1^{\text{IS}}(Q^2) \{ (\boldsymbol{\tau}_1 \cdot \mathbf{T}_2) F_{\rho\pi\Delta N}^{\text{dis}}(\mathbf{p}_1^2, \mathbf{p}_2^2) (\mathbf{p}_2 \cdot \mathbf{S}_2) [i\mathbf{p}_1 \times \mathbf{p}_2] + (1 \leftrightarrow 2) \}, \quad (\text{B.7c})$$

$$\mathbf{j}_{\omega\pi\Delta N}^{[2]}(\mathbf{Q}, \mathbf{p}_1, \mathbf{p}_2) = -f_1^{\text{IV}}(Q^2) \{ T_{2z} F_{\omega\pi\Delta N}^{\text{dis}}(\mathbf{p}_1^2, \mathbf{p}_2^2) (\mathbf{p}_2 \cdot \mathbf{S}_2) [i\mathbf{p}_1 \times \mathbf{p}_2] + (1 \leftrightarrow 2) \}, \quad (\text{B.7d})$$

$$\begin{aligned} \mathbf{j}_{\pi\Delta\Delta}^{[2]}(\mathbf{Q}, \mathbf{p}_1, \mathbf{p}_2) = & -f_1^{\text{IV}}(Q^2) \{ [i\boldsymbol{\tau}_1 \times \boldsymbol{\tau}_{\Delta 2}]_z F_{\pi\Delta\Delta}^{\text{con, d}}(\mathbf{p}_2^2) (\mathbf{p}_2 \cdot \boldsymbol{\sigma}_{\Delta 2}) \boldsymbol{\sigma}_1 + (1 \leftrightarrow 2) \} \\ & - f_1^{\text{IV}}(Q^2) \{ [i\boldsymbol{\tau}_{\Delta 1} \times \boldsymbol{\tau}_2]_z F_{\pi\Delta\Delta}^{\text{con, d}}(\mathbf{p}_2^2) (\mathbf{p}_2 \cdot \boldsymbol{\sigma}_2) \boldsymbol{\sigma}_{\Delta 1} + (1 \leftrightarrow 2) \} \\ & + f_1^{\text{IV}}(Q^2) \{ [i\boldsymbol{\tau}_1 \times \boldsymbol{\tau}_{\Delta 2}]_z F_{\pi\Delta\Delta}^{\text{mes, d}}(\mathbf{p}_1^2, \mathbf{p}_2^2) (\mathbf{p}_1 \cdot \boldsymbol{\sigma}_1) (\mathbf{p}_2 \cdot \boldsymbol{\sigma}_{\Delta 2}) (\mathbf{p}_1 - \mathbf{p}_2) + (1 \leftrightarrow 2) \} \\ & - f_1^{\text{IV}}(Q^2) \{ [i\mathbf{T}_1^\dagger \times \mathbf{T}_2]_z F_{\pi\Delta\Delta}^{\text{con, e}}(\mathbf{p}_2^2) (\mathbf{p}_2 \cdot \mathbf{S}_2) \mathbf{S}_1^\dagger + (1 \leftrightarrow 2) \} \\ & - f_1^{\text{IV}}(Q^2) \{ [i\mathbf{T}_1 \times \mathbf{T}_2^\dagger]_z F_{\pi\Delta\Delta}^{\text{con, e}}(\mathbf{p}_2^2) (\mathbf{p}_2 \cdot \mathbf{S}_2^\dagger) \mathbf{S}_1 + (1 \leftrightarrow 2) \} \\ & + f_1^{\text{IV}}(Q^2) \{ [i\mathbf{T}_1^\dagger \times \mathbf{T}_2]_z F_{\pi\Delta\Delta}^{\text{mes, e}}(\mathbf{p}_1^2, \mathbf{p}_2^2) (\mathbf{p}_1 \cdot \mathbf{S}_1^\dagger) (\mathbf{p}_2 \cdot \mathbf{S}_2) (\mathbf{p}_1 - \mathbf{p}_2) + (1 \leftrightarrow 2) \}. \end{aligned} \quad (\text{B.8})$$

I note: The contribution to the two-nucleon  $\rho$ -exchange current, proportional to  $F_{\rho NN}^{\text{mes1}}(\mathbf{p}_1^2, \mathbf{p}_2^2)$  Eq. (B.6b) is not contained in the standard collection of exchange currents of Refs. [20, 38, 41, 62], used till now in the context of other potentials; it is necessitated in this thesis by the full form of the  $\rho$  exchange implemented in the CD-Bonn potential. Other contributions arising from the full  $\rho$  exchange [39] are of higher order compared to  $F_{\rho NN}^{\text{mes1}}(\mathbf{p}_1^2, \mathbf{p}_2^2)$  and are therefore neglected in the standard calculations; however, their effect is discussed in Sec. 6.3.3.

The  $F$  functions used in the above expressions are potential-dependent. For meson-exchange potentials they are built from meson-baryon coupling constants, hadronic form factors and meson propagators. For contact currents the  $F$ -functions have the following forms:

$$F_{\pi NN}^{\text{con}}(\mathbf{p}^2) = \frac{1}{8\pi^2 m_N^2} \frac{g_{\pi NN}^2}{4\pi} \frac{F_{\pi N}^2(\mathbf{p}^2)}{m_\pi^2 + \mathbf{p}^2}, \quad (\text{B.9a})$$

$$F_{\rho NN}^{\text{con}}(\mathbf{p}^2) = \frac{1}{8\pi^2 m_N^2} \frac{g_{\rho NN}^2 (1 + \kappa_\rho)^2}{4\pi} \frac{F_{\rho N}^2(\mathbf{p}^2)}{m_\rho^2 + \mathbf{p}^2}, \quad (\text{B.9b})$$

$$F_{\pi\Delta N}^{\text{con}}(\mathbf{p}^2) = \frac{1}{8\pi^2 m_N^2} \frac{g_{\pi NN}^2}{4\pi} \frac{f_{\pi N\Delta}}{f_{\pi NN}} \frac{F_{\pi N}(\mathbf{p}^2) F_{\pi\Delta}(\mathbf{p}^2)}{m_\pi^2 + \mathbf{p}^2}, \quad (\text{B.9c})$$

$$F_{\rho\Delta N}^{\text{con}}(\mathbf{p}^2) = \frac{1}{8\pi^2 m_N^2} \frac{g_{\rho NN}^2 (1 + \kappa_\rho)^2}{4\pi} \frac{f_{\rho N\Delta}}{f_{\rho NN}} \frac{F_{\rho N}(\mathbf{p}^2) F_{\rho\Delta}(\mathbf{p}^2)}{m_\rho^2 + \mathbf{p}^2}, \quad (\text{B.9d})$$

$$F_{\pi\Delta\Delta}^{\text{con, d}}(\mathbf{p}^2) = \frac{1}{8\pi^2 m_N^2} \frac{g_{\pi NN}^2}{4\pi} \frac{f_{\pi\Delta\Delta}}{f_{\pi NN}} \frac{F_{\pi N}(\mathbf{p}^2) F_{\pi\Delta}(\mathbf{p}^2)}{m_\pi^2 + \mathbf{p}^2}, \quad (\text{B.9e})$$

$$F_{\pi\Delta\Delta}^{\text{con, e}}(\mathbf{p}^2) = \frac{1}{8\pi^2 m_N^2} \frac{g_{\pi NN}^2}{4\pi} \frac{f_{\pi N\Delta}^2}{f_{\pi NN}^2} \frac{F_{\pi\Delta}^2(\mathbf{p}^2)}{m_\pi^2 + \mathbf{p}^2}. \quad (\text{B.9f})$$

For meson in flight currents the corresponding expressions are

$$F_{\xi B'B}^{\text{mes}}(\mathbf{p}_1^2, \mathbf{p}_2^2) = -\frac{1}{\mathbf{p}_1^2 - \mathbf{p}_2^2} [F_{\xi B'B}^{\text{con}}(\mathbf{p}_1^2) - F_{\xi B'B}^{\text{con}}(\mathbf{p}_2^2)], \quad (\text{B.10a})$$

$$F_{\rho NN}^{\text{mes1}}(\mathbf{p}_1^2, \mathbf{p}_2^2) = \frac{4m_N^2}{(1 + \kappa_\rho)^2} F_{\rho NN}^{\text{mes}}(\mathbf{p}_1^2, \mathbf{p}_2^2), \quad (\text{B.10b})$$

$$F_{\pi\Delta\Delta}^{\text{mes, d(e)}}(\mathbf{p}_1^2, \mathbf{p}_2^2) = -\frac{1}{\mathbf{p}_1^2 - \mathbf{p}_2^2} [F_{\pi\Delta\Delta}^{\text{con, d(e)}}(\mathbf{p}_1^2) - F_{\pi\Delta\Delta}^{\text{con, d(e)}}(\mathbf{p}_2^2)]. \quad (\text{B.10c})$$

Finally, the functions for nondiagonal meson-exchange currents (also called dispersion currents) are defined to be

$$F_{\xi\xi' NN}^{\text{dis}}(\mathbf{p}_1^2, \mathbf{p}_2^2) = \frac{1}{4\pi^2 m_N^2} \frac{g_{\xi NN} g_{\xi' NN}}{4\pi} \frac{m_N}{m_\xi} \frac{F_{\xi N}(\mathbf{p}_1^2) F_{\xi' N}(\mathbf{p}_2^2)}{m_\xi^2 + \mathbf{p}_1^2} \frac{1}{m_{\xi'}^2 + \mathbf{p}_2^2}, \quad (\text{B.11a})$$

$$F_{\xi\xi' \Delta N}^{\text{dis}}(\mathbf{p}_1^2, \mathbf{p}_2^2) = \frac{1}{4\pi^2 m_N^2} \frac{g_{\xi NN} g_{\xi' NN}}{4\pi} \frac{f_{\pi N\Delta}}{f_{\pi NN}} \frac{m_N}{m_\xi} \frac{F_{\xi N}(\mathbf{p}_1^2) F_{\xi' \Delta}(\mathbf{p}_2^2)}{m_\xi^2 + \mathbf{p}_1^2} \frac{1}{m_{\xi'}^2 + \mathbf{p}_2^2}. \quad (\text{B.11b})$$

All hadronic parameters are collected in Table A.2. The hadronic form factors  $F_{\xi B}(\mathbf{p}^2)$  are defined in Eq. (2.8e). The e.m. meson-photon coupling constants have the values  $g_{\rho\pi\gamma} = 0.56$  and  $g_{\omega\pi\gamma} = 0.68$  according to Ref. [86].

### B.3 Operator Corrections of Lowest Relativistic Order

Operator corrections of relativistic order are given for the charge density. They are of one-baryon and of two-baryon nature:

$$\rho_{NN}^{[1]\text{rc}}(\mathbf{Q}, \mathbf{k}', \mathbf{k}) = -\frac{e(Q^2) + 2\kappa(Q^2)}{8m_N^2} \{ \mathbf{Q}^2 + [i\boldsymbol{\sigma} \times (\mathbf{k}' + \mathbf{k})] \cdot \mathbf{Q} \}, \quad (\text{B.12a})$$

$$\rho_{\Delta N}^{[1]\text{rc}}(\mathbf{Q}, \mathbf{k}', \mathbf{k}) = -\frac{1}{4m_N m_\Delta} g_{\Delta N}^{\text{M1}}(Q^2) [i\mathbf{S} \times (\mathbf{k}' + \mathbf{k})] \cdot \mathbf{Q} T_z, \quad (\text{B.12b})$$

$$\rho_{\pi NN}^{[2]\text{rc}}(\mathbf{Q}, \mathbf{p}_1, \mathbf{p}_2) = \frac{1}{2m_N} [f_1^{\text{IS}}(Q^2) \boldsymbol{\tau}_1 \cdot \boldsymbol{\tau}_2 + f_1^{\text{IV}}(Q^2) \tau_{2z}] F_{\pi NN}^{\text{con}}(\mathbf{p}_2^2) (\boldsymbol{\sigma}_1 \cdot \mathbf{Q}) (\boldsymbol{\sigma}_2 \cdot \mathbf{p}_2) + (1 \leftrightarrow 2) \quad (\text{B.12c})$$

The contributions (B.12) are the Darwin-Foldy and spin-orbit corrections of the one-nucleon charge density, the one-baryon correction due to nucleon- $\Delta$  transition and the two-nucleon correction due to  $\pi$  exchange, respectively; the two-nucleon contribution (B.12c) is local and therefore often exclusively used; there are, however, other nonlocal two-nucleon contributions of the same order. The contributions (B.12) are used in this thesis in Sec. 6.3.3 for the Siegert form of the current. Since they are relativistic corrections, they violate current conservation in the considered order. However, the calculated trinucleon elastic charge form factors need all three contributions in order to become almost quantitatively consistent with the experimental data [41].

# C

## Numerical Solution of Three-Particle Equations

The integral equations to be solved are (3.6) for the Faddeev component  $|\Psi_\alpha\rangle$  of the bound state, (3.19a) for the multichannel transition matrix  $U(Z)$  of elastic nucleon-deuteron scattering and (3.24b) for the auxiliary state  $|J^\mu(Z)\rangle$  of e.m. reactions. In contrast to the Schrödinger equation (3.1a) and the Lippmann-Schwinger equations (3.14), they are suitable for numerical solution, since their kernels get connected after iteration and are compact for short-range potentials. In the following I concentrate on the equations (3.19a) and (3.24b). The breakup transition matrix  $U_0(Z)$  and the nuclear current matrix elements of e.m. reactions follow then by quadrature.

### C.1 Chebyshev Interpolation

References [17–19] solved the three-nucleon equations with  $\Delta$ -isobar excitation by a separable expansion of the two-baryon transition matrix; the separable expansion made the dependence on the continuous variable  $p$ , the relative pair momentum, discrete in an efficient way. Though the validity of the separable expansion was checked in Ref. [46] and was confirmed to be quite reliable in the context of the three-nucleon bound state and of low energy nucleon-deuteron scattering, the need for a separable expansion made the calculational technique of Refs. [17–19] inflexible in applications. In contrast, an alternative technique based on the Chebyshev expansion of the two-baryon transition matrix [22] and allowing to use directly any two-nucleon potential and any coupled-channel extension of it as dynamic input for the description of the three-nucleon system is proposed and used in calculations of this thesis.

I solve Eq. (3.19a) in the momentum-space partial-wave basis (2.2). The channel-states (3.8) and (3.10) are expanded into the partial-wave coupled states according to

$$|\phi_\alpha(\mathbf{q})\mathbf{v}_\alpha\rangle = \sum_{JM_J T M_T j m_j l m_l} |dq\{[I_0(l s_0)j]JM_J(T_0 t_0)T M_T b_0\}\rangle_\alpha \langle I_0 M_I j m_j | JM_J \rangle \times \langle l m_l s_0 m_s | j m_j \rangle \langle T_0 M_{T_0} t_0 m_t | T M_T \rangle Y_{m_l}^{l*}(\hat{\mathbf{q}}), \quad (\text{C.1a})$$

$$|\phi_0(\mathbf{p}\mathbf{q})\mathbf{v}_0\rangle = \sum_{JM_J T M_T} \sum_{LM_L SM_S IM_I TM_T} \sum_{l m_l j m_j} |pq[(LS)I(l s_\alpha)j]JM_J(T t_\alpha)T M_T B b\rangle_\alpha \times \langle IM_I j m_j | JM_J \rangle \langle LM_L SM_S | IM_I \rangle Y_{M_L}^{L*}(\hat{\mathbf{p}}) \langle s_\beta m_{s_\beta} s_\gamma m_{s_\gamma} | SM_S \rangle \langle l m_l s_\alpha m_{s_\alpha} | j m_j \rangle Y_{m_l}^{l*}(\hat{\mathbf{q}}) \times \langle T M_T t_\alpha m_{t_\alpha} | T M_T \rangle \langle t_\beta m_{t_\beta} t_\gamma m_{t_\gamma} | T M_T \rangle \sqrt{2} \quad (\text{C.1b})$$

with the abbreviation  $|dq\chi_d\rangle_\alpha$  for the partial-wave projected nucleon-deuteron state, i.e.,

$$|dq\chi_d\rangle_\alpha \equiv |dq\{[I_0(l s_0)j]JM_J(T_0 t_0)T M_T b_0\}\rangle_\alpha. \quad (\text{C.1c})$$

In the notation  $|dq\chi_d\rangle_\alpha$  of the coupled state the symbol  $\chi_d$  stands for the set  $(\pi_0 I_0 T_0 s_0 j t_0 b_0)$  of quantum numbers with  $\pi_0 = 1$ ; there are two (three) distinct coupled states for each set of three-particle quantum numbers  $(\Pi J M_J M_T)$  with  $J = \frac{1}{2}$  ( $J \geq \frac{3}{2}$ ); those three-particle quantum numbers are notationally suppressed in  $|dq\chi_d\rangle_\alpha$ . The factor  $\sqrt{2}$  arises in Eq. (C.1b), since the basis states  $|pqv(Ij)\rangle_\alpha$  are antisymmetrized in the pair  $(\beta\gamma)$  by  $(1 - P_{\beta\gamma})/2$ , whereas  $|\phi_0(\mathbf{p}\mathbf{q})v_0\rangle$  in Eq. (3.10) by  $(1 - P_{\beta\gamma})/\sqrt{2}$ .

According to the properties of the operators acting in the assumed Hilbert space I introduce the following abbreviations for the sets of the discrete quantum numbers. Among them, three-particle parity  $\Pi$ , total angular momentum  $J$  with projection  $M_J$  and, if charge independence of the interaction is assumed, total isospin  $T$  with projection  $M_T$ , are conserved and can be fixed for the operators once and for all; due to rotational symmetry all operators, except for the current operator  $j^\mu(\mathbf{Q}, \mathbf{K}_+)$ , are even independent of  $M_J$ , in case of charge independence even independent of  $M_T$ ; I will therefore often omit those quantum numbers  $(\Pi J M_J T M_T)$  in my explicit notation. The two-baryon transition matrix in three-baryon space  $T_\alpha(Z)$  which carries the dynamics is – due to geometric reasons – diagonal with respect to all discrete *spectator* quantum numbers, indicated in Fig. 2.2, i.e., orbital angular momentum  $l$ , spin  $s$ , total angular momentum  $j$ , isospin  $t$  and baryon character  $b$ . With respect to pair quantum numbers,  $T_\alpha(Z)$  is – due to dynamic reasons – diagonal in the pair parity  $\pi = (-)^L$ , in the total pair angular momentum  $I$  and in the total pair isospin  $T$ , but it can couple states with different pair orbital angular momentum  $L$ , spin  $S$  and baryonic content  $B$ . The abbreviation  $\eta = (LSB)$  stands for all nonconserved quantum numbers, the abbreviation  $\chi$ , i.e.,  $\chi = (\pi I T l s j t b)$ , for all conserved ones. Thus, there are three sets of discrete three-particle quantum numbers, which the notation will distinguish, i.e.,  $v(Ij) = [\eta, \chi, (\Pi J M_J T M_T)]$ . However, in contrast to the two-baryon transition matrix  $T_\alpha(Z)$  and to the free resolvent  $G_0(Z)$ , the permutation operator  $P$  couples not only the quantum numbers  $\eta$ , but also the dynamically conserved quantum numbers  $\chi$ .

If charge dependence is allowed for as in the calculations of this thesis, the two-baryon transition matrix  $T_\alpha(Z)$  couples states of total isospin  $T = \frac{1}{2}$  and  $T = \frac{3}{2}$  as described in Sec. 3.4. Thus, for the case of charge dependence the discrete three-particle quantum numbers are therefore to be split up into different sets, i.e.,  $v(Ij) = [\eta, \chi, (\Pi J M_J T M_T)]$ , compared with charge independence. The total isospin  $T$  has to be included among the nonconserved quantum numbers  $\eta = (LSBT)$ . Otherwise, the formalism to be developed remains entirely unchanged.

The solutions of the integral equations (3.19a) and (3.24b) are constructed from the corresponding Neumann series (3.22) and (3.24a) of finite order using the method of Padé approximants described in Sec. C.4. Because of the permutation operator  $P$ , at each iteration step in Eqs. (3.22) and (3.24a) interpolation is required in at least two continuous variables, depending on the used representation of  $P$ . The most convenient one is

$${}_\alpha \langle p' q' v' (I' j') | P | p q v (I j) \rangle_\alpha = \int_{-1}^{+1} dx \frac{\delta(p' - \bar{p}'(q', q, x))}{p'^{L'+2}} \frac{\delta(p - \bar{p}(q', q, x))}{p^{L+2}} G_{v'v}(q', q, x); \quad (\text{C.2})$$

the functions  $\bar{p}(q', q, x)$ ,  $\bar{p}'(q', q, x)$  and  $G_{v'v}(q', q, x)$  are given in Appendix A of Ref. [17]. Because of the  $\delta$  functions, the quantities to be interpolated in the context of Eqs. (3.22) and (3.24a) are the two-baryon transition matrix  $T_\alpha(Z)$  with respect to both the initial  $p$  and final  $p'$  relative momenta of the interacting pair and the deuteron wave function  $|dI_0 M_I T_0 M_{T_0}\rangle_\alpha$ . Traditionally, cubic spline interpolation is used. However, in this work I present an alternative and, as I think, superior interpolation technique in terms of Chebyshev polynomials. That novel interpolation technique will then yield a novel technique for solving the three-particle equations.

### C.1.1 Two-Baryon Transition Matrix and Deuteron Wave Function

The two-baryon transition matrix  $T_\alpha(Z)$  in three-particle space is calculated using the full form of the two-baryon potential  $v_\alpha$ , but for further applications  $T_\alpha(Z)$  is rewritten in an approximate Chebyshev representation, employed later on for an efficient interpolation.  $T_\alpha(Z)$  is of the general structure

$$T_\alpha(Z) = v_\alpha + v_\alpha G_0(Z) T_\alpha(Z), \quad (\text{C.3a})$$

$$T_\alpha(Z) = v_\alpha + v_\alpha G_\alpha(Z) v_\alpha, \quad (\text{C.3b})$$

$$T_\alpha(Z) = \sum_{\mathbf{v}'\mathbf{v}} \int p'^2 dp' \int q'^2 dq' \int p^2 dp \int q^2 dq \\ \times |p'q'\mathbf{v}'(I'j')\rangle_{\alpha\alpha} \langle p'q'\mathbf{v}'(I'j')| T_\alpha(Z) |pq\mathbf{v}(Ij)\rangle_{\alpha\alpha} \langle pq\mathbf{v}(Ij)|. \quad (\text{C.3c})$$

According to Eq. (C.3b) the dependence of  $T_\alpha(Z)$  on the final and initial pair momenta  $p'$  and  $p$  arises from the momentum dependence of the potential  $v_\alpha$ ; that dependence is represented in terms of Chebyshev polynomials as follows:

$$T_\alpha(Z) \approx \sum_{\mathbf{v}'\mathbf{v}} \int q^2 dq \int p'^2 dp' \int p^2 dp \\ \times |p'q'\mathbf{v}'(I'j')\rangle_{\alpha} \sum_{r',r=0}^{n_c-1} t_{L'}^{r'}(p') \delta_{\chi'\chi} T_{\eta'\eta}^{r'r}(\chi q, Z) t_L^r(p) \langle pq\mathbf{v}(Ij)|, \quad (\text{C.4a})$$

$$T_\alpha(Z) \approx \sum_{\mathbf{v}'\mathbf{v}} \int q'^2 dq' \int q^2 dq \sum_{r',r=0}^{n_c-1} |t^{r'}q'\mathbf{v}'\rangle_{\alpha} (r'q'\mathbf{v}'| \mathbf{T}_\alpha(Z) |rq\mathbf{v}\rangle_{\alpha} \langle t^r q\mathbf{v}|, \quad (\text{C.4b})$$

$$T_\alpha(Z) \approx |\mathbf{t}_\alpha\rangle \mathbf{T}_\alpha(Z) \langle \mathbf{t}_\alpha|. \quad (\text{C.4c})$$

The representation (C.4a) of the two-baryon transition matrix is only approximate, since the expansion is in a finite number  $n_c$  of polynomials. The employed momentum functions

$$t_L^r(p) = \frac{p^L}{(p^2 + a_L^2)^{L/2}} T_r(x_c(p)) \quad (\text{C.5})$$

are related to the Chebyshev polynomials  $T_r(x) = \cos(r \arccos x)$ , defined in the interval  $[-1, 1]$ .  $x_c(p) = (p^2 - a^2)/(p^2 + a^2)$  is the function which maps the interval  $[0, \infty)$  of the physical values of momentum  $p$  to the interval  $[-1, 1]$ . The form of the mapping function  $x_c(p)$  and the parameters  $a$  and  $a_L$  are chosen beforehand by experience. The properties of the Chebyshev polynomials are discussed in detail in Sec. C.1.3. The parameters  $a$  and  $a_L$  are taken to be the same for all polynomials. Separating out factors of type  $p^L/(p^2 + a_L^2)^{L/2}$  makes the remaining function, which is to be represented by Chebyshev polynomials, smoother and ensures correct asymptotic behavior of the expansion for small momenta of the interacting pair. The expansion parameters are the Chebyshev coefficients  $T_{\eta'\eta}^{r'r}(\chi q, Z)$ . They are independent of the pair label  $\alpha$ . They are calculated for  $(r', r) = 0, \dots, N-1$ ,  $N \geq n_c$  in Sec. C.1.3 from the exact matrix elements of  $T_\alpha(Z)$  at the pair momenta  $p'_k$  and  $p_k$  corresponding to all the  $N$  zeros of  $T_N(x)$ , i.e.,  $T_N(x_c(p_k)) = 0$ . The representation (C.4a) is exact for all those momenta  $p'_k$  and  $p_k$ , provided  $n_c$  is chosen as  $n_c = N$  for the number of Chebyshev polynomials [87]; in this case the representation (C.4a) is a true interpolation between the momenta  $p'_k$  and  $p_k$ . If  $n_c < N$ , the representation (C.4a) is an approximation also for the momenta  $p'_k$  and  $p_k$ ; I shall usually choose  $n_c < N$ , but nevertheless I shall call representation (C.4a) an interpolation scheme.

In Eq. (C.4b) the states

$$|t^r q\mathbf{v}\rangle_{\alpha} := \int p^2 dp |pq\mathbf{v}(Ij)\rangle_{\alpha} t_L^r(p) \quad (\text{C.6})$$

are introduced for compact notation. They arise, when interchanging the order of the summation on the Chebyshev label  $r$  and the corresponding integration on the momentum  $p$ ; that interchange has to be done with care; however, I note, that in all calculations only the components  ${}_{\alpha}\langle p'q'v'(I'j')|t^r qv\rangle_{\alpha}$  of those states together with well-behaved operators will be needed. In Eq. (C.4c) the states  $|t^r qv\rangle_{\alpha}$  are collected into the vector  $|\mathbf{t}_{\alpha}\rangle$  whose components are to be differentiated by the Chebyshev label  $r$ , by the continuous variable  $q$  and by the discrete three-particle quantum numbers  $\mathbf{v}$ . In the same spirit, a matrix-element form is introduced in Eq. (C.4b) for the Chebyshev coefficients, i.e.,

$$(r'q'v'|\mathbf{T}_{\alpha}(Z)|rqv) := \frac{\delta(q'-q)}{q^2} \delta_{\chi\chi} T_{\eta'\eta}^{r'r}(\chi q, Z). \quad (\text{C.7})$$

Those matrix elements are collected into the operator  $\mathbf{T}_{\alpha}(Z)$ . Thus, Eq. (C.4c) is a concisely abbreviated form of the two-baryon transition matrix used for developing the integral equation to be solved in practice; then, the operator dependence on the continuous variable  $q$  and on the discrete three-particle quantum numbers  $\mathbf{v}$  has to be recovered.

A similar expansion can be given for the nucleon-deuteron states  $|dq\chi_d\rangle_{\alpha}$ ; the most advantageous form is

$$G_0^{-1}(E+i0)|dq\chi_d\rangle_{\alpha} = v_{\alpha}|dq\chi_d\rangle_{\alpha}, \quad (\text{C.8a})$$

$$G_0^{-1}(E+i0)|dq\chi_d\rangle_{\alpha} = \sum_{\mathbf{v}} \int p^2 dp \int q^2 dq' |pq'v(Ij)\rangle_{\alpha\alpha} \langle pq'v(Ij)| v_{\alpha} |dq\chi_d\rangle_{\alpha} \quad (\text{C.8b})$$

with  $E = e_d + q^2/2M_{\alpha}$ . The resulting expansion corresponding to the expansion of the two-baryon transition matrix (C.4) is

$$G_0^{-1}(E+i0)|dq\chi_d\rangle_{\alpha} \approx \sum_{\mathbf{v}} \int p^2 dp |pqv(Ij)\rangle_{\alpha} \delta_{\chi\chi_d} \sum_{r=0}^{n_c-1} t_L^r(p) d_L^r, \quad (\text{C.9a})$$

$$G_0^{-1}(E+i0)|dq\chi_d\rangle_{\alpha} \approx \sum_{\mathbf{v}} \sum_{r=0}^{n_c-1} |t^r qv\rangle_{\alpha} \delta_{\chi\chi_d} d_L^r, \quad (\text{C.9b})$$

$$\left(|dq\chi_d\rangle_{\alpha}\right) \approx G_0(E+i0)|\mathbf{t}_{\alpha}\rangle \mathbf{d}. \quad (\text{C.9c})$$

The calculation of the Chebyshev coefficients  $d_L^r$  is also described in Appendix C.1.3. In Eq. (C.9c) the compact notation of Eq. (C.4c) is taken over; the round brackets on the left hand side indicate that all distinct coupled states  $|dq\chi_d\rangle_{\alpha}$  are considered together; the matrix  $\mathbf{d}$  abbreviates the  $\delta_{\chi\chi_d} d_L^r$  for all those states.

The expansion (C.9) represents the dependence of  $v_{\alpha}|dq\chi_d\rangle_{\alpha}$  on the pair momentum in the same way as the corresponding expansion of the two-baryon transition matrix  $T_{\alpha}(Z)$ . Furthermore,  $v_{\alpha}|dq\chi_d\rangle_{\alpha\alpha}\langle dq\chi_d|v_{\alpha}$  builds up the residue of  $T_{\alpha}(Z)$  at the deuteron pole; at that pole the singular factor is separated out analytically and the residue is expanded according to Eqs. (C.8) and (C.9), i.e., the Chebyshev coefficients of the two-baryon transition matrix (C.4a) at the deuteron pole are

$$T_{\eta'\eta}^{r'r}(\chi_d q, Z) = \frac{d_L^{r'} d_L^r}{Z - e_d - q^2/2M_{\alpha}}. \quad (\text{C.10})$$

### C.1.2 Three-Particle Equations

#### Three-Nucleon Continuum

Using the Chebyshev representation of the two baryon-transition matrix (C.4) both Neumann series (3.22) and (3.24a) can be written as

$$|X(E_i+i0)\rangle = \sum_{n=0}^{\infty} [G_0(E_i+i0)P|\mathbf{t}_\alpha\rangle\mathbf{T}_\alpha(E_i+i0)\langle\mathbf{t}_\alpha|]^n |X_0(E_i+i0)\rangle \quad (\text{C.11a})$$

with

$$|X(E_i+i0)\rangle = G_0(E_i+i0)U(E_i+i0)|dq_i\chi_{d_i}\rangle_\alpha, \quad (\text{C.11b})$$

$$|X_0(E_i+i0)\rangle = P|dq_i\chi_{d_i}\rangle_\alpha \quad (\text{C.11c})$$

for nucleon-deuteron scattering with the available energy  $E_i = e_d + 3q_i^2/4m_N$ , and with

$$|X(E_i+i0)\rangle = G_0(E_i+i0)|J^\mu(E_i+i0)\rangle, \quad (\text{C.11d})$$

$$|X_0(E_i+i0)\rangle = G_0(E_i+i0)(1+P)j^\mu(\mathbf{Q}, \mathbf{K}_+)|B\rangle \quad (\text{C.11e})$$

for e.m. reactions with the same available energy  $E_i$ . The dependence of  $|X(E_i+i0)\rangle$  and  $|X_0(E_i+i0)\rangle$  on the initial state parameters is suppressed in my notation. Though  $|X(E_i+i0)\rangle$  is singular, the calculation of all observables in hadronic and e.m. reactions requires it in the regular form  ${}_\alpha\langle t^i q \mathbf{v} | X(E_i+i0)\rangle$  only. Thus, the Neumann series to be calculated is for  $\langle \mathbf{t}_\alpha | X(E_i+i0)\rangle$ , i.e.,

$$\langle \mathbf{t}_\alpha | X(E_i+i0)\rangle = \sum_{n=0}^{\infty} \langle \mathbf{t}_\alpha | X_n(E_i+i0)\rangle, \quad (\text{C.12a})$$

$$\langle \mathbf{t}_\alpha | X_n(E_i+i0)\rangle = \langle \mathbf{t}_\alpha | G_0(E_i+i0)P|\mathbf{t}_\alpha\rangle\mathbf{T}_\alpha(E_i+i0)\langle \mathbf{t}_\alpha | X_{n-1}(E_i+i0)\rangle. \quad (\text{C.12b})$$

I note, that the structure of Eq. (C.12b) is formally the same as Eq. (A4) of Ref. [19]; it arises there from the separable expansion of the two-baryon transition matrix. *In fact, any discretization of the two-baryon transition matrix  $T_\alpha(Z)$ , i.e., any interpolation scheme which assumes  $T_\alpha(Z)$  to be calculated for a finite set of initial and final momenta and which then interpolates  $T_\alpha(Z)$  to any desired momenta with the help of an expansion into a set of analytic functions, can formally be treated as a separable expansion.* However, in practical calculations the difference between the separable expansion of Ref. [19] and the Chebyshev expansion of this thesis is enormous.

I now explain the technique for practically calculating the Neumann series (C.12); I make all integrations and summations, hidden in the compact form (C.12b), explicit, i.e.,

$$\begin{aligned} & {}_\alpha\langle t^{r'} q' \mathbf{v}' | X_n(E_i+i0)\rangle \\ &= \sum_{r\mathbf{v}} \sum_{r'\mathbf{v}'} \int_0^\infty q^2 dq \int_{-1}^1 dx \frac{t_{L'}^{r'}(\bar{p}'(q', q, x))}{\bar{p}^{L'}(q', q, x)} \frac{G_{\mathbf{v}'\mathbf{v}}(q', q, x)}{E_i+i0 - \delta M - \frac{q'^2}{2\mu_\alpha} - \frac{q^2}{2\mu_\alpha} - \frac{q'q}{m_\alpha}x} \frac{t_L^r(\bar{p}(q', q, x))}{\bar{p}^L(q', q, x)} \\ & \quad \times \delta_{\chi\chi'} T_{\eta\eta'}^{rr''}(\chi q, E_i+i0) {}_\alpha\langle t^{r''} q \mathbf{v}'' | X_{n-1}(E_i+i0)\rangle \end{aligned} \quad (\text{C.13})$$

for  $n \geq 1$ . The total baryon content  $B+b$  is the same in the channels  $\mathbf{v}$  and  $\mathbf{v}'$ . The integral (C.13) contains singularities. The term  $(E_i+i0 - \delta M - \frac{q'^2}{2\mu_\alpha} - \frac{q^2}{2\mu_\alpha} - \frac{q'q}{m_\alpha}x)^{-1}$ , arising from the free resolvent  $G_0(E_i+i0)$ , develops so-called *moving* singularities of kinematical origin above breakup threshold, whereas the matrix of the Chebyshev coefficients  $T_{\eta\eta'}^{rr''}(\chi q, E_i+i0)$  shows the deuteron bound state pole (C.10). The treatment of those singularities is described in Sec. C.2. The first term in the

Neumann series (C.12), i.e.,  ${}_{\alpha}\langle t^{r'} q' v' | X_0(E_i + i0) \rangle$ , is calculated according to

$$\begin{aligned} {}_{\alpha}\langle t^{r'} q' v' | X_0(E_i + i0) \rangle &\equiv {}_{\alpha}\langle t^{r'} q' v' | P | d q_i \chi_{d_i} \rangle_{\alpha} \\ &= \sum_{rv} \int_{-1}^1 dx \frac{t_L^{r'}(\bar{p}'(q', q_i, x))}{\bar{p}'^{L'}(q', q_i, x)} \frac{G_{v'v}(q', q_i, x)}{E_i - \frac{q'^2}{m_N} - \frac{q_i^2}{m_N} - \frac{q' q_i}{m_N} x} \frac{t_L^r(\bar{p}(q', q_i, x))}{\bar{p}^L(q', q_i, x)} \delta_{\chi \chi_{d_i}} d_L^r \end{aligned} \quad (C.14)$$

for nucleon-deuteron scattering and according to

$$\begin{aligned} {}_{\alpha}\langle t^{r'} q' v' | X_0(E_i + i0) \rangle &\equiv {}_{\alpha}\langle t^{r'} q' v' | G_0(E_i + i0) (1 + P) j^{\mu}(\mathbf{Q}, \mathbf{K}_+) | B \rangle \\ &= \int_0^{\infty} p'^2 dp' \frac{t_L^{r'}(p')}{E_i + i0 - \delta M' - \frac{p'^2}{2\mu_{\alpha}} - \frac{q'^2}{2M_{\alpha}}} {}_{\alpha}\langle p' q' v' (Ij) | j^{\mu}(\mathbf{Q}, \mathbf{K}_+) | B \rangle \\ &\quad + \sum_v \int_0^{\infty} q^2 dq \int_{-1}^1 dx \frac{t_L^{r'}(\bar{p}'(q', q, x))}{\bar{p}'^{L'}(q', q, x)} \frac{G_{v'v}(q', q, x)}{E_i + i0 - \delta M - \frac{q'^2}{2\mu_{\alpha}} - \frac{q^2}{2\mu_{\alpha}} - \frac{q' q}{m_{\alpha}} x} \frac{1}{\bar{p}^L(q', q, x)} \\ &\quad \times {}_{\alpha}\langle \bar{p}(q', q, x) q v (Ij) | j^{\mu}(\mathbf{Q}, \mathbf{K}_+) | B \rangle \end{aligned} \quad (C.15)$$

for e.m. processes. The integrand of Eq. (C.14) is regular, whereas the one of Eq. (C.15) contains integrable singularities; the first term of (C.15) is calculated using the standard subtraction technique, and the singularities of the second term in (C.15) are the *moving* singularities of Eq. (C.13). Matrix elements of the e.m. current  ${}_{\alpha}\langle p' q' v' (Ij) | j^{\mu}(\mathbf{Q}, \mathbf{K}_+) | B \rangle$  are calculated according to Appendix E. Equation (C.15) needs interpolation of those matrix elements in the same way as the iteration step (C.13) needs interpolation of the two-baryon transition matrix; in contrast to Eq. (C.13) I use in Eq. (C.15) the spline interpolation described in Sec. C.3. Otherwise, compared to the iteration step (C.13), Eqs. (C.14) and (C.15) in principle does not yield any new difficulties and therefore will not be discussed separately.

The iterative calculation of  ${}_{\alpha}\langle t^{r'} q' v' | X_n(E_i + i0) \rangle$  requires many matrix multiplications. Two options for this task are discussed in Ref. [22]. The *first option* which follows the strategy of Refs. [17, 19] for a separable expansion of the two-baryon transition matrix and which – after use of the separable expansion – keeps only the *one-dimensional* integration on  $q$  in Eq. (C.13), is very uneconomical in case of a substantial number of Chebyshev polynomials in the adopted interpolation scheme; that number is usually much larger than the corresponding ranks of the separable expansion in Refs. [17–19, 46]. I therefore propose a different technique, called *second option* in Ref. [22]. The integrations and summations in Eq. (C.13) are carried out, whenever they arise, starting from right to left. Though I am left with *two-dimensional* integrations, this is the natural order of matrix multiplications taking advantage of the block-diagonal structure of the quantities entering Eq. (C.13). This procedure reduces the number of required floating point operations considerably. Furthermore, the actual computer time for the new technique depends only weakly on the number of Chebyshev polynomials employed. That important logistic change constitutes the new technique of this thesis for solving the three-particle equations, compared with the technique of separable expansion used before in Refs. [17–19, 46].

Finally, the partial-wave projected matrix elements of Eqs. (3.19) needed for the calculation of the observables of elastic and inelastic nucleon-deuteron scattering follow from  ${}_{\alpha}\langle t^{r'} q v | X(E_i + i0) \rangle$  in the



forms

$$\alpha \langle dq_i \chi_{d_f} | U(E_i + i0) | dq_i \chi_{d_i} \rangle_\alpha = \sum_{r\nu} \delta_{\chi\chi_{d_f}} d_L^r \alpha \langle t^r q\nu | X(E_i + i0) \rangle, \quad (\text{C.16a})$$

$$\begin{aligned} \alpha \langle pq\nu(Ij) | T_\alpha(E_i + i0) G_0(E_i + i0) U(E_i + i0) | dq_i \chi_{d_i} \rangle_\alpha \\ = \sum_r t_L^r(p) \sum_{r'\nu'} \delta_{\chi\chi'} T_{\eta\eta'}^{rr'}(\chi q, E_i + i0) \alpha \langle t^{r'} q\nu' | X(E_i + i0) \rangle. \end{aligned} \quad (\text{C.16b})$$

The on-shell elements of the symmetrized multichannel transition matrix  $U(E_i + i0)$  between two-body channels (3.8) are obtained from the result (C.16a). The on-shell elements of the full symmetrized breakup transition matrix  $U_0(E_i + i0)$  are obtained from the result (C.16b) according to Eq. (3.19b); it is advantageous to transform the matrix elements (C.16b) first to plane-wave basis and then to apply also the permutation operator  $P$  of the part  $(1 + P)$  according to Eq. (3.19b) in that plane-wave basis.

The partial-wave projected matrix elements (3.25) needed for the calculation of the observables of e.m. reactions, i.e.,  $\alpha \langle dq_f \chi_{d_f} | J^\mu(E_i + i0) \rangle$  and  $\alpha \langle pq\nu(Ij) | T_\alpha(E_i + i0) G_0(E_i + i0) J^\mu(E_i + i0) \rangle$ , follow from  $\alpha \langle t^r q\nu | X(E_i + i0) \rangle$  in close correspondence with Eqs. (C.16).

### Three-Nucleon Bound-State

I solve the homogeneous integral equation for the Faddeev amplitude (3.6) using Lanczos method [88]. With respect to the permutation operator  $P$ , I face the same problem as for three-particle scattering, i.e., at each Lanczos-iteration step interpolation in two continuous variables is required. Again, I use the Chebyshev representation (C.4a) of the two-baryon transition matrix. This immediately implies that also the dependence of the Faddeev amplitude on the pair momentum  $p$  is represented by Chebyshev polynomials in the form

$$G_0^{-1}(E_B) |\Psi_\alpha\rangle \approx \sum_{\nu} \int q^2 dq \sum_{r=0}^{n_c-1} |t^r q\nu\rangle_\alpha (rq\nu | \Psi_\alpha\rangle. \quad (\text{C.17})$$

The homogeneous integral equation (3.6) yields directly the Chebyshev coefficients  $(rq\nu | \Psi_\alpha\rangle$  of the Faddeev amplitude, i.e.,

$$\begin{aligned} (r'q'\nu' | \Psi_\alpha\rangle = \sum_{r''\nu''} \sum_{r\nu} \int_0^\infty q^2 dq \int_{-1}^1 dx \delta_{\chi'\chi''} T_{\eta'\eta''}^{r'r''}(\chi' q', E_B) \frac{t_{L''}^{r''}(\vec{p}'(q', q, x))}{\vec{p}'^{L''}(q', q, x)} \\ \times \frac{G_{\nu''\nu}(q', q, x)}{E_B - \delta M - \frac{q'^2}{2\mu_\alpha} - \frac{q^2}{2\mu'_\alpha} - \frac{q'q}{m_\alpha}} \frac{t_L^r(\vec{p}(q', q, x))}{\vec{p}^L(q', q, x)} (rq\nu | \Psi_\alpha\rangle. \end{aligned} \quad (\text{C.18})$$

Since Eq. (C.18) has no singularities, it is far simpler than the corresponding equation (C.13) for three-particle continuum.

### C.1.3 Calculation of Chebyshev Coefficients

In this section some important properties of the Chebyshev expansion of functions are collected. More details can be found in Ref. [87].

The Chebyshev polynomial of degree  $r$  is

$$T_r(x) = \cos(r \arccos x). \quad (\text{C.19})$$

The Chebyshev polynomials are orthogonal in the interval  $[-1, 1]$  over the weight  $1/\sqrt{1-x^2}$ , i.e.,

$$\int_{-1}^1 \frac{T_r(x) T_k(x)}{\sqrt{1-x^2}} dx = \frac{\pi}{2} \delta_{rk} (1 + \delta_{r0}). \quad (\text{C.20})$$

The Gauss-Chebyshev quadrature formula

$$\int_{-1}^1 \frac{f(x)}{\sqrt{1-x^2}} dx \approx \sum_{k=1}^N w_k f(x_k), \quad (\text{C.21})$$

the abscissas  $x_k = \cos(\frac{\pi}{N}(k - \frac{1}{2}))$  being all the  $N$  zeros of  $T_N(x)$  and the weights being  $w_k = \frac{\pi}{N}$ , were exact, if the function  $f(x)$  could be expressed as a linear combination of Chebyshev polynomials up to degree  $2N - 1$ . Using Eqs. (C.20) and (C.21), it is easy to show that the Chebyshev expansion of any arbitrary function  $f(x)$ , defined in the interval  $[-1, 1]$ , i.e.,

$$f(x) \approx \sum_{r=0}^{n_c-1} c_r T_r(x) \quad (\text{C.22a})$$

with the Chebyshev coefficients

$$c_r = \frac{2}{N(1 + \delta_{r0})} \sum_{k=1}^N f(x_k) T_r(x_k), \quad (\text{C.22b})$$

is exact for all  $x$  equal to the  $N$  zeros of  $T_N(x)$ , provided  $n_c = N$ .

What is the advantage of the Chebyshev expansion (C.22) for the interpolation of the function  $f(x)$ , in comparison with interpolation schemes based on other polynomial? Suppose  $N$  is so large that the expansion (C.22a) with  $n_c = N$  is probably a perfect representation of  $f(x)$ . That representation is not necessarily more accurate than other polynomial expansions of the same order  $N$ , exact on some other set of  $N$  points. However, the truncated Chebyshev expansion (C.22a) with  $n_c = N_<$ ,  $N_<$  being considerably smaller than  $N$ , may still be sufficiently accurate, since in typical cases the coefficients  $c_r$  are rapidly decreasing. In fact, if  $f(x)$  has no singularities in the interval  $[-1, 1]$ , the convergence of the Chebyshev expansion (C.22) is *geometric*, i.e.,  $|c_r| \sim \exp(-\gamma r)$  for sufficiently large  $r$ . Singularities of  $f(x)$  in the complex plane can slow down that convergence, but they can never destroy it, as demonstrated in Ref. [87]. The difference between the Chebyshev expansions (C.22) with  $n_c = N$  and  $n_c = N_<$  can be no larger than the sum of the absolute values of all neglected Chebyshev coefficients  $\sum_{r=N_<}^{N-1} |c_r|$ , since all  $|T_r(x)| \leq 1$ . In fact, the error is dominated by  $c_{N_<} T_{N_<}(x)$ , an oscillatory function with  $N_<$  equal extrema distributed smoothly over the interval  $[-1, 1]$ . This smooth spreading out of the error is a very important property of the Chebyshev expansion (C.22): The Chebyshev expansion is close to the representation by the so-called *minimax polynomial*, which among all polynomials of the same degree has the smallest maximum deviation from the true function  $f(x)$ . That minimax polynomial is very difficult to find; the Chebyshev expansion is an efficient substitute for it.

The Chebyshev expansion (C.22) can be extended to arbitrary intervals of definition by an appropriate mapping of  $[-1, 1]$  and to functions of several variables. When mapping to infinite or semi-infinite intervals, the convergence may become *subgeometric*, i.e.,  $|c_r| \sim \exp(-\gamma r^w)$  with  $0 < w < 1$  for sufficiently large  $r$ . However, the asymptotic rate of convergence will often be academic for practical applications anyhow: The expansion (C.22) may already be sufficiently accurate for the desired accuracy of the problem even without reaching the asymptotic region.

Finally, I give the definition of the Chebyshev coefficients of the two-baryon transition matrix and of the deuteron wave function as used in the calculations of this thesis, i.e.,

$$\delta_{\chi'\chi} \frac{\delta(q' - q)}{q^2} T_{\eta'\eta}^{r'r}(\chi q, Z) = \sum_{k', k=1}^N \tilde{t}_{L'}^{r'}(p_{k'}) \alpha \langle p_{k'} q' v' (I' j') | T_\alpha(Z) | p_k q v (I j) \rangle_\alpha \tilde{t}_L^r(p_k), \quad (\text{C.23a})$$

$$d_L^r = \sum_{k=1}^N \tilde{t}_L^r(p_k) \langle p_k (LS) I_0 M_I T_0 M_{T_0} B | v_\alpha | d I_0 M_I T_0 M_{T_0} \rangle. \quad (\text{C.23b})$$

Here, the relative pair momenta  $p_k$  and  $p_{k'}$  correspond to all the  $N$  zeros of  $T_N(x)$ , i.e.,  $T_N(x_c(p_k)) = T_N(x_c(p_{k'})) = 0$ . The functions  $\tilde{t}_L^r(p_k)$  are defined to be

$$\tilde{t}_L^r(p_k) = \frac{2}{N(1 + \delta_{r0})} \frac{(p_k^2 + a_L^2)^{L/2}}{p_k^L} T_r(x_c(p_k)); \quad (\text{C.23c})$$

they are related to the  $t_L^r(p)$  of Eq. (C.5) used in the Chebyshev expansions (C.4) and (C.9). Examples for the convergence and accuracy of the Chebyshev expansion are given in Figs. 5.1 and 5.2.

## C.2 Treatment of Singularities

This section deals with the singularities of the kernel of the three-particle scattering equations, i.e., with the singularities in the integral (C.13). Since the matrix structure of Eq. (C.13) is already discussed in detail in Sec. C.1.2, for the clarity of explanations I adopt a compact notation which explicitly indicates only the dependence on the continuous variables, e.g., all matrix elements  $\alpha \langle t^{r'} q' v' | X_n(E_i + i0) \rangle$  of Eq. (C.13) are abbreviated by the matrix  $\mathbf{X}(q')$ . According to the singularity structure I split the integral (C.13) into four contributions, i.e.,

$$\mathbf{X}(q') = \mathbf{X}_{\text{sg}}(q') + \mathbf{X}_d(q') + \mathbf{X}_{\bar{d}}(q') + \mathbf{X}_\Delta(q'), \quad (\text{C.24})$$

being differentiated by the integration domain and by some of the three-baryon discrete quantum numbers contained in the set  $\mathbf{v}$  which is summed over.

- The contribution

$$\mathbf{X}_{\text{sg}}(q') = \int_0^{q_{\text{sg}}} q^2 dq \int_{-1}^1 dx \frac{\mathbf{F}_{\text{sg}}(q', q, x)}{m_N E_i + i0 - q'^2 - q^2 - q' q x} \quad (\text{C.25})$$

corresponds to *all* purely nucleonic channels  $\mathbf{v}$  with  $B + b = \frac{3}{2}$ . The term  $(m_N E_i + i0 - q'^2 - q^2 - q' q x)^{-1}$ , arising from the free resolvent  $G_0(E_i + i0)$ , develops so-called *moving* singularities of kinematical origin above breakup threshold for momenta  $q', q \leq q_{\text{sg}} = \sqrt{4m_N E_i/3}$ ; all remaining factors are abbreviated by the regular matrix  $\mathbf{F}_{\text{sg}}(q', q, x)$  which can be read off from the Eq. (C.13). For  $q' \geq q_{\text{sg}}$  the integrand is regular and the integral (C.25) can be calculated numerically using the standard technique; I use Gauss-Legendre integration [89, 90]. Note that the integration  $[q_{\text{sg}}, \infty)$  is contained in the contributions  $\mathbf{X}_d(q')$  and  $\mathbf{X}_{\bar{d}}(q')$ .

- The matrix of the Chebyshev coefficients  $T_{\eta\eta''}^{rr'}(\chi q, E_i + i0)$  in nucleon-deuteron channels  $\nu$  with  $\chi \in \{\chi_d\}$  shows the deuteron bound-state pole of Eq. (C.10) at  $q = q_i = \sqrt{4m_N(E_i - e_d)/3} > q_{sg}$ . The contribution of those channels is

$$\mathbf{X}_d(q') = \int_{q_{sg}}^{\infty} q^2 dq \int_{-1}^1 dx \frac{\mathbf{F}_d(q', q, x)}{q_i^2 + i0 - q^2}; \quad (\text{C.26})$$

again, the regular matrix  $\mathbf{F}_d(q', q, x)$  can be read off from Eqs. (C.10) and (C.13). Thus, it is convenient to split the  $q$  integration with the domain  $[0, \infty)$  in Eq. (C.13) in two intervals  $[0, q_{sg}]$  and  $[q_{sg}, \infty)$ , in order to separate the arising singularities of two different types.

- The term  $\mathbf{X}_{\bar{d}}(q')$  corresponds to the contribution of the remaining purely nucleonic channels, i.e., those with  $\chi \notin \{\chi_d\}$ , in the interval  $[q_{sg}, \infty)$ ; that integral contains no singularities and is calculated numerically using the standard Gauss-Legendre integration.
- In the considered energy regime the integrand of Eq. (C.13) has no singularities in the nucleon- $\Delta$  channels  $\nu$  with  $B + b = \frac{1}{2}$ . Thus, the corresponding contribution  $\mathbf{X}_{\Delta}(q')$  is also calculated numerically using the standard Gauss-Legendre integration.

The following subsections describe calculation of the integrals (C.25) and (C.26) containing integrable singularities.

### C.2.1 Deuteron Bound-State Pole

Integral (C.26) is the simpler case. The  $x$  integration in Eq. (C.26) involves no singularities and can be carried out resulting

$$\mathbf{F}_d(q', q) = \int_{-1}^1 dx \mathbf{F}_d(q', q, x). \quad (\text{C.27})$$

Using the identity

$$\frac{1}{x + i0} = P \frac{1}{x} - i\pi\delta(x) \quad (\text{C.28})$$

and the subtraction technique for the principal part singularity, the  $q$  integration is regularized as follows, i.e.,

$$\mathbf{X}_d(q') = \int_{q_{sg}}^{\infty} dq \frac{q^2 \mathbf{F}_d(q', q) - q_i^2 \mathbf{F}_d(q', q_i)}{q_i^2 - q^2} - \left( i\pi + \ln \frac{q_i + q_{sg}}{q_i - q_{sg}} \right) \frac{q_i}{2} \mathbf{F}_d(q', q_i). \quad (\text{C.29})$$

The integrand is now regular; thus, the principal-part singularity symbol  $P$  is not required anymore and the integral (C.29) can be calculated numerically using standard Gauss-Legendre integration.

### C.2.2 Kinematical Singularities

First I consider the integral (C.25) for one special case, i.e., for  $q' = 0$ . In that case the singularity in the  $x$  integration disappear and the singularity in the  $q$  integration is a simple pole at  $q = q_0 = \sqrt{3/4} q_{sg}$ . That pole can be treated in a similar way as the deuteron bound state pole, resulting

$$\mathbf{X}_{sg}(0) = \int_0^{q_{sg}} dq \frac{q^2 \mathbf{F}_{sg}(0, q) - q_0^2 \mathbf{F}_{sg}(0, q_0)}{q_0^2 - q^2} - \left( i\pi - \ln \frac{q_0 + q_{sg}}{q_{sg} - q_0} \right) \frac{q_0}{2} \mathbf{F}_{sg}(0, q_0) \quad (\text{C.30a})$$

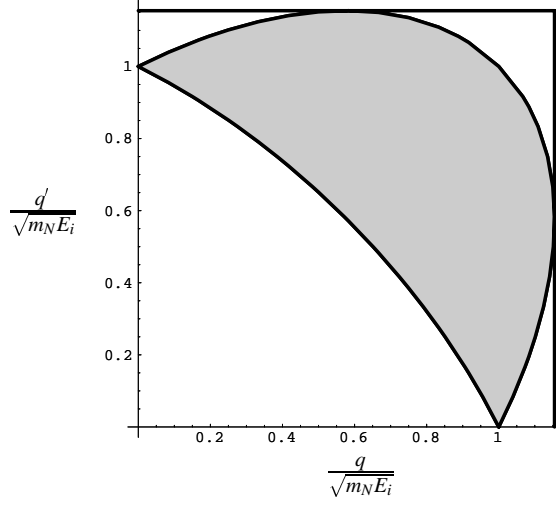


Figure C.1: The area  $|u(q', q)| \leq 1$  where the integrand of Eq. (C.25) has integrable singularities.

with

$$\mathbf{F}_{\text{sg}}(0, q) = \int_{-1}^1 dx \mathbf{F}_{\text{sg}}(0, q, x). \quad (\text{C.30b})$$

For  $0 < q' < q_{\text{sg}}$  and  $|u(q', q)| \leq 1$  with  $u(q', q) = (m_N E_i - q'^2 - q^2)/q'q$  the singularities arise already in the  $x$  integration; the area  $|u(q', q)| \leq 1$  is indicated in Fig. C.1. As will be demonstrated, on the border of that area the singularities remain even after the  $x$  integration. I therefore introduce an extended area  $|u(q', q)| \leq 1 + \varepsilon$  with small positive  $\varepsilon$ , typically  $\varepsilon = 10^{-3}$ ; that area fully isolates the singularities, i.e., outside it the integrand is regular. When calculating the integral (C.25) for  $0 < q' < q_{\text{sg}}$  I use the identity (C.28) together with the subtraction technique for the principal part singularity, this time, however, for the  $x$  integration, and I obtain

$$\begin{aligned} \mathbf{X}_{\text{sg}}(q') = \int_0^{q_{\text{sg}}} q^2 dq \frac{1}{q'q} \left\{ \int_{-1}^1 dx \frac{\mathbf{F}_{\text{sg}}(q', q, x) - \Theta(1 + \varepsilon - |u(q', q)|) \mathbf{F}_{\text{sg}}(q', q, u(q', q))}{u(q', q) - x} \right. \\ \left. - \left[ i\pi\Theta(1 - |u(q', q)|) - \Theta(1 + \varepsilon - |u(q', q)|) \ln \left| \frac{1 + u(q', q)}{1 - u(q', q)} \right| \right] \mathbf{F}_{\text{sg}}(q', q, u(q', q)) \right\}, \end{aligned} \quad (\text{C.31})$$

$\Theta(t)$  being the Heaviside step function. Thus, the only remaining singular term in the integrand of Eq. (C.31) is the one proportional to  $\ln|[1 + u(q', q)]/[1 - u(q', q)]|$ ; it has integrable logarithmic singularities at  $|u(q', q)| = 1$ . The corresponding integral is calculated numerically using the technique of the *special weights*, described in Sec. C.2.3. All other integrations are performed using the Gauss-Legendre integration.

The set of mesh points  $\{q'\}$  at which  $\mathbf{X}(q')$  is calculated and the sets of mesh points  $\{q\}$  used for integration have to be chosen very carefully in order to ensure the stability of the results with a relatively small number of the mesh points. The chosen distribution of the mesh points has to take into account the behavior of the integrand, e.g., concentrating the mesh points in the intervals where the integrand has rapid variations. Whereas for integrals  $\mathbf{X}_d(q')$ ,  $\mathbf{X}_{\bar{d}}(q')$  and  $\mathbf{X}_\Delta(q')$  I choose the mesh points  $\{q\}$  such that  $\{q\} \subset \{q'\}$ , the nature of the moving singularities requires a very special distribution of the mesh points  $\{q\}$  for calculating  $\mathbf{X}_{\text{sg}}(q')$  as shown in Fig. C.2; in fact, for each  $q'$  a different set  $\{q\}$  has to be used. Thus, it is necessary to access the integrand  $\mathbf{F}_{\text{sg}}(q', q, x)$ , i.e.,

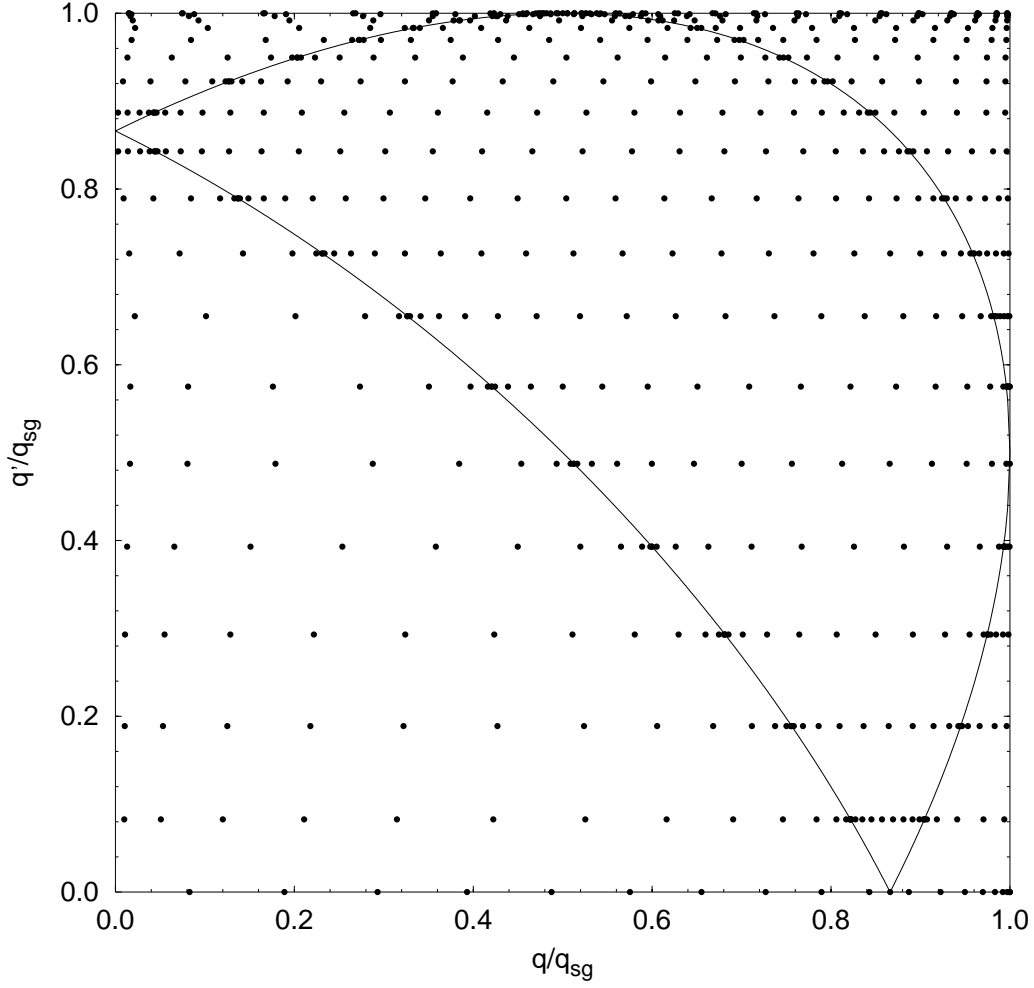


Figure C.2: The distribution of mesh points for  $0 \leq q, q' \leq q_{\text{sg}}$ . One clearly sees more dense distribution of mesh points around singularities.

the part  $\sum_{r''v''} \delta_{\chi\chi''} T_{\eta\eta''}^{rr''}(\chi q, E_i + i0) \propto \langle t^{r''} q v'' | X_{n-1}(E_i + i0) \rangle$  in Eq. (C.13), at untabulated arguments  $q$  in the interval  $[0, q_{\text{sg}}]$ . Therefore, an interpolation scheme becomes mandatory which has to be accurate and efficient at the same time, since it will be used frequently in the step (C.13). I use cubic spline interpolation described in Sec. C.3 to accomplish this task. The advantage of the spline interpolation compared to Chebyshev interpolation is more freedom in choosing the grid points. This is important in the context of moving singularities; e.g., in my calculations an additional point  $q' = 0$  is included among the grid points  $\{q'\}$  used for interpolation. My particular feature of interpolation is the choice of different interpolation variables in different intervals, i.e.,  $q$  in the vicinity of 0 and  $\sqrt{q_{\text{sg}}^2 - q^2}$  in the vicinity of  $q_{\text{sg}}$ , the reason for the latter choice being the fact that the imaginary part of the two-baryon transition matrix, thus, also the imaginary part of the matrix  $T_{\alpha}(E_i + i0)$  containing the Chebyshev coefficients, behaves in that limit as  $\text{const} \sqrt{q_{\text{sg}}^2 - q^2}$ . Those special choices greatly enhance the numerical accuracy. In the intermediate regime interpolation in any of these variables works equally well.

The above described particular features of the calculational scheme are indeed important for the numerical stability of the results, especially for three-nucleon breakup reactions in the vicinity of collinearity points, i.e., for small values of  $q'$ . In this context, I note that some results of Ref. [61], e.g., the deuteron analyzing powers  $A_{xx}$  and  $A_{yy}$  of nucleon-deuteron breakup at 135 MeV nucleon lab energy, show rather strange rapid oscillations which, according to my experience, are numerical instabilities and which I do not see in my results for the same observables as shown in Figs. 5.18 and 8.4.

### C.2.3 Numerical Integration by Special Weights

The employed technique for calculating the integrals containing integrable singularities is taken over from Refs. [19, 91]. It is described for an integral of the form

$$I = \int_a^b dx w(x) f(x), \quad (\text{C.32a})$$

where  $f : [a, b] \mapsto \mathbb{R}$  is a regular test function and  $w : [a, b] \mapsto \mathbb{R}$  is a function which carries the integrable singularities in  $(a, b)$ . Here I use standard mathematics notation, though I have the  $q$  integration of Eq. (C.31) in mind. For that integral (C.32a) I seek a simple integration rule

$$I \approx \sum_{j=1}^N w_j f(x_j) \quad (\text{C.32b})$$

involving a given finite set  $\{x_1, \dots, x_N\}$  of mesh points with *weights*  $w_j$  to be determined. Note, that the presence of the singular function  $w(x)$  will be completely hidden in the weights  $w_j$  of the integration rule (C.32b). Thus, once the weights are calculated, all occurring singular integrals can be as easily evaluated in the same way as the familiar Gauss-Legendre integration rule allows for regular functions. The calculation of weights  $w_j$  is described and the superiority of the integration rule (C.32b) over the standard Gauss-Legendre quadrature with subtraction is demonstrated in Refs. [19, 91].

## C.3 Spline Interpolation

I use *Chebyshev interpolation* for the two-baryon transition matrix and for the deuteron wave function. I remind of its advantage: The two-baryon transition matrix and the deuteron wave function have to be calculated only *once*, they are expanded in Chebyshev polynomials and then the *truncated* expansions are used in *all* subsequent calculations.

The situation is completely different for other quantities to be interpolated as discussed below under items 1. and 2.; I therefore use *spline interpolation* for them. Though in principle the Chebyshev interpolation could be used also for them and, in fact, this has been done in tentative calculations, I found – as expected – that in those applications the Chebyshev interpolation loses its superiority over the spline interpolation; furthermore, in particular cases the spline interpolation is numerically even more accurate.

The spline interpolation has the general form

$$f(x) \approx \sum_r f(x_r) S_r(x) \quad (\text{C.33})$$

with exact function values  $f(x_r)$  at an appropriately chosen set of grid points and known functions  $S_r(x)$  described in detail in Refs. [89, 92, 93]. A slightly different spline interpolation algorithm is

proposed and used in Refs. [19, 91], more appropriate there. In the calculations of this thesis spline interpolation is used in three different contexts:

1. The calculation of the integral (C.31) involving moving singularities requires interpolation of the quantity  $\sum_{r',v''} \delta_{\chi\chi''} T_{\eta\eta''}^{rr''}(\chi q, E_i + i0) \alpha \langle t^{r''} q v'' | X_{n-1}(E_i + i0) \rangle$  in the variables  $q$  and  $\sqrt{q_{\text{sg}}^2 - q^2}$  as discussed in Sec. C.2.2. The spline interpolation provides more freedom in choosing the grid points than the Chebyshev interpolation; this feature becomes important in the context of moving singularities.
2. The calculation of the integral (C.15) requires interpolation of the quantity  $\alpha \langle p q v(Ij) | j^\mu(\mathbf{Q}, \mathbf{K}_+) | B \rangle$  in the variable  $p$ .
3. Spline interpolation is used as alternative for the Chebyshev interpolation of the two-baryon transition matrix and of the deuteron wave function in tentative calculations. Since the spline interpolation (C.33) and the interpolation in terms of the Chebyshev polynomials (C.22) have the same general structure, it is obvious that the numerical technique of this thesis for solving Eqs. (C.13) and (C.18) can also be based on spline interpolation. The only difference is that the functions  $t_L^r(p)$  and  $\tilde{t}_L^r(p_k)$  of Sec. C.1 are

$$t_L^r(p) = \frac{p^L}{(p^2 + a_L^2)^{L/2}} S_r(p), \quad (\text{C.34a})$$

$$\tilde{t}_L^r(p_k) = \frac{(p_k^2 + a_L^2)^{L/2}}{p_k^L} \delta_{rk} \quad (\text{C.34b})$$

in case of spline interpolation. Of course, the grid points  $p_k$  are in this case not necessarily chosen as the zeros of a Chebyshev polynomial.

## C.4 Padé Summation

In this section I sum up the Neumann series (C.12) by the Padé method [94]. The matrix structure of  $\langle \mathbf{t}_\alpha | X(E_i + i0) \rangle$ , i.e., its dependence on the Chebyshev label, discrete quantum numbers and continuous variables, is entirely irrelevant for the present consideration, since the Padé summation is carried out for each element of  $\langle \mathbf{t}_\alpha | X(E_i + i0) \rangle$  individually. I introduce a function  $K^{(M)}(\lambda)$  containing the information on the first  $M + 1$  terms of the Neumann series (C.12) in the form

$$K^{(M)}(\lambda) = \sum_{m=0}^M K_m \lambda^m \quad (\text{C.35})$$

with  $K_m = \alpha \langle t^{r'} q' v' | X_m(E_i + i0) \rangle$ . If the series (C.12) converges,  $K^{(M)}(\lambda = 1)$  with  $M$  large enough may be a good approximation for  $\langle \mathbf{t}_\alpha | X(E_i + i0) \rangle$ . However, the Neumann series might not be globally convergent. The Padé method deals with the problem of non-convergence or slow convergence by generating an approximating, better converging rational function  $R(\lambda) = P(\lambda)/Q(\lambda)$  from the coefficients  $\{K_m\}$  according to two conditions:

- Improved convergence is achieved by requiring the order of the denominator polynomial  $Q(\lambda)$  to be equal or at least close to the order of the numerator polynomial  $P(\lambda)$ . The convergence of the Neumann series is spoiled by poles in the complex plane. By introducing a rational approximation, which generates isolated poles in the complex plane, the behavior of the underlying function should be better approximated as by the Neumann series.



- The rational function  $R(\lambda)$  is required to be equivalent to  $K^{(M)}(\lambda)$  up to the order in  $\lambda$  to which  $K^{(M)}(\lambda)$  is defined, i.e.,  $|R(\lambda) - K^{(M)}(\lambda)| = O(\lambda^{M+1})$ .

I remind that all coefficients  $\{K_m\}$  are vectors with respect to their dependence on the discretized set  $\{q'\}$  of the continuous spectator momentum, on the Chebyshev label  $r'$  and on the discrete three-body quantum numbers  $\mathbf{v}'$ . Thus, the numerator and denominator polynomials are constructed separately for each momentum  $q'$  and for each of the discrete labels and quantum numbers. I assume, that all coefficients  $\{K_m | m = 1, \dots, M\}$  are nonzero. In practice, this assumption is true except for the momentum  $q' = 0$  and particular quantum numbers. However, in this exceptional case *all*  $\{K_m\}$  vanish due to geometric reasons; thus, there is no need for a Padé resummation. In my use of the Padé method, the approximating, better converging rational function  $R(\lambda)$  is obtained in three steps.

The *first* step rewrites  $K^{(M)}(\lambda)$  in form of a continued fraction  $K_{\text{cf}}^{(n)}(\lambda)$ . Its definition is iterative, where the  $n$ -th iteration is given by

$$K_{\text{cf}}^{(n)}(\lambda) = K_0 + \frac{a_1(\lambda)}{1 +} \frac{a_2(\lambda)}{1 +} \dots \frac{a_n(\lambda)}{1 + p^{(n)}(\lambda)/q^{(n)}(\lambda)} \quad (\text{C.36a})$$

with

$$a_n(\lambda) = \alpha_n \lambda^{l(n)} \quad (\text{C.36b})$$

being powers of order  $l(n)$  in  $\lambda$  and  $p^{(n)}(\lambda)$  and  $q^{(n)}(\lambda)$  being polynomials in  $\lambda$ . The notation for a continued fraction is a standard one, e.g., as given in Ref. [89]. The quantities  $a_{n+1}(\lambda)$ ,  $p^{(n+1)}(\lambda)$  and  $q^{(n+1)}(\lambda)$  are obtained from the corresponding quantities in the previous iteration step.  $a_{n+1}(\lambda)$  is the lowest order term of  $p^{(n)}(\lambda)$ ;  $p^{(n+1)}(\lambda)$  and  $q^{(n+1)}(\lambda)$  are obtained using the transformation of Viskovatov [95]

$$\begin{aligned} \frac{p^{(n)}(\lambda)}{q^{(n)}(\lambda)} &= \frac{a_{n+1}(\lambda)}{q^{(n)}(\lambda) [a_{n+1}(\lambda)/p^{(n)}(\lambda)]} \\ &= \frac{a_{n+1}(\lambda)}{1 + q^{(n)}(\lambda) [a_{n+1}(\lambda)/p^{(n)}(\lambda)] - 1} \\ &= \frac{a_{n+1}(\lambda)}{1 + p^{(n+1)}(\lambda)/q^{(n+1)}(\lambda)} \end{aligned} \quad (\text{C.37})$$

with  $q^{(n+1)}(\lambda) = p^{(n)}(\lambda)/a_{n+1}(\lambda)$  and  $p^{(n+1)}(\lambda) = q^{(n)}(\lambda) - q^{(n+1)}(\lambda)$ . The lowest-order term of any  $q^{(n)}(\lambda)$  is always 1, the lowest-order term of any  $p^{(n)}(\lambda)$  is at least of power 1. The iteration is started by putting  $p^{(0)}(\lambda) = K^{(M)}(\lambda) - K_0$  and  $q^{(0)}(\lambda) = 1$ ; that starting step yields  $a_1(\lambda)$ ,  $p^{(1)}(\lambda)$  and  $q^{(1)}(\lambda)$  for the continued fraction  $K_{\text{cf}}^{(1)}(\lambda)$  of lowest order. In each iteration step  $K_{\text{cf}}^{(n)}(\lambda) = K^{(M)}(\lambda)$ . The iteration terminates after  $2M$  steps at most, i.e.,  $p^{(2M)}(\lambda) = 0$  and  $a_{2M+1}(\lambda) = 0$ . Since also  $K_{\text{cf}}^{(2M)}(\lambda) = K^{(M)}(\lambda)$ , the problem of non-convergence still persists.

The exercise of continued fraction is only required to provide the quantities  $a_n(\lambda)$  of Eq. (C.36b) for  $n = 1, \dots, M$ , which are needed for the later *second* step of constructing the rational function  $R(\lambda)$ . My algorithm for the coefficients  $\alpha_n$  in  $a_n(\lambda)$  is derived from the continued fraction (C.36a) and runs as follows: I assume that the coefficients  $\{\alpha_i | i = 1, \dots, m-1\}$  are determined from the coefficients  $\{K_i | i = 1, \dots, m-1\}$ ; the determination of  $\alpha_{m-1}$  requires auxiliary quantities  $\{\gamma_i(m-1) | i = 2, \dots, m\}$  which are saved for the determination of  $\alpha_m$ . The step from  $(m-1)$  to  $m$  has the three sequences (a)-(c):

(a)

$$\beta_1(m) = K_m, \quad (C.38a)$$

$$\beta_i(m) = \gamma_i(m-1), \quad i = 2, \dots, m; \quad (C.38b)$$

(b) The auxiliary quantities  $\{\gamma_i(m) \mid i = 2, \dots, m+1\}$  are redefined by

$$\gamma_2(m) = 0, \quad (C.38c)$$

$$\gamma_{i+1}(m) = \frac{\beta_{i-1}(m) - \gamma_i(m)}{\alpha_{i-1}}, \quad i = 2, \dots, m; \quad (C.38d)$$

(c)

$$\alpha_m = \beta_m(m) - \gamma_{m+1}(m). \quad (C.38e)$$

The algorithm does not need to determine the power  $l(n)$  of  $\lambda$  in  $a_n(\lambda)$  of Eq. (C.36b), since the rational function  $R(\lambda)$  will be considered only for  $\lambda = 1$ .

In the *second* step the rational function  $R(\lambda)$  is generated by a recurrence relation for the polynomials  $P^{(n)}(\lambda)$  and  $Q^{(n)}(\lambda)$ , i.e.,

$$P^{(n)}(\lambda) = P^{(n-1)}(\lambda) + a_n(\lambda)P^{(n-2)}(\lambda), \quad (C.39a)$$

$$Q^{(n)}(\lambda) = Q^{(n-1)}(\lambda) + a_n(\lambda)Q^{(n-2)}(\lambda), \quad (C.39b)$$

which is started by

$$P^{(-1)}(\lambda) = 1, \quad Q^{(-1)}(\lambda) = 0, \quad (C.39c)$$

$$P^{(0)}(\lambda) = K_0, \quad Q^{(0)}(\lambda) = 1. \quad (C.39d)$$

The recurrence relations (C.39) were first derived by J. Wallis in 1655 [96]. The recurrence uses the functions  $a_n(\lambda)$  of the continued fraction  $K_{cf}^{(n)}(\lambda)$ . It terminates at  $n = n_{\max}$  when  $a_{n_{\max}+1}(\lambda) = 0$ . However, if the natural termination of the continued fraction were used, i.e.,  $n_{\max} = 2M$  (in exceptional cases  $n_{\max} < 2M$ ), nothing would be gained; in that case  $P^{(2M)}(\lambda) = K^{(M)}(\lambda)$  and  $Q^{(2M)}(\lambda) = 1$ . If, however, the continued fraction is terminated at  $n_{\max} = M$  putting  $a_{M+1}(\lambda) = 0$ , the rational function  $R(\lambda)$  satisfies the two desired properties, spelt out at the beginning of this subsection. The construction of the rational function  $R(\lambda)$  in the second step appears awkward, since it is based on the continued fraction of the first step. However, it is chosen, since it is numerically stable, in contrast to other possible techniques.

In the *third* step the convergence of the Padé summation is checked. I am satisfied with the obtained approximating rational function  $R(\lambda)$ , if for a given order  $M$  of the Neumann series the deviation of the complete vectors is small in successive orders, i.e.,  $\|P^{(M)}(\lambda)/Q^{(M)}(\lambda) - P^{(M-1)}(\lambda)/Q^{(M-1)}(\lambda)\|_{\lambda=1} < \varepsilon$ ,  $\varepsilon$  being the required accuracy. Computer economy calls for as small a number  $M$  as reasonable. The number  $M$  is found by starting the accuracy check already for  $M = 1$ ; the Neumann series (C.35) is carried to a higher order  $M + 1$ , requiring a repetition of the steps one to three only when that accuracy check fails. The actual number  $M$  used depends on the scattering energy as well as on the total three-baryon quantum numbers  $\Pi$  and  $J$ .

# D

## Scattering Observables

### D.1 Spin-Dependent Observables

The differential cross sections of all considered reactions for transitions between pure spin states are given in Chapters 5 – 7. However, in experiments the particles usually are not in pure spin states but in a statistical mixtures of them. The spin dependence of the initially prepared states is described by the Hermitian density matrix  $\rho_i$ , normalized to  $\text{Tr} \rho_i = 1$ . The final-state polarization measurement is described by the projection operator  $\rho_f$ , i.e.  $\rho_f^2 = \rho_f$ .

#### D.1.1 Elastic Nucleon-Deuteron Scattering

The density matrix  $\rho_i$  of the initially prepared nucleon-deuteron states is the tensor product of density matrices for the nucleon and the deuteron, i.e.,

$$\rho_i = \rho^N \otimes \rho^d. \quad (\text{D.1})$$

The nucleon and deuteron density matrices are parameterized in the standard forms

$$\rho^N = \frac{1}{2} [I^{(2)} + \mathbf{n} \cdot \boldsymbol{\sigma}], \quad (\text{D.2a})$$

$$\rho^d = \frac{1}{3} \left[ I^{(3)} + \frac{3}{2} \mathbf{n}_d \cdot \mathbf{S} + \frac{1}{3} \sum_{ij} t_{dij} S_{ij} \right]. \quad (\text{D.2b})$$

Their spin dependence is carried for the spin- $\frac{1}{2}$  part by the operators  $I^{(2)}$  and  $\boldsymbol{\sigma}$ , the two-dimensional unity and the vector of Pauli matrices, and for the spin-1 part by the three-dimensional unity  $I^{(3)}$ , by the vector of spin operators  $\mathbf{S}$  for spin-1 particle and by the symmetric traceless Cartesian tensor operator  $S_{ij} = \frac{3}{2}(S_i S_j + S_j S_i) - \delta_{ij} \mathbf{S}^2$  of order two. For a compact description of the density matrices I collectively combine the spin- $\frac{1}{2}$  operators  $\{I^{(2)}, \boldsymbol{\sigma}\}$  to the set  $\{S^{a_2}\}$  of four operators with  $a_2 = 0, \dots, 3$  and the spin-1 operators  $\{I^{(3)}, \mathbf{S}, S_{ij}\}$  to the set  $\{S^{a_3}\}$  of nine independent operators with  $a_3 = 0, \dots, 8$  which are defined as  $S^0 = I^{(3)}$ ,  $S^1 = \sqrt{\frac{3}{2}} S_x$ ,  $S^2 = \sqrt{\frac{3}{2}} S_y$ ,  $S^3 = \sqrt{\frac{3}{2}} S_z$ ,  $S^4 = \sqrt{\frac{2}{3}} S_{xy}$ ,  $S^5 = \sqrt{\frac{2}{3}} S_{yz}$ ,  $S^6 = \sqrt{\frac{2}{3}} S_{xz}$ ,  $S^7 = \sqrt{\frac{1}{6}} (S_{xx} - S_{yy})$ ,  $S^8 = \sqrt{\frac{1}{2}} S_{zz}$ . In addition I form the set of product operators  $\{S^a\} = \{S^{a_2} \otimes S^{a_3}\}$  which are normalized by

$$\text{Tr}[S^a S^b] = 6 \delta_{ab}, \quad (\text{D.3})$$

the factor 6 being the dimension of the density matrix  $\rho_i$ . It arises, since the individual operator sets  $\{S^{a_2}\}$  and  $\{S^{a_3}\}$  are normalized in a corresponding way to their dimension. With the product operators

$S^a$  the density matrix gets the concise form

$$\rho_i = \frac{1}{6} \sum_a \text{Tr}[\rho S^a] S^a. \quad (\text{D.4})$$

The parameters of density matrix  $\rho$  are  $\mathbf{n}$ ,  $\mathbf{n}_d$  and  $t_d$ , the polarization vector of the nucleon, the polarization vector and the symmetric traceless polarization tensor of the deuteron; the characteristics of the initially prepared channel states are contained in those parameters. If state is quantum-mechanically pure, i.e.,  $\rho^2 = \rho$ , the parameters are constrained by  $\mathbf{n}^2 = 1$ ,  $\mathbf{n}_d^2 = 1$  and  $t_d$  being determined by  $\mathbf{n}_d$ . If state is statistical mixture, the constraints on the parameters get relaxed.

The final-state projection operator  $\rho_f$  is the tensor product of the corresponding projection operators for the nucleon and the deuteron, i.e.,

$$\rho_f = N_f \rho^N \otimes \rho^d, \quad (\text{D.5})$$

with  $N_f = 2^{1-N_N} 3^{1-N_d}$ ,  $N_N$  ( $N_d$ ) being the number of polarization measurements of the nucleon (deuteron). Equation (D.5) corrects the imprecise description of this point in Ref. [17].  $\rho_f$  is normalized to  $\text{Tr} \rho_f = N_f$ . The operators  $\rho^N$  and  $\rho^d$  are parameterized in the form (D.2), i.e., with vanishing values of parameters  $\mathbf{n}$ ,  $\mathbf{n}_d$  and  $t_d$  in case of no polarization measurement and with the values of those parameters corresponding to the pure states in case of an ideal polarization measurement. Thus, the projection operator  $\rho_f$  can be parametrized in terms of product operators  $\{S^a\}$  in the same way as the initial-state density matrix  $\rho_i$ , i.e.,

$$\rho_f = \frac{1}{6} \sum_a \text{Tr}[\rho S^a] S^a. \quad (\text{D.6})$$

In terms of the scattering amplitude  $M(E_i \mathbf{q}_f)$ , of the initial-state density matrix  $\rho_i$  and of the final-state projection operator  $\rho_f$  the spin-dependent differential cross section becomes

$$\frac{d^2 \sigma}{d^2 \hat{\mathbf{q}}_f} = \text{Tr}[M(E_i \mathbf{q}_f) \rho_i M^\dagger(E_i \mathbf{q}_f) \rho_f] \text{fps}. \quad (\text{D.7})$$

Using the spin-averaged differential cross section  $\overline{d^2 \sigma} / d^2 \hat{\mathbf{q}}_f$  of Eq. (5.8) and the expansions (D.4) and (D.6) for the initial-state density matrix  $\rho_i$  and the final-state projection operator  $\rho_f$ , the spin-dependent differential cross section takes the form

$$\frac{d^2 \sigma}{d^2 \hat{\mathbf{q}}_f} = \frac{\overline{d^2 \sigma}}{d^2 \hat{\mathbf{q}}_f} \frac{1}{6} \sum_{a_i a_f} \text{Tr}[\rho_i S^{a_i}] \text{Tr}[\rho_f S^{a_f}] \frac{\text{Tr}[M(E_i \mathbf{q}_f) S^{a_i} M^\dagger(E_i \mathbf{q}_f) S^{a_f}]}{\text{Tr}[M(E_i \mathbf{q}_f) M^\dagger(E_i \mathbf{q}_f)]}. \quad (\text{D.8})$$

Characteristic for the experimental setup of the studied reaction are the parameters in the initial-state density matrix  $\rho_i$  and in the final-state projection operator  $\rho_f$  which determine the expansion coefficients  $\text{Tr}[\rho_i S^{a_i}] \text{Tr}[\rho_f S^{a_f}]$  in Eq. (D.8). Characteristic for the spin dependence of the reaction mechanism is the way in which the spin operators  $S^{a_i}$  of  $\rho_i$  and  $S^{a_f}$  of  $\rho_f$  weigh the matrix elements of the scattering amplitude. The experiment therefore aims at determining observables of the type  $\text{Tr}[M(E_i \mathbf{q}_f) S^{a_i} M^\dagger(E_i \mathbf{q}_f) S^{a_f}] / \text{Tr}[M(E_i \mathbf{q}_f) M^\dagger(E_i \mathbf{q}_f)]$ . A particular choice of the spin operators  $S^{a_i}$  and  $S^{b_f}$  defines particular spin observables. Their notation is standardized in Ref. [97].

I give definitions of the nucleon-deuteron spin observables shown in the figures in Chapter 5. In my notation I suppress their dependence on the initial energy and scattering angle.

- Nucleon analyzing powers  $A_i(N)$  and deuteron vector and tensor analyzing powers  $A_i(d)$  and  $A_{kl}$ :

$$A_i(N) = \frac{\text{Tr}[M(E_i \mathbf{q}_f) \boldsymbol{\sigma}_i M^\dagger(E_i \mathbf{q}_f)]}{\text{Tr}[M(E_i \mathbf{q}_f) M^\dagger(E_i \mathbf{q}_f)]}, \quad (\text{D.9a})$$

$$A_i(d) = \frac{\text{Tr}[M(E_i \mathbf{q}_f) S_i M^\dagger(E_i \mathbf{q}_f)]}{\text{Tr}[M(E_i \mathbf{q}_f) M^\dagger(E_i \mathbf{q}_f)]}, \quad (\text{D.9b})$$

$$A_{kl} = \frac{\text{Tr}[M(E_i \mathbf{q}_f) S_{kl} M^\dagger(E_i \mathbf{q}_f)]}{\text{Tr}[M(E_i \mathbf{q}_f) M^\dagger(E_i \mathbf{q}_f)]}. \quad (\text{D.9c})$$

- Nucleon to nucleon polarization transfer coefficients  $K_i^{j'}(NN)$  and deuteron to nucleon vector-vector and tensor-vector polarization transfer coefficients  $K_i^{j'}(dN)$  and  $K_{kl}^{j'}(dN)$ :

$$K_i^{j'}(NN) = \frac{\text{Tr}[M(E_i \mathbf{q}_f) \boldsymbol{\sigma}_i M^\dagger(E_i \mathbf{q}_f) \boldsymbol{\sigma}_{j'}]}{\text{Tr}[M(E_i \mathbf{q}_f) M^\dagger(E_i \mathbf{q}_f)]}, \quad (\text{D.10a})$$

$$K_i^{j'}(dN) = \frac{\text{Tr}[M(E_i \mathbf{q}_f) S_i M^\dagger(E_i \mathbf{q}_f) \boldsymbol{\sigma}_{j'}]}{\text{Tr}[M(E_i \mathbf{q}_f) M^\dagger(E_i \mathbf{q}_f)]}, \quad (\text{D.10b})$$

$$K_{kl}^{j'}(dN) = \frac{\text{Tr}[M(E_i \mathbf{q}_f) S_{kl} M^\dagger(E_i \mathbf{q}_f) \boldsymbol{\sigma}_{j'}]}{\text{Tr}[M(E_i \mathbf{q}_f) M^\dagger(E_i \mathbf{q}_f)]}. \quad (\text{D.10c})$$

- Initial state nucleon-deuteron vector-vector spin correlation coefficients  $C_{i,j}$

$$C_{i,j} = \frac{\text{Tr}[M(E_i \mathbf{q}_f) \boldsymbol{\sigma}_i S_j M^\dagger(E_i \mathbf{q}_f)]}{\text{Tr}[M(E_i \mathbf{q}_f) M^\dagger(E_i \mathbf{q}_f)]}. \quad (\text{D.11})$$

Other coefficients, e.g., nucleon to deuteron and deuteron to deuteron polarization transfer coefficients, can be defined correspondingly. In the final state the quantization axis for particle spin is the direction of the particle momentum in the lab system. Usually, the  $x$ - $z$  plane is defined to be the scattering plane; in that case, due to the rotational invariance and parity conservation, only the observables with even number of indices  $x$  and  $z$  are nonzero, e.g., among all analyzing powers (D.9) only  $A_y(N)$ ,  $A_y(d)$ ,  $A_{xx}$ ,  $A_{yy}$ ,  $A_{zz}$  and  $A_{xz}$  are nonzero.

## D.1.2 Nucleon-Deuteron Breakup

The spin-dependent observables in the nucleon-deuteron breakup are defined in close correspondence with elastic scattering. The spin dependence of the initially prepared states is described by the density matrix (D.1). The final-state polarization measurement is described by the projection operator  $\rho_f$ , i.e.,  $\rho_f^2 = \rho_f$ , which is the tensor product of corresponding projection operators for the three nucleons, i.e.,

$$\rho_f = N_f \rho^N \otimes \rho^N \otimes \rho^N, \quad (\text{D.12})$$

with  $N_f = 2^{3-N}$ ,  $N$  being the number of polarization measurements.  $\rho_f$  is normalized to  $\text{Tr} \rho_f = N_f$ . The operators  $\rho^N$  are parameterized in the form of the nucleon density matrix (D.2a). Their individual spin-dependence is carried by the spin- $\frac{1}{2}$  operators  $S^{a_2}$ . The set of product operators  $\{S^{a_f}\} = \{S^{a_2} \otimes S^{a_2} \otimes S^{a_2}\}$  is formed, which are normalized by

$$\text{Tr}[S^{a_f} S^{b_f}] = 8 \delta_{a_f b_f}. \quad (\text{D.13})$$

With these product operators  $S^{a_f}$  the projection operator  $\rho_f$  gets the concise form

$$\rho_f = \frac{1}{8} \sum_{a_f} \text{Tr}[\rho_f S^{a_f}] S^{a_f}. \quad (\text{D.14})$$

In terms of the scattering amplitude  $M(E_i \mathbf{p}_f \mathbf{q}_f)$ , of the initial-state density matrix  $\rho_i$  and of the final-state projection operator  $\rho_f$  the spin-dependent differential cross section becomes

$$\frac{d^5 \sigma}{dS d^2 \hat{\mathbf{k}}_1 d^2 \hat{\mathbf{k}}_2} = \text{Tr}[M(E_i \mathbf{p}_f \mathbf{q}_f) \rho_i M^\dagger(E_i \mathbf{q}_f \mathbf{q}_f) \rho_f] \text{ fps}. \quad (\text{D.15})$$

Using the spin-averaged differential cross section  $\overline{d^5 \sigma} / dS d^2 \hat{\mathbf{k}}_1 d^2 \hat{\mathbf{k}}_2$  of Eq. (5.12) and the expansions (D.4) and (D.14) for the initial-state density matrix  $\rho_i$  and the final-state projection operator  $\rho_f$ , the spin-dependent differential cross section takes the form

$$\frac{d^5 \sigma}{dS d^2 \hat{\mathbf{k}}_1 d^2 \hat{\mathbf{k}}_2} = \frac{\overline{d^5 \sigma}}{dS d^2 \hat{\mathbf{k}}_1 d^2 \hat{\mathbf{k}}_2} \frac{1}{8} \sum_{a_i a_f} \text{Tr}[\rho_i S^{a_i}] \text{Tr}[\rho_f S^{a_f}] \frac{\text{Tr}[M(E_i \mathbf{p}_f \mathbf{q}_f) S^{a_i} M^\dagger(E_i \mathbf{p}_f \mathbf{q}_f) S^{a_f}]}{\text{Tr}[M(E_i \mathbf{p}_f \mathbf{q}_f) M^\dagger(E_i \mathbf{p}_f \mathbf{q}_f)]}. \quad (\text{D.16})$$

The spin observables are defined as in Eqs. (D.9) – (D.11) just replacing the elastic scattering amplitude  $M(E_i \mathbf{q}_f)$  by the corresponding one  $M(E_i \mathbf{p}_f \mathbf{q}_f)$  for breakup.

### D.1.3 Electromagnetic Reactions

The spin-dependent observables of the considered e.m. reactions can be defined in a similar way as for nucleon-deuteron scattering. However, in the description of the e.m. reactions given in this thesis I only consider polarization in the initial nucleon-deuteron state of radiative capture; the calculated nucleon and deuteron analyzing powers are defined as in Eqs. (D.9) just replacing the elastic nucleon-deuteron scattering amplitude  $M(E_i \mathbf{q}_f)$  by the corresponding one  $M_\gamma(E_i \mathbf{k}_\gamma)$  for radiative capture. A detailed discussion of polarization observables in electron scattering from hadrons can be found in Refs. [75, 98].

## D.2 Problem in the Comparison of Theoretical Predictions and Experimental Data for Breakup

The experimental setup for breakup usually works with two particle detectors at two fixed angles measuring  $\hat{\mathbf{k}}_1$  and  $\hat{\mathbf{k}}_2$  and determines observables as functions of the arclength  $S$  along the kinematical curve corresponding to the two kinetic energies  $E_1$  and  $E_2$ . A sound comparison requires the same kinematical curve for the experimental interpretation of data and for the theoretical prediction. However, the experimental interpretation of data usually prefers relativistic kinematics, whereas theory prefers nonrelativistic kinematics, since the description of dynamics is nonrelativistic anyhow. Without a relativistic treatment of the dynamics there is no fully consistent comparison of the experimental data and of the theoretical prediction. Thus, approximative identification procedures have to be applied; a discussion of this point and a suggestion for identification is given in Ref. [57]. In order to estimate the theoretical uncertainty due to the use of nonrelativistic kinematics I follow a somehow different procedure. At the energies considered the resulting kinematical curves, defined in Eq. (5.10), are often quite similar for relativistic and nonrelativistic kinematics, but there are special situations with dramatic differences. Figures D.1 and D.2 give examples for either case at 135 MeV nucleon lab energy and at 52 MeV deuteron lab energy, respectively.

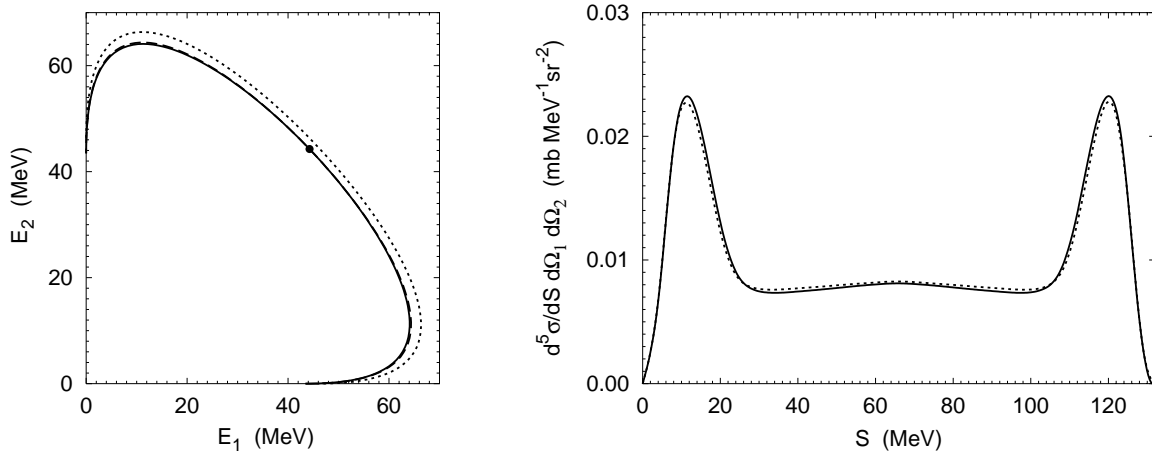


Figure D.1: Left side: Kinematical curves for relativistic space star configuration ( $53.4^\circ, 53.4^\circ, 120.0^\circ$ ) with relativistic (dashed) and nonrelativistic (dotted) kinematics and for the nonrelativistic space star configuration ( $54.4^\circ, 54.4^\circ, 120.0^\circ$ ) with nonrelativistic kinematics (solid) at 135 MeV nucleon lab energy; the total arc lengths are 131.5, 134.7 and 132.1 MeV, respectively. The solid and dashed curves are almost indistinguishable in the plot. The dot indicates the position of the exact space star point.

Right side: Differential cross section of  $Nd$  breakup at 135 MeV nucleon lab energy as function of the arclength  $S$  along the kinematical curve in the space star configuration. As in all calculations of this thesis, the results are obtained with a nonrelativistic arclength  $S$ . Results for the nonrelativistic space star configuration ( $54.4^\circ, 54.4^\circ, 120.0^\circ$ ) (solid curve) and for the relativistic space star configuration ( $53.4^\circ, 53.4^\circ, 120.0^\circ$ ) (dotted curve) are compared.

Figure D.1 refers to the space star configuration at 135 MeV nucleon lab energy, which is realized for relativistic and nonrelativistic kinematics at slightly different scattering angles. There are only minor differences between the relativistic and nonrelativistic kinematical curves corresponding to the same angles; however, the kinematical curves for slightly different angles corresponding to the exact space star configuration with relativistic and nonrelativistic kinematics are even almost identical. The right-hand side of Fig. D.1 shows a sample effect on observables, which arises from differences in the kinematical curves; correspondence is obtained by scaling all considered kinematical curves to the length of the relativistic arclength; the length of the kinematical curves before scaling is recorded in the figure caption; the discrepancy between the results of different identification procedures is small.

The example of Fig. D.2 is more dramatic. It refers to the QFS configuration at 52 MeV deuteron lab energy. Again, this special situation is with relativistic and nonrelativistic kinematics realized for slightly different scattering angles. However, in this case there are quite large differences between the relativistic and nonrelativistic kinematical curves corresponding to the same angles; the reason is that the critical situation ( $42.26^\circ, 42.26^\circ, 180.0^\circ$ ), at which the relativistic locus collapses to a point, is near and that in nonrelativistic kinematics that critical situation occurs at larger angles. In contrast, the kinematical curves for slightly different angles corresponding to the exact QFS configuration with relativistic and nonrelativistic kinematics are quite close. The right-hand side of Fig. D.2 shows a sample effect on observables, which arises from differences in the kinematical curves; correspondence is naturally achieved without scaling, since the experimental data at this energy are given as function of  $S/S_{\max}$ ,  $S_{\max}$  being the full arclength of the relativistic kinematical curve. The respective length of the

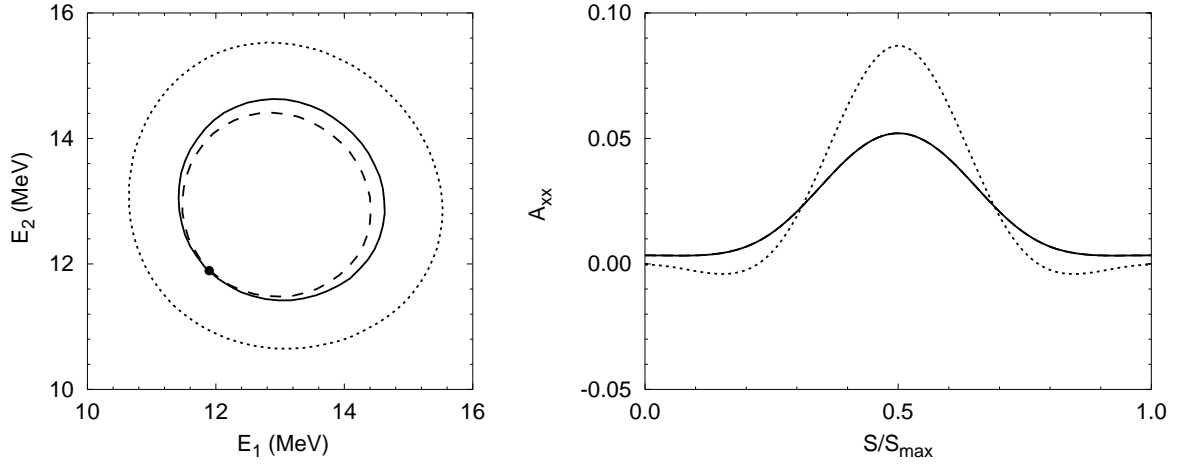


Figure D.2: Left side: Kinematical curves for relativistic QFS configuration  $(42.16^\circ, 42.16^\circ, 180.0^\circ)$  with relativistic (dashed) and nonrelativistic (dotted) kinematics and for nonrelativistic QFS configuration  $(42.32^\circ, 42.32^\circ, 180.0^\circ)$  with nonrelativistic kinematics (solid) at 52 MeV deuteron lab energy; total arc lengths are 9.22, 15.34 and 10.09 MeV, respectively. The dot indicates the position of the exact QFS point.

Right side: Deuteron tensor analyzing power  $A_{xx}$  of  $Nd$  breakup at 52 MeV deuteron lab energy as function of the fractional arclength  $S/S_{\max}$  along the kinematical curve in QFS configuration. As in all calculations of this thesis, the results are obtained with a nonrelativistic arclength  $S$ . Results for nonrelativistic QFS configuration  $(42.32^\circ, 42.32^\circ, 180.0^\circ)$  (solid) and for relativistic QFS configuration  $(42.16^\circ, 42.16^\circ, 180.0^\circ)$  (dotted) are compared.

kinematical curves is recorded in the figure caption. The sensitivity on the chosen kinematical curve is alarmingly large. This observation also implies, that the corrections arising from finite geometry can become sizable in this kinematical configuration.

The predictions of the nucleon-deuteron breakup shown in Figs. 5.14 – 5.18 refer to the kinematical configurations which are quite far from such a critical situations. In the light of the accuracy of present-day data, I therefore conclude that the theoretical uncertainty due to the use of nonrelativistic kinematics is rather inconsequential.



# E

## Calculation of Current Matrix Elements

The computation of the e.m. current matrix elements  $\langle \Psi_{\alpha}^{(-)}(\mathbf{q}_f) v_{\alpha_f} | j^{\mu}(\mathbf{Q}, \mathbf{K}_+) | B \rangle$  and  $\langle \Psi_0^{(-)}(\mathbf{p}_f \mathbf{q}_f) v_{0_f} | j^{\mu}(\mathbf{Q}, \mathbf{K}_+) | B \rangle$  is based on the partial-wave decompositions of the initial and final hadronic states, described in Appendix C, and on the multipole decomposition of the e.m. current to be discussed in this appendix.

### E.1 Multipole Decomposition of Current

The Coulomb (C) multipoles of the charge density  $\rho(\mathbf{Q}, \mathbf{K}_+)$ , which is the spherical tensor of rank zero, i.e.,  $j^{(0)}(\mathbf{Q}, \mathbf{K}_+)$ , and the electric (E), magnetic (M) and longitudinal (L) multipoles of the spatial current  $\mathbf{j}(\mathbf{Q}, \mathbf{K}_+)$  which is the spherical tensor of rank one, i.e.,  $j^{(1)}(\mathbf{Q}, \mathbf{K}_+)$ , are defined by

$$T_{Cm_j}^{(j)}(\mathbf{Q}) = T_{m_j}^{([j,0]j)}(\mathbf{Q}), \quad (\text{E.1a})$$

$$T_{Em_j}^{(j)}(\mathbf{Q}) = -\sqrt{\frac{j+1}{2j+1}} T_{m_j}^{([j-1,1]j)}(\mathbf{Q}) - \sqrt{\frac{j}{2j+1}} T_{m_j}^{([j+1,1]j)}(\mathbf{Q}), \quad (\text{E.1b})$$

$$T_{Mm_j}^{(j)}(\mathbf{Q}) = T_{m_j}^{([j,1]j)}(\mathbf{Q}), \quad (\text{E.1c})$$

$$T_{Lm_j}^{(j)}(\mathbf{Q}) = \sqrt{\frac{j}{2j+1}} T_{m_j}^{([j-1,1]j)}(\mathbf{Q}) - \sqrt{\frac{j+1}{2j+1}} T_{m_j}^{([j+1,1]j)}(\mathbf{Q}) \quad (\text{E.1d})$$

with

$$T_{m_j}^{([I,a]j)}(\mathbf{Q}) = \frac{1}{4\pi} \int d^2\hat{\mathbf{Q}} \{ Y^{(I)}(\hat{\mathbf{Q}}) \otimes j^{(a)}(\mathbf{Q}, \mathbf{K}_+) \}_{m_j}^{(j)}, \quad (\text{E.1e})$$

$Y^{(I)}(\hat{\mathbf{Q}})$  being the spherical tensor of the rank  $I$  corresponding to the spherical harmonics  $Y_{m_I}^I(\hat{\mathbf{Q}})$  and  $\mathbf{Q} = |\mathbf{Q}|$ . The multipoles (E.1e) are calculated either in c.m. system, i.e.,  $\mathbf{K}_+ = -\mathbf{Q}$ , or in lab system, i.e.,  $\mathbf{K}_+ = \mathbf{Q}$ . Thus, once the reference system is specified, the e.m. current  $j^{\mu}(\mathbf{Q}, \mathbf{K}_+)$  becomes dependent on the momentum transfer  $\mathbf{Q}$  only; this is why I drop the dependence on  $\mathbf{K}_+$  in the notation of the current multipoles.

The continuity equation (2.17) in terms of multipoles (E.1) reads

$$Q T_{Lm_j}^{(j)}(\mathbf{Q}) = [H, T_{Cm_j}^{(j)}(\mathbf{Q})]. \quad (\text{E.2a})$$

Thus, assuming current conservation, the longitudinal multipoles can be replaced by the Coulomb multipoles according to Eq. (E.2a). Furthermore, using Eqs. (E.1d) and (E.2a) the dominant part

of the electric multipoles, proportional to  $T_{m_j}^{([j-1,1]j)}(\mathbf{Q})$ , can be rewritten in terms of the Coulomb multipoles and higher order contributions  $T_{m_j}^{([j+1,1]j)}(\mathbf{Q})$ , resulting in the Siegert form of the electric multipoles, i.e.,

$$T_{Em_j}^{(j)}(\mathbf{Q}) = -\sqrt{\frac{2j+1}{j}} T_{m_j}^{([j+1,1]j)}(\mathbf{Q}) - \sqrt{\frac{j+1}{j}} \frac{1}{Q} [H, T_{Cm_j}^{(j)}(\mathbf{Q})]. \quad (\text{E.2b})$$

The spatial current and the charge density can be recovered by

$$\rho(\mathbf{Q}, \mathbf{K}_+) = 4\pi \sum_{jm_j} T_{Cm_j}^{(j)}(\mathbf{Q}) Y_{m_j}^{j*}(\hat{\mathbf{Q}}), \quad (\text{E.3a})$$

$$\mathbf{j}(\mathbf{Q}, \mathbf{K}_+) = 4\pi \sum_{jm_j l} T_{m_j}^{([l,1]j)}(\mathbf{Q}) [\{Y^{(l)}(\hat{\mathbf{Q}}) \otimes \mathbf{e}^{(1)}\}_{m_j}^{(j)*}] \quad (\text{E.3b})$$

from the multipoles with the spherical unit vectors  $\mathbf{e}_\lambda^{(1)} = \delta_{\lambda 0} \hat{\mathbf{z}} - \lambda(\hat{\mathbf{x}} + i\lambda \hat{\mathbf{y}})/\sqrt{2}$ .

It is most convenient to perform the calculations in the system with  $z$ -axis parallel to the momentum transfer  $\mathbf{Q}$ , i.e.,  $\mathbf{Q} = Q\hat{\mathbf{z}}$ . In that system the polarization vectors  $\varepsilon(Q\lambda)$  take the form

$$\varepsilon(Q\pm)|_{\mathbf{Q}=Q\hat{\mathbf{z}}} = \mp \frac{1}{\sqrt{2}}(0, 1, \pm i, 0), \quad (\text{E.4a})$$

$$\varepsilon(Q0)|_{\mathbf{Q}=Q\hat{\mathbf{z}}} = \frac{1}{\sqrt{-Q^2}}(Q, 0, 0, Q_0). \quad (\text{E.4b})$$

For photo reactions only the electric and magnetic multipoles are needed in the form

$$j^\mu(\mathbf{Q}, \mathbf{K}_+) \varepsilon_\mu(Q\lambda)|_{\mathbf{Q}=Q\hat{\mathbf{z}}} = \sqrt{2\pi} \sum_{j=1}^{\infty} \sqrt{2j+1} [T_{E\lambda}^{(j)}(\mathbf{Q}) + \lambda T_{M\lambda}^{(j)}(\mathbf{Q})] \quad (\text{E.5a})$$

with  $\lambda = \pm 1$  corresponding to the polarizations of transverse photon. Calculation of electron scattering from the trinucleon bound state needs also Coulomb multipoles explicitly; under the assumption  $\mathbf{Q} = Q\hat{\mathbf{z}}$  the charge density of Eq. (E.3a) takes the form

$$\rho(\mathbf{Q}, \mathbf{K}_+)|_{\mathbf{Q}=Q\hat{\mathbf{z}}} = \sqrt{4\pi} \sum_{j=0}^{\infty} \sqrt{2j+1} T_{C0}^{(j)}(\mathbf{Q}). \quad (\text{E.5b})$$

One notes that in matrix elements of the current operators (E.5) between the three-particle states with definite total angular momentum and parity only a finite number of multipoles contributes.

## E.2 Instability Problem in Calculation of Current Matrix Elements

The computation of the current multipoles (E.1e) is quite involved and will not be spelt out in detail in this appendix; it is given in Ref. [62]. For computational purposes, each current contribution  $j^{(a)}(\mathbf{Q}, \mathbf{K}_+)$  is tensorially recoupled as a tensor product of orbital, spin and isospin operators. The advantage of that calculational scheme is that most angular integrations arising in the multipole decomposition of the current can be performed analytically. However, that calculational scheme also has numerical problems, similar to those of Ref. [99] when calculating matrix elements of the irreducible three-nucleon force. The contributions arising from higher current multipoles and from higher angular momenta in the hadronic states get computationally split up into a series of rather large numbers

with alternating signs, the full results being comparatively small; thus, the straightforward evaluation of those series becomes instable. In order to avoid this problem, Ref. [20] neglected higher quantum numbers of the decomposition; that approximation was found to be quite reliable for all previous calculations. However, in this thesis I use an alternative treatment of instabilities, whose validity can be monitored much better.

The source of instabilities is an integral of the type

$$Q_\rho(q', q, k) = q' q \int d^2 \hat{\mathbf{q}}' \int d^2 \hat{\mathbf{q}} Y_m^{l'*}(\hat{\mathbf{q}}') Y_m^l(\hat{\mathbf{q}}) Y_0^\rho(\hat{\mathbf{q}}_-) \delta(q_- - k) \quad (\text{E.6})$$

with  $\mathbf{q}_- = \mathbf{q}' - \mathbf{q}$  and  $k = \frac{1}{3}|\mathbf{Q}|$ ; the dependence of  $Q_\rho(q', q, k)$  on the quantum numbers  $l'$ ,  $l$  and  $m$  is suppressed. Using the standard decomposition of spherical harmonics into separate  $\hat{\mathbf{q}}$  and  $\hat{\mathbf{q}}'$  dependences, the integration can be performed analytically; however, the result is a series of terms with alternating sign proportional to  $(q/k)^n (q'/k)^{p-n}$ . For  $q$  and  $q'$  large enough the occurring roundoff errors become much larger than the full result. Thus, such a calculational scheme can be applied safely only for  $q, q' \leq q_{\text{pmax}}(k)$ . However, in the limit  $q, q' \rightarrow \infty$  the above mentioned integration can again be performed analytically without using the decomposition formula for spherical harmonics, the result  $Q_{\rho\infty}(q' - q, k) \equiv \lim_{q', q \rightarrow \infty, |q' - q| \leq k} Q_\rho(q', q, k)$  being proportional to the Legendre polynomial  $P_\rho((q' - q)/k)$  without any other dependence on  $q'$  and  $q$ . The values of  $Q_\rho(q', q, k)$  for finite  $q, q' > q_{\text{pmax}}(k)$  with fixed  $q' - q$  are smooth and can therefore be easily and reliably obtained via a *one-dimensional* interpolation between values at  $q = q_{\text{pmax}}(k)$  and  $q \rightarrow \infty$ , i.e.,

$$Q_\rho(q', q, k) \approx \frac{q_{\text{pmax}}(k)}{q} Q_\rho(q_{\text{pmax}}(k) + q' - q, q_{\text{pmax}}(k), k) + \left[ 1 - \frac{q_{\text{pmax}}(k)}{q} \right] Q_{\rho\infty}(q' - q, k). \quad (\text{E.7})$$

The reliability of this approximation was confirmed by comparing it with the exact results obtained using higher precision floating point arithmetics.



# Bibliography

- [1] L. D. Faddeev, Zh. Eksp. Theor. Fiz. **39**, 1459 (1960), [Sov. Phys. JETP **12**, 1014 (1961)].
- [2] E. O. Alt, P. Grassberger, and W. Sandhas, Nucl. Phys. **B2**, 167 (1967).
- [3] R. Machleidt, Phys. Rev. C **63**, 024001 (2001).
- [4] V. G. J. Stoks, R. A. M. Klomp, C. P. F. Terheggen, and J. J. de Swart, Phys. Rev. C **49**, 2950 (1994).
- [5] R. B. Wiringa, V. G. J. Stoks, and R. Schiavilla, Phys. Rev. C **51**, 38 (1995).
- [6] S. C. Pieper, V. R. Pandharipande, R. B. Wiringa, and J. Carlson, Phys. Rev. C **64**, 014001 (2001).
- [7] W. Glöckle *et al.*, Phys. Rep. **274**, 107 (1996).
- [8] A. Kievsky, M. Viviani, and S. Rosati, Phys. Rev. C **64**, 024002 (2001).
- [9] K. Ermisch *et al.*, Phys. Rev. Lett. **86**, 5862 (2001).
- [10] K. Ermisch, Ph.D. thesis, University of Groningen, 2003.
- [11] K. Sekiguchi *et al.*, Phys. Rev. C **65**, 034003 (2002).
- [12] K. Sekiguchi, Ph.D. thesis, University of Tokyo, 2001.
- [13] K. Hatanaka *et al.*, Phys. Rev. C **66**, 044002 (2002).
- [14] J. Fujita and H. Miyazawa, Prog. Theor. Phys. **17**, 360 (1957).
- [15] P. U. Sauer, Prog. Part. Nucl. Phys. **16**, 35 (1986).
- [16] C. Hajduk, P. U. Sauer, and W. Strueve, Nucl. Phys. **A405**, 581 (1983).
- [17] S. Nemoto *et al.*, Few-Body Systems **24**, 241 (1998).
- [18] S. Nemoto, K. Chmielewski, S. Oryu, and P. U. Sauer, Phys. Rev. C **58**, 2599 (1998).
- [19] K. Chmielewski *et al.*, Phys. Rev. C **67**, 014002 (2003).
- [20] L. P. Yuan *et al.*, Few-Body Systems **32**, 83 (2002).
- [21] L. P. Yuan *et al.*, Phys. Rev. C **66**, 054004 (2002).
- [22] A. Deltuva, K. Chmielewski, and P. U. Sauer, Phys. Rev. C **67**, 034001 (2003).

- [23] M. Lacombe *et al.*, Phys. Rev. C **21**, 861 (1980).
- [24] A. Picklesimer, R. A. Rice, and R. Brandenburg, Phys. Rev. C **44**, 1359 (1991).
- [25] A. Deltuva, R. Machleidt, and P. U. Sauer, Phys. Rev. C **68**, 024005 (2003).
- [26] H. Pöpping, P. U. Sauer, and X.-Z. Zhang, Nucl. Phys. **A474**, 557 (1987), Nucl. Phys. **A550**, 563(E) (1992).
- [27] M. T. Peña, H. Garcilazo, U. Oelfke, and P. U. Sauer, Phys. Rev. C **45**, 1487 (1992).
- [28] M. T. Peña, H. Henning, and P. U. Sauer, Phys. Rev. C **42**, 855 (1990).
- [29] R. Machleidt, K. Holinde, and C. Elster, Phys. Rep. **149**, 1 (1987).
- [30] V. G. J. Stoks, R. A. M. Klomp, M. C. M. Rentmeester, and J. J. de Swart, Phys. Rev. C **48**, 792 (1993).
- [31] V. Stoks and J. J. de Swart, Phys. Rev. C **47**, 761 (1993).
- [32] C. R. Howell *et al.*, Phys. Lett. B **444**, 252 (1998).
- [33] S. A. Coon *et al.*, Nucl. Phys. **A317**, 242 (1979).
- [34] A. J. F. Siegert, Phys. Rev. **52**, 787 (1937).
- [35] J. Golak *et al.*, Phys. Rev. C **62**, 054005 (2000).
- [36] R. Skibiński *et al.*, Phys. Rev. C **67**, 054001 (2003).
- [37] R. Skibiński *et al.*, Phys. Rev. C **67**, 054002 (2003).
- [38] W. Struve, C. Hajduk, P. U. Sauer, and W. Theis, Nucl. Phys. **A465**, 651 (1987).
- [39] J. Adam Jr., E. Truhlík, and D. Adamova, Nucl. Phys. **A492**, 556 (1989).
- [40] J. Adam Jr. *et al.*, Nucl. Phys. **A531**, 623 (1991).
- [41] H. Henning, P. U. Sauer, and W. Theis, Nucl. Phys. **A537**, 367 (1992).
- [42] E. W. Schmid and H. Ziegelmann, *The Quantum Mechanical Three-Body Problem*, edited by H. Stumpf (Vieweg, Braunschweig, 1974).
- [43] W. Glöckle, *The Quantum Mechanical Few-Body Problem* (Springer-Verlag, Berlin, 1983).
- [44] G. Derrick and J. M. Blatt, Nucl. Phys. **8**, 310 (1958).
- [45] E. P. Harper, Y. E. Kim, and A. Tubis, Phys. Rev. C **6**, 126 (1972).
- [46] S. Nemoto *et al.*, Few-Body Systems **24**, 213 (1998).
- [47] C. R. Howell *et al.*, Few-Body Systems **2**, 19 (1987).
- [48] J. Strate *et al.*, Nucl. Phys. **A501**, 51 (1989).
- [49] A. Kievsky, Phys. Rev. C **60**, 034001 (1999).

- 
- [50] R. Bieber *et al.*, Phys. Rev. Lett. **84**, 606 (2000).
- [51] R. V. Cadman *et al.*, Phys. Rev. Lett. **86**, 967 (2001).
- [52] H. Witała *et al.*, Phys. Rev. C **63**, 024007 (2001).
- [53] J. L. Friar, D. Hüber, and U. van Kolck, Phys. Rev. C **59**, 53 (1999).
- [54] B. S. Pudliner *et al.*, Phys. Rev. C **56**, 1720 (1997).
- [55] G. Rauprich *et al.*, Nucl. Phys. **A535**, 313 (1991).
- [56] S. Buttazzoni, Ph.D. thesis, University of Basel, 1999.
- [57] M. Allet *et al.*, Phys. Rev. C **50**, 602 (1994).
- [58] J. Zejma *et al.*, Phys. Rev. C **55**, 42 (1997).
- [59] M. Allet *et al.*, Few-Body Systems **20**, 27 (1996).
- [60] K. Bodek *et al.*, Nucl. Phys. **A631**, 687c (1998).
- [61] J. Kuros-Zolnierczuk *et al.*, Phys. Rev. C **66**, 024003 (2002).
- [62] M. Oelsner, Ph.D. thesis, Universität Hannover, 1999.
- [63] C. E. Carlson, Phys. Rev. D **34**, 2704 (1986).
- [64] D. Lin and M. K. Liou, Phys. Rev. C **43**, R930 (1991).
- [65] M. A. Pickar *et al.*, Phys. Rev. C **35**, 37 (1987).
- [66] T. Yagita *et al.*, Mod. Phys. Lett. **A18**, 322 (2003).
- [67] D. D. Faul, B. L. Berman, P. Meyer, and D. L. Olson, Phys. Rev. C **24**, 849 (1981).
- [68] N. R. Kolb *et al.*, Phys. Rev. C **44**, 37 (1991).
- [69] A. J. Sarty *et al.*, Phys. Rev. C **47**, 459 (1993).
- [70] B. D. Belt, C. R. Bingham, M. L. Halbert, and A. van der Woude, Phys. Rev. Lett. **24**, 1120 (1970).
- [71] W. K. Pitts *et al.*, Phys. Rev. C **37**, 1 (1988).
- [72] J. Messchendorp *et al.*, Phys. Lett. **B481**, 171 (2000).
- [73] D. O. Riska, Phys. Scr. **31**, 107 (1985).
- [74] H. Arenhövel, Few-Body Systems **26**, 43 (1999).
- [75] T. W. Donnelly and A. S. Raskin, Ann. Phys. (N.Y.) **169**, 247 (1986).
- [76] P. Mergell, U. G. Meissner, and D. Drechsel, Nucl. Phys. **A596**, 367 (1996).
- [77] J. Golak, private communication.

- [78] P. H. M. Keizer, Ph.D. thesis, University of Amsterdam, 1986.
- [79] K. Dow *et al.*, Phys. Rev. Lett. **61**, 1706 (1988).
- [80] C. Marchand *et al.*, Phys. Lett. B **153**, 29 (1985).
- [81] A. Deltuva, K. Chmielewski, and P. U. Sauer, Phys. Rev. C **67**, 054004 (2003).
- [82] C. Hajduk, P. U. Sauer, and S. N. Yang, Nucl. Phys. **A405**, 605 (1983).
- [83] R. Machleidt, Adv. Nucl. Phys. **19**, 189 (1989).
- [84] J. Kuros-Zolnierczuk *et al.*, Phys. Rev. C **66**, 024004 (2002).
- [85] R. A. Arndt *et al.*, Phys. Rev. D **28**, 97 (1983).
- [86] J. Carlson and R. Schiavilla, Rev. Mod. Phys. **70**, 743 (1998).
- [87] J. P. Boyd, *Chebyshev and Fourier Spectral Methods* (Springer, Berlin, 1989).
- [88] G. H. Golub and C. F. Van Loan, *Matrix Computations*, 3rd ed. (John Hopkins University Press, Baltimore, 1996).
- [89] W. H. Press, S. A. Teukolsky, W. T. Vetterling, and B. P. Flannery, *Numerical Recipes in C*, 2nd ed. (Cambridge University Press, Cambridge, 1992).
- [90] W. H. Press, S. A. Teukolsky, W. T. Vetterling, and B. P. Flannery, *Numerical Recipes in Fortran 90* (Cambridge University Press, Cambridge, 1996).
- [91] K. Chmielewski, Ph.D. thesis, Universität Hannover, 1999.
- [92] C. de Boor, *A Practical Guide to Splines* (Springer Verlag, New York, 1978).
- [93] W. Glöckle, G. Hasberg, and A. R. Neghabian, Z. Phys. **A305**, 217 (1982).
- [94] G. A. Baker, *Essentials of Padé Approximants* (Academic Press, New York, 1975).
- [95] C. T. Fike, *Computer Evaluation of Mathematical Functions* (Prentice-Hall, Englewood Cliffs, New Jersey, 1968).
- [96] J. Wallis, *Arithmetica infinitorum* (Oxford, 1655, reprinted by Georg Olms Verlag, Hildesheim, 1972).
- [97] *Polarization Phenomena in Nuclear Reactions*, edited by H. H. Barshall and W. Haeberli (University of Wisconsin, Madison, 1970), p. xxv.
- [98] V. Dmitrasinovic and F. Gross, Phys. Rev. C **40**, 2479 (1989).
- [99] D. Hüber *et al.*, Few-Body Systems **22**, 107 (1997).



## Acknowledgments

Special thanks to Prof. Dr. Peter U. Sauer for giving me the opportunity to study in Hannover, for his proper guidance and many interesting discussions.

Special thanks to Dr. Karsten Chmielewski for providing me with his computer codes and for many useful discussions on practical calculations.

Special thanks to Prof. R. Machleidt for providing me with part of his computer codes and for collaboration on the potential fit.

Thanks to Prof. Dr. D. Zawischa for reading and correcting the thesis.

Thanks to Dr. J. Adam, Prof. A. C. Fonseca, Dr. J. Golak, Dr. R. Timmermans, and Dr. L. Yuan for helpful discussions.

Thanks to Dr. K. Ermisch and Dr. N. Kalantar-Nayestanaki for discussions of experimental data and for inviting me to KVI Groningen.

Thanks to experimental colleagues Dr. K. Hatanaka, Dr. J. Jourdan, Dr. J. Messchendorp, Dr. K. Sagara, and Dr. K. Sekiguchi and to Cracow group theorists Dr. J. Golak, Dr. R. Skibiński, and Prof. H. Witała for providing me with the experimental data.

Thanks to everyone who has helped me – also without direct contribution in physics – during the time I did my PhD research and who made that period more pleasant. While it is impossible to list here everybody, I would like to particularly mention Dipl. Phys. Carsten Luckmann and Dr. Stephan Venzke.

Last, but not least, I thank Deutscher Akademischer Austauschdienst (DAAD) for PhD scholarship.



## Curriculum Vitae

16.07.1976	Born in Kazlų Rūdos sav., Lithuania
1983 - 1986	Attendance of Elementary School in Jūrė
1986 - 1994	Attendance of Middle School in Kazlų Rūda
1994 - 2000	Study of Physics at Vilnius University
1998	BSc in Physics from Vilnius University
2000	MSc in Theoretical Physics from Vilnius University
2000 - 2003	PhD Study of Theoretical Physics at Hannover University

## List of Publications

1. *Breakup in Nucleon-Deuteron Scattering with  $\Delta$ -Isobar Excitation*,  
K. Chmielewski, A. Deltuva, A. C. Fonseca, S. Nemoto, and P. U. Sauer, Phys. Rev. C **67**, 014002 (2003).
2. *Nucleon-Deuteron Scattering with  $\Delta$ -Isobar Excitation: Chebyshev Expansion of Two-Baryon Transition Matrix*,  
A. Deltuva, K. Chmielewski, and P. U. Sauer, Phys. Rev. C **67**, 034001 (2003).
3. *Nucleon-Deuteron Scattering with  $\Delta$ -Isobar Excitation: Perturbation Theory*,  
A. Deltuva, K. Chmielewski, and P. U. Sauer, Phys. Rev. C **67**, 054004 (2003).
4. *Realistic Two-Baryon Potential Coupling Two-Nucleon and Nucleon- $\Delta$ -Isobar States: Fit and Applications to Three-Nucleon System*,  
A. Deltuva, R. Machleidt, and P. U. Sauer, Phys. Rev. C **68**, 024005 (2003).
5. *Trinucleon Photonuclear Reactions with  $\Delta$ -Isobar Excitation: Processes below Pion-Production Threshold*,  
A. Deltuva, L. P. Yuan, J. Adam Jr., A. C. Fonseca, and P. U. Sauer, Phys. Rev. C (to be published); nucl-th/0308045.